UC San Diego

UC San Diego Electronic Theses and Dissertations

Title

Optical Fiber Sensors for Infrasonic Wind Noise Reduction and Earth Strain Measurement /

Permalink

https://escholarship.org/uc/item/2qf3v75g

Author

DeWolf, Scott

Publication Date

2014

Peer reviewed|Thesis/dissertation

eScholarship.org Powered by the California Digital Library
University of California

UNIVERSITY OF CALIFORNIA, SAN DIEGO

Optical Fiber Sensors for Infrasonic Wind Noise Reduction and Earth Strain Measurement

A dissertation submitted in partial satisfaction of the
requirements for the degree
Doctor of Philosophy

in

Oceanography

by

Scott DeWolf

Committee in charge:

Mark A. Zumberge, Chair
Duncan C. Agnew
Michael J. Buckingham
Robert Pinkel
Michael D. Todd
Frank K. Wyatt

2014

Copyright
Scott DeWolf, 2014
All rights reserved.

The dissertation of Scott DeWolf is approved, and it is acceptable in quality and form for publication on microfilm and electronically:

_____

_____

_____

_____

_____

_____

Chair

University of California, San Diego

2014

DEDICATION

To Sarah and Delilah.

EPIGRAPH

A wise man once told me nothing.
I believe him.
—Adam DeLaMartre

TABLE OF CONTENTS

Signature Page iii

Dedication iv

Epigraph v

Table of Contents vi

List of Figures x

List of Tables xiii

Acknowledgements xiv

Vita xvi

Abstract of the Dissertation xvii

Chapter 1 Introduction 1
1.1 Geophysical Applications of Optical Fiber Sensors 2
1.1.1 Optical Fibers for Acoustics 2
1.1.2 Optical Fibers for Earth Strain 3
1.2 Electronic Distance Measurement in an Optical Fiber 4
1.3 Optical Fiber Interferometry 7
1.3.1 Real-Time Fringe Counting 11
1.4 Strain and Thermo Optic Effects 14
1.4.1 The Strain-Optic Effect 14
1.4.2 The Thermo-Optic Effect 15
1.5 Implications for Strainmeter Design 16
1.5.1 Strain and Temperature 16
1.5.2 Calibration 17
1.5.3 Maximum Strain Rate 18
1.5.4 Laser Frequency Stability 19
1.6 Organization of this Dissertation 19
REFERENCES 21

Chapter 2 Efficacy of Spatial Averaging Infrasonic Pressure in Varying Wind Speeds 23
2.1 Introduction 23
2.1.1 Global infrasonic monitoring 23

2.1.2 Wind noise reduction (WNR) methods 25
2.1.3 Rationale for this study 26
2.2 Setup 28
2.2.1 Installation and Configuration 28
2.2.2 Calibration 30
2.3 Data Analyses 31
2.4 Omnidirectional WNR Results 34
2.5 Directional WNR Results 36
2.6 Predicting directional WNR 37
2.6.1 Theory 37
2.6.2 Comparing Predicted and Observed WNR for a Line 42
2.7 Time Series Signal-to-Noise Ratio Comparison 42
2.8 Discussion 44
2.8.1 Deviation between predicted and observed WNR . 44
2.8.2 Performance of the 270 m long OFIS with respect to the IS57 array elements 45
2.9 Conclusions 46
2.10 Acknowledgments 47
REFERENCES 48

Chapter 3 Optical Fiber Borehole Strainmeter Arrays for Measuring Sediment Compaction in Bangladesh 51
3.1 Introduction 52
3.1.1 Geohazards in Bangladesh 52
3.1.2 Sediment Compaction Measurement 52
3.1.3 Rationale for this Study 54
3.2 Setup 54
3.2.1 Strainmeter Design 54
3.2.2 Deployment 56
3.2.3 Electronic Distance Measurement and Data Collection 60
3.3 Data Analyses 63
3.4 Results 68
3.4.1 Lab Tests 68
3.4.2 In-Situ Measurements 70
3.4.3 Campaign Measurements 71
3.5 Discussion 78
3.6 Conclusions and Future Work 79
3.7 Acknowledgments 80
REFERENCES 82

Chapter 4 Development of the Borehole Optical Fiber Strainmeter 83
4.1 Introduction 83
4.1.1 Strain Sensing 83
4.1.2 Rationale for this Development 85
4.2 Mechanical Design 86
4.2.1 Optical Fiber Cables 86
4.2.2 Upper Sonde 89
4.2.3 Lower Sonde and Areal Strainmeter 90
4.2.4 Wellhead 92
4.3 Optical Design 94
4.4 Fabrication and Deployment 97
4.4.1 Fabrication 99
4.4.2 Deployment 102
4.5 Laboratory and Field Tests 107
4.5.1 Areal Strainmeter Epoxy Tests 108
4.5.2 Areal Strainmeter Pressure Tests 110
4.5.3 Areal Strainmeter Load Tests 111
4.5.4 Other Post-Installation Tests 113
4.5.5 Relative Path Lengths and Calibration 115
4.6 Conclusions and Future Work 118
4.7 Acknowledgments 120
REFERENCES 121

Chapter 5 Observations from the Borehole Optical Fiber Strainmeter . . 123
5.1 Introduction 123
5.2 Data Analyses 124
5.2.1 Up-Hole Laser Wavelength Correction 125
5.2.2 Down-Hole Laser Wavelength Correction 126
5.2.3 Time and Frequency Domain Comparisons Between the Up-Hole and Down-Hole Correction Methods 128
5.3 General Observations 129
5.3.1 Time Series 129
5.3.2 Spectra 132
5.3.3 Temperature 137
5.3.4 Other Environmental Noise 138
5.4 Geophysical Signals 141
5.4.1 Earth Tides 141
5.4.2 Surface Waves 144
5.4.3 Coseismic Offsets 147
5.5 Discussion 149
5.5.1 Data Analyses 149
5.5.2 General Observations 151

5.5.3 Geophysical Signals 151
5.6 Conclusions and Future Work 152
5.7 Acknowledgments 154
REFERENCES 155

Chapter 6 The Trench Optical Fiber Strainmeter 156
6.1 Introduction 156
6.2 Design, Fabrication, and Deployment 157
6.2.1 Mechanical and Optical Design 157
6.2.2 Fabrication 163
6.2.3 Deployment 165
6.2.4 Calibration 167
6.3 Data Analyses 169
6.4 General Observations 170
6.4.1 Time Series 170
6.4.2 Power Spectra 171
6.4.3 Temperature 175
6.4.4 Wind Noise and Barometric Pressure 178
6.5 Geophysical Signals 181
6.5.1 Earth Tides 181
6.5.2 Microseisms 185
6.5.3 Surface Waves 187
6.5.4 Coseismic Offsets 192
6.6 Discussion 193
6.6.1 Design, Fabrication, and Deployment 193
6.6.2 General Observations 195
6.6.3 Geophysical Signals 197
6.7 Conclusions and Future Work 199
6.8 Acknowledgments 201
REFERENCES 202

Appendix A Borehole Optical Fiber Strainmeter Corrections 204

Appendix B Earthquakes Used In Surface Wave Analyses 212

LIST OF FIGURES

Figure 1.1: Schematic of a phase difference EDM. 5
Figure 1.2: Schematic of an optical fiber Michelson interferometer. 8
Figure 1.3: Schematic of a polarization insensitive optical fiber Michelson interferometer using the path length modulation scheme. 10
Figure 1.4: Schematic of a polarization insensitive optical fiber Michelson interferometer using a 3×3 coupler. 11
Figure 1.5: Example of how two phase-shifted interference fringe signals are converted to an optical phase difference. 13

Figure 2.1: Schematic of the two pipe arrays considered in this chapter. . . 24
Figure 2.2: OFIS schematic. 27
Figure 2.3: PFO OFIS and IS57 layout. 29
Figure 2.4: PFO OFIS Layout. 30
Figure 2.5: Interior and exterior of the calibrator used in this experiment. . 32
Figure 2.6: Median spectra for 1 to 2 and 5 to 6 m/s wind speeds. 35
Figure 2.7: Wind noise reduction (WNR) as a function of OFIS length with respect to the 18 m rosettes of IS57. 38
Figure 2.8: WNR as a function of OFIS length with respect to the 70 m rosettes of IS57 for different frequency bands and wind speeds. . 39
Figure 2.9: Signal-to-noise ratio comparison for the October 8^{th}, 2009 Delta II Vandenberg rocket launch. 44

Figure 3.1: Topographical map of Bangladesh. 53
Figure 3.2: Cutaway schematic showing the basic components of a deployed strainmeter. 57
Figure 3.3: Detailed cutaway schematics of the upper (a) and lower (b) strainmeter termination points. 58
Figure 3.4: Pictures taken during the Khulna strainmeter deployment. . . . 61
Figure 3.5: Pictures taken of each site two years after deployment. 62
Figure 3.6: Simplified strainmeter schematic. 67
Figure 3.7: Evidence for laser temperature and received intensity dependence. 68
Figure 3.8: Two year displacement time series from Jamalganj. 72
Figure 3.9: Two year displacement time series from Khulna. 73
Figure 3.10: Comparison of strainmeter displacements to collocated GPS receiver. 75
Figure 3.11: Calculated displacements at Jamalganj compared with residual temperature and borehole water level. 77

Figure 4.1: Signal amplitude as a function of characteristic event time showing where seismic, strain, and GPS technologies overlap. 84

Figure 4.2: PFO layout showing the location of BOFS as well as the three LSMs and GTSM. 87
Figure 4.3: Cutaway schematic of BOFS. 88
Figure 4.4: Upper sonde, showing the internal view in its planned design and during the actual build. 91
Figure 4.5: Lower sonde, showing the internal view this assembly in its planned design and immediately before final assembly. 93
Figure 4.6: BOFS wellhead with counterweight assembly. 95
Figure 4.7: Optical schematic for the BOFS upper, lower, and auxiliary sondes. 98
Figure 4.8: Several views of showing the assembly of the lower sonde. . . . 103
Figure 4.9: Interior and deployed views of the BOFS reference interferometer. 106
Figure 4.10: Uncorrected time series examples of the two lasers illuminating the BOFS primary vertical strainmeter. 108
Figure 4.11: Results from the wellhead concrete pad loading experiment. . . 114
Figure 4.12: Example fit between the phase output of the primary vertical strainmeter and the reference interferometer. 117

Figure 5.1: Raw primary vertical strainmeter record along with both the up-hole and down-hole correction series. 130
Figure 5.2: Cross spectra between the up-hole and down-hole corrected series. 131
Figure 5.3: 18-month time series plots of the up-hole and down-hole corrected BOFS along with the equivalent vertical strain derived from the LSM and GTSM areal strain. 133
Figure 5.4: Tided and detided time series excerpt from the previous plot. . 134
Figure 5.5: Spectra from the BOFS primary vertical strainmeter and the inferred vertical strain. 135
Figure 5.6: Combined spectra from the LSM, both up-hole and down-hole corrected BOFS, and their difference. 136
Figure 5.7: Cross spectrum between the up-hole and down-hole corrected vertical strain and borehole temperature. 139
Figure 5.8: Time series of the up-hole corrected vertical strain and several environmental observables. 140
Figure 5.9: Surface wave fit results from 1 of the 36 teleseismic earthquakes used to compare BOFS to the LSM and GTSM. 148
Figure 5.10: Example of a coseismic offset from the M4.7 Anza earthquake. . 150

Figure 6.1: Cutaway schematic of TOFS. 158
Figure 6.2: Cutaway view of the front termination fixture. 159
Figure 6.3: Cutaway schematic of the rear termination fixture assembly. . . 160
Figure 6.4: Partially exploded view of the mandrel box. 162
Figure 6.5: Mechano-optical design for TOFS. 163
Figure 6.6: Plan view and several pictures of the TOFS deployment. 168

Figure 6.7: 10-month time series plots of some of the signals under consideration in this chapter. 172
Figure 6.8: A select 50-day time series of the 180 m TOFS, after 2-day high pass filtering, along with the NWSE LSM and their difference. . 173
Figure 6.9: Individual spectra from each of the four collocated strainmeters at PFO. 174
Figure 6.10: Combined spectra from the LSM, both TOFS, and the difference between the two TOFS. 175
Figure 6.11: Strain temperature calibration factor as a function of time. . . . 177
Figure 6.12: Two adaptive sine multitaper empirical strain-temperature transfer function estimates. 179
Figure 6.13: Mean strain power versus wind speed for both fiber strainmeters and the NWSE LSM. 181
Figure 6.14: Strain-pressure empirical transfer function estimates using an adaptive sine multitaper method. 182
Figure 6.15: Tidal fits to filtered and unfiltered TOFS data. 184
Figure 6.16: Strain-strain empirical transfer function estimates using the adaptive sine multitaper method. 188
Figure 6.17: Closeup of the median strain-strain ETFEs in the microseism band. 189
Figure 6.18: Surface wave fits for the M6.9 Russian earthquake. 191
Figure 6.19: Example of a coseismic offset from the largest Brawley swarm earthquake. 194

Figure A.1: Cross spectra and time series for the up-hole temperature correction to the raw reference mandrel record. 205
Figure A.2: Cross spectra and time series for the up-hole laser wavelength correction to the raw primary vertical strainmeter record. . . . 206
Figure A.3: Cross spectra and time series for the barometric pressure correction to the up-hole-corrected primary vertical strainmeter record. 207
Figure A.4: Cross spectra and time series for the down-hole water level correction to the raw areal strainmeter record. 208
Figure A.5: Cross spectra and time series for the down-hole barometric pressure correction to the water level corrected areal strainmeter record. 209
Figure A.6: Cross spectra and time series for the down-hole laser wavelength correction to the raw primary vertical strainmeter record. . . . 210
Figure A.7: Cross spectra and time series for the final barometric pressure correction to the down-hole-corrected primary vertical strainmeter record. 211

LIST OF TABLES

Table 3.1: Table of quantities used to compute the corrected strainmeter gauge length displacement. 69
Table 3.2: Summary the Jamalganj well measurements taken before and after tensioning. 71
Table 3.3: Annual linear subsidence rates for each site. 74
Table 3.4: Jamalganj strainmeter monument positions relative to the GPS tower. 76
Table 3.5: Khulna strainmeter monument positions relative to the GPS tower. 76

Table 4.1: Scale factors relating the length of the reference interferometer to each BOFS strainmeter. 116

Table 5.1: Best-fit amplitudes and phases from the vertical and areal strain records M2 tidal constituent. 142
Table 5.2: Best-fit amplitudes and phases from the vertical and areal strain records O1 tidal constituent. 143
Table 5.3: Inferred Poisson's ratio results using the vertical and areal strain amplitudes of the best-fit M2 tidal constituent. 144
Table 5.4: Inferred Poisson's ratio results using the vertical and areal strain amplitudes of the best-fit O1 tidal constituent. 144
Table 5.5: Intercomparison of the BOFS vertical strainmeter amplitude rations for the M2 and O1 tidal lines. 145
Table 5.6: Ensemble averages for the Poisson's ratio using 36 earthquakes. . 147
Table 5.7: Intercomparison of the BOFS vertical strainmeter amplitude ratios using 36 earthquakes. 147
Table 5.8: Summary of the Poisson's ratio results from tidal lines M2, O1, and the surface wave fits. 152

Table 6.1: Least-squares fit results for the M2 tidal constituent. 185
Table 6.2: Medians and confidence intervals for the amplitude ratios of the strainmeters in the microseismic band. 187
Table 6.3: Ensemble statistics for the amplitude ratios for the strainmeters from 69 surface wave fits. 191
Table 6.4: Ensemble statistics for best-fit GTSM gauge coefficients to the 180 m TOFS strainmeter. 192
Table 6.5: Summary of amplitude ratios from the tidal, microseismic, and surface wave analyses. 197

Table B.1: Earthquakes used in the surface wave analyses. 213

ACKNOWLEDGEMENTS

This dissertation is the culmination of many years of effort that has been supported by many people at differing times and in varying amounts. Throughout this, however, has been my advisor Mark Zumberge who has not only supported me financially, but has also given me enough slack to pursue some of the new ideas presented in this work.

I am especially indebted to Kris Walker for bearing the brunt of my transition to research from years of coursework. This includes many lengthy emails, thousands of lines of codes shared back-and-forth, and hundreds of hours of discussion that have significantly shaped how I solve problems and pursue research ideas.

I have benefitted immensely from the mentorship of Frank Wyatt, whose seemingly limitless enthusiasm and advocacy has inspired me to go beyond what has been done before to advance these long baseline optical fiber sensing technologies, and to really flesh out their performance in the field to better understand what can be done to improve them in the future.

Much of the experimental work has been guided by the expertise of Glenn Sasagawa. I have matured considerably as an experimental physicist thanks to Glenn's insights, and am very appreciative of his candor during our many discussions.

This work was supported by a great number of individuals such as Joel White, Don Elliott, Billy Hatfield, Mike Kirk, Michael Davis, and Heinz Wuhrmann, whose talents and work ethic are above and beyond those of someone simply hired to do a job, and are good friends in addition to being exceptional coworkers.

Portions of this dissertation are published, being considered for publication, or are intended to be submitted for publication in various journals.

Chapter 2 is an excerpt from the publication:
Scott DeWolf, Kristoffer T. Walker, Mark A. Zumberge, and Stephane Denis. "Efficacy of Spatial Averaging Infrasonic Pressure in Varying Wind Speeds." *The Journal of the Acoustical Society of America*, 133(6), 3739–3750, 2013

Chapter 3 is currently being prepared for the publication:
Scott DeWolf, Scott L. Nooner, Michael S. Steckler, Mark A. Zumberge, Syed Humayun Akhter. "Optical Fiber Borehole Strainmeter Arrays for Measuring Sediment Compaction in Bangladesh."

Chapters 4 and 5 are currently being prepared for the publication:
Scott DeWolf, Frank K. Wyatt, and Mark A. Zumberge. "Improved Vertical Optical Fiber Borehole Strainmeter Design for Measuring Earth Strain."

VITA

2004-2006	Undergraduate Researcher, University of Wisconsin, River Falls
2006	Visiting Undergraduate Researcher, National Center for Physical Acoustics, University of Mississippi, Oxford
2007	B. S. in Physics *magna cum laude*, University of Wisconsin, River Falls
2007	B. S. in Mathematics *magna cum laude*, University of Wisconsin, River Falls
2009	M. S. in Earth Sciences, Scripps Institution of Oceanography, University of California, San Diego
2007-2013	Graduate Researcher, Scripps Institution of Oceanography, University of California, San Diego
2014	Ph. D. in Oceanography, Scripps Institution of Oceanography, University of California, San Diego

PUBLICATIONS

Scott DeWolf. *Optical and Mechanical Behavior of the Optical Fiber Infrasound Sensor*. M.S. thesis, University of California San Diego, 2009.

Scott DeWolf, Kristoffer T. Walker, Mark A. Zumberge, and Stephane Denis. "Efficacy of Spatial Averaging of Infrasonic Pressure in Varying Wind Speeds." *The Journal of the Acoustical Society of America*, 133(6):3739-3750, 2013.

ABSTRACT OF THE DISSERTATION

Optical Fiber Sensors for Infrasonic Wind Noise Reduction and Earth Strain Measurement

by

Scott DeWolf

Doctor of Philosophy in Oceanography

University of California, San Diego, 2014

Mark A. Zumberge, Chair

Fiber-based interferometers provide the means to sense very small displacements over long baselines, and have the advantage of being nearly completely passive in their operation, making them particularly well suited for geophysical applications. This work presents the development and results from four new systems: one in atmospheric acoustics and three in Earth strain.

Turbulent pressure fluctuations (wind noise) are a significant limiting factor in low-frequency atmospheric acoustic measurements. The Optical Fiber Infrasound Sensor (OFIS) provides an alternative to traditional infrasonic wind noise reduction (WNR) techniques by providing an instantaneous average over a large spatial extent. This study shows that linear OFISs ranging in length from 30 to

270 m provide a WNR of up to 30 dB in winds up to 5 m/s, in good agreement with a new analytical model.

Arrays of optical fiber strainmeters were deployed to measure sediment compaction at two sites in Bangladesh. One array at Jamalganj (in the north) consists of 20, 40, 60, and 100 m long strainmeters, while the second near Khulna (in the south) also includes lengths of 80 and 300 m. Two years of weekly measurements show a clear seasonal signal and subsidence at both sites that is in reasonable agreement with collocated GPS receivers.

A new 250-meter, interferometric vertical borehole strainmeter has been developed based completely on passive optical components. Details of the prototyping, design, and deployment at the Piñon Flat Observatory (PFO) are presented. Power spectra show an intertidal noise level of -130 dB (re. 1 ϵ/Hz), consistent within 1-3 dB between redundant components. Examination of its response to Earth tides and earthquakes relative to the areal strain recorded by an orthogonal pair of collocated, 730 m horizontal laser strainmeters yield a Poissons ratio of 0.26.

Two prototype horizontal strainmeters were also developed to explore the use of similar interferometric optical fiber technology for near-surface, long baseline strain measurement. Both instruments are shown to faithfully record earthquakes and yield very good estimates of the M2 tidal constituent, despite unexplained 2-8% amplitude discrepancies between the 90 and 180 m long instruments relative to the collocated laser strainmeter and each other.

Chapter 1

Introduction

Optical fiber sensors have a long history and a range of applications stemming from their intrinsic response of their index of refraction to strain and temperature. There are many types of optical fibers with a variety of optical characteristics, as well as diverse methods of interrogation to observe changes in their refractive index. This work focuses primarily on using standard telecommunications-grade, single mode optical fiber (Corning SMF-28 and its variants) intended for use in the infrared band (either at 1310 nm or 1550 nm), interrogated either interferometrically from a continuous wave source or by the phase of an amplitude-modulated carrier.

The purpose of this chapter is to present the two applications of optical fiber sensors pursued in this thesis as well as a brief survey of the relevant interrogation methods. The first application is the sensing of low-frequency (infrasonic) atmospheric pressure waves with the Optical Fiber Infrasound Sensor (OFIS) using interferometry. The remaining applications are for sensing Earth strain associated with earthquakes, tidal forces, sedimentary processes, and tectonics using either laser interferometry or electronic distance measurement (EDM). This is concluded with an overview of the interference fringe counting system and the basics of the strain and thermo optic effects.

1.1 Geophysical Applications of Optical Fiber Sensors

1.1.1 Optical Fibers for Acoustics

Optical fiber hydrophones have been developed for observing underwater acoustic signals since the late 1970s [13], and more recently for atmospheric acoustics, because of their high sensitivity, large bandwidth, and immunity to electromagnetic interference. Of these sensors, the design discussed here is a compliant cylinder helically wrapped with optical fiber whose pressure-induced circumferential deformation is tracked by the fiber and measured interferometrically. This sensor is known as the Optical Fiber Infrasound Sensor (OFIS) [20], and is considered in Chapter 2. The design objective of the OFIS is to exploit the advantages of optical fiber sensors to average out incoherent acoustic noise generated by wind, over as large a spatial extent as possible while still preserving coherent acoustic signals.

The current state of the art in spatial filtering for infrasonic pressure measurements are large pipe arrays with many inlets (Figure 2.1). While these have proven effective, they also have several important limitations. First, they are limited in size because they begin to attenuate coherent signals when their spatial extent is comparable to the acoustic wavelengths of interest. They are also prone to undesirable resonances at higher wind speeds (so-called organ pipe modes), and can require regular maintenance to avoid leaks. Other wind noise reduction techniques such as semipermeable enclosures can also be effective [9, 12, 7], but are equally cumbersome to deploy and maintain.

A linear interferometric microphone provides an almost instantaneous spatial average (given that the speed of light is much greater than the speed of sound), can be made almost arbitrarily long (due to the low attenuation of light in an optical fiber), and does not attenuate coherent acoustic signals propagating broadside to the sensor. Since the OFIS is both a pressure sensor and a spatial averaging noise filter, it provides an alternative to complex and high maintenance pipe arrays. Previous work has characterized the directional resolving power for different

array geometries using a varying number of line sensors (OFISs), which takes into consideration the attenuation of off-broadside incident signals with wavelengths comparable to the sensor length [16]. Given that the OFIS can provide nearly instantaneous averages of the pressure field, and that different array geometries can compensate for the coherent attenuation from long sensors, one key question addressed in Chapter 2 is what scale length is optimal (i.e., how does the wind noise reduction vary with sensor length).

1.1.2 Optical Fibers for Earth Strain

Earth strain is an important observable for geophysical deformations associated with earthquakes, slope stability (both on land and under water), ocean ridge spreading, as well as for geotechnical measurements for hydrocarbon reservoir management. While many methods exist for strain measurement, they all seek to detect changes in length, ΔL, over some baseline, L_0, to estimate the strain, $\epsilon = \Delta L/L_0$. It is often the case that the dominant source of noise comes from imperfect end-point coupling to the ground [11] and this can be improved by increasing the baseline. Optical methods are one way to observe very small changes in ΔL over very long L_0, and can be made stable for long periods of time, making them an attractive candidate for strain measurement.

One such laser strainmeter design has been deployed at the Piñon Flat Observatory (PFO) near Palm Desert, CA, three of which have been running for over four decades. These instruments consist of $\sim$730 m long unequal arm Michelson interferometers whose beam paths propagate between end monuments through 15 cm diameter evacuated tubes. In fact, while many modifications have been made to the three laser strainmeters at PFO, one has been the use of optical fiber "anchors." These correct for local motions of the near-surface end monuments by interferometrically monitoring fibers tensioned between the monuments and fixtures cemented at shallow depth [22], measuring over short distances.

Given the low cost and simpler installation of optical fibers compared to laser strainmeters, a natural extension of the optical anchor is to use fibers as the principle pathway for measuring Earth strain, especially in places inaccessible to

GPS and hostile to electronics. Optical fiber strainmeters have been developed over the past several decades to measure horizontal seafloor strain [17], and in boreholes to measure ice compaction [21, 18] and now sediment compaction (Chapter 3). A 782 m interferometric optical fiber borehole strainmeter known as the San Andreas Fault Observatory at Depth (SAFOD) strainmeter has been operating since 2004 near the fault to examine strain and earthquake behavior [4], as well as a 2,125 m borehole strainmeter near Mammoth Lakes, CA to study volcanic activity. These earlier systems each have shortcomings which limits their consideration for broader use.

1.2 Electronic Distance Measurement in an Optical Fiber

Since not all applications require the picometer displacement resolution of interferometric sensors, there is a simpler time-of-flight electronic distance measurement (EDM) technique that can determine the absolute length of an optical fiber with the resolution of several tenths of a millimeter. Commercial EDMs can be quite compact and low power, making them ideal for campaign style measurements where the expected displacement is greater than their resolution.

There are two main electronic distance measurement (EDM) techniques: the pulse time-of-flight method and phase difference method. However, it is only the EDMs using the phase difference method that are considered herein. This is the same method used by the fiber-coupled EDMs in previous experiments like the Leica Wild DISTOMAT DI2002 used in the Antarctic ice sheet compaction study [21, 18], the Dimetix DLS-A15 for interrogating the fiber optic seafloor strainmeter [5, 3], and the Dimetix DLS-C10 units used in Chapter 3.

Following the development shown by Rüeger [14], the phase difference EDM emits an intensity modulated signal y_E at an angular frequency ω that is received

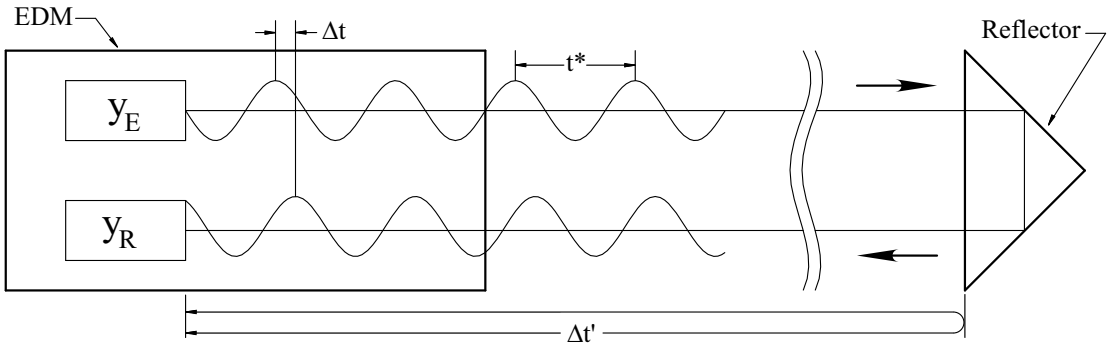


Figure 1.1: Schematic of a phase difference EDM (adapted from Rüeger [14]). Note that the times are those proportional to the distance being measured and the speed of propagation.

some time $\Delta t'$ later, denoted by y_R (Figure 1.1):

$$\begin{aligned} y_E &= A\sin(\omega t) \\ &= A\sin(\Phi) \end{aligned} \tag{1.1}$$

$$\begin{aligned} y_R &= A\sin[\omega(t+\Delta t)] \\ &= A\sin(\Phi+\Delta\Phi), \end{aligned} \tag{1.2}$$

where A is the amplitude of the modulation and apparent phase lead time Δt. Since the time difference is to a reflector, the distance can be expressed as:

$$d = \frac{c}{2}\Delta t', \tag{1.3}$$

where c is the speed of light in air. It is essential to note that since there is an integer wavelength ambiguity, and that the desired lead time Δt is related to the measured time difference $\Delta t'$ as:

$$\Delta t' = mt^* + \Delta t, \tag{1.4}$$

where m is an integer, and t^* is the propagation time of one cycle. Using the relationship $\omega = 2\pi f$ between the angular and temporal frequency f, as well as $c = f\lambda$, where λ is the wavelength, the phase shift $\Delta\Phi$ in Equation 1.2 can be expressed in terms of the desired time difference:

$$\Delta t = \frac{\Delta\Phi\lambda}{2\pi c}. \tag{1.5}$$

Substituting $\Delta\Phi = 2\pi$ into the previous equation yields the propagation time of one cycle:

$$t^* = \frac{\lambda}{c}, \tag{1.6}$$

and the measured distance can be restated by inserting Equation 1.4 into Equation 1.3 as:

$$\begin{aligned} d &= \frac{c}{2}\left(mt^* + \Delta t\right) \\ &= \frac{c}{2}\left(m\frac{\lambda}{c} + \frac{\Delta\Phi}{2\pi}\frac{\lambda}{c}\right) \\ &= m\frac{\lambda}{2} + \frac{\Delta\Phi}{2\pi}\frac{\lambda}{2}. \end{aligned} \tag{1.7}$$

Defining the "unit length" as:

$$\mathcal{U} = \frac{\lambda}{2}, \tag{1.8}$$

and the fractional unit length:

$$\begin{aligned} \mathcal{L} &= \frac{\lambda}{2}\frac{\Delta\Phi}{2\pi} \\ &= \frac{\Delta\Phi}{2\pi}\mathcal{U}, \end{aligned} \tag{1.9}$$

the measured distance simplifies to:

$$d = m\mathcal{U} + \mathcal{L}. \tag{1.10}$$

The only unknown in Equation 1.10 is the integer m, which can be determined through the use of several unit lengths by modulating at different frequencies.

As an example, consider a hypothetical EDM operating at multiple frequencies, the highest being $f_0 = 50$ MHz. By Equation 1.8, the unit length is:

$$\mathcal{U} = \frac{\lambda}{2} = \frac{c}{2f_0} \approx 2.989 \text{ m},$$

assuming that $c = 2.99 \times 10^8$ m/s, roughly the speed of light in air. To maintain millimeter repeatability in the unit length requires that the frequency be stable to 1 part in 10,000. Note that the time difference for light to propagate $\Delta d = 1$ mm in air is about 3.3 ps, which from Equation 1.5 translates to a phase difference of:

$$\Delta\Phi = \frac{2\pi c}{\lambda} = 2\pi f_0 \Delta t = \frac{4\pi f_0 \Delta d}{c} \approx 0.12^\circ.$$

As in this example, the Dimetix FLS-C10 used in Chapter 3 has a stated accuracy of about ± 1 mm. This is improved upon by about a factor of 2/3 since the speed of light in an optical fiber is inversely proportionate to its index of refraction, discussed below.

1.3 Optical Fiber Interferometry

One of the most basic optical fiber interferometers is the Michelson interferometer shown in Figure 1.2. A light source of an arbitrary initial polarization state is injected into one of the four arms of a 2×2 fused optical fiber coupler where the light is split into two paths. After propagating down their respective paths, the two light rays reflect off mirrors (retroreflectors) and return back through their same paths and recombine at the 2×2 coupler to form interference fringes.

The total optical phase of light propagating in an optical fiber can be expressed as:

$$\theta = \frac{2\pi n l}{\lambda},$$

where the index of refraction $n = c/v$ is the ratio of the speed of light in air c and the speed in the material v, l is the path length, and λ is the wavelength. The optical phase shift ϕ is related to the difference between the optical phase of the light propagating in the sensing arm θ_S and reference arm θ_R, respectively, as:

$$\begin{aligned} \phi &= \theta_S - \theta_R \\ &= \frac{2\pi n}{\lambda} (l_S - l_R) \\ &= \frac{2\pi n L}{\lambda}, \end{aligned} \tag{1.11}$$

where $L = l_S - l_R$ is the physical length difference between the two interferometer arms.

The intensity at the output of the 2×2 coupler as seen by the output (voltage) x of the photodetector can be expressed as:

$$x = a \sin(2\phi), \tag{1.12}$$

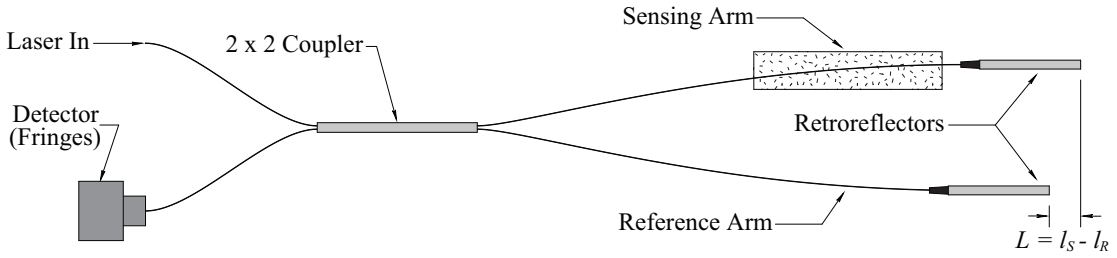


Figure 1.2: Schematic of an optical fiber Michelson interferometer. The patterned box around the sensing arm represents exposure to some environmental variable such as temperature, strain, or pressure.

where a is the amplitude, and the factor of 2 is a result of the reflection (i.e., the light travels through its path twice). Therefore, changes in the optical path length difference nL between the sensing and reference arms of the interferometer manifest themselves as changes in the output voltage of the photodetector. However, there have been two main limitations to this technique, and it is these that have been addressed in this research.

One well known difficulty with optical fiber interferometers is decreased fringe contrast caused by differential polarization changes. This occurs after the light is split in two since each pathway is then subjected to different environmental conditions (strain, temperature, pressure, etc.), and these can alter the birefringence and therefore the state of polarization in one arm relative to the other. The amplitude of the (returned) interfering light, the fringe contrast, depends upon this relative polarization state of the two returning beams; in the extreme, with orthogonal polarizations, the returning beams do not interfere with each other. This is remedied with phase-conjugating, or Faraday mirrors first used in fiber interferometers by Kersey [10]. These consist of a Faraday rotator (typically a rare-earth magnet surrounding a high Verdet constant optical material) and a plane mirror. This creates a non-reciprocal reflection that rotates the polarization state of the incoming light by 90°, forcing what had been the component of the electric field propagating along the fast axis (low n) to propagate back to the coupler along the slow axis (high n) and vice-versa. The result is return-beams restored to their original polarization (rotated by 90°) and nearly perfect fringe contrast as long as the polarization perturbations do not occur faster than the propagation time.

Faraday mirrors are compact and inexpensive, and can be used in place of the retroreflectors in Figure 1.2.

The second obstacle relates to the bidirectional phase ambiguity shown in Equation 1.12. Consider the case where the output intensity is a maximum, i.e., where the optical phase is $\phi = \pi/2$, or optical path length difference $nL = \lambda/2$. An increase or decrease in L results in a decrease in intensity seen by the photodetector, thereby making it impossible to discriminate between expansive and contractive path length changes. Two techniques used to determine directional fringe information are outlined below.

The first and older scheme for obtaining directional fringe information is the modulation-demodulation technique that is used for the Optical Fiber Infrasound Sensor in the Piñon Flat Observatory experiment (Chapter 2). This is accomplished by modulating the path length of the interferometer by a small amount ($\ll \lambda/2$) at a known frequency well above the frequency range of interest (156.25 kHz in this case) by wrapping a segment of fiber from each interferometer arm around a piezoelectric cylinder (Figure 1.3). The returned modulated fringe signal captured by the photodetector is electronically split into two signals where one is low pass filtered to obtain the original unmodulated fringe signal (i.e., x). The second is passed into a phase-sensitive detector that multiplies the signal by a square wave at the modulation frequency and low pass filters the result with a cutoff frequency well above the signals of interest. This produces a second fringe signal y that is proportional to the derivative of the original, since:

$$\Delta x = a\cos(2\phi)(2\Delta\phi)$$
$$\frac{\Delta x}{\Delta L} = a\cos(2\phi)\left(\frac{4\pi n}{\lambda}\right).$$

Defining a new amplitude $b = 4\pi na/\lambda$ to absorb the various constants results in the final form of the fringe signal derivative:

$$y = b\cos(2\phi). \tag{1.13}$$

This second fringe signal is said to be in "quadrature," or phase-shifted by 90° from the original, and takes the same form as Equation 1.12. How these two voltages x

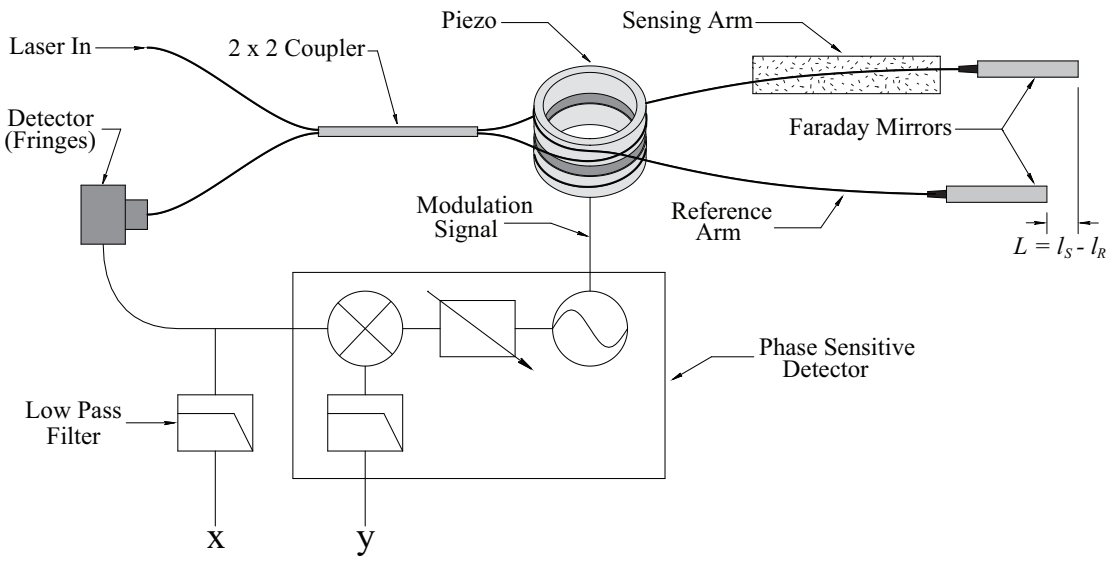


Figure 1.3: Schematic of a polarization insensitive optical fiber Michelson interferometer using the path length modulation scheme to generate the second fringe in quadrature with the first. Note that in practice the piezoelectric cylinder is split so that each arm can be modulated independently, and is arranged so that the arms are varied out of phase (i.e., one expands while the other contracts) to double the sensitivity.

and y can be used to provide the directional fringe information is given in Section 1.3.1.

The second method, new to these studies, involves exploiting the evanescent waveguide properties of the coupler used to split and recombine the two interferometer arms. Fused optical fiber couplers are fabricated by grinding down the cladding on a pair of fibers such that light "leaks" from one waveguide to the other when fused together. In addition to the amplitude being split, there is also a phase shift induced in proportion to the distance between the waveguides and the wavelength of light. For an ideal 3 dB 2×2 coupler (50/50 splitting ratio), the light in the second fiber is phase-shifted by 180°; unfortunately this provides no new information since it is just -1 times the original. However, in an evenly split 3×3 fused coupler the other two fibers undergo a 120° phase shift. Therefore, for a (polarization-insensitive) optical fiber Michelson interferometer using a 3×3 coupler (Figure 1.4), there are three fringe signals 120° phase-shifted from each other. It is then possible to take advantage of this for the recombined light returning

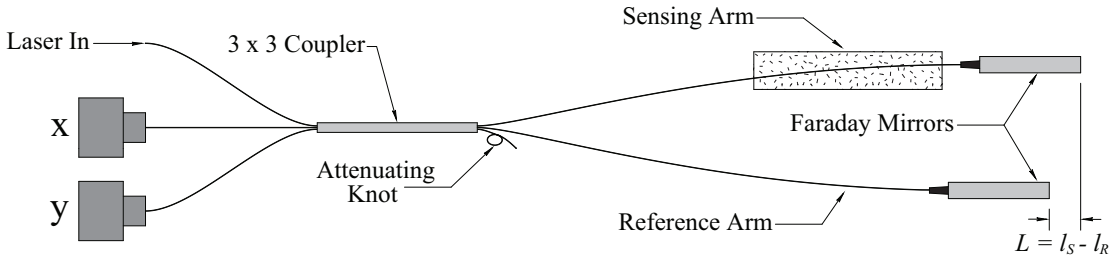


Figure 1.4: Schematic of a polarization insensitive optical fiber Michelson interferometer using a 3×3 coupler to passively generate the second fringe 120° phase shifted with the first.

from the sensing arms for resolving directional fringe information. Sheem [15] was among the first to publish results of a fiber optic gyroscope using 3×3 couplers, and there have been many dozens of other published works using this technique in Michelson and Mach-Zehnder optical fiber interferometers, and it forms the basis for both the Borehole and Trench Optical Fiber Strainmeters discussed in Chapters 4, 5, and 6.

1.3.1 Real-Time Fringe Counting

A real-time digital signal processing system has been previously developed to extract the optical phase difference from two phase-shifted interference fringe signals [19], and is used with the optical fiber interferometers presented here. This system has been dubbed the "femtometer," since initial results revealed a noise level of about 500×10^{-15} m at 1 Hz when used with a null interferometer [19]. To understand the basics of how the femtometer operates, one must recognize that the two photodetector voltages shown in Equations 1.12 and 1.13 are in the form of the (left-handed) parametric Equations of a circle. However, in practice the photodetectors are used with an amplifier and x and y are never *perfectly* in quadrature (particularly so in the case of the 3×3 couplers), requiring the definition of Equations 1.12 and 1.13 to be expanded to the parametric equations

for an ellipse of the form:

$$x = x_0 + a \sin(\Delta p + p_0) \tag{1.14}$$

$$y = y_0 + b \cos(\Delta p), \tag{1.15}$$

where x_0 and y_0 are the x and y DC-offsets, p_0 is the phase offset (sometimes called the quadrature error), and $\Delta p = 2\phi$ is the optical phase difference — the desired quantity. Equations 1.14 and 1.15 can be rearranged to solve for the optical phase difference (with the help of several trigonometric identities) to obtain:

$$\Delta p = \arctan\left[\frac{b}{a}\left(\frac{x - x_0}{y - y_0}\right)\frac{1}{\cos(p_0)} - \tan(p_0)\right]. \tag{1.16}$$

Equation 1.16 requires knowledge of the ellipse shape, i.e., the five ellipse parameters a, b, x_0, y_0, and p_0 must be estimated. This is accomplished by a least-squares fit to a collection of x, y pairs maintained in a circular buffer whose size and duration can specified depending upon the application (e.g., slowly straining systems require longer ellipse buffers to build up an adequate sampling of the ellipse perimeter). The fit itself can be mapped into a linear problem by rewriting Equations 1.14 and 1.15 in standard quadratic form [19].

It is essential to note that the codomain of the `ATAN2` function used to compute Equation 1.16 is $(-\pi, \pi)$. This implies that $\pm\pi$ phase changes happening faster than the digitizer sampling rate will limit the bandwidth of the femtometer because of ambiguities in the sign of the change. The bandwidth can therefore be increased by digitizing x, y faster and evaluating Equation 1.16 at a rate much higher (50 kHz in this dissertation) than the desired output sample rate, and adding or subtracting integer multiples of 2π when necessary. The femtometer has been designed to output the "unwrapped" optical phase difference so long as it does not exceed π radians in one digitizer sample period (20 μs). This limit is further discussed in Section 1.5.3.

Figure 1.5 shows an example of how the femtometer estimates the optical phase difference from a pair of phase-shifted interference fringe time series. The top two plots (Figures 1.5a,b) show the x and y photodetector time series for the optical phase change time series shown in the bottom panel (Figure 1.5d). Figure

1.5c presents the elliptical pattern traced out by plotting x versus y for all times along with the best-fit ellipse in red. The final trace (Figure 1.5d) shows the desired unwrapped optical phase difference time series by evaluating Equation 1.16 for each x, y pair using the five best-fit ellipse parameters. Consider the phase angle p shown in Figure 1.5c as an example, with best-fit parameters $a = b = 0.9$ Volts, $x_0 = y_0 = 1$ Volts, and $p_0 = -\pi/6$ radians. The values of x and y shown in Figures 1.4c and 1.5c as blue and green dots at $t = 0.28$ seconds, respectively, are $x = 1.56$ and $y = 1.32$ Volts. This leads to a phase estimate of approximately $p = 1.2$ radians shown by the cyan dot in Figure 1.5d.

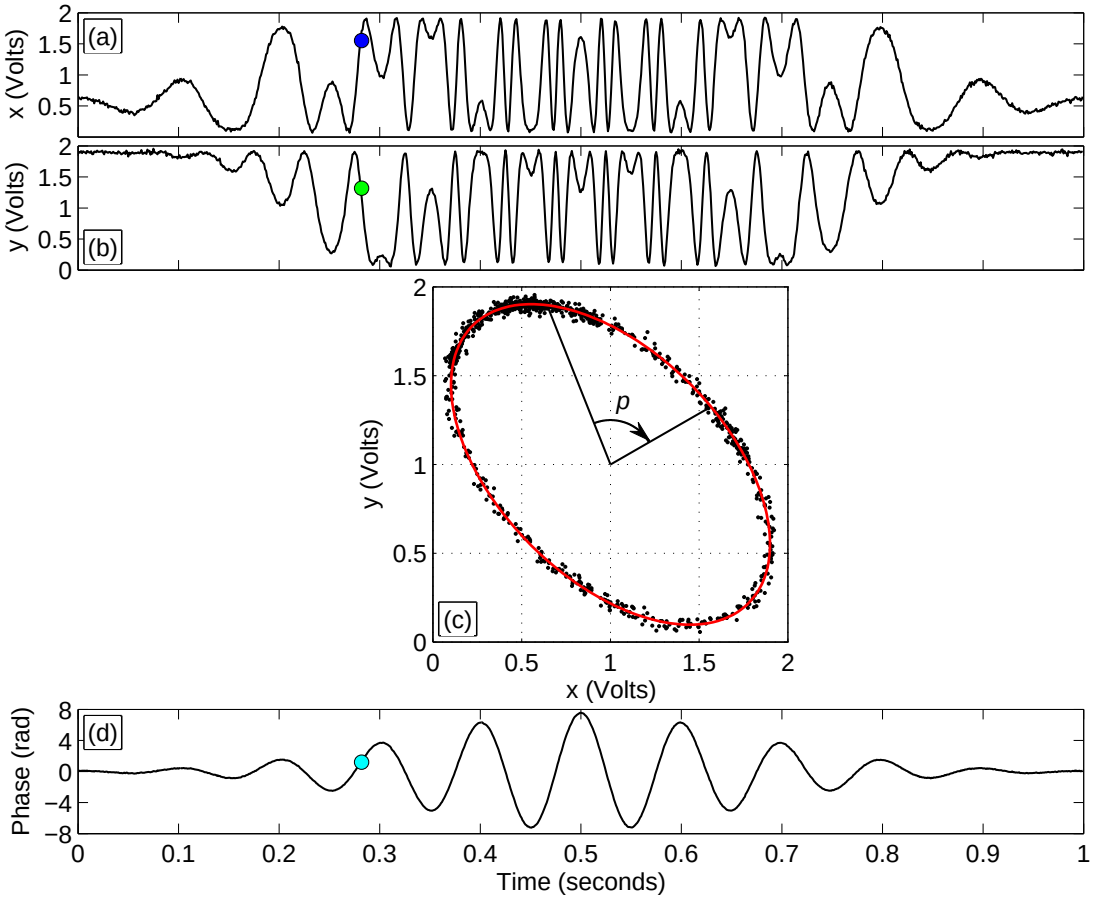


Figure 1.5: Example of how two phase-shifted interference fringe signals are converted to an optical phase difference. The blue and green dots at $t = 0.28$ seconds in (a) and (b) represent the x and y voltages that lead to the phase estimate shown by the angle p in (c) and the cyan dot in (d).

1.4 Strain and Thermo Optic Effects

Equation 1.11 states that the optical phase is a function of not only the path length difference L between the sensing and reference arms of the interferometer, but also the wavelength λ and the index of refraction n. Assuming the wavelength to be constant, the change in optical phase can be simplified to describing just the change in the optical path length:

$$L_{opt} = nL. \tag{1.17}$$

What follows are two brief derivations of how strain and temperature influence the optical path length and therefore the observed signal.

1.4.1 The Strain-Optic Effect

When strained, the change in the optical length becomes:

$$\Delta L_{opt} = n\Delta L + L\Delta n. \tag{1.18}$$

In the case of axial strain in an optical fiber, we can use the Butter and Hocker relationship [6]:

$$\Delta n = -\frac{n^3}{2}\left[\frac{\Delta L}{L}\left(1-\nu\right)p_{12} - \nu\frac{\Delta L}{L}p_{11}\right] \tag{1.19}$$

where ν is the Poisson's ratio of the optical fiber, and p_{11} and p_{12} are the two components of the isotropic strain-optic tensor (the so-called Pockel's coefficients). Therefore, the optical length as a function of the physical length becomes:

$$\Delta L_{opt} = n\Delta L - \frac{n^3}{2}\left[\left(1-\nu\right)p_{12} - \nu p_{11}\right]\Delta L \tag{1.20}$$

$$= \left(n+k\right)\Delta L \tag{1.21}$$

$$= \mu\Delta L, \tag{1.22}$$

where:

$$k = -\frac{n^3}{2}\left[\left(1-\nu\right)p_{12} - \nu p_{11}\right] \tag{1.23}$$

$$\mu = n + k. \tag{1.24}$$

Using the results of Bertholds and Dändliker [2] for a fused silica fiber and a Helium-Neon laser ($\lambda = 632.8$ nm):

$$\begin{aligned} \nu &= 0.154 \pm 0.018 \\ p_{11} &= 0.113 \pm 0.005 \\ p_{12} &= 0.252 \pm 0.005, \end{aligned}$$

but with the index of refraction of the fiber used in this dissertation (Corning SMF-28 and its variants) [1] at an infrared wavelength:

$$n\left(\lambda = 1550 \text{ nm}\right) = 1.4682,$$

such that, with the propagation of uncertainties the strain-optic coefficient is:

$$\mu = 1.158 \pm 0.012. \tag{1.25}$$

Therefore, the optical path length as a function of the physical length is simply:

$$\Delta L_{opt}\left(\Delta L\right) = \mu \Delta L. \tag{1.26}$$

Furthermore, the optical phase difference as a function of the physical length change (e.g., a strained fiber) can be expressed as:

$$\begin{aligned} \Delta p\left(\Delta L\right) &= 2\,\Delta\phi\left(\Delta L_{opt}\right) \\ &= \frac{4\pi}{\lambda}\Delta L_{opt}\left(\Delta L\right) \\ &= \frac{4\pi\mu}{\lambda}\Delta L, \end{aligned} \tag{1.27}$$

which for 1550 nm light gives a coefficient of approximately 9.4×10^{-3} radians per nanometer, or inversely about 106 nm per radian. Note that one fringe (2π radians) is the result of a physical length change of $\sim$670 nm.

1.4.2 The Thermo-Optic Effect

When a length of fiber is subjected to a temperature change, the resultant change in the optical length can be expressed as:

$$\frac{dL_{opt}}{dT} = n\frac{dL}{dT} + L\frac{dn}{dT}. \tag{1.28}$$

The optical fibers in this dissertation are anchored under tension between two points, or wrapped under tension around either a silicone rubber tube (OFIS) or an aluminum or quartz cylinder (for reference lengths). This implies that the physical expansion in the first term is controlled by the thermal behavior of what the fiber is bound to, and therefore can be ignored (i.e., $L = L_0$). This allows for the definition of the coefficient of index of refraction change per unit temperature:

$$\begin{aligned} \alpha &= \frac{1}{L_0}\frac{dL_{opt}}{dT} = \frac{dn}{dT} \\ &= (1.17 \pm 0.03) \times 10^{-5}\ ^{\circ}\mathrm{C}^{-1}, \end{aligned} \tag{1.29}$$

as empirically determined by Zumberge et al. [23], again for $\lambda = 632.8$ nm. This definition also reduces the thermo-optic relationship in terms of the optical length and physical length to:

$$\Delta L_{opt}\left(\Delta T\right) = \alpha L_0 \Delta T, \tag{1.30}$$

and in terms of optical phase (following the development of Equation 1.27):

$$\Delta p\left(\Delta T\right) = \frac{4\pi\alpha L_0}{\lambda}\Delta T. \tag{1.31}$$

For an optical fiber interferometer illuminated with $\lambda = 1550$ nm light, Equation 1.31 implies a phase change of approximately 15 radians per degree C per meter, or about 3.8×10^3 radians/°C for a $L_0 = 250$ m strainmeter.

1.5 Implications for Strainmeter Design

1.5.1 Strain and Temperature

It is essential to note that the temperature sensitivity of an optical fiber interferometer can be quite significant compared to the signals of interest, thereby leading to some rather difficult design challenges and/or elaborate compensation methods. As an example, consider again the $L_0 = 250$ m baseline optical fiber

strainmeter operating at $\lambda = 1550$ nm. Dividing Equation 1.27 by L_0, the instrument calibration factor is roughly 0.4 nϵ per radian. However, the temperature sensitivity for the same 250 m instrument is nearly 4,000 radians per °C, implying an equivalent strain-temperature relationship of $\alpha/\mu \approx 1 \times 10^{-6}\ \epsilon/\,^{\circ}\mathrm{C}$. Given that the amplitude of the solid Earth tides in the vertical is approximately 10 to 20 nϵ, implies that the temperature would have to vary less than 10 to $20 \times 10^{-4}\,^{\circ}\mathrm{C}$ to be comparable to the tidal amplitude. This is a very difficult condition to arrange, and therefore is a fundamental limitation in all the observations reported here.

1.5.2 Calibration

While the complex, helically wrapped geometry of the OFISs in Chapter 2 require calibration through experiment, the theory outlined above is adequate to derive analytical calibration factors for the vertical and horizontal strainmeters used in this work. This is already done in the case of the strainmeters used in Chapter 3, since Equation 1.26 describes the conversion between the optical path length measured by the EDM in terms of the desired physical length change. For the interferometric strainmeters, the calibration factor in units of nanostrain (nϵ) per radian of optical phase change can be found by dividing both sides of Equation 1.27 by the instrument base length L_0:

$$\begin{aligned}\frac{\Delta p}{L_0} &= \frac{4\pi\mu}{\lambda}\left(\frac{\Delta L}{L_0}\right) \\ &= \frac{4\pi\mu}{\lambda}\epsilon,\end{aligned}$$

where $\epsilon = \Delta L/L_0$. The strain-phase calibration factor C can be defined as:

$$C = \frac{\Delta p}{\epsilon},$$

which results in:

$$C = \frac{4\pi\mu}{\lambda}L_0. \tag{1.32}$$

It is essential to note that this calibration result is only applicable for straight fibers under axial stress (i.e., where the Butter and Hocker relationship in Equation 1.19 is valid).

1.5.3 Maximum Strain Rate

A very important limitation for the real-time fringe counting system used by the interferometric optical fiber strainmeters and discussed in Chapters 4, 5, and 6 is the maximum strain rate that can be measured before phase ambiguities occur as a result of a large and/or near-field event. Consider the time rate of change of the femtometer phase (Equation 1.27):

$$\frac{d\Delta p}{dt} = \frac{4\pi\mu}{\lambda}\frac{d\Delta L}{dt}, \tag{1.33}$$

Assuming a sinusoidal displacement signal of amplitude A and frequency f_A:

$$\begin{aligned}\dot{\Delta L} &= \frac{d}{dt}\left[A\sin\left(2\pi f_A t\right)\right] \\ &= 2\pi f_A A\cos\left(2\pi f_A t\right),\end{aligned}$$

the maximum displacement signal that can be tracked occurs when $2\pi f_A t$ is an integer number of π (i.e., the onset of phase-change direction ambiguities):

$$\begin{aligned}\dot{\Delta L}_{max} &= 2\pi f_A A \\ &= 2\pi\, v_{max},\end{aligned} \tag{1.34}$$

where the maximum velocity is defined as $v_{max} = f_A A$. Given that the phase must not exceed π in one sample period $1/f_s$, the maximum velocity can be determined from Equations 1.27 and 1.34 as:

$$v_{max} = \frac{f_s\lambda}{8\pi\mu}. \tag{1.35}$$

For a digitization rate of $f_s = 50$ kHz and an infrared source of $\lambda = 1550$ nm, the maximum velocity is approximately 2.5 mm/s. Since the instruments under consideration are optical fiber strainmeters, one can multiply both sides of Equation 1.35 by the instrument length L_0 to obtain:

$$\frac{v_{max}}{L_0} = \dot{\epsilon}_{max} = \frac{f_s\lambda}{8\pi\mu L_0}. \tag{1.36}$$

For an instrument $L_0 = 250$ meters in length, this translates to a maximum strain rate of about 10 $\mu\epsilon$/s.

1.5.4 Laser Frequency Stability

The behavior of the laser source is absolutely integral to the performance of the optical fiber sensor it illuminates. Both the travel time estimated by the EDM (Equation 1.5) and the measured optical phase (Equation 1.27) are a function of the laser wavelength. This implies that wavelength changes are indistinguishable from physical length changes, in other words:

$$\frac{\Delta\lambda}{\lambda_0} = \frac{\Delta L}{L_0}. \tag{1.37}$$

Since the laser wavelength is also a function of its thermal environment, it provides yet another way for temperature to appear in the strain measurement.

This relationship leads to an interesting interplay between the choice of laser and the strainmeter design. Given the lack of commercial frequency-stabilized infrared lasers, perhaps the most straight forward approach is to use an equal-arm interferometer such that wavelength fluctuations cancel out since they are common to both paths. This is the approach used for the OFIS (Chapter 2) and the horizontal strainmeters (Chapter 6). However, having an equal length of highly sensitive and delicate optical fiber in close proximity to the principle sensing fiber presents a variety of other challenges, such as how to limit its creep and exposure to other environmental variables.

Another method is to use a pair of unequal arm interferometers where one records both the desired signal with the wavelength fluctuations, while the other (ideally) only records the laser wavelength changes. This is the approach used in the SAFOD borehole strainmeter as well as those considered in Chapters 4 and 5. While this external "reference interferometer" can also suffer from creep and environmental contamination, it is much easier to isolate since it does not have to be adjacent to the sensing arm.

1.6 Organization of this Dissertation

This dissertation will cover four different instruments. The first is a linear array of Optical Fiber Infrasound Sensors (Chapter 2) and an analysis of wind

noise reduction. This represents the most recent part of my involvement with the OFIS project; the technical opto-mechanical aspects were the subject of my masters thesis [8]. Chapter 3 describes the development, deployment, and analysis from two arrays of optical fiber borehole strainmeters as a part of a large, multi-institutional collaboration for studying potential geohazards in Bangladesh. The design and deployment of a 250 m long (vertical) borehole optical fiber strainmeter is presented in Chapter 4, and observations made during its first 18 months of operation are described in Chapter 5. Chapter 6 describes both the development of and observations from two collocated horizontal optical fiber strainmeters. Step-by-step cross-spectrum and time series plots for the corrections to the vertical strain records discussed in Chapter 5 are presented in Appendix A, and a catalog of the earthquake events analyzed in both Chapters 5 and 6 are shown in Appendix B.

REFERENCES

[1] Corning® SMF-28™ Optical Fiber Product Information, April 2002.

[2] A. Bertholds and R. Dändliker. Deformation of single-mode optical fibers under static longitudinal stress. *Journal of Lightwave Technology*, 5(7):895–900, 1987.

[3] John A. Blum. *Development of sensors and techniques to assess earthquake hazards and submarine slope stability*. Ph.D. thesis, University of California San Diego, 2010.

[4] John A. Blum, Heiner Igel, and Mark A. Zumberge. Observations of Rayleigh-Wave Phase Velocity and Coseismic Deformation Using an Optical Fiber, Interferometric Vertical Strainmeter at the SAFOD Borehole, California. *Bulletin of the Seismological Society of America*, 100(5A):1879–1891, 2010.

[5] John A. Blum, Scott L. Nooner, and Mark A. Zumberge. Recording Earth Strain With Optical Fibers. *IEEE Sensors Journal*, 8(7):1152–1160, July 2008.

[6] C. D. Butter and G. B. Hocker. Fiber optics strain gauge. *Applied Optics*, 17(18):2867–2869, 1978.

[7] Douglas R. Christie and Paola Campus. The IMS infrasound network: design and establishment of infrasound stations. In *Infrasound Monitoring for Atmospheric Studies*, chapter 2, pages 29–75. Springer, Secaucus, New Jersey, 2010.

[8] Scott DeWolf. *Optical and Mechanical Behavior of the Optical Fiber Infrasound Sensor*. M.S. thesis, University of California San Diego, 2009.

[9] Michael A. H. Hedlin and Richard Raspet. Infrasonic wind noise reduction by barriers and spatial filters. *Journal of the Acoustical Society of America*, 114(3):1379–1386, 2003.

[10] Alan D. Kersey, M. J. Marrone, and Michael A. Davis. Polarisation-Insensitive Fibre Optic Michelson Interferometer. *Electronics Letters*, 27(6):518–520, 1991.

[11] John Langbein, Frank K. Wyatt, Hadley Johnson, Duane Hamann, and Paul Zimmer. Improved stability of a deeply anchored geodetic monument for deformation monitoring. *Geophysical Research Letters*, 22(24):3533–3536, 1995.

[12] L. Liszka. Infrasound: a summary of 35 years of infrasound research. IRF Scientific Report 291, Swedish Institute of Space Physics, Umeå, Sweden, 2008. ISBN 978-91-977255-0-7, 150 pages.

[13] Phillip J. Nash. Review of interferometric optical fibre hydrophone technology. *IEE Proceedings - Radar, Sonar and Navigation*, 143(3):204–209, 1996.

[14] Jean M. Rüeger. *Electronic Distance Measurement: An Introduction*. Springer-Verlag, Berlin, third edition, 1990. 266 pages.

[15] Sang K. Sheem. Fiber-optic gyroscope with [3×3] directional coupler. *Applied Physics Letters*, 37(10):869–871, 1980.

[16] Kristoffer T. Walker, Mark A. Zumberge, Michael A. H. Hedlin, and Peter M. Shearer. Methods for determining infrasound phase velocity direction with an array of line sensors. *The Journal of the Acoustical Society of America*, 124(4):2090–2099, 2008.

[17] Mark A. Zumberge. Precise optical path length measurement through an optical fiber: Application to seafloor strain monitoring. *Ocean Engineering*, 24(6):531–542, June 1997.

[18] Mark A. Zumberge. Vertical strain determination in the Antarctic ice sheet using optical fibers. *Proceedings of SPIE*, 5050:52–60, 2003.

[19] Mark A. Zumberge, Jonathan Berger, Matthew A. Dzieciuch, and Robert L. Parker. Resolving Quadrature Fringes in Real Time. *Applied Optics*, 43(4):771–775, February 2004.

[20] Mark A. Zumberge, Jonathan Berger, Michael A. H. Hedlin, Eric Husmann, Scott L. Nooner, Richard Hilt, and Rudolf Widmer-Schnidrig. An optical fiber infrasound sensor: A new lower limit on atmospheric pressure noise between 1 and 10 Hz. *The Journal of the Acoustical Society of America*, 113(5):2474–2479, 2003.

[21] Mark A. Zumberge, Daniel H. Elsberg, William D. Harrison, Eric Husmann, John L. Morack, Erin C. Pettit, and Edwin D. Waddington. Measurement of vertical strain and velocity at Siple Dome, Antarctica, with optical sensors. *Journal of Glaciology*, 48(161):217–225, January 2002.

[22] Mark A. Zumberge and Frank K. Wyatt. Optical Fiber Interferometers for Referencing Surface Benchmarks to Depth. *Pure and Applied Geophysics*, 152:221–246, 1998.

[23] Mark A. Zumberge, Frank K. Wyatt, Dong X. Yu, and Hideo Hanada. Optical fibers for measurement of earth strain. *Applied Optics*, 27(19):4131–4138, October 1988.

Chapter 2

Efficacy of Spatial Averaging Infrasonic Pressure in Varying Wind Speeds

2.1 Introduction

2.1.1 Global infrasonic monitoring

Infrasound travels thousands of kilometers through atmospheric ducts with relatively little attenuation [13]. Measurement of infrasound in the 0.02 Hz to 10 Hz band has been of interest to atmospheric physicists since barometers around the world inadvertently recorded infrasound from the 1883 eruption of Krakatau [6]. More recently, measurements of infrasound have been used for verification of nuclear test ban treaty compliance, as both underground and atmospheric explosions generate infrasound.

The Preparatory Commission for the Comprehensive Nuclear Test Ban Treaty Organization (CTBTO) has established 60 infrasonic detector arrays around the world [3]. Each array in this International Monitoring System (IMS) includes several microbarometers. The recorded noise associated with increasing winds, so familiar to us in the audio band, is also a severe problem in the infrasonic band. To reduce such noise, most IMS microbarometers are connected through an array

of pipes to a series of inlet ports distributed on the ground around it to perform spatial averaging [1, 2]. While the method does reduce wind noise, it suffers from a number of difficulties, mostly because the design requires the propagation of low-frequency sound through the pipes to the sensor [8, 7]. Typically the pipe arrays consist of dozens of inlets distributed in a circular pattern ranging in diameter from 18 to 70 m (Figure 2.1). Larger arrays could reduce the noise level further, but they attenuate the desirable infrasound at frequencies of interest, effectively limiting the signal-to-noise gain one can achieve with rosettes.

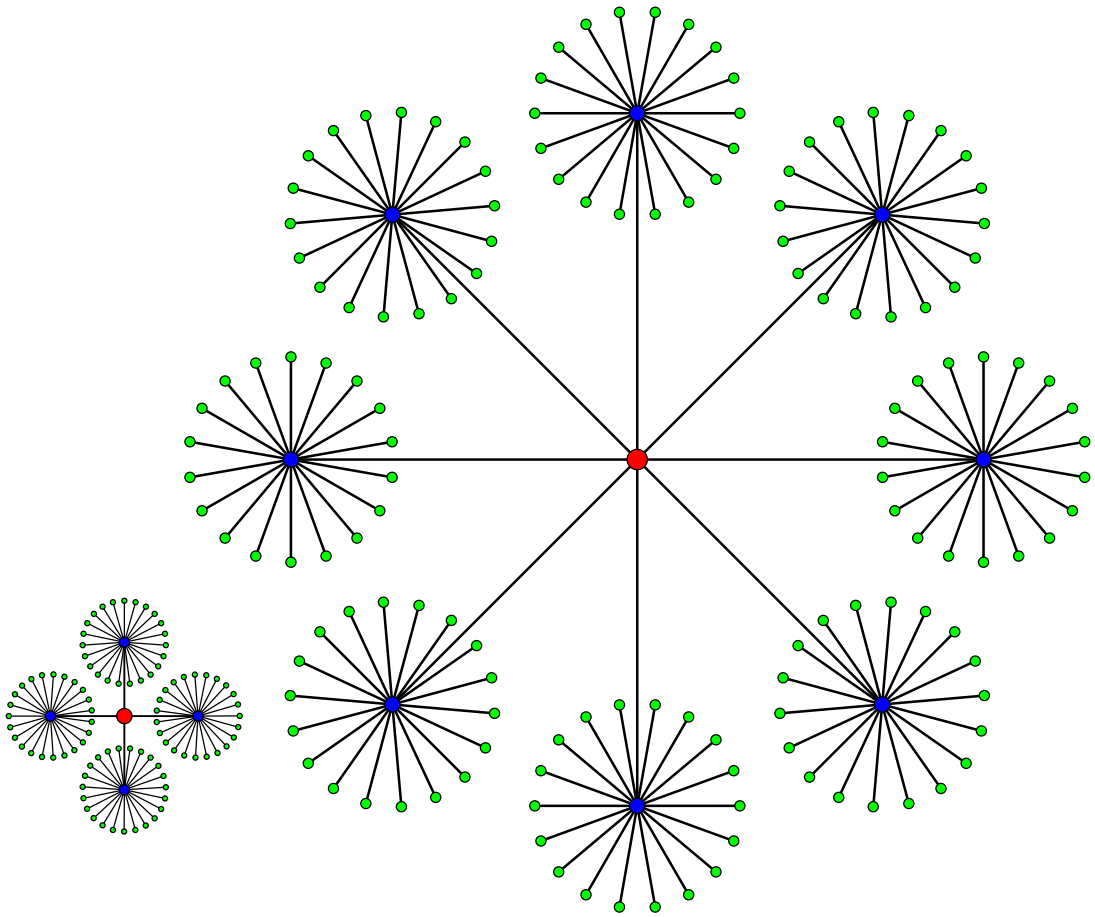


Figure 2.1: Schematic of the two pipe arrays considered in this chapter, with the 92-inlet, 18 m diameter shown in the lower left corner and the 144-inlet, 70 m diameter shown on the right. The central red circles represent the location of the central summing manifold and the microbarometer. The blue circles are the locations of the subarray manifolds that sum the pressure field at the inlets shown in green.

2.1.2 Wind noise reduction (WNR) methods

The theory of wind noise is an area of active research. There are several types of wind noise. The three main types that were first introduced and investigated by Raspet [16] are stagnation pressure fluctuation, turbulence-turbulence interaction, and turbulence-mean shear interaction. An important source of noise on IMS infrasonic arrays is likely stagnation pressure fluctuation noise, which occurs when the wind velocity blowing over a sensor (or inlet mesh) is fluctuating. The stagnation pressure is the pressure that forms at the front of the sensor owing to the impact of the wind. Therefore, variations in wind velocity (due to turbulence) lead to measured variations in pressure. This type of wind noise is mitigated by making the sensor (or inlet) more aerodynamic or larger in surface area. However, the predominant type of wind noise observed by IMS infrasonic stations is likely turbulence-mean shear interaction [16], which is important on or just above the ground where there exists a significant vertical gradient of the mean horizontal wind speed. Horizontal changes in vertical wind velocities in turbulence cells interact with this vertical gradient in horizontal wind to create pressure anomalies. Both of these sources of wind noise are effectively advected across the sensor or inlet at the mean horizontal wind speed.

There are a number of other methods to reduce wind noise in its various forms. We briefly mention three of these below; a review is presented by Walker and Hedlin[20]. In a number of cases, a wind filter has been formed from a set of inexpensive microporous irrigation hoses connected to a microbarometer inlet port. One IMS station (IS59, Hawaii) uses these as the primary filter. Recently problems with this filter have become apparent; the instrument response is not easily predictable, and the performance of the filter varies with time and environmental conditions [15, 11].

Another approach is to bury microbarometers in rigid porous media. Herrin predicted WNR by analyzing the downward propagation of pressure variations though media [10]. Yu, et. al theoretically and experimentally investigated the potential WNR for below-ground microphones covered by aluminum foam [23, 22]. We performed experiments using several types of porous media that confirm burial

of microbarometers (or inlets) in gravel can improve the signal-to-noise ratio by several dB in light to moderate wind (2 to 4 m/s), but only for frequencies above ∼1 Hz.

Lastly, wind barriers have been constructed around microbarometers to stop the flow of wind over them [9, 14, 3]. Although encouraging, preliminary results show differences in the performance of these structures. Hedlin and Raspet analyzed the efficacy of a compact wind filter and conclude that such filters may only provide an effective spatial average of the pressure field along the enclosure walls, implying that such enclosures over a rosette would not provide additional signal-to-noise improvement [9]. However, Christie and Campus found that the wind noise experienced by a 12-m diameter, six-inlet reference pipe array was 5 to 20 dB higher (at 1 Hz) than that recorded by an adjacent six-inlet pipe array surrounded by a wind filtering enclosure [3]. The extent to which the number of inlets in the pipe arrays influenced the results is unknown. Specifically, if the Hedlin and Raspet hypothesis is correct, then a larger number of inlets in the pipe arrays would lead to a convergence between the WNR purely from the enclosure and that purely from the pipe array, implying no gain in WNR would be achieved by retrofitting existing IMS rosettes.

2.1.3 Rationale for this study

The Optical Fiber Infrasound Sensor (OFIS) [24] uses optical fibers helically wrapped around a 2.5-cm diameter compliant tube to measure the instantaneous average pressure variation along the tube length (Figure 2.2). Given the low attenuation of light in an optical fiber, the OFIS can be made almost as long as desired. The flexibility of the OFIS allows it to be deployed in nearly any geometric shape. Many have been deployed in array configurations with sensor lengths from 1 to 90 m, almost exclusively as straight lines to exploit their high directivity using array processing techniques [21].

Since the OFIS does not rely on pressure waves propagating inside a tube to a point sensor, and the measurement is done using lasers at the speed of light, the practical limit to the size of an OFIS is far beyond that of a pipe array. Further-

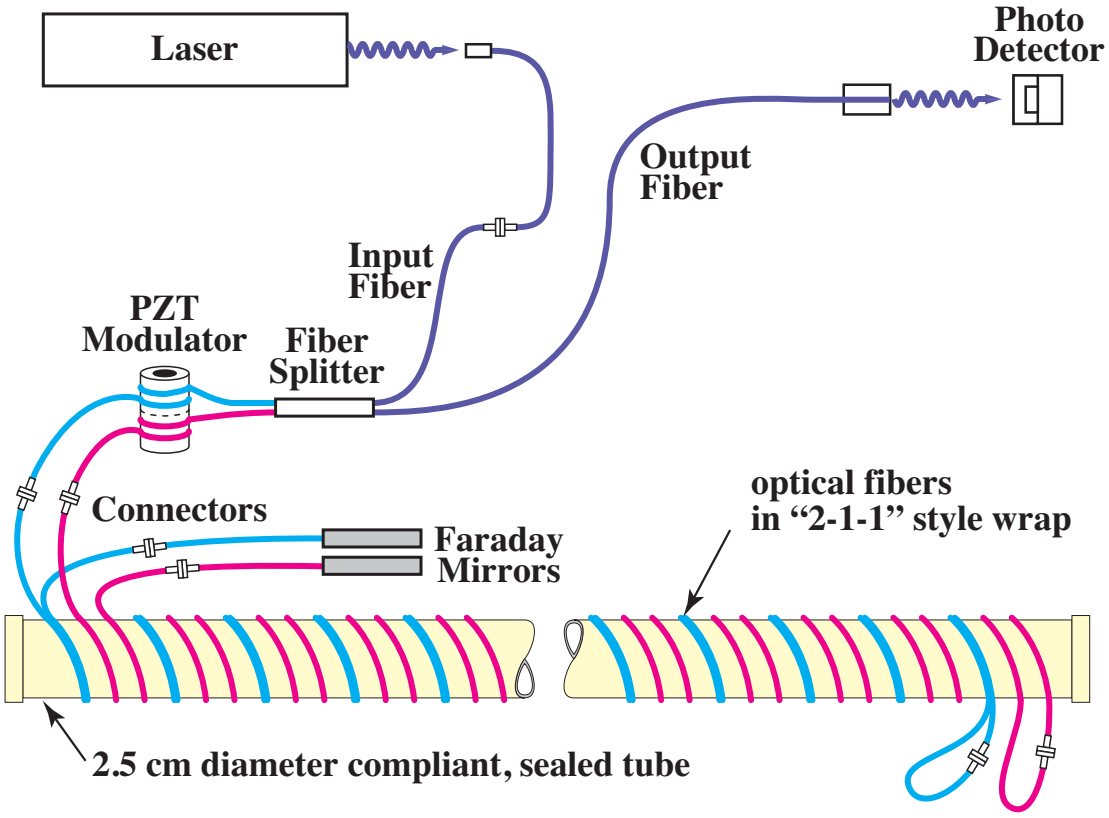


Figure 2.2: OFIS schematic. The OFIS is a Michelson interferometer that measures the volumetric change of a sealed compliant tube imparted by a passing pressure wave. The double wrapped fiber (blue) deforms less than the single wrapped fiber (red), thereby providing a fringe signal when the two fibers are recombined on the output side of the fiber splitter.

more, the OFIS provides a truly continuous average of the pressure signal along its length that could only be achieved with a dense array of point microphones. It is therefore useful to learn the extent to which WNR can be improved by increasing OFIS length.

We investigated the directional wind noise reduction capabilities of a line sensor by measuring WNR as a function of OFIS length. We analyzed recordings from linear OFISs with lengths varying from 30 to 270 m buried in gravel subjected to a range of wind speeds. This experiment was done at Piñon Flat Observatory (PFO) in southern California during 2009 and 2010. As a reference we used the eight collocated elements (four 18 m diameter rosettes and four 70 m diameter rosettes connected to MB2000 microbarometers) of the recently revalidated IMS

IS57 (Piñon Flat, CA) infrasonic array. We conclude this analysis with a time series example of an infrasonic signal recorded at the Piñon Flat Observatory by the 270 m OFIS and IS57 infrasound array.

2.2 Setup

2.2.1 Installation and Configuration

Nine 30-m long, linear OFISs were installed end-to-end in southern California at the Piñon Flat Observatory (PFO), adjacent to the IS57 infrasound array (Figure 2.3) during the summer of 2009. These were deployed along a line north-northeast to south-southwest (29° clockwise from north), buried approximately 20 cm below ground, and covered with 6-mm diameter gravel. Three primary junction boxes were installed at the head of each set of three OFISs for sending and receiving light and making pneumatic connections for in situ calibration. Secondary junction boxes were installed between each of the remaining OFISs for inter-OFIS optical and pneumatic connections. This allowed for simultaneous operation of up to three OFISs whose lengths could be reconfigured in multiples of 30 meters (Figure 2.4).

The first data collected with the nine 30 m segments were from a configuration as a single 270 m OFIS in late 2009. Along with the standard eight MB2000 sensors that were connected to rosettes of the IS57 array, a Chaparral 50 microphone was connected to element L2 for two weeks. The OFISs were reconfigured in 2010 as sensors of 30, 60, and 180 m in length. Approximately three weeks of data were acquired in this configuration. In 2011, the first 30 m of the 180 m OFIS was added to the 60 m to form a 90 m OFIS, while the remaining 150 m was used to form the third OFIS. We left the original 30 m OFIS unmodified to maintain a connection between the 2010 and 2011 data sets. While about two weeks of data were acquired, a bad digitizer rendered the 150 m OFIS data unsuitable for publication. However, the 30 and 90 m data from 2011 are used in Section 2.3.

The wind data was collected with a Vaisala WXT-510 combination weather station that was installed about 200 m away from the center of the OFIS line at a

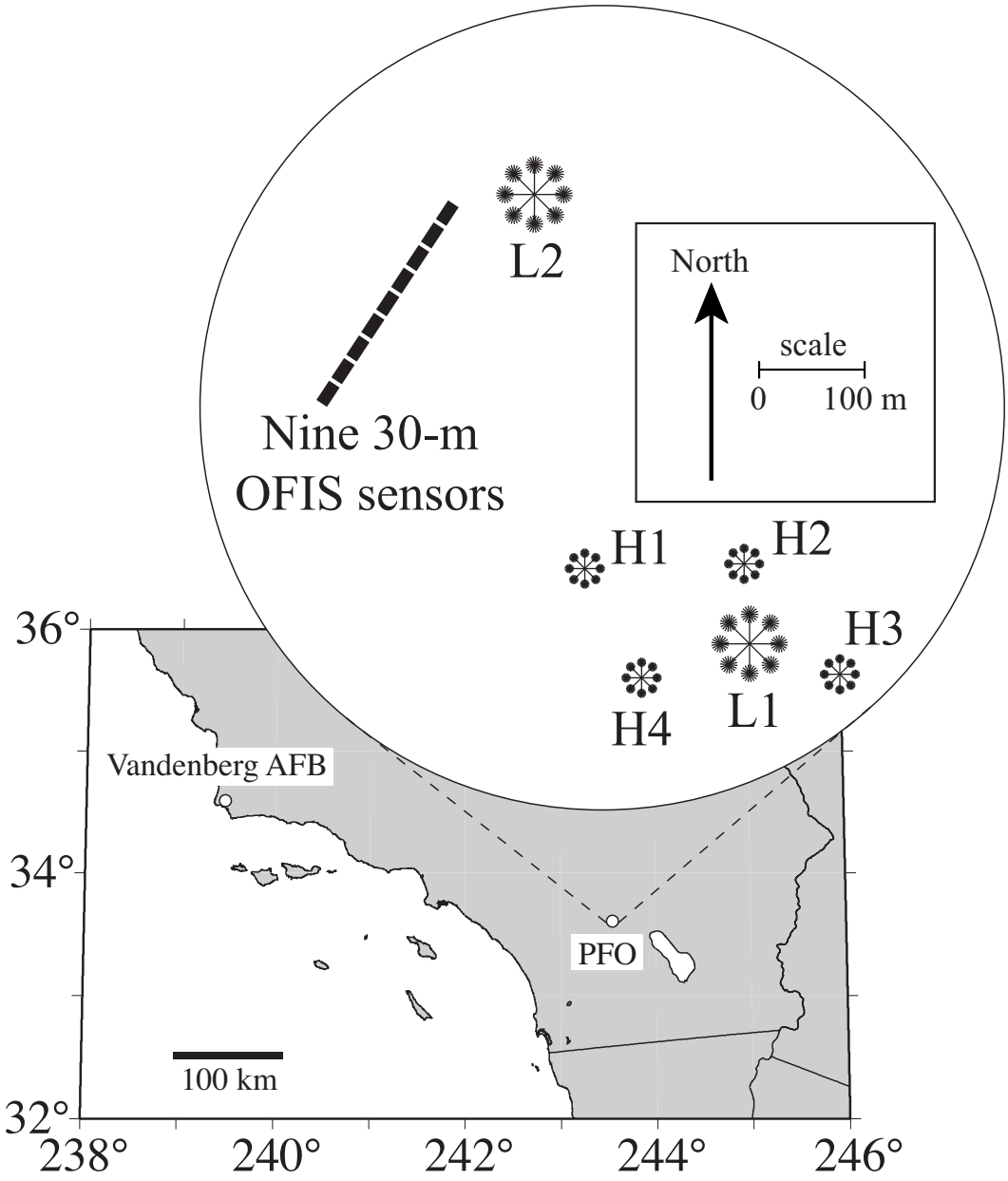


Figure 2.3: PFO OFIS and IS57 layout. Circular clusters indicate the locations of some of the circular spatial averaging rosettes of the IS57 infrasonic array. The IS57 rosette filters have two diameters. The high-frequency (H) and low-frequency (L) filters have diameters of 18 and 70 m, respectively. The nine 30 m OFIS segments start near IS57 L2 element and run to the south-southeast. The 30, 60, and 180 meter OFISs used were the first, the second and third, and fourth through ninth 30 m segments, respectively, starting from the north-northeast (i.e. closest to L2).

height of 2.5 m above the ground. This device includes an ultrasonic anemometer that recorded wind speed and direction throughout both experiments with accuracies of ±0.3 m/s in wind speed and ±3° in azimuth.

2.2.2 Calibration

Previous unpublished studies have found that the OFIS has a flat response to broadside signals from about 20 mHz to 1 kHz. We calibrated each OFIS segment in the lab and in-situ after installation at PFO using a calibrator system of original design (Figure 2.5). This unit contains a 17 cm diameter loudspeaker sealed to a plate with a pneumatic outlet to divert the pressure induced by driving the loudspeaker to both the OFIS interior and a Setra 265 calibrated pressure transducer. For the lab calibrations, the loudspeaker is driven with a 0.5 Hz sinusoid at five different amplitudes. The calibration factor in units of Pascals per radian of optical phase change was found by a linear least-squares fit to the amplitudes of the Setra versus the OFIS.

Since the calibration factor for the OFIS is known to vary with temperature [4], each OFIS was calibrated in the field before collecting the wind noise data.

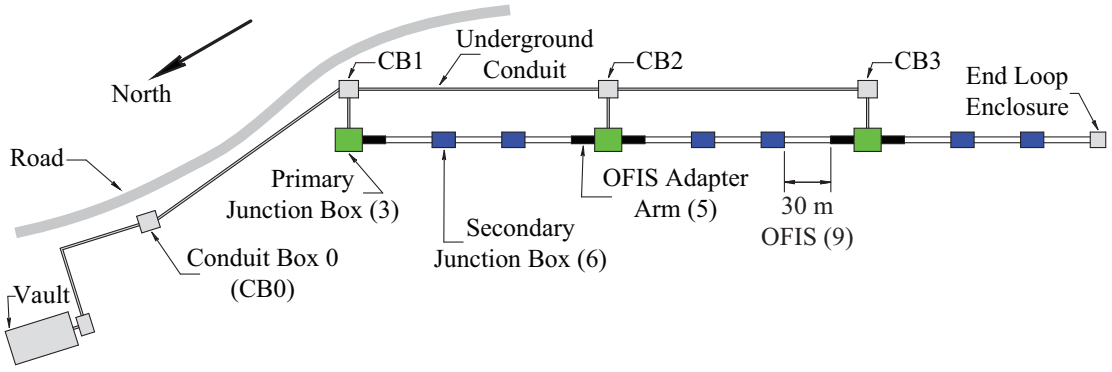


Figure 2.4: PFO OFIS Layout. (a) The nine 30 m OFIS and the primary (green) and secondary (blue) junction boxes with a path to the vault containing the laser and femtometer. (b) The inside of the primary junction box containing the calibrator (labeled as "CAL-108," the design of which is discussed in Section 2.2.2) near the top and "modulator box" (holding the fiber-wrapped piezoelectric cylinder, 2×2 coupler, and Faraday mirrors) at the bottom. (c) The inside of the secondary junction box where the OFIS can either terminate or pass through.

For the 2010 experiment, HOBO U23-004 temperature loggers were installed at the center of each 30 m OFIS segment immediately adjacent to the silicone tube. A 0.5 Hz sinusoidal pressure signal at a constant amplitude was applied to the interior of the three OFISs for 48 hours. The resultant temperature dependence was found by bandpass filtering the Setra and OFIS time series, computing their envelope functions (via the Hilbert transform), and performing a least-squares fit between the ratio of the envelope functions and the HOBO temperature data. The results were (in percentage relative to 20°C):

$$\left(\frac{1}{C}\frac{dC}{dT}\right)_{30\,m} = -1.18 \pm 0.15\,\%\ ^{\circ}\mathrm{C}^{-1} \tag{2.1}$$

$$\left(\frac{1}{C}\frac{dC}{dT}\right)_{60\,m} = -3.40 \pm 0.43\,\%\ ^{\circ}\mathrm{C}^{-1} \tag{2.2}$$

$$\left(\frac{1}{C}\frac{dC}{dT}\right)_{180\,m} = -2.17 \pm 0.24\,\%\ ^{\circ}\mathrm{C}^{-1}. \tag{2.3}$$

The 5^{th} to 95^{th} percent confidence temperature range experienced by the OFIS during the three week data collection period was approximately 2.3°C, which translates into a variation of about 0.2 to 0.6 dB throughout the course of the 2010 experiment.

The calibration factors were further tested by comparing their recordings of the microbaroms in very low-wind conditions (0-1 m/s) to those from the IS57 array elements. We found that the median power spectral densities of the OFISs in the microbarom range of approximately 0.15 to 0.30 Hz agreed with those of the IS57 elements. Even though the elements average over differently shaped paths, the comparison is valid because the microbarom wavelengths are much longer than the OFIS lengths and rosette diameters.

2.3 Data Analyses

A well-known method of analyzing the performance of WNR methods is to compare the power spectral densities of the recorded pressure time series under different wind conditions. In the absence of background acoustic energy or high levels of sensor self-noise, the recorded pressure "noise spectrum" is the convolu-

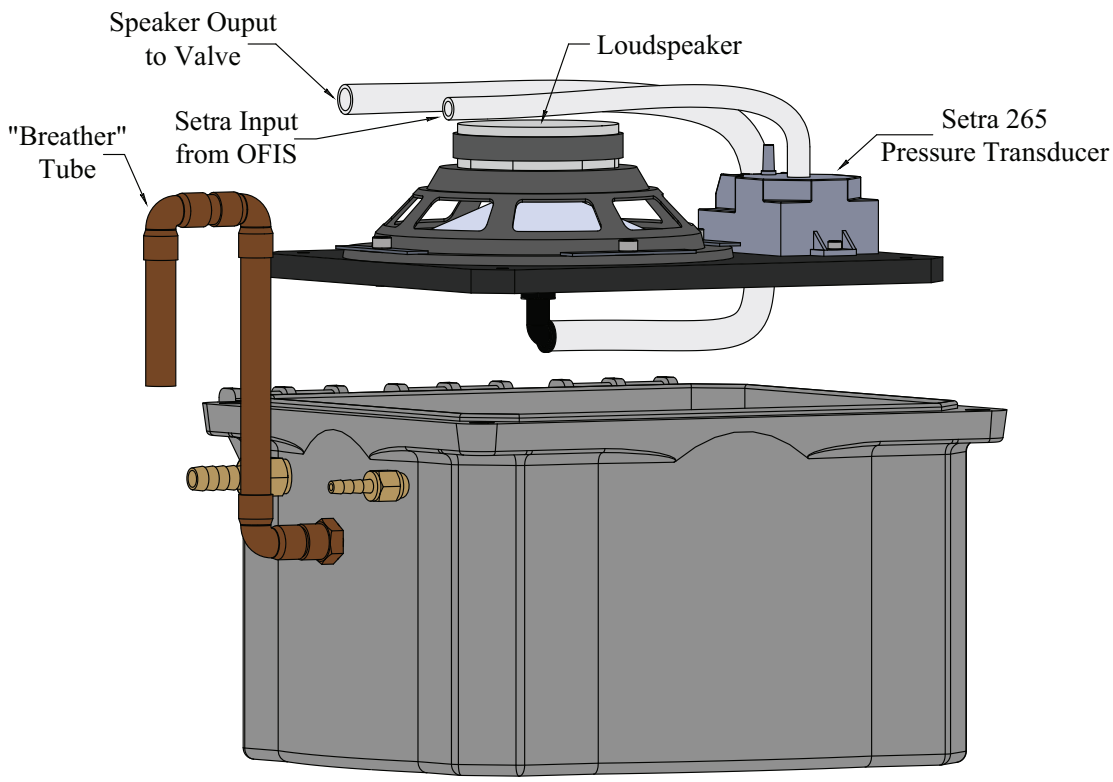


Figure 2.5: Interior (above) and exterior (below) of the calibrator used in this experiment. This unit contains a speaker sealed to a plate with an outlet that diverts pressure to the interior volume of the OFIS and a Setra 265 pressure transducer. Note that the calibration pneumatics are connected to a valve to remove the speaker diaphragm from the OFIS volume during wind noise data collection while leaving the Setra connected.

tion of the wind filter response, sensor response, and the continuously evolving turbulence field advected across the wind filter. It is generally thought that the statistical representation (via time averages) of the turbulence field at the ground surface is repeatable for the same wind speeds and directions [18, 12]. We make the same assumption, which implies that power spectra of long pressure time series recorded in similar winds yield similar noise spectra.

Since it is difficult to obtain long time recordings in consistent winds, we segment our pressure recordings into 50 second, non-overlapping time windows. These time series segments are sorted based on their average wind speed and direction into 1 m/s wind speed and 22.5° azimuthal bins. This defines several hundreds to many thousands of time windows for each wind speed and direction

bin. A Hamming-weighted periodogram spectrum estimate is made for each time window. The median spectrum is computed for each wind speed without regard to azimuth for omnidirectional analysis, and for each wind speed and direction for directional analysis.

Although the number of actual contiguous OFIS lengths in the 2010 Piñon Flat experiment were only 30, 60, and 180 m, we digitally summed (in post-processing) different combinations of the shorter OFISs to obtain recordings of what would have been recorded by OFISs of different lengths. For example, an OFIS recording of 90 m length can be constructed by summing the 30 m OFIS recording that is weighted by a factor of 1/3 and the contiguous 60 m OFIS recording weighted by a factor of 2/3. Using this approach, we used the 30, 60, and 180 m OFIS time series segments collected in 2010 to create time series and spectra for 90, 210, 240, and 270 m OFISs.

There is little reason to doubt the validity of this approach; in one case the records are summed digitally in post-processing, in the other they are summed optically in real time. Nevertheless, we compared the median spectra of the estimated 90 m OFIS from 2010 with the median spectra of an actual 90 m OFIS recorded in 2011. The R^2 value between the two ranges from 0.96 to 0.99. We also compared the median spectra from the 30 m OFIS in 2010 with the same 30 m OFIS in 2011 for the same wind speeds and directions. The correlation had about the same level of variation (R^2 was 0.95 to 0.99), suggesting that the variation in both cases was simply due to time-dependent changes in the atmosphere and that our length-weighted averaging method for estimating OFIS time series of different lengths was valid.

The space in which WNR can be evaluated has many dimensions: OFIS length, rosette size, wind speed, wind direction, and frequency. For our analyses that do not take into account wind direction, we present noise spectra from two different wind speeds spanning frequencies from 0.1 Hz to 10 Hz for one set of experiments and from 0.02 to 10 Hz for another, covering most of the band of interest for nuclear test monitoring. When we add yet another variable — wind direction — the number of full spectral plots needed to convey the results becomes

unmanageable. Instead we plot values of the spectra integrated over two bands: 0.1 to 1 Hz and 1 to 5 Hz. These limits were selected to avoid non-wind-related noise in the two sensor types: thermal noise below 0.1 Hz in the OFIS and pipe resonance noise above 5 Hz in the case of the rosettes. For every time window the integrated OFIS spectral values were compared to those from the 18 and 70 m rosettes to compute the WNR of the OFIS relative to rosettes as a function of OFIS length. We did this for both winds that were roughly parallel (downwind) and perpendicular (crosswind) to the OFIS. Therefore, for each of the seven OFIS lengths, there are four empirically derived calculations of WNR improvement for each frequency band. We used the bootstrap method with the spectral ratios to estimate the uncertainty [5].

2.4 Omnidirectional WNR Results

Figure 2.4 shows the omnidirectional median spectra for data collected in 2009 and 2010 under light winds (1-2 m/s) and moderate winds (5-6 m/s). In the upper plot we compare spectra from the 270 m OFIS obtained in 2009 to spectra from the median of the four 18 m and the four 70 m rosettes connected to MB2000 microbarometers. A spectrum estimate from a Chaparral 50 microbarometer connected to the L2 rosette (70 m) is also shown to permit the discrimination of features in the spectra otherwise obscured by the self-noise of the standard MB2000. The lower plot also shows the median 18 and 70 m rosette spectra with the spectra from the shortest (30 m) and longest (270 m) OFIS lengths recorded in 2010. Both plots show the effects of anti-aliasing filters at about 5 and 8 Hz for the OFIS and IS57 elements, respectively.

There are several features of the OFIS spectra in low-wind conditions. At frequencies below the microbarom peak, the spectral levels of the OFISs appear to match, at best, those of the rosettes. The small mismatch with the Chaparral 50 spectra is most likely due to the thermal behavior of the OFIS; an effect that is attenuated, especially at higher frequencies, by the OFIS insulation, burial, and spatial averaging property [24]. Comparison at higher frequencies is more difficult

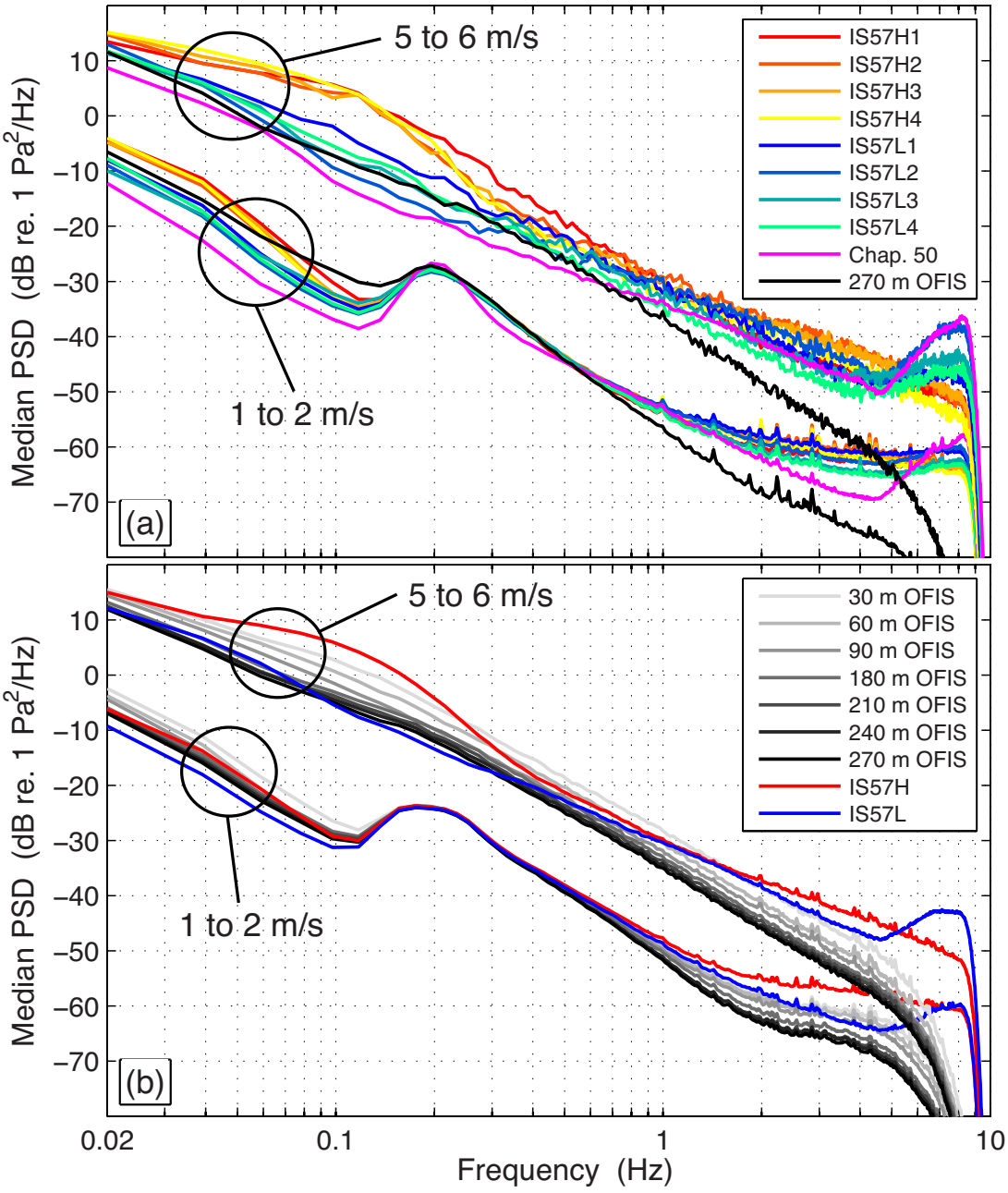


Figure 2.6: Median spectra for 1 to 2 and 5 to 6 m/s wind speeds. (a) The 270 m OFIS spectra are compared with all eight the rosette spectra as well as the Chaparral 50 connected to L2 for the 2009 experiment. (b) The spectra for the seven OFIS lengths are compared with the median 18 and 70 m rosette spectra for the 2010 experiment.

given the very different instrument responses of the OFISs and the rosettes to coherent acoustic background noise in low-wind conditions.

Below 1 Hz in moderate wind, the OFISs have a lower spectral level than the 18 m rosettes. Once again only the 270 m OFIS has a spectral level similar to the 70 m rosette. Above 1 Hz in moderate wind, the OFISs have lower spectral levels when their length is greater than the diameter of the rosette and the spectral level decreases with increasing OFIS length.

The moderate wind results presented above may be influenced by the linear geometry of the OFIS. Since the omnidirectional spectrum estimates are taken without regard to wind direction, there may be biasing due to the azimuthal distribution of winds (i.e. more time windows parallel or perpendicular to the OFIS). We further investigate this directional dependence in the next section.

2.5 Directional WNR Results

We found a consistent dependence of WNR on wind direction of several dB for the OFIS. There was also a WNR dependence on wind direction for the IS57 rosettes, but the variation was not consistent among the different rosettes and across different frequencies. We restrict our analysis to moderate wind speeds to limit the effect of coherent acoustic background such as the microbaroms at low frequencies, and signals that may be attenuated by the instrument response at higher frequencies. An upper frequency limit of 5 Hz is imposed to eliminate any significant effects of anti-aliasing filters and the resonances in the 70 m rosettes. We further restrict our analysis to exclude one of the four 70 m rosettes (L4) due to a known broadband noise problem associated with the central manifold that started in 2010 (C. Coon, personal communication, 2013).

To compare noise levels we integrate the spectra over two frequency bands of various OFIS lengths and rosette sizes for two wind directions: downwind and crosswind to the OFIS. The observed WNR of the OFIS relative to the 18 and 70 m rosettes for two moderate wind speed cases is shown in Figures 2.7 and 2.8, respectively. The 0 dB line represents equal WNR in the OFIS and the rosettes.

The solid lines in Figures 2.7 and 2.8 are the logarithmic predictions based on equations 2.8 and 2.9 in the next section; while the data do not match the predictions exactly the logarithmic character appears to be an appropriate guide. The OFIS is more effective at reducing wind noise than both rosettes in the high frequency (HF) band when the OFIS is longer than the rosette diameter. Also, there is a clear and consistent separation between the crosswind and downwind WNR, with an approximately 3-5 dB greater WNR in the downwind direction.

There are only modest changes in the WNR as the wind increases from 3-4 m/s to 5-6 m/s. For example, the HF WNR increases slightly in the downwind direction, while the crosswind appears to tend towards lower WNR. There is an increase in the LF WNR of 1 to 3 dB relative to the 18 m rosettes (Figure 2.7) due to the "hump" that emerges below the microbarom peak (see the red curve for the 5-6 m/s wind speeds in Figure 2.6b). In contrast the LF WNR relative to the 70 m rosettes appears to slightly decrease (as the wind increases) for the crosswind direction. For the downwind direction, the LF WNR remains relatively unchanged for the longer OFISs, and only slightly decreases ($\sim$1 dB) for the shorter OFISs.

2.6 Predicting directional WNR

2.6.1 Theory

To help interpret the sources of complexity in the observed WNR, we predicted WNR from an implementation of spatial averaging theory. It is well known that if atmospheric pressure is sampled at n locations spaced far enough apart so that the pressure variations from wind noise are uncorrelated, but close enough such that the infrasonic signal remains coherent and in phase, summing the time series will increase the noise power by n and the signal power by n^2, resulting in a signal-to-noise gain G of $10\log_{10}(n)$.

To estimate the wind noise reduction provided by an OFIS, we implement the empirical measurements of spatial correlation distance as a function of wind speed, wind direction, and central period reported by Shields [17]. The spatial correlation distance of pressure anomalies associated with turbulence and advected

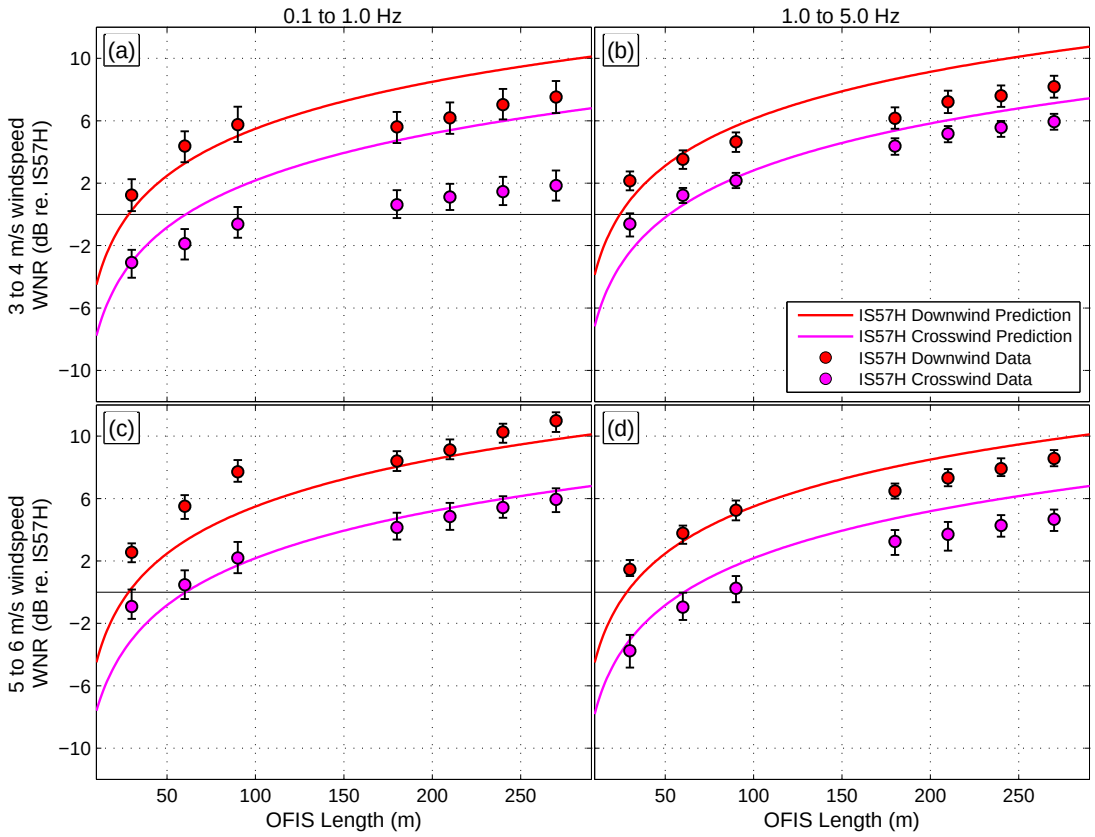


Figure 2.7: Wind noise reduction (WNR) as a function of OFIS length with respect to the 18 m rosettes of IS57. The columns represent different frequency bands [0.1 to 1 Hz for (a) and (c), and 1 to 5 Hz for (b) and (d)] and rows for the two wind speeds [3-4 m/s for (a) and (b), and 5-6 m/s for (c) and (d)]. Because we are plotting noise *reduction*, a positive value in dB means the integrated noise spectrum for the OFIS is lower than that for the IS57 array element. The circles and error bars correspond to the observations, while the solid curves represent the predicted WNR shown in equations 2.8 and 2.9.

in the mean airflow has the property of self-similarity in the sense that a single number describes the correlation distance across a broad range of periods and wind speeds. The advective wavelength is:

$$\lambda_a = \bar{v}\, T, \tag{2.4}$$

where $\bar{v}$ is the mean horizontal wind speed and T is the central period. Shields [17] cross-correlated time series recorded by linear arrays of point microphones oriented in the directions parallel to and orthogonal to the mean wind direction for different

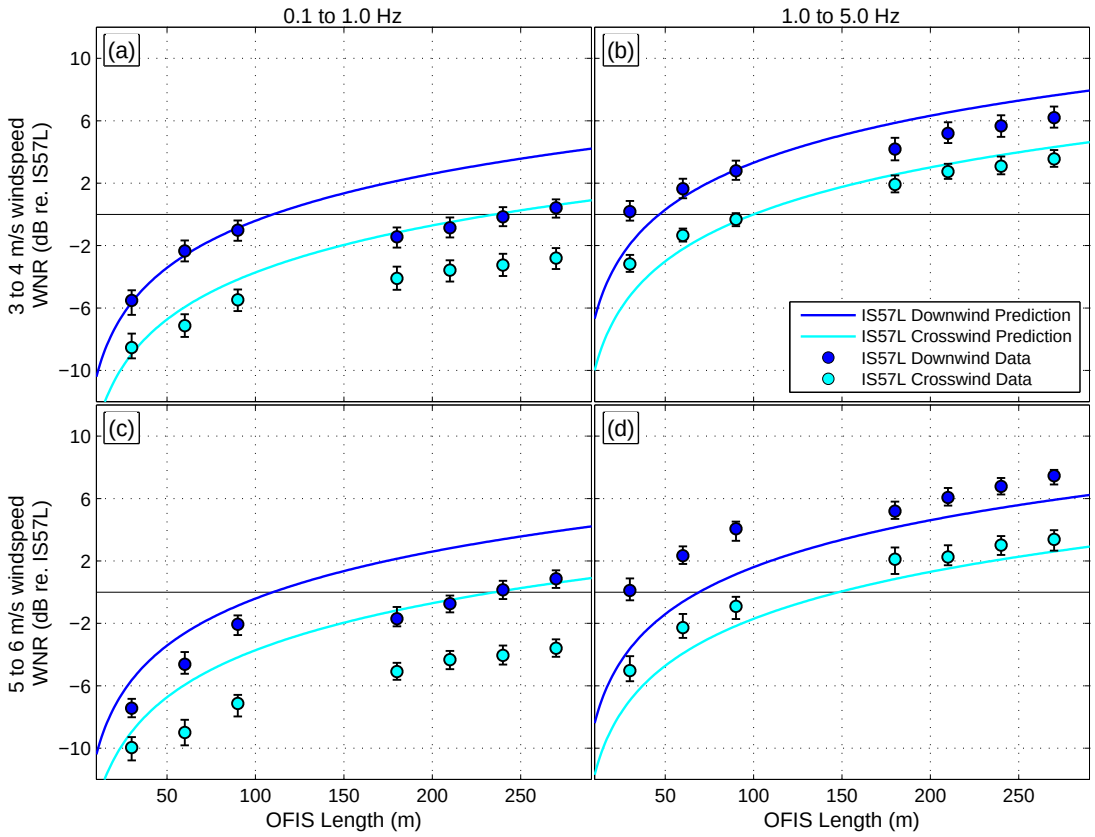


Figure 2.8: WNR as a function of OFIS length with respect to the 70 m rosettes of IS57 for different frequency bands and wind speeds. As in Figure 2.7, the LF, HF, and two wind speed subplots are similarly laid out, and the data and their uncertainties are shown as filled circles and the solid curves are the predicted WNR.

wind speeds and central periods. He found that the turbulence in the wind gives rise to spatially coherent pressure changes for a limited distance that depends on frequency and wind speed in the downwind and crosswind directions. Specifically, he found that the correlation distances D_d and D_c (where the subscripts denote the downwind and crosswind directions) are related to λ_a by dimensionless constants: $D_d = 0.28\,\lambda_a$ and $D_c = 0.60\,\lambda_a$. If we assume a linear OFIS of length L can be approximated by $n = L/D$ independent point sensors that measure incoherent noise from turbulence, the WNR of a linear OFIS in the downwind and crosswind

directions with respect to a point measurement is:

$$G_d = \max\left\{10\log_{10}\left(\frac{Lf}{0.28\,\bar{v}}\right), 0\right\} \tag{2.5}$$

$$G_c = \max\left\{10\log_{10}\left(\frac{Lf}{0.60\,\bar{v}}\right), 0\right\}, \tag{2.6}$$

where the frequency $f = 1/T$. We apply the restriction $n \geq 1$ (defined by the max function) for when the correlation distance exceeds the OFIS length in the case of very high winds or low frequencies. Note that if $n \geq 1$, subtracting Equation 2.6 from 2.5 yields a predicted downwind WNR of 3.3 dB greater than the crosswind WNR that is independent of OFIS length, frequency, and wind speed.

Because we are interested in knowing the OFIS WNR improvement with respect to a rosette of n_r inlets, we also need to predict the WNR of a rosette with respect to a point measurement. We use two different approaches for this calculation. Our first is to use the method above and approximate the rosette as a circle, which is justified because the infrasonic plane-wave responses of a rosette and a circle of the same diameter are quite similar in the frequency band that we are considering. Performing a circular average of the sums of the dot products of the circular arcs with the downwind and crosswind coherence distance vectors yields an effective correlation distance of $D_r = 0.56\,\lambda_a$. Several other numerical experiments derived the same relationship for both 18 and 70 m rosettes. A circle of diameter d therefore represents $\pi d/D_r$ sensors, and the wind noise reduction of the rosette with respect to a point measurement is:

$$G_r = \min\left\{\max\left\{10\log_{10}\left(\frac{\pi d\, f}{0.56\,\bar{v}}\right), 0\right\}, 10\log_{10}\left(n_r\right)\right\}. \tag{2.7}$$

As before we do not allow n to be less than 1. In the case of rosettes with n_r inlets we must restrict n to be no more than n_r (defined by the min function).

Our second approach is to use the combined empirical and electroacoustic model of Alcoverro and Le Pichon [2] for the rosettes (hereinafter referred to as the "AL method"), since averaging with a rosette in reality is a hybrid between averaging around a circle and across a disc. The WNR predictions from this model are functions of wind speed, frequency, and rosette configuration and size. However, the circular configuration of the rosette implies that the WNR should not

vary with wind direction.

Predictions of rosette WNR with respect to a point source using the two different methods described above (Equation 2.7 and the AL method) have been compared. Both methods yield similar WNR curves as a function of wind speed and frequency, although the AL method yields a more heterogeneous spectrum due to taking into account the approximate positions of the inlets. We also computed the ratio of the integrated predicted WNR curves over the same two frequency bands as the observations for the range of OFIS lengths used in the PFO experiment. The resulting predicted values were found to be consistent, with a maximum deviation of about 2 dB in the LF band at higher wind speeds.

Because the AL method is not adaptable to an OFIS and assumes a different correlation distance for wind noise, we used the spatial averaging method (which gives very similar results) for both the rosette (Equation 2.7) and the OFIS (Equations 2.5 and 2.6) to predict WNR of an OFIS relative to a rosette as a function of OFIS length, rosette diameter, and wind speed. Therefore, the predicted WNR integrated over a given frequency band (f_1 to f_2) of an OFIS of length L relative to a rosette of diameter d can be expressed as:

$$\mathrm{WNR}_d\left(L,\bar{v}\right) = 10\log_{10}\left(\frac{\int_{f_1}^{f_2}\max\left\{\frac{Lf}{0.28\bar{v}},1\right\}df}{\int_{f_1}^{f_2}\min\left\{\max\left\{\frac{\pi df}{0.56\bar{v}},1\right\},n_r\right\}df}\right) \tag{2.8}$$

$$\mathrm{WNR}_c\left(L,\bar{v}\right) = 10\log_{10}\left(\frac{\int_{f_1}^{f_2}\max\left\{\frac{Lf}{0.60\bar{v}},1\right\}df}{\int_{f_1}^{f_2}\min\left\{\max\left\{\frac{\pi df}{0.56\bar{v}},1\right\},n_r\right\}df}\right), \tag{2.9}$$

for the downwind and crosswind directions, respectively. In other words, we compute the frequency-dependent WNR curves for a given OFIS length, rosette diameter, and wind speed, then apply the min/max restrictions, and finally integrate over the chosen frequency band.

2.6.2 Comparing Predicted and Observed WNR for a Line

The predicted WNR as a function of OFIS length (Equations 2.8 and 2.9) are shown in Figures 2.7 and 2.8 for the LF ($f_1 = 0.1$ and $f_2 = 1$ Hz) and HF ($f_1 = 1$ and $f_2 = 5$ Hz) bands, at two wind speeds ($\bar{v} = 3.5$ and 5.5 m/s) for both rosette diameters ($d = 18$ and 70 m). Note that the maximum number of inlets is $n_r = 92$ and 144 for the 18 and 70 m rosettes, respectively. These show that the OFIS WNR difference with respect to the 18 and 70 m rosettes increases logarithmically with increasing frequency, decreasing wind speed, and increasing OFIS length (Figures 2.7 and 2.8). The predicted OFIS WNR with respect to the 18 m rosettes does not change significantly across the LF and HF bands. As the wind increases there is no apparent change in the predicted LF WNR for the 70 m rosette, although the predicted HF WNR drops by about 2 dB. The downwind/crosswind separation remains the same as the wind increases.

Overall the predictions fit the general features observed in the data. There is clear separation between all the downwind and crosswind predictions and observations, although there is as much as a 5 dB absolute variation. The 18 m LF and 70 m HF results seem to agree more closely at higher wind speeds. However, the 70 m LF agreement is poor for OFIS lengths greater than 180 m.

2.7 Time Series Signal-to-Noise Ratio Comparison

In this section we present a time-domain example of the WNR improvement of a 270 m linear OFIS. A Delta II rocket was launched from Vandenberg Air Force Base, located about 400 km to the west-northwest of Piñon Flat Observatory on October 8$^{\text{th}}$, 2009. The 270 m OFIS was oriented orthogonal to the Vandenberg azimuth. This implies that there was no signal attenuation due to averaging across infrasonic waves because the wavefronts of the rocket-generated infrasound were parallel to the OFIS. Since the prevailing winds were 2 to 3 m/s and roughly downwind of the OFIS, this signal represents a nearly ideal example

of WNR leading to improved SNR.

To estimate the ratio of the signal power to the wind noise power, we used a frequency-time beamforming program called "FTBeam" to determine the back azimuth (direction of arrival) for signals of interest that are determined to be statistically significant. A complete description of this method can be found in [19]. We identified several detections from the Vandenberg direction (approximately 286° clockwise from north) after each rocket launch. Using the known rocket launch time and position as a reference, the group velocities of these arrivals for both rockets are the same (250 to 300 m/s). Using this information, we defined a precursory noise window and a signal window (roughly the first and second thirds of Figure 2.9a, respectively). For all eight IS57 array elements and the 270 m OFIS, the median value of the envelope function is measured as the noise level. The maximum absolute value is measured for the signal level. The SNR of the 18 and 70 m rosette recordings was ∼5 dB. The OFIS SNR was consistently ∼10 dB higher than all eight of the IS57 rosettes. This is perhaps best exemplified by the first arrival since the signal between 400 and 440 seconds, completely buried by wind noise on the two IS57 array elements, is prominent in the OFIS recording.

This rocket launch signal shows some of the tradeoffs involved in spatial averaging. The 18 m rosettes observed the high infrasonic frequencies well because there was little spatial attenuation due to the small rosette diameter. However, they did not attenuate the wind noise well. Conversely, the 70 m rosettes attenuated the wind noise more, but did not faithfully measure the full infrasonic signal spectrum above 2 Hz due to infrasonic signal attenuation. The OFIS recorded the full fidelity of the infrasound (like the 18 m rosettes) while providing a much greater level of wind noise reduction, better even than that provided by the 70 m rosettes. This 10 dB improvement would be reduced by several dB for winds perpendicular to the OFIS. In addition, the 270 m OFIS would attenuate signals in this frequency range for oblique arrival angles; one requires an array of OFIS sensors in different orientations to record the full signal spectrum for all arrival angles.

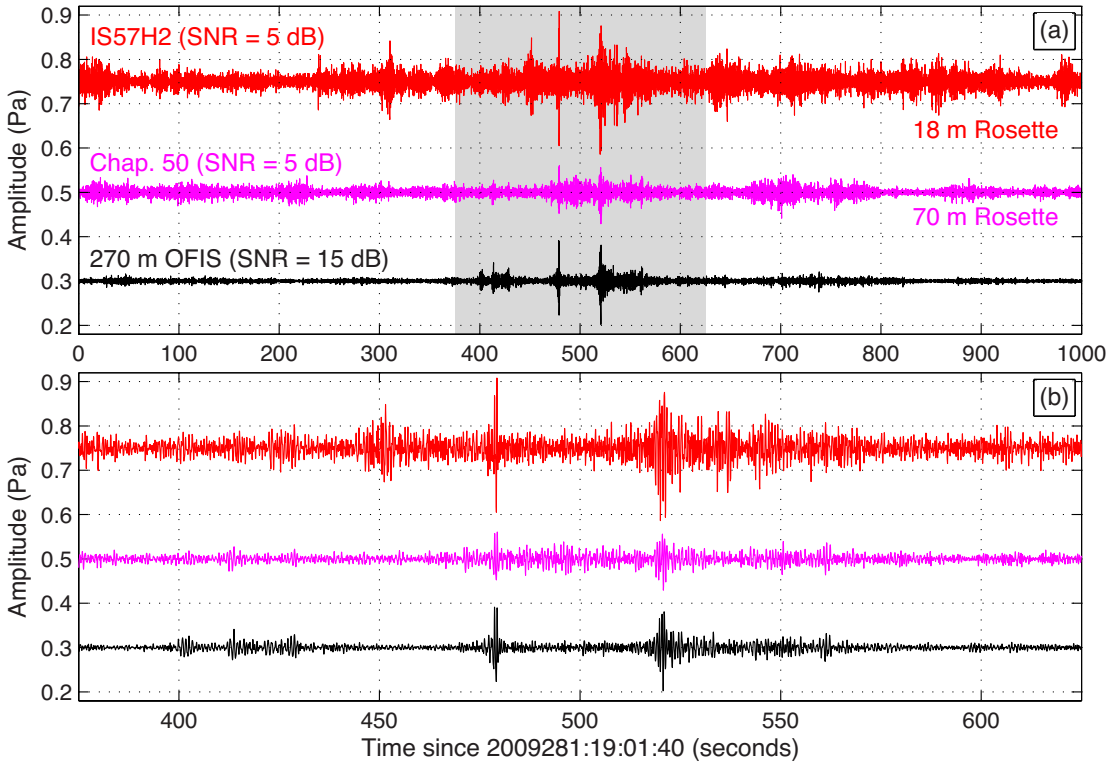


Figure 2.9: Signal-to-noise ratio comparison for the October 8th, 2009 Delta II Vandenberg rocket launch that generated infrasound in the 1 to 5 Hz band during moderate winds at PFO. (a) 1,000 seconds centered around the three signals of interest. (b) Closeup of the three signals clearly showing the improved wind noise reduction of the 270 m OFIS compared to both rosette sizes, and reduced signal attenuation compared to the 70 m rosette.

2.8 Discussion

2.8.1 Deviation between predicted and observed WNR

The general logarithmic trend of the predicted WNR that increases with OFIS length appears to be reasonable (Figures 2.7 and 2.8). In addition, the predicted separation of the downwind and crosswind WNR clearly matches the observations for both frequency bands in moderate winds, although the absolute values deviate here by as much as 5 dB. The absolute deviation for these moderate wind speed cases can be explained by several sources. The spectral ratio observations have error bars of as much as 1.5 dB (95% confidence region). In addition,

the variation in the predictions using the circle (Equation 2.7) and AL method can be as much as 2 dB in the LF band at higher wind speeds. However, we interpret the LF deviation for the 70 m to be due to additional noise that is not included in the rosette WNR model. The results for OFIS lengths greater than 180 m (and therefore the longer OFISs derived from it) are clearly offset from those 90 m and shorter due to a persistent, unknown noise source between 0.1 and 0.3 Hz (Figure 2.6b).

2.8.2 Performance of the 270 m long OFIS with respect to the IS57 array elements

The three different analyses of WNR for a 270 m OFIS described above yield internally consistent results. First, the comparison of rocket-generated infrasound recorded in moderate wind indicates an average SNR improvement relative to all eight IS57 array elements of ∼10 dB (Figure 2.9). Second, the wind blowing across the OFIS at this time was generally blowing along the OFIS length ("downwind"). Indeed, the downwind SNR improvement in moderate winds for the 1 to 5 Hz band is ∼10 dB for the OFIS relative to both the 18 and 70 m rosettes (Figures 2.7 and 2.8). Third, the omnidirectional OFIS WNR analysis shows that in moderate wind the 270 m OFIS attenuates wind noise in the 1 to 5 Hz band, with respect to the 18 and 70 m rosettes, by an average of ∼8.5 dB (Figure 2.6), which is also the average value of the downwind and crosswind HF spectral ratios in moderate wind (Figures 2.7 and 2.8).

The analysis above shows that an OFIS can be increased in length to achieve a desired wind noise reduction that can exceed the performance of even the largest of IMS-certifiable rosettes (70 m). The best improvement is achieved in the downwind direction. As shown, the 270 m OFIS provides a ∼10 dB improvement to that provided by either an 18 or 70 m rosette in moderate wind blowing approximately parallel to the OFIS length. For crosswind scenarios, the 270 m OFIS provides ∼6 dB improvement.

2.9 Conclusions

In this chapter, the efficacies of the OFIS and rosette wind filters in attenuating wind-induced infrasonic pressure fluctuations in moderate winds have been quantified and compared. Two different analyses of data recorded during an experiment using nine 30-m long, gravel-buried OFISs at Piñon Flat Observatory and the implementation of two different methods for predicting WNR suggests that the level of WNR (in dB) provided by a linear OFIS is a logarithmic function of OFIS length, frequency, wind speed, and wind direction with respect to the OFIS. Analytical WNR models based on spatial averaging theory are developed for both the pipe arrays and OFIS. The analytical predictions for the pipe array WNR are within 2 dB of that predicted by the electroacoustic model of [2]. Although the analytical relations do not predict the data perfectly, suggesting there is additional physics that remains to be added to the model, the predictions do explain the general features of the observations. Specifically, WNR increases with OFIS length and frequency, decreases with wind speed, and is 3 to 6 dB greater when the wind is moving along the length of the OFIS rather than across it. In such a "downwind" case, a 270 m long OFIS in moderate wind provides an $\sim$8.5 dB WNR improvement in the 1 to 5 Hz band over that achieved by all eight IMS-certified rosettes of the IS57 infrasonic array. In the 0.1 to 1 Hz band under the same conditions, the downwind OFIS provides an $\sim$11 and 2 dB improvement over the 18 and 70 m rosettes, respectively. Shorter OFISs in some cases (even some OFISs that are longer than the diameter of the rosettes) provide less WNR than the rosettes, mostly because of the longer coherence distances for crosswind scenarios.

Our observations and analytical noise model suggest that the wind noise reduction with an OFIS continues to improve as the sensor is made longer. This implies that, for a given maximum wind speed and frequency band of interest, an array of OFISs can be designed to achieve, for all possible signal directions, a signal-to-noise gain greater than that attainable by a pipe array, enhancing detection capability in windy environments.

2.10 Acknowledgments

There are numerous individuals that helped bring this study into being. David Horwitt, David Chavez, and Jui-Yuan Chang for provided the hardware and software engineering and support for acquiring the OFIS data, and Hans-Werner Braun managed the data network infrastructure. Michael Hedlin and Clint Coon provided IS57 data and connected the Chaparral 50 to the L2 array element. Clint Coon, Michael Davis, Don Elliott, Mike Kirk, Glen Offield, José Otero, Glenn Sasagawa, Rich Shelby, John Unwin, Joel White, and Heinz Wuhrmann all provided assistance with fieldwork.

Much of this chapter has been published in the following manuscript: **Scott DeWolf, Kristoffer T. Walker, Mark A. Zumberge, and Stephane Denis. "Efficacy of Spatial Averaging Infrasonic Pressure in Varying Wind Speeds."** ***The Journal of the Acoustical Society of America*****, 133(6), 3739–3750, 2013**. The author's contribution to this study was to coordinate and lead the fabrication of the instruments, perform laboratory and field calibrations, assist in the installation, prepare the instruments for data collection, analyze the data, and prepare the manuscript.

REFERENCES

[1] Benoit Alcoverro. Acoustic filters design and experimental results. In *Proceedings Workshop on Infrasound (DASE, Commissariat à l'Energie, Bruyères-le-Châtel, France, 21-24 July 1998)*, 1998.

[2] Benoit Alcoverro and Alexis Le Pichon. Design and optimization of a noise reduction system for infrasonic measurements using elements with low acoustic impedance. *Journal of the Acoustical Society of America*, 117(4):1717–1727, 2005.

[3] Douglas R. Christie and Paola Campus. The IMS infrasound network: design and establishment of infrasound stations. In *Infrasound Monitoring for Atmospheric Studies*, chapter 2, pages 29–75. Springer, Secaucus, New Jersey, 2010.

[4] Scott DeWolf. *Optical and Mechanical Behavior of the Optical Fiber Infrasound Sensor*. M.S. thesis, University of California San Diego, 2009.

[5] B. Efron and R. J. Tibshirani. *An Introduction to the Bootstrap*. Monographs on Statistics and Applied Probability 57. Chapman and Hall, New York, 1993. 456 pages.

[6] Laslo G. Evers and H. W. Haak. The characteristics of infrasound, its propagation and some early history. In *Infrasound Monitoring for Atmospheric Studies*, chapter 1, pages 3–27. Springer, Secaucus, New Jersey, 2010.

[7] Michael A. H. Hedlin and Benoit Alcoverro. The use of impedance matching capillaries for reducing resonance in rosette infrasonic spatial filters. *Journal of the Acoustical Society of America*, 117(4):1880–1888, 2005.

[8] Michael A. H. Hedlin, Benoit Alcoverro, and Gerald D'Spain. Evaluation of rosette infrasonic noise-reducing spatial filters. *Journal of the Acoustical Society of America*, 114(4):1807–1820, 2003.

[9] Michael A. H. Hedlin and Richard Raspet. Infrasonic wind noise reduction by barriers and spatial filters. *Journal of the Acoustical Society of America*, 114(3):1379–1386, 2003.

[10] E. Herrin, G. G. Sorrels, P. Negaru, J. G. Swanson, P. Golden, and C. Mulcahy. Comparative evaluation of selected infrasound noise reduction methods. In *Proceedings of the 23rd Seismic Research Review (Jackson Hole, Wyoming, 2-5 October 2001)*, pages 131–139, 2001.

[11] Wheeler Howard, Kevin Dillion, and F. Douglas Shields. Acoustical properties of porous hose wind noise filters. *Journal of the Acoustical Society of America*, 122(5):2985, 2007.

[12] A. N. Kolmogorov. Local structure of turbulence in an incompressible fluid at very high reynolds numbers. *Dokl. Akad. Nauk SSSR*, 30:299–303, 1941.

[13] L. D. Landau and E. M. Lifshitz. *Fluid Mechanics*. Pergamon, Oxford, 1959. 536 pages.

[14] L. Liszka. Infrasound: a summary of 35 years of infrasound research. IRF Scientific Report 291, Swedish Institute of Space Physics, Umeå, Sweden, 2008. ISBN 978-91-977255-0-7, 150 pages.

[15] S. D. Noel and R. W. Whitaker. Comparison of noise reduction systems. Los Alamos National Laboratory Report LA-12003-MS, Los Alamos National Laboratory, Los Alamos, New Mexico, 1991.

[16] Richard Raspet, Jeremy Webster, and Kevin Dillion. Framework for wind noise studies. *Journal of the Acoustical Society of America*, 119(2):834–843, 2006.

[17] F. Douglas Shields. Low-frequency wind noise correlation in microphone arrays. *Journal of the Acoustical Society of America*, 117(6):3498–3496, 2005.

[18] G. I. Taylor. The spectrum of turbulence. *Proceedings of the Royal Society of London. Series A, Mathematical and Physical Sciences*, 164(919):476–490, 1938.

[19] Kristoffer T. Walker. Evaluating the opposing wave interaction hypothesis for the generation of microbaroms in the eastern north pacific. *Journal of Geophysical Research*, 117:C12016, 2012.

[20] Kristoffer T. Walker and Michael A. H. Hedlin. A review of wind noise reduction methodologies. In *Infrasound Monitoring for Atmospheric Studies*, chapter 5, pages 141–182. Springer, Secaucus, New Jersey, 2010.

[21] Kristoffer T. Walker, Mark A. Zumberge, Michael A. H. Hedlin, and Peter M. Shearer. Methods for determining infrasound phase velocity direction with an array of line sensors. *The Journal of the Acoustical Society of America*, 124(4):2090–2099, 2008.

[22] Jiao Yu, Richard Raspet, Jeremy Webster, and JohnPaul Abbott. Improved prediction of the turbulence-shear contribution to wind noise pressure spectra. *Journal of the Acoustical Society of America*, 130(6):3590–3594, 2011.

[23] Jiao Yu, Richard Raspet, Jeremy Webster, and JohnPaul Abbott. Wind noise measured at the ground surface. *Journal of the Acoustical Society of America*, 129(2):622–632, 2011.

[24] Mark A. Zumberge, Jonathan Berger, Michael A. H. Hedlin, Eric Husmann, Scott L. Nooner, Richard Hilt, and Rudolf Widmer-Schnidrig. An optical fiber infrasound sensor: A new lower limit on atmospheric pressure noise between 1 and 10 Hz. *The Journal of the Acoustical Society of America*, 113(5):2474–2479, 2003.

Chapter 3

Optical Fiber Borehole Strainmeter Arrays for Measuring Sediment Compaction in Bangladesh

This chapter concerns a collaborative effort between the Scripps Institution of Oceanography and the Lamont-Doherty Earth Observatory at Columbia University (LDEO) to design, fabricate, and install twelve fiber optic borehole strainmeters to measure sediment compaction at two sites in Bangladesh as a part of a large project funded by the National Science Foundation. The vertical displacement profiles from these strainmeter arrays are intended to be used along with a number of other ongoing studies: sediment profiles collected from approximately 200 other wells, seismic chirp profiles taken from river boats during the flooding season, and an expanded GPS and seismic network. This data will then be integrated into analytic, finite-difference, and finite-element models of the regional geologic structure currently being developed by LDEO and other collaborating institutions.

3.1 Introduction

3.1.1 Geohazards in Bangladesh

Naturally one must consider the geologic setting to understand the significance of geophysical research in Bangladesh. Erosion from the Himalayas over the past 35 million years has formed the world's largest river delta and thickest sediment bed. An estimated 1 gigaton per year flux of sediments (6-8% of the total global sediment flux into the ocean worldwide [4, 7]) is discharged from the Ganges and Brahmaputra into the Bay of Bengal. Coupled with the fact that Bangladesh is actively being subducted between the Himalaya and Burma arcs (Figure 3.1) is that the sediment layers are compressing under their own weight, and these processes are believed to contribute to an overall subsidence rate of 2 to 14 mm per year depending upon location [5]. Finally, seasonal flooding covers 20-30% of the country on average, and sometimes up to 70% as in 1998, causing a seasonal ground displacement anomaly of up to 5 to 6 cm as inferred from GPS [5].

It is necessary to quantify the spatial variability of these subsidence rates to assess the geophysical hazards faced by the Bangladeshi people. Bangladesh is home to an estimated 164.4 million people occupying approximately 57,000 square miles, which is over half of the population of the United States in an area the size of the state of Iowa. Furthermore, about 50% of the land area is less than 3 m above sea level, making it the potentially largest population to be displaced by sea level rise.

3.1.2 Sediment Compaction Measurement

Sediment compaction is generally defined as the loss of porosity due to loading, which in this case manifests itself as changes in vertical sediment column height due to periodic water loading (seasonal time scales) and increasing overburden from ongoing deposition (interannual time scales). While there are diverse instruments for measuring sediment compaction rates, the type most comparable to the optical fiber strainmeters in this study are borehole extensometers. Of these

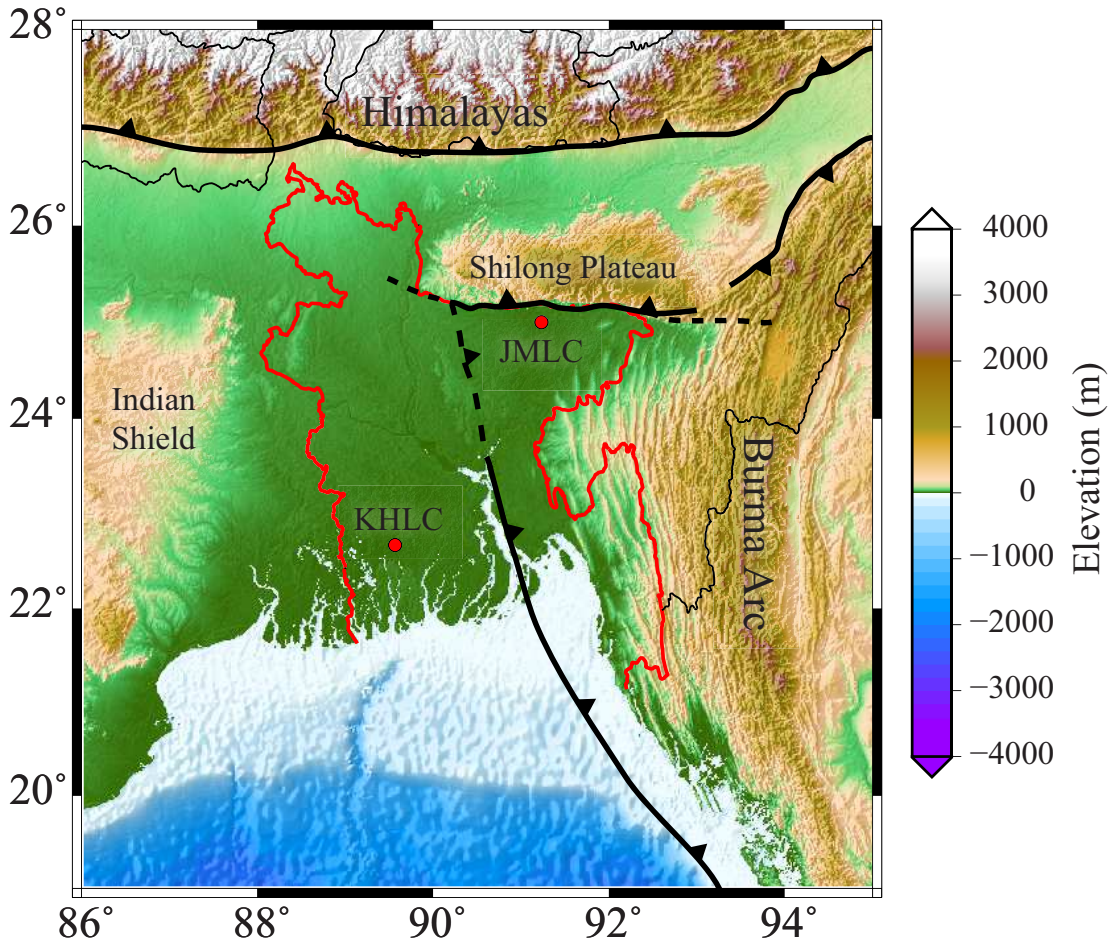


Figure 3.1: Topographical map of Bangladesh (bordered in red), showing several geologic features. The subduction regions are shown as black lines as are the two site locations, Jamalganj (JMLC) in the north and Khulna (KHLC) in the south. Note that the color scale refers to height above sea level in meters.

there are two main variants: the taught wire and fixed rod extensometers, however, only the latter type appear to be available commercially. The basic design principle behind the borehole extensometer is that of a wire or pipe fixed to the bottom of a borehole whose length protruding from the borehole relative to some surface benchmark is monitored using any number of suitable displacement transducers [1].

The most common application for borehole extensometers has been for measuring subsidence rates from areas of water abstraction. One notable experiment was by Lofgren, who used about 30 taught wire extensometers to measure sub-

sidence in the San Joaquin Valley, California. These were reported to have an accuracy of "a few ten-thousandths of a foot" (∼30 μm) using a 1/8" (∼3 mm) diameter stranded stainless steel cable [3].

3.1.3 Rationale for this Study

Optical fiber strainmeters are an attractive alternative to borehole extensometers since they are relatively robust and easy to deploy, and their lengths can be determined within several hundred microns in campaign-style measurements using an electronic distance meter (EDM). Since the measured path is inside an optical fiber, they do not require a straight open borehole. While the temperature coefficient of the optical fiber's index of refraction (and therefore apparent length) is quite large (10^{-5} °C^{-1}), it can be removed with the help of coincident temperature measurements using commercially available thermistors.

Our contribution to the effort of assessing geohazards in Bangladesh was to monitor compaction rates in sediment by designing, fabricating, and assisting in installation of twelve optical fiber borehole strainmeters at two sites in Bangladesh: Jamalganj in the north and Khulna in the south (also shown in Figure 3.1). The plan was that each site would consist of an array of six fiber strainmeters of 20, 40, 60, 80, 100, and 300 m lengths for deployment in 5 cm diameter, PVC-lined boreholes drilled shortly before deployment. The site selection was done in advance based on the local geology such that the vertical displacement profile as a function of depth might be obtained for locations with differing stratigraphy (as laid down by flooding) and tectonic settings (subduction and accretion).

3.2 Setup

3.2.1 Strainmeter Design

The strainmeters in this study measure sediment compaction by cementing one end of an optical fiber to the bottom of a borehole and securing the other end under tension to a concrete surface monument such that ground deformation

between these two ends, both positive and negative strains, can be tracked by the elastic fiber. The principle component of the optical fiber strainmeters is the "fiber cable" consisting of four 250 μm diameter, tight-buffered Corning SMF-28e+ optical fibers contained in a 1.32 mm diameter, 0.13 mm wall stainless steel tube that also contains a water inhibiting gel. This fiber cable is capable of elastic strain to approximately 0.5%, and fails at $\sim$1%. Both the stainless tubing and optical fibers within it are immobilized at both ends in the upper and lower termination fixtures, where strain-relief boots provide a robust transition between the fiber cable and termination fixtures. Cables with four internal fibers allowed two fiber loops to be formed by splicing pairs together at depth. This results in each strainmeter containing two redundant down-and-back fiber loops spanning the depth of each well.

An idealized version of a deployed strainmeter is shown in Figure 3.2. The concrete surface monument has a base of approximately 1 m square, and the roughly 0.3 m square monument pedestal height varies among the installations from 0.75 to 1.25 m. The wellhead provides padlocked access to the optical fiber "pigtails" for measuring the length of each strainmeter. The well casing is separated from the monument using a tapered monument-well casing adapter such that the two are decoupled. A survey marker is embedded into one corner of each monument so that their relative heights can be measured with respect to the GPS monument discussed in Section 3.2.2. At the bottom end, the well extends below the casing such that both the anchor chain at the lower termination point of the strainmeter (labeled as the "splice bottle") and well casing can be cemented into the ground.

Figure 3.3a shows a detailed view of the contents of the wellhead. The wellhead base and concrete anchors were set into the concrete during the pouring of the surface monuments. These threaded anchors hold the strainmeter upper termination fixture bridge, which can be adjusted up or down via the four jam nuts holding it in place. The upper termination fixture is an upside-down, ANSI 5/8"-11 stainless steel threaded rod that has been drilled out to provide a small cavity where the four individual optical fibers transition out of the fiber cable and

into the fiber pigtails. This small cavity, labeled as the "epoxy volume" is filled with very strong, low-viscosity epoxy that secures both the stainless tube and the optical fibers. The individual optical fiber pigtails terminate in standard FC optical fiber connectors for interrogation.

The bottom end detail schematic (Figure 3.3b) shows the lower termination point and optical fiber turn-around for the strainmeter known as the "splice bottle." This splice bottle is a 25.4 mm diameter, 1.6 mm wall, 21.6 cm long stainless steel tube capped at both ends. These caps are secured with epoxy that also acts as a seal to prevent water from coming into contact with the fiber and the splices. The top cap also serves as the lower termination point where the individual optical fibers transition out of the fiber cable. As in the upper termination fixture, the constituents of the fiber cable are immobilized within the epoxy volume. A "splice tray" that mounts to the underside of the top cap guides the fiber into a well-behaved loop (to limit optical bending loss) where both pairs of fibers are spliced together to form a loop. The bottom cap simply contains a blind threaded hole to accept the anchor bolt to connect a 3 m long anchor chain, which is discussed further in Section 3.2.2.

3.2.2 Deployment

Installation of the strainmeters was carried out from mid-February to mid-March of 2011. Each well was drilled by local contractors by first setting up bamboo towers like the one shown in Figure 3.4a. A central pipe with a spade bit at the end (Figure 3.4b) was turned by hand using a large pipe wrench while water was manually pumped through the center of the pipe to flush out loosened sediment. As the well deepened, additional pipes were added until reaching the desired depth determined by the cumulative length of drill pipes. At this point the drill pipe was removed and the full depth of the well was cased with a 5 cm diameter PVC pipe. Each completed well was then flushed using a water pump and a length of 2.5 cm diameter flexible PVC pipe to prevent mud from entering the well.

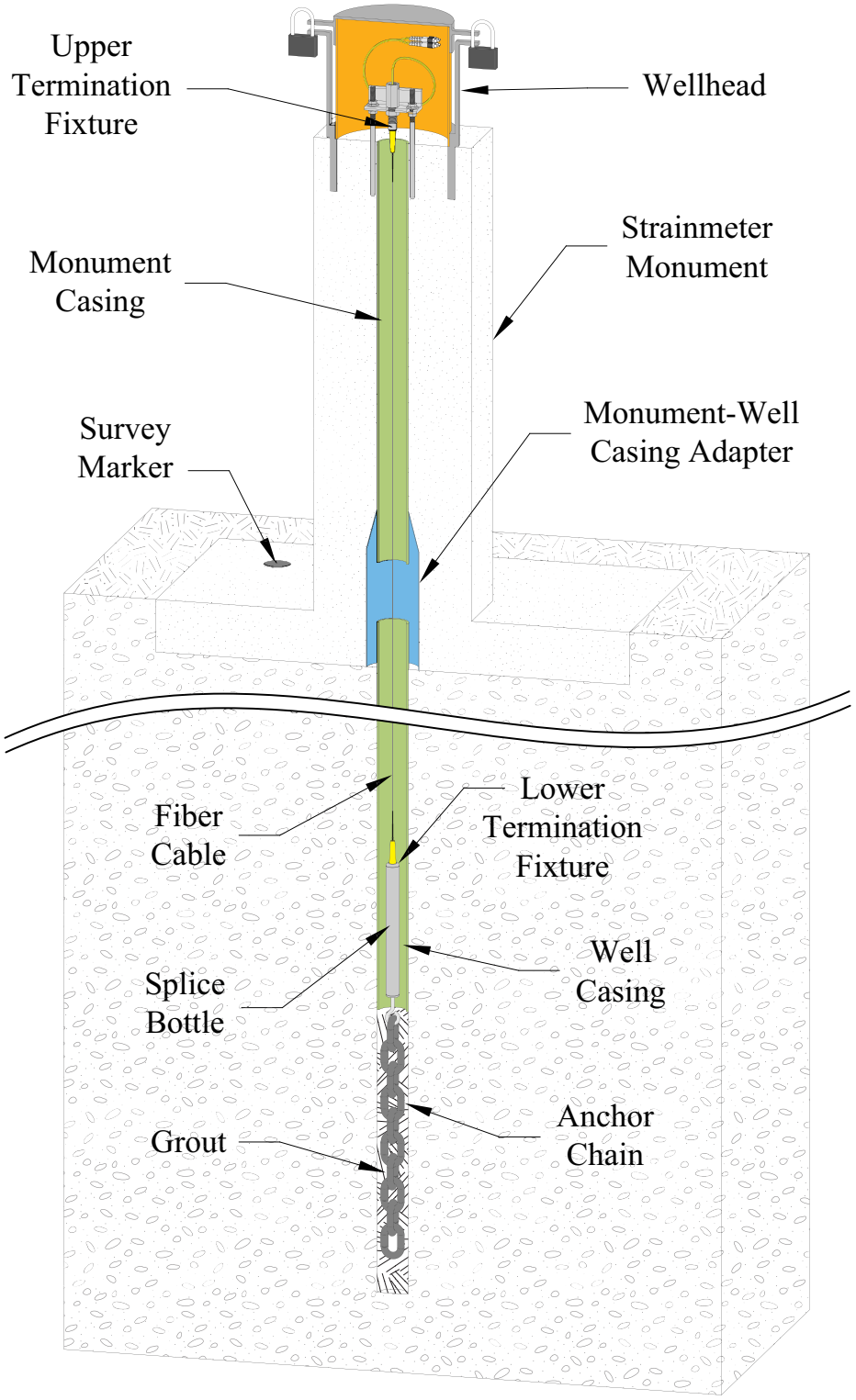


Figure 3.2: Cutaway schematic showing the basic components of a deployed strainmeter. The fiber cable is anchored under tension between two points: one at depth, and the other at the surface.

Each strainmeter was installed after the flush water became clear of intruding mud and repeated depth soundings where made. We first delivered a ∼15 liter mixture of low-viscosity grout (developed in-house) to the bottom of each borehole through the flush pipe inserted into the well. This mixture also included a compound to retard the curing of the grout (Euclid Chemical admixture Eucon DS) such that there was sufficient time to lower each instrument. After attaching the anchoring chain to the splice bottle, the strainmeter was lowered into place and

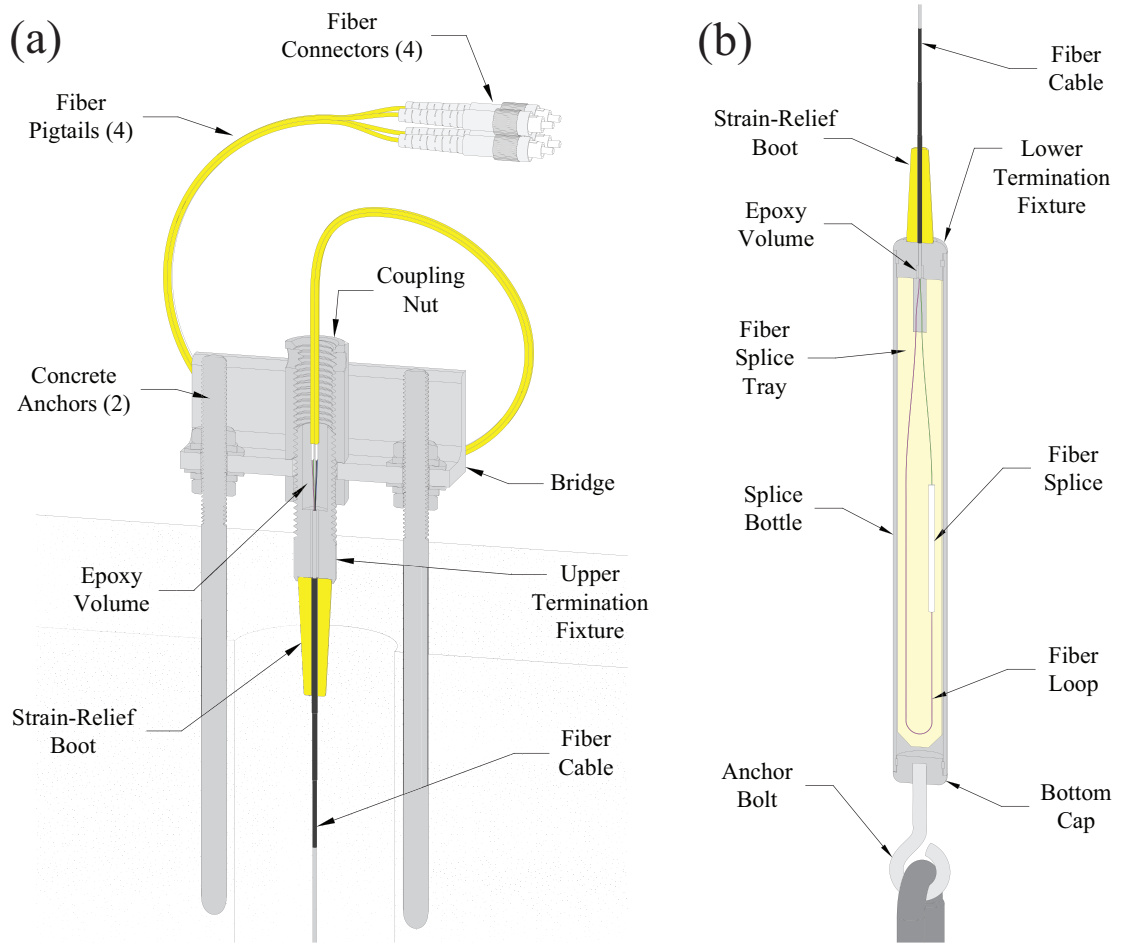


Figure 3.3: Detailed cutaway schematics of the upper (a) and lower (b) strainmeter termination points. (a) The wellhead (with cap and sleeve removed) reveals the adjustable bridge, upper termination fixture, and connectorized optical fiber pigtails. (b) The down-hole end, or "splice bottle," contains the fiber loops secured to the splice tray. Note that the axisymmetric grooves at the ends of the splice bottle are used to epoxy both end caps to the bottle cylinder.

secured to a tripod at the surface (Figure 3.4c). While the grout cured, thereby anchoring the chain, the wellhead monument was poured and the wellhead cap and the upper termination fixture bridge were installed into the wet concrete. After the bottom grout and monument had cured, the fiber cable was tensioned and locked into the adjustable bridge cemented into the wellhead monument. It is essential to note that the depth of the fibers and the height of the wellhead monuments were computed such that a 0.2% initial strain was imparted to each when the upper termination fixture was locked into place. This initial strain places a limit on the amount of compression that can be recorded without re-tensioning. Finally, a string of thermistors was lowered into one of the wells to obtain the temperature profile during each weekly measurement.

The main problem encountered during the deployment was the intermittent inability to get some of the strainmeters down to their full depths. This occurred despite repeated soundings that assured us that the wells were in fact deeper than needed. Since the boreholes were not perfectly vertical it is not unreasonable to assume that the chain was dragging along the borehole casing at depth. We believe this must have caused the chain to start piling up, or jamming in the well before entering the grout. Before this consideration, however, the strainmeters were able to be installed by repeated deployment. The final, 300 m well at the second site in Khulna was installed on its first attempt by attaching a $\sim$1 m long bundle of 10 mm diameter rebar to the end of the anchor chain, therefore supporting our chain-jamming hypothesis.

In the end, four of the six strainmeters were installed at the first site in Jamalganj, and all six at the second site in Khulna. The 80 m well in Jamalganj was lost due to the grout pipe becoming stuck in the bottom of the well and breaking off during extraction. The deepest, 300 m well in Jamalganj had to be shortened to 233 m since the sediments became too compacted to complete the drilling in a timely manner. This prefabricated strainmeter was shortened in the field, but ultimately did not appear to anchor into the grout since we were not able to tension it. We believe that the over-flushing of this well in an attempt to reach 300 m resulted in a large pocket at the bottom that would have required much more

grout than the other wells.

Figure 3.5 shows each completed strainmeter array two years after deployment. The large tower (ideally) serves as an absolute position reference, where its foundation depth is equal to its height to improve stability. This is topped with a GPS receiver that monitors the horizontal and vertical position of the monument and therefore the displacements of each site. A smaller well cased with a steel pipe (clearly seen at the center of Figure 3.5b) contains a pair of piezometers, one of which is near the surface and the other at depth that record pressure as a proxy for the water table height.

3.2.3 Electronic Distance Measurement and Data Collection

Each fiber loop within each strainmeter is interrogated with an electronic distance meter (EDM) that determines their lengths by measuring the phase difference between an emitted and received intensity modulated pulse of light. The devices used in this experiment are commercially available, free-space Dimetix brand (FLS-C10) EDMs that are commonly used in land surveying and industrial applications. These have been coupled to an optical fiber and repackaged by OZ Optics (Ottawa, Canada), as their "Optical Fiber Length Meter" (model OFLM-100-2-S/M-3-U).

Software provided by OZ Optics allows the user to perform a single length measurement or the average of a series of measurements, but proved to be inadequate for several reasons. Occasionally the Dimetix FLS-C10 will incorrectly report a measured length of 0.0257 m, thereby corrupting any running average. The software also does not report the uncertainty when taking a series of measurements, which makes it impossible to determine when faulty measurements are made. This software also requires repeated single measurements in order to obtain the uncertainty of an ensemble of measurements, which would be time consuming and cumbersome for the operator.

To overcome the limitations of the included software, data collection is performed using a script written in the `MATLAB` programming environment operating

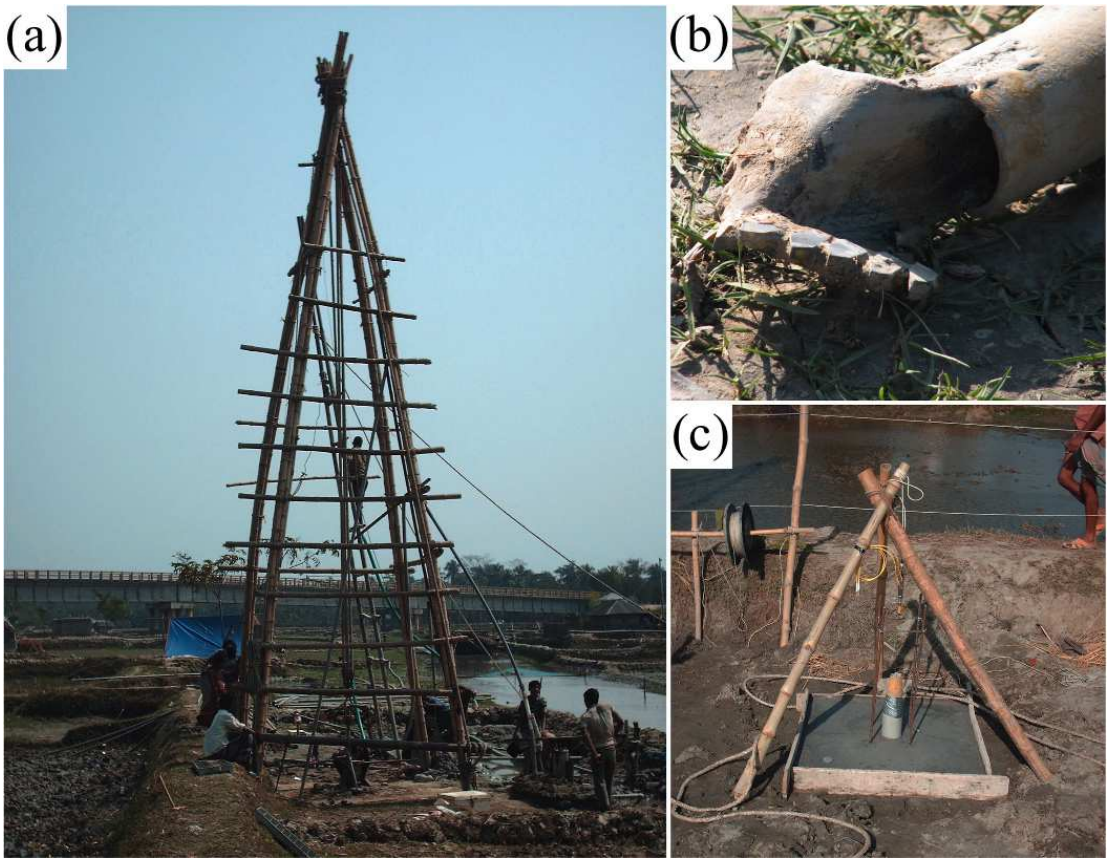


Figure 3.4: Pictures taken during the Khulna strainmeter deployment. (a) The bamboo drilling tower used for excavating each well, showing the water pump head near the surface. (b) The spade bit attached to the end of the first drill pipe. (c) Partially completed surface monument showing the upper termination fixture and fiber pigtails attached to the tripod while the grout cured. Note the central monument-well casing adapter as well as the survey marker (embedded in the lower left corner of the monument pad).

on a small notebook computer. This script accesses the EDM using low-level commands sent through its serial port, and is a heavily modified version of the script originally written by Blum [2]. The script records the measured distance, laser temperature, and received intensity from the EDM every 1 to 2 seconds for a time interval specified by the operator (typically 300 seconds), and reports the mean and standard deviation as well as writes these three time series to a text file.

Starting in March of 2011 weekly length data-collection have been carried out by a local resident at each site, with the intent of continuing these measure-

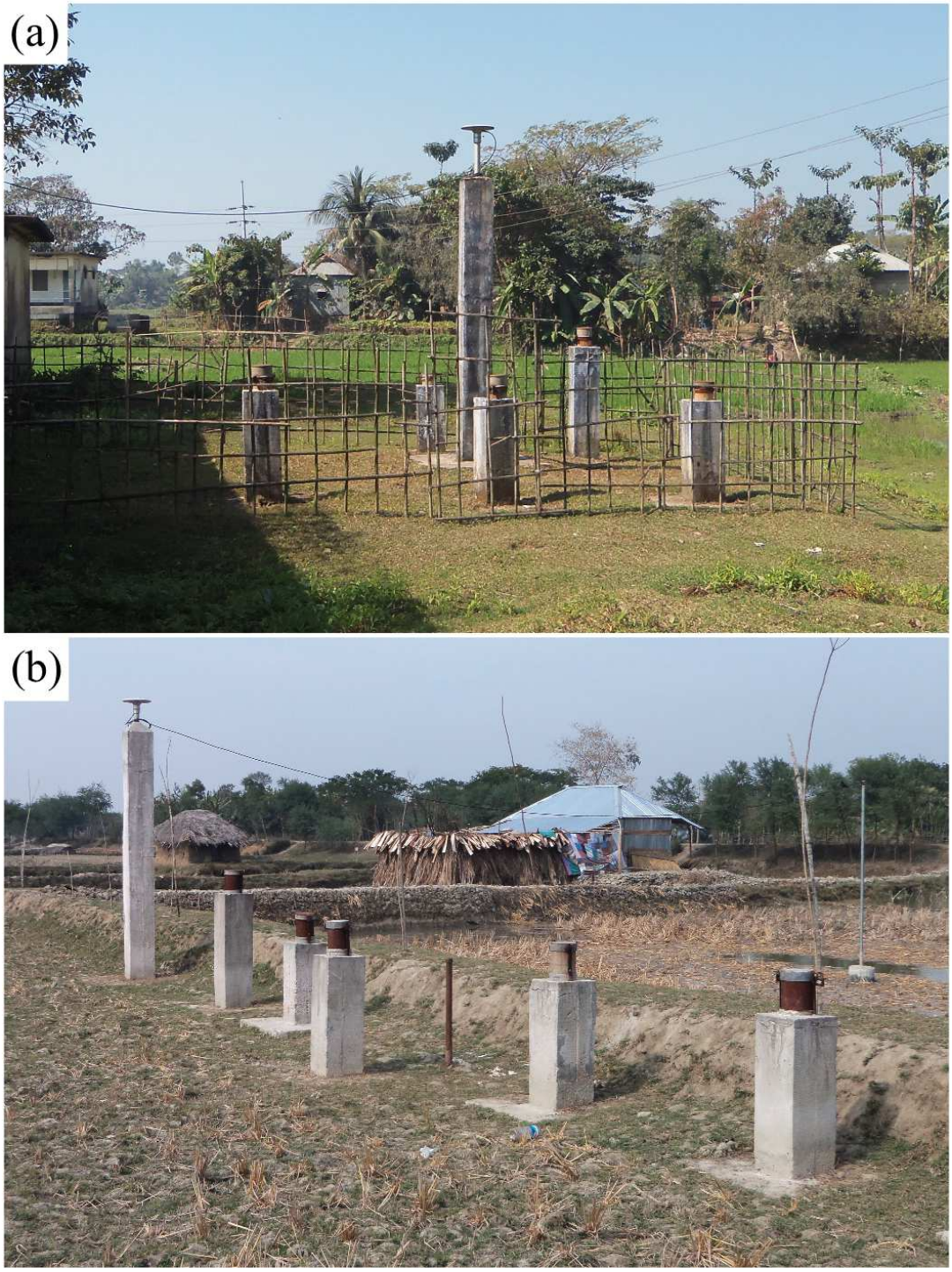


Figure 3.5: Pictures taken of each site two years after deployment. (a) The Jamalganj strainmeter array site with central GPS monument. Note that the left-most well is the defunct 233 m strainmeter. (b) The Khulna strainmeter array site deployed in a line along the river off to the left (this is the same river on the right-hand side of Figure 3.4a).

ments for five years. Accompanying the fiber length recordings are measurements of the resistances of each of the five thermistors at depths of 0.5, 1, 3, 4, and 5 m to correct for the thermally-induced apparent length (index of refraction) changes in the optical fiber near the surface. In February of 2013 an additional ∼125 m long reference fiber coil embedded in epoxy was added to the weekly fiber length measurement sequence. This was done as a check on the long-term behavior of the EDM as well as an additional check on the thermo-optic correction discussed in Section 3.3. Additionally, a small box containing a low-temperature coefficient (1 ppm) resistor and thermistor was introduced to allow weekly measurements to be made for checking on potential errors in the voltmeter used to read the thermistors, and also estimate the air temperature at the time of each measurement.

Data recovery has occurred once per year during visits to each site. The text files from each pair of fibers from each well are copied off the notebook computer. At this time the GPS antenna is replaced with a automatic level to measure the vertical displacements of the strainmeter monuments relative to the GPS monument. This is done by placing a leveling rod on the survey markers embedded in each monument pad. The water level data is also recovered manually by extracting the autonomous piezometers from their wells and downloading their internal memory to a laptop computer.

3.3 Data Analyses

The EDM used in this experiment assumes that the path being measured is to a distant reflector through air, and therefore must be converted into to a physical length since the path is actually a loop of optical fiber subjected to strain and temperature. To derive a suitable correction, first consider the simplified strainmeter schematic shown in Figure 3.6. The optical path length L_{opt} is defined as the product of the physical length L and the index of refraction n, which are both functions of the strain, ϵ, and temperature, T:

$$L_{opt}(\epsilon, T) = n(\epsilon, T)\, L(\epsilon, T). \tag{3.1}$$

Expanding L_{opt} in a first-order Taylor series expansion about zero strain and some temperature T_0:

$$L_{opt}(\epsilon, T) \approx n(0, T_0) L(0, T_0) + \frac{\partial L_{opt}}{\partial \epsilon}(\epsilon - 0) + \frac{\partial L_{opt}}{\partial T}(T - T_0), \tag{3.2}$$

where it is assumed that the partial derivatives are evaluated at $\epsilon = 0$ and $T = T_0$. The strain dependence of the optical path length can be expressed through the strain-optic effect (Equation 1.26) as:

$$\frac{\partial L_{opt}}{\partial \epsilon}(\epsilon - 0) = 2\mu \Delta L_g, \tag{3.3}$$

which only impacts the "gauge" length of the strainmeter, L_g, since it is the only segment subjected to mechanical strain, and the factor of two is a result of the fiber forming a loop at depth. The temperature effects can be broken into two components: the thermal expansion in the unconstrained fiber pigtail and the thermo-optic path length change in the entire strainmeter. Assuming that the thermal expansion of the fiber pigtail is small, the net thermo-optic effect can be expressed as:

$$\frac{\partial L_{opt}}{\partial T}(T - T_0) = 2\alpha (L_p \Delta T_a + L_w \Delta T_w), \tag{3.4}$$

where ΔT_a is the air temperature change that the fiber pigtail length L_p is subjected to, and similarly ΔT_w is the well temperature change affecting a length of fiber cable L_w. The final factor α is the thermo-optic coefficient derived in Equation 1.29. Subtracting the constant term from each side of Equation 3.2 and inserting Equations 3.3 and 3.4:

$$\begin{aligned} L_{opt}(\epsilon, T) - L_{opt}(0, T_0) &= 2\mu \Delta L_g + 2\alpha (L_p \Delta T_a + L_w \Delta T_w) \\ \Delta L_{opt} &= 2[\mu \Delta L_g + \alpha (L_p \Delta T_a + L_w \Delta T_w)]. \end{aligned} \tag{3.5}$$

Note that the fiber loop length L_l in Figure 3.6 does not appear in this equation since it is assumed that it is not subjected to strain, and is sufficiently deep and short ($\sim$0.2 m) to not be significantly affected by temperature changes.

Previous results from an earlier model of the EDM used in this experiment [2] as well as preliminary analysis of these data have shown that the length measurements vary with the laser temperature and received intensity. Examples of

this behavior are shown in Figure 3.7, which clearly shows a laser temperature effect of approximately -2 mm per °C (or about $-1 \times 10^{-5}\,°\mathrm{C}^{-1}$ dividing by the round trip 200 m fiber length for this well). This effect is most likely caused by the sensing laser wavelength increasing with temperature, which decreases the optical path length (Equation 3.1) since the index of refraction decreases with increasing wavelength. Lab experiments have also shown that there is also a small laser temperature dependence of the received intensity, most likely due to improved efficiency in the laser diode at cooler temperatures. The dependence on the received intensity is less well understood since it is the result of a combination of nonlinear electro-optical effects [6].

To derive a suitable EDM laser temperature and received intensity correction, consider again a first-order Taylor series expansion of a generic function L_{EDM} that is a function of the EDM temperature T_E and intensity I_E about some temperature T_{E_0} and intensity I_{E_0}:

$$\begin{aligned} L_{EDM}\left(T_E, I_E\right) &\approx L_{EDM}\left(T_{E_0}, I_{E_0}\right) + \frac{\partial L_{EDM}}{\partial T_E}\left(T_E - T_{E_0}\right) + \frac{\partial L_{EDM}}{\partial I_E}\left(I_E - I_{E_0}\right) \\ &= L_{EDM_0}\left(1 + \beta \Delta T_E + \gamma \Delta I_E\right), \end{aligned} \tag{3.6}$$

where:

$$\beta = \frac{1}{L_{EDM_0}} \frac{\partial L_{EDM}}{\partial T_E} \tag{3.7}$$

$$\gamma = \frac{1}{L_{EDM_0}} \frac{\partial L_{EDM}}{\partial I_E}, \tag{3.8}$$

are the definitions of the laser temperature and intensity correction coefficients, respectively. A final correction equation can be formed by recognizing that the EDM reports one-half the total optical path length, in other words:

$$\Delta L_{EDM_0} = \frac{\Delta L_{opt}}{2}.$$

Combining Equations 3.5 and 3.6, the desired gauge length change can be expressed as:

$$\Delta L_g = \frac{1}{\mu}\left[\frac{\Delta L_{EDM}}{1 + \beta \Delta T_E + \gamma \Delta I_E} - \alpha\left(L_p \Delta T_a + L_w \Delta T_w\right)\right]. \tag{3.9}$$

Table 3.1 summarizes the various coefficients in Equation 3.9 and their uncertainties. The strain-optic and thermo-optic coefficients are from previous lab measurements that can be found in the literature [8, 2]. The length of the strainmeter affected by well temperature changes is chosen to be the length interval of our thermistor string. We are forced to assume that temperature changes below 5 m are negligible because of the difficulty of fitting a model to the temperature profile that is sufficiently well-behaved to safely extrapolate. This is not a significant limitation given that the observed temperature change at 5 m depth is only 2 to 3 °C over this 2-year analysis period .

Estimating the laser temperature and received intensity corrections by least-squares fits to the field data proved to be very problematic since the signal-to-noise varied quite significantly from measurement-to-measurement. For example, the uncertainty in the received intensity correction coefficient was found to be several times larger than the coefficient itself. Therefore, the laser intensity correction has been disregarded. The laser temperature correction coefficient was able to be estimated from the data with a 36% uncertainty. However, this is a very modest correction and therefore this error does not significantly impact the final result (see Section 3.5).

The corrected gauge length displacements and their uncertainties for each fiber and weekly measurement are computed using Equation 3.9 and the values found in Table 3.1. Since no air temperature measurements were taken for the first two years, the first weekly laser temperature measurement is used. The thermistor string resistances are converted to °C by linearly interpolating the manufacturer's calibration table. Weighted averages and uncertainties are also computed for each well where both redundant fiber measurements exist. A handful of anomalous 0.0257 m length measurements were also excluded from the analysis. Data from the collocated GPS receiver at each site was processed by Dhaka University.

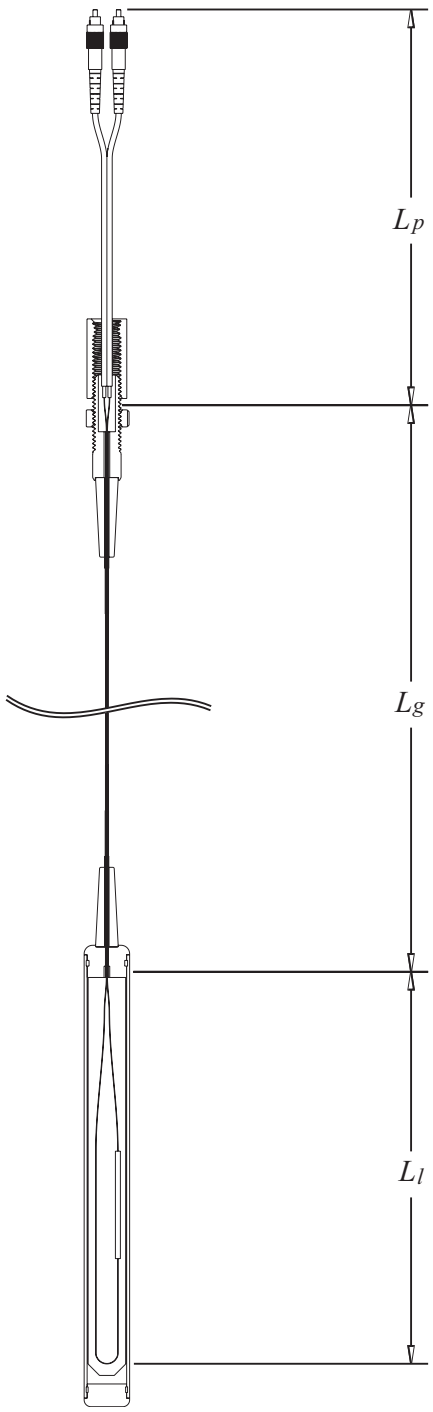


Figure 3.6: Simplified strainmeter schematic showing the three path lengths under consideration. The first is the optical fiber pigtail, length L_p that is subjected to air temperature T_a. Next is the so-called gauge length, L_g, that is partially subjected to well temperature T_w and is the only portion that is subjected to mechanical strain. The lower-most portion is the fiber loop or length L_l, which ideally remains unperturbed.

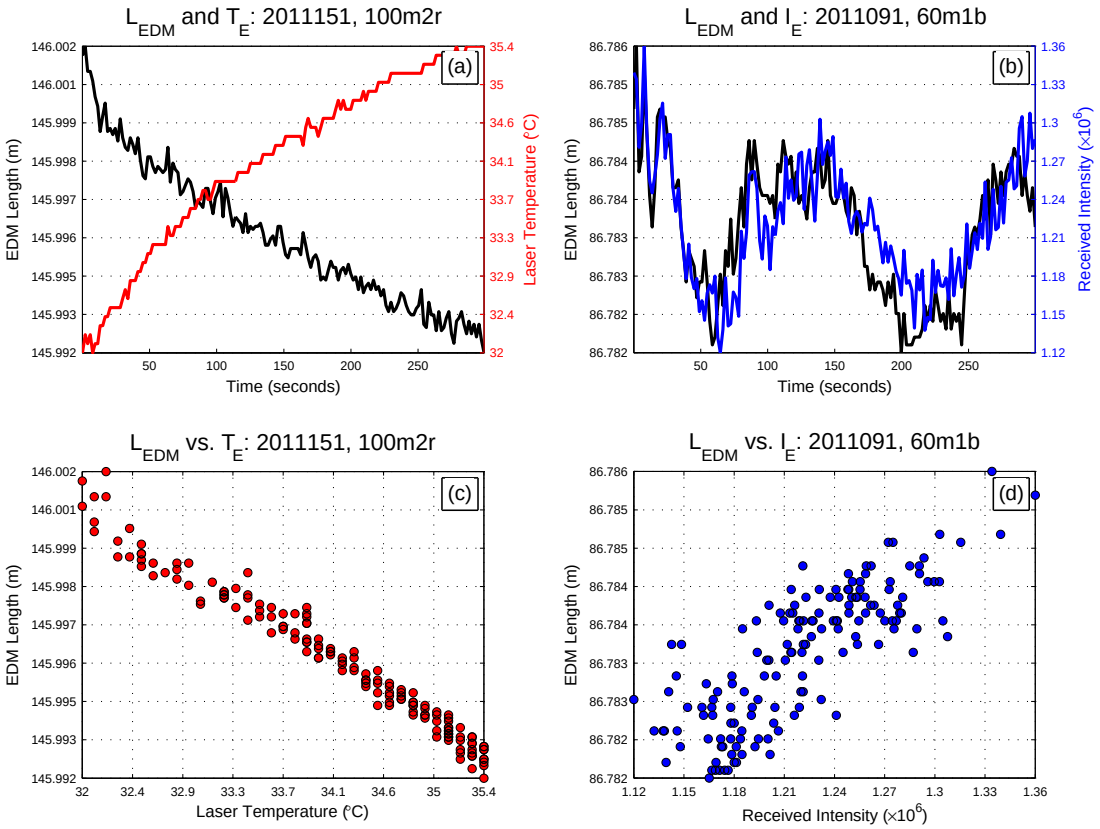


Figure 3.7: Evidence for laser temperature and received intensity dependence from two example 300 second measurement periods. (a) EDM length measurement and laser temperature time series for a fiber in the 100 m Khulna well. (b) EDM length measurement and received intensity time series for a fiber in the 60 m Jamalganj well. (c) EDM length versus laser temperature from the time series shown in (a). (d) EDM length versus received intensity from the time series shown in (b).

3.4 Results

3.4.1 Lab Tests

A series of lab tests was performed to assess the performance of the EDMs, epoxy, and fiber cables as well as determine the amount of tension needed to induce a given strain. The first was to determine the breaking strength of the fiber cables epoxied into their end termination fixtures. Several 1 m lengths were epoxied into test termination fixtures such that hanging masses could easily be added to one

Table 3.1: Table of quantities used to compute the corrected strainmeter gauge length displacement shown in Equation 3.9.

Symbol	Name	Value
μ	Strain-optic coefficient	1.158 ± 0.012
α	Thermo-optic coefficient	$(1.17 \pm 0.03) \times 10^{-5}$ °C^{-1}
β	EDM laser temperature coefficient	$(1.1 \pm 0.4) \times 10^{-5}$ °C^{-1}
L_p	Pigtail Length	1.50 ± 0.01 m
L_w	ΔT_w fiber length	4.50 ± 0.01 m
T_{a_0}	Reference air temperature	25°C
T_{w_0}	Reference well temperature	25°C
T_{E_0}	Reference EDM temperature	25°C

end. We found that the fiber cable broke at a strain of approximately 1%, at a tension of about 585 N (60 kg or 132 pounds under local gravity). Next, four 8.5 m long fiber cables were epoxied into similar test fixtures and stretched between two points where the physical length could be measured along with the tension and optical length. The strain, ϵ, as a function of tension, τ_a, was found to be:

$$\frac{\epsilon}{\tau_a} = 11.65 \pm 0.44 \; \mu\epsilon/\text{N} \; (3.8\%),$$

implying that hanging about 17.5 kg (38.6 lbs) under local gravity is needed to produce the 169 N to stretch the fiber cable assembly by approximately 0.2%. Similarly, a plot of the changes in optical length versus the physical length for each pair of fibers for all four fiber cables during the stretch experiment resulted in an average value of:

$$\mu = 1.10 \pm 0.25 \;\; (22\%) \, .$$

While technically in agreement with the expected value of 1.158 ± 0.012 in Equation 1.25, the unacceptably large uncertainty in this experiment was the result of laser temperature variations and aforementioned anomalous length measurements

using the provided software. This lead to the development of the `MATLAB` script for operating the EDM. Unfortunately we were not able to repeat this experiment before deployment to achieve a better constrained estimate. However, similar experiments by Blum [2] and predecessors have confirmed the value of μ in Equation 1.25, and slight differences are inconsequential given the scatter in the data.

3.4.2 In-Situ Measurements

An in-situ test was performed at each site after deployment to verify that the strainmeters were functioning. At Jamalganj, the wellhead design did not permit access to the adjustment bolts on the upper termination fixture bridge. However, length measurements were made before and after tensioning the fiber cables that are summarized in Table 3.2. While the measured length change in the field was calculated using Equation 1.22 ($\Delta L_{opt} = \mu \Delta L$), the expected value was computed from the pre-deployment, lab-measured EDM lengths of the two fibers in each strainmeter as:

$$\text{Expected } \Delta L = 0.002 \times \left(\frac{L_{EDM_1} + L_{EDM_2}}{2n} - L_p - L_l \right),$$

where 0.002 is the intended strain from the initial deployment tensioning, and the pigtail (L_p) and loop (L_l) lengths have been subtracted off after converting the average optical path length of the two fibers (L_{EDM_1} and L_{EDM_2}) to a physical path length. The measured displacements for the 40 and 60 m strainmeters are in agreement with the predicted displacements, and the 10 mm ($\sim 3\sigma$) mismatch in the 100 m strainmeter is only about 5% of the expected displacement. However, the 20 m strainmeter is off by almost a factor of 2, which may be indicative of overfilling the well with grout since proper tensioning did occur. This would imply a gauge length of only 9.3 ± 0.2 meters.

At Khulna the wellhead design was revised and each pair of fibers were measured under tension where the adjustable bridge was displaced five times in 5 mm increments. The average of the fits to the optical length (corrected for the laser temperature) versus displacement for all six strainmeters yielded:

$$\mu = 1.16 \pm 0.16 \ (14\%),$$

Table 3.2: Summary the Jamalganj well measurements taken before and after tensioning. Note that the EDM values measured in the field were single-shot measurements and therefore no uncertainty was reported. The uncertainty in ΔL is derived from the strain-optic coefficient and the estimated gauge length of the strainmeter, which dominates the omitted uncertainty for the expected displacement.

Well	ΔL_{EDM} (mm)	ΔL (mm)	Expected ΔL (mm)	Difference (mm)
20 m	21.5	18.6 ± 0.3	33.8	-15.2 ± 0.3
40 m	87.7	76.0 ± 1.2	74.2	$+1.8 \pm 1.2$
60 m	133.9	116.1 ± 1.8	115.1	$+1.0 \pm 1.8$
100 m	215.1	186.4 ± 2.9	196.4	-10.0 ± 2.9

in complete agreement with the expected value computed in Equation 1.25. While the 14% uncertainty is still very large, it was sufficient to show that the strainmeters were tensioned over their intended intervals.

3.4.3 Campaign Measurements

Results from the weekly strainmeter measurements are shown in Figures 3.8 and 3.9 for Jamalganj in the north and Khulna in the south, respectively. Both figures show only the three shortest strainmeters at each site. In Jamalganj (Figure 3.8), recall that only the 20, 40, 60, 100 m strainmeters were successfully installed. Unfortunately, both fiber pigtails broke on the 100 m strainmeter within two months of deployment, thereby rendering the instrument unusable. (These have been repaired and producing data as of February, 2013.) The three deepest (80, 100, and 300 m) wells in Khulna are difficult to interpret. While the 80 m well also suffered two broken pigtails within the first year of operation, the variance in these three strainmeters is too large to plot with the shorter wells using the same axis limits.

The long term linear subsidence rates have also been computed for each strainmeter. These accompany the results from the three shortest strainmeters in Figures 3.8 and 3.9, and summarized with their uncertainties in Table 3.3. This

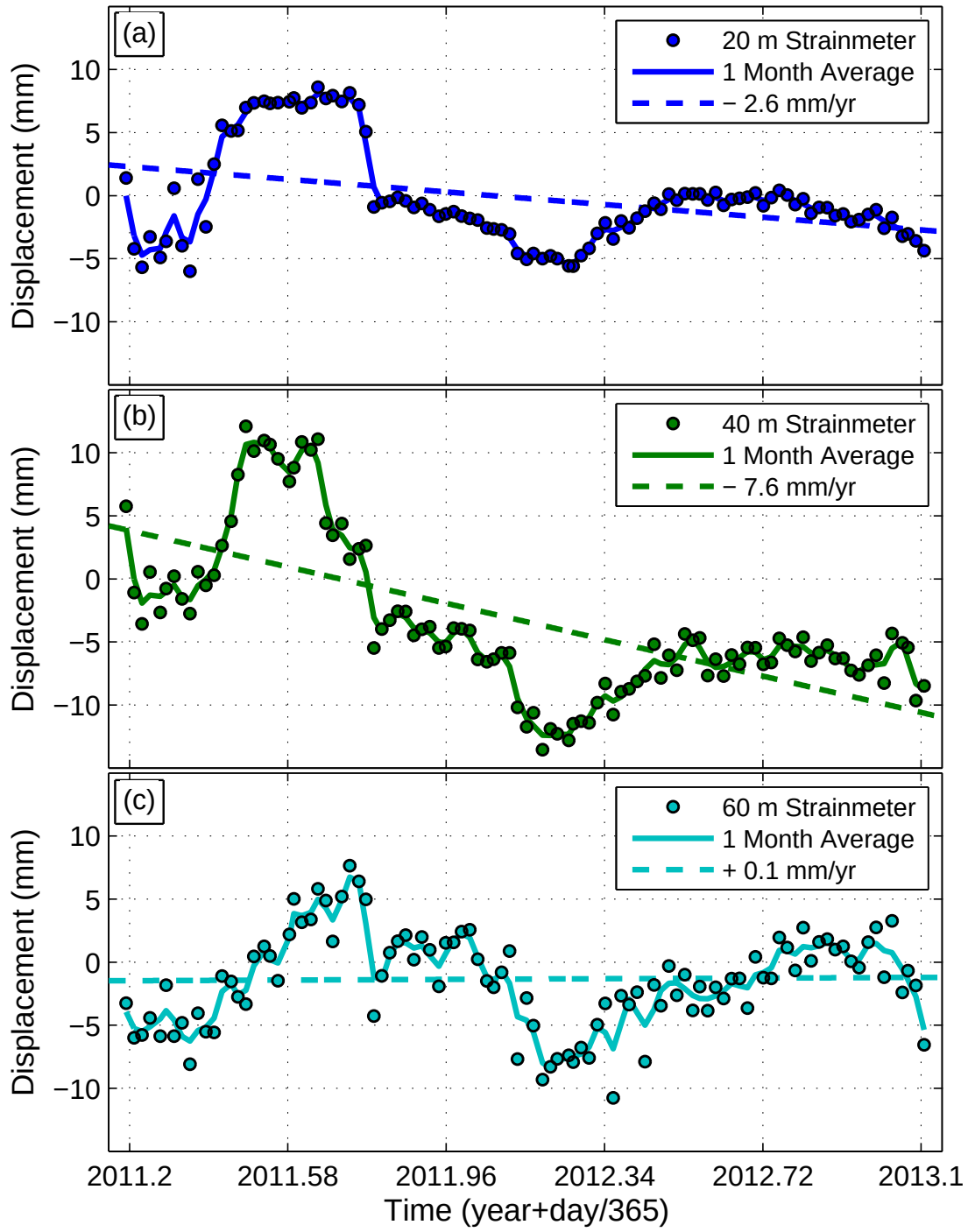


Figure 3.8: Two year displacement time series from Jamalganj from the weekly measurements accompanied by their one month moving averages and linear trends. (a) Results from the 20 m strainmeter, (b) 40 m strainmeter, and (c) 60 m strainmeter.

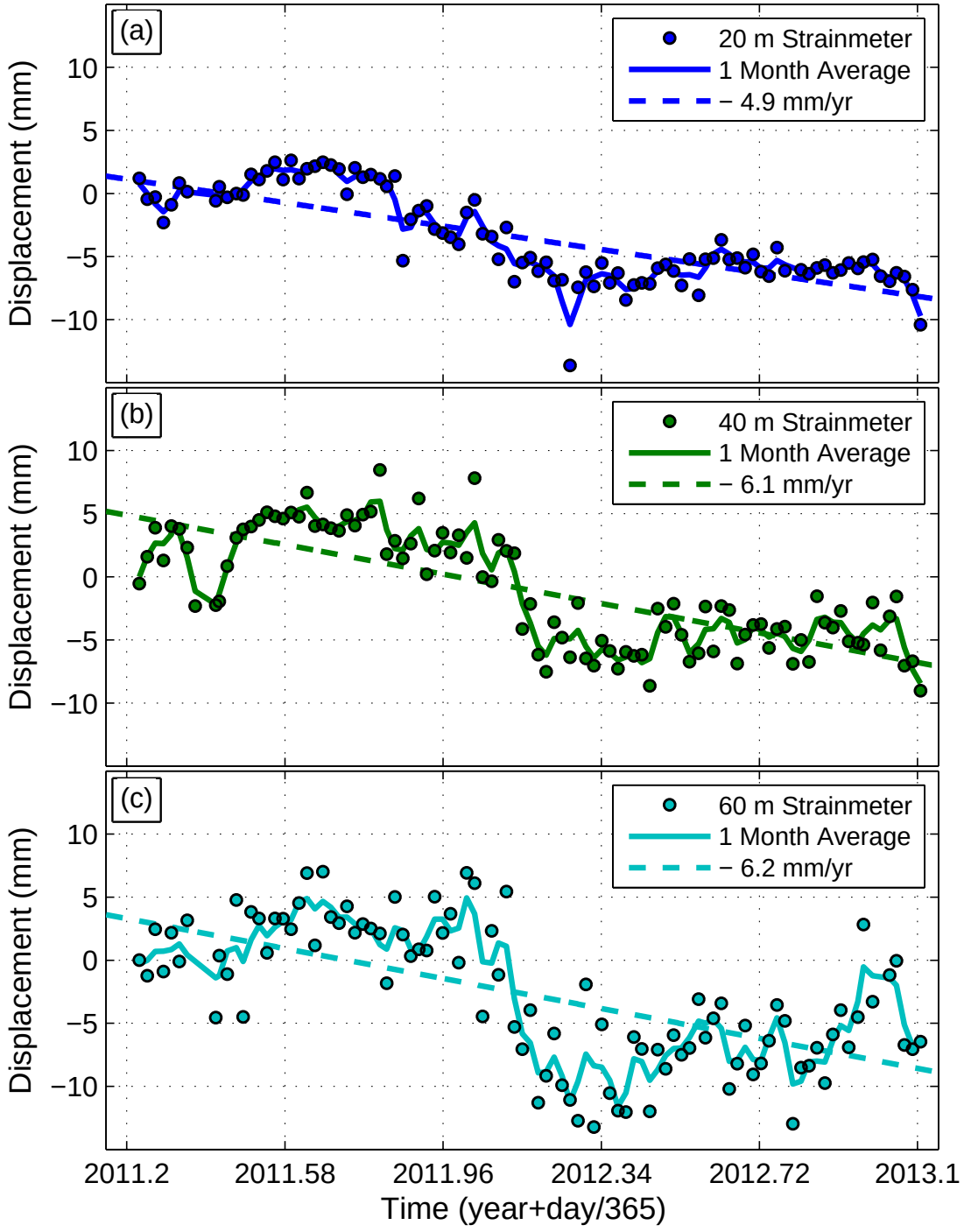


Figure 3.9: Two year displacement time series from Khulna from the weekly measurements accompanied by their one month moving averages and linear trends. (a) Results from the 20 m strainmeter, (b) 40 m strainmeter, and (c) 60 m strainmeter.

Table 3.3: Annual linear subsidence rates for each site from strainmeter and GPS measurements.

JMLC	Rate (mm/yr)
20 m	-2.6 ± 0.6
40 m	-7.6 ± 0.9
60 m	$+0.1 \pm 0.7$
GPS	-7.8 ± 0.6

KHLC	Rate (mm/yr)
20 m	-4.9 ± 0.4
40 m	-6.1 ± 0.6
60 m	-6.2 ± 0.8
100 m	-0.2 ± 1.0
300 m	-29.4 ± 5.6
GPS	-23.7 ± 0.5

table also shows the results for the 100 and 300 m Khulna strainmeters as well as the subsidence rates for each of the collocated GPS receivers. The 1-month moving average strainmeter and vertical GPS displacement time series are presented in Figure 3.10.

The monument level data and their uncertainties are shown in Table 3.4 for Jamalganj and Table 3.5 for Khulna. While there are no figures presented for some of the strainmeters, their monument heights are reported to show the overall variability in the subsidence rates of the monuments at each site. Due to problems with the automatic level, most of the initial monument heights from Khulna in 2011 were not recorded. Note that the monument level data have not been incorporated into the plots or rate calculations because of their minor contribution.

The 1-month moving averaged well temperature and water level time series for the Jamalganj site are presented in Figure 3.11. Results from the Khulna site show similar features. Both series show a strong seasonal signal, despite correcting for the well temperature in computing the strainmeter displacements. However, the temperature time data appear to lead the displacements whereas the water height appears to be in-phase.

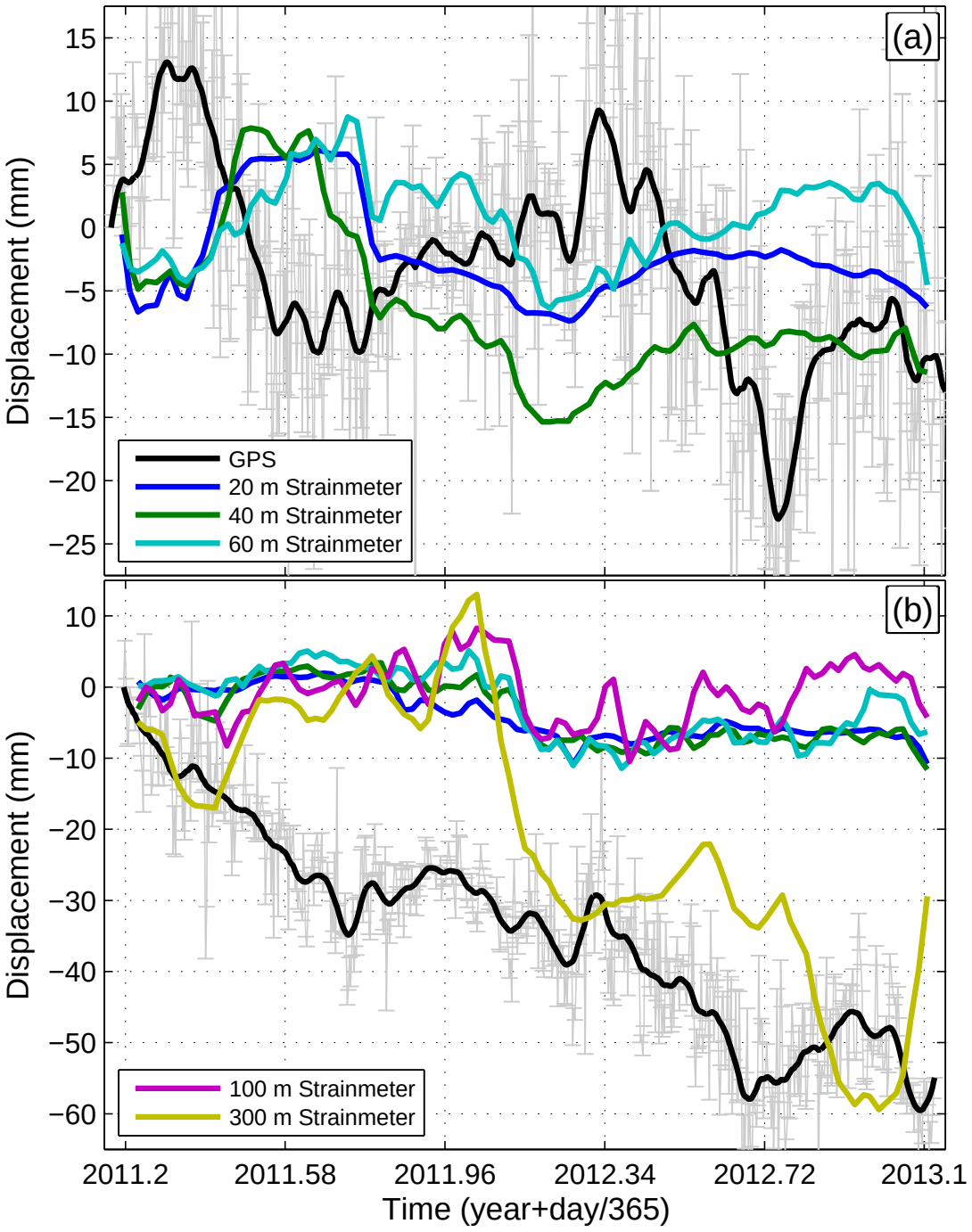


Figure 3.10: Comparison of the 1 month average strainmeter displacements to the vertical displacements from the collocated GPS receiver at (a) Jamalganj, and (b) Khulna. Note that the error bars for each GPS measurement are shown in gray.

Table 3.4: Jamalganj strainmeter monument positions relative to the GPS tower. All uncertainties are ±2 mm.

Well	2011 (mm)	2012 (mm)	2013 (mm)	Rate (mm/yr)
20 m	2,535	2,534	2,535	-0
40 m	2,514	2,513	2,514	-0
60 m	2,566	2,564	2,561	-3
100 m	2,427	2,424	2,422	-2
300 m	2,599	2,596	2,596	-2

Table 3.5: Khulna strainmeter monument positions relative to the GPS tower. All uncertainties are ±2 mm.

Well	2011 (mm)	2012 (mm)	2013 (mm)	Rate (mm/yr)
20 m	2,698	2,775	2,770	-5
40 m	n/a	2,696	2,687	-9
60 m	n/a	2,656	2,639	-17
80 m	n/a	2,692	2,686	-6
100 m	n/a	2,723	2,722	-1
300 m	2,764	2,712	2,711	-1

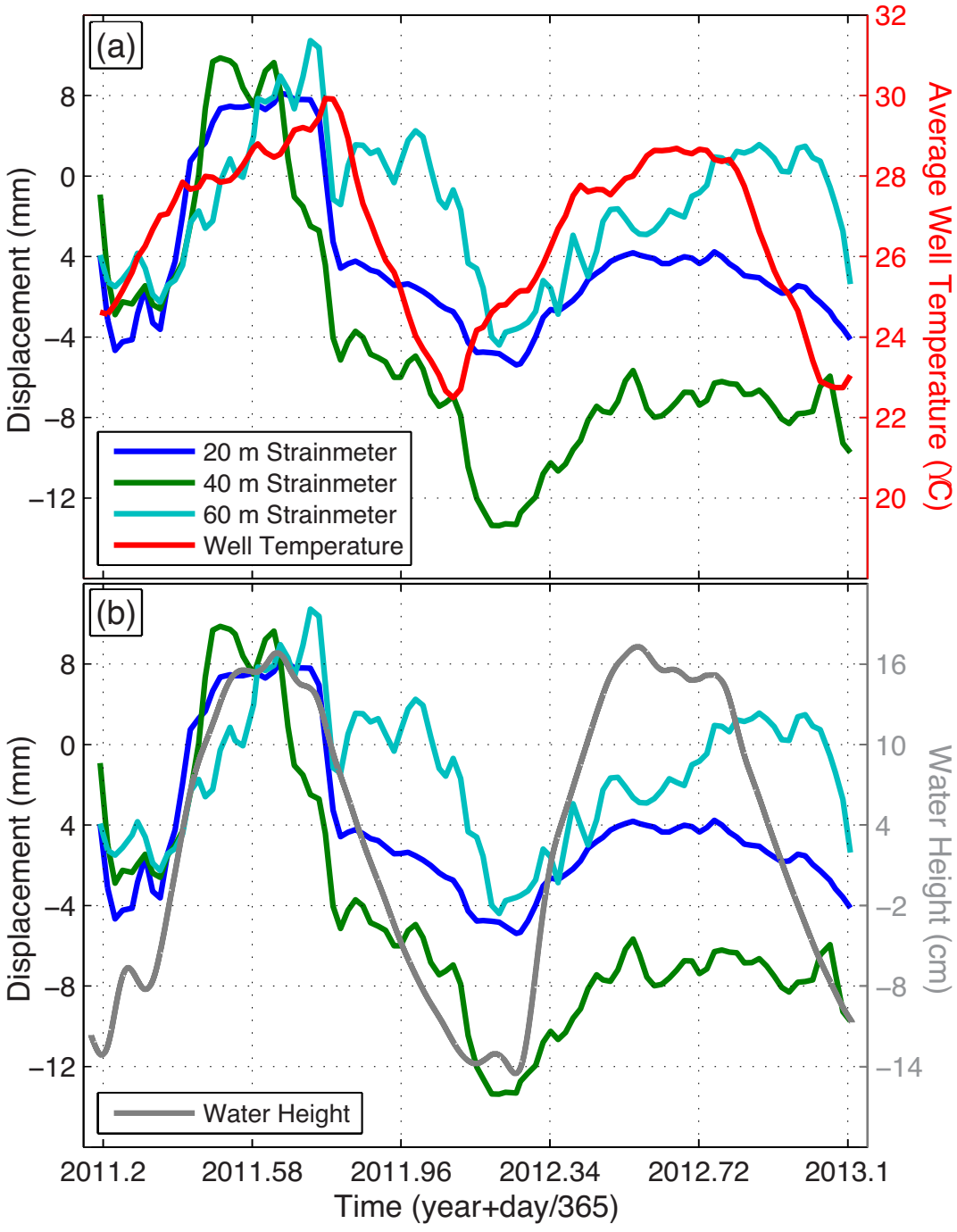


Figure 3.11: Calculated displacements at Jamalganj compared with (a) residual temperature and (b) borehole water level. While only the data from Jamalganj are presented, the Khulna results are similar.

3.5 Discussion

The two year displacement records for the strainmeters at each site show the evidence for ground deformation and the potential of the fiber systems for measuring sediment compaction. In Jamalganj (Figure 3.8) there is some initial settling or other anomalous behavior until about 2011.8, after which the record appears to be comprised of a long-term trend and a seasonal signal. Fits to the displacement records do show a secular trend that is in reasonable agreement with the GPS results. This is in contrast to the Khulna results where the shallow wells do not resemble the GPS data. While the four shallowest wells in Khulna show approximately the same small seasonal and approximately 6 mm/yr subsidence rate, only the deepest 300 m strainmeter seems to follow the very high GPS subsidence rate of 25 mm/yr rate. This result suggests that the majority of the compaction may lie between 100 and 300 m depth.

Another notable feature in all the strainmeter data is that the seasonal signals appear to be anti-correlated with the GPS. For example, the seasonal lows at approximately 2011.7 and 2012.7 in the GPS data are seasonal highs in the strainmeter data. This is less obvious in the Khulna data given the scale difference between the two plots to capture the range of GPS displacements. While the seasonal lows in the GPS data are known to be from water overburden during monsoonal floods [5], the monsoonal highs in the displacement record were not expected. Ruling out the effect of temperature (the net effects of which are discussed below), it is believed that this is expansion of the sediment column due to water saturation. If so, it is possible that the overburden (seasonal lows) seen in the GPS are lessened by this effect, which may play an important role in the regional models being developed by collaborating institutions.

In terms of instrument performance, the most important observation is that of the increase in week-to-week variability as the strainmeter length increases. While the statistical uncertainties are about 400 μm for a given measurement, there is a clear repeatability issue related to either the EDM, strainmeter, or changes in their environmental conditions. Temperature changes are always suspect, however a 20°C temperature change in the 1.5 m long fiber pigtail should only result in a

350 μm length change. The laser temperature correction could be another source of error since it scales with the length of the strainmeter at about 1.1 mm per °C per 100 meters of fiber.

Despite removing three different temperature estimates from the data (air, well, and laser), there still appears to be some correlation between the well temperature and the displacement measurements (Figure 3.11). This appears to be more significant for the Jamalganj strainmeters. One approach to suppress this effect is to let the length of the strainmeter affected by well temperature changes, L_w, vary to minimize this correlation. While this does reduce the apparent seasonal signal for the Jamalganj strainmeters, the Khulna results are largely unchanged. Varying the laser temperature correction, which is also correlated with the well temperature, by $\pm 1\sigma$ also did not appear to minimize this correlation.

3.6 Conclusions and Future Work

Optical fiber strainmeters interrogated with fiber-coupled EDMs can be an effective tool for measuring sediment compaction. While more data are needed to better determine the compaction rates in the presence of seasonal signals, both strainmeter arrays appear to be collecting meaningful results. The results from Khulna suggests that most of the compaction signal seen by the GPS may be contained between 100 and 300 meters depth. Results from Jamalganj show a similar inter-annual trend as the GPS, and both sites exhibit seasonal displacement highs where the GPS shows displacement lows. Examination of borehole temperature and water level data indicate that this anticorrelation may be due to sediment saturation during the monsoon.

The largest source of uncertainty appears to be the week-to-week variability in the EDM measurements. This inconsistency appears to be progressively more problematic for longer length fibers. This may be due to the limits of the EDM as it operates farther away from some optimal length range and/or increased sensitivity of the EDM components to environmental conditions.

While measurements are expected to continue for another three years, new

ancillary measurements started in February 2013 are hoped to improve the quality of the data. The first is that of a true air temperature measurement to obtain a better estimate of the environmental conditions of the EDM. The second, and perhaps most significant, is the introduction of an encapsulated 100 m reference fiber loop that will help characterize the long term behavior of the EDM as well as provide a fixed reference for better constraining the laser temperature correction coefficient.

Repairs to 8 of the 20 individual fiber pigtails were performed in February of 2013. This is believed to be a result of the increased fragility of the optical fiber within the pigtail, since it appeared that the acrylate tight-buffer was sloughing off of the glass fiber due to prolonged exposure to excessive temperature at the wellhead. One potential solution is the use of high-temperature polyimide-jacketed fiber inside each pigtail. A more innovative approach would be to develop a combined upper termination fixture and fiber connector such that each strainmeter fiber could be interrogated with a separable pigtail. This would also allow for the length of the pigtail to be more easily removed from the weekly displacement records since it could be measured independently of the tensioned fibers.

Future work on this project will consist of further analysis and interpretation of the combined strainmeter and GPS data. While there is interest in additional deployments for optical fiber strainmeters in Bangladesh, these will most likely be more similar to the instrument described in Chapters 4 and 5. This includes interferometric interrogation and a new down-hole clamping method for the upper termination fixture to limit exposure to surface temperature changes.

3.7 Acknowledgments

We would like to thank a number of people who assisted in this effort. Frank Wyatt, Don Elliott, and Billy Hatfield provided very valuable assistance with the down-hole grout mixture used for each strainmeter. John Bjork, Joel White, and Heinz Wuhrmann provided assistance with the fabrication and assembly of various instrument components. We are especially indebted to Shahin Alam and Hafizur

Rahaman for weekly data collection and Dhiman Mondal for all of his outstanding assistance during the site selection and deployment phases.

Portions of this chapter are being prepared for publication in the following manuscript: **Scott DeWolf, Scott L. Nooner, Michael S. Steckler, Mark A. Zumberge, and Syed Humayun Akhter. "Optical Fiber Borehole Strainmeter Arrays for Measuring Sediment Compaction in Bangladesh."** The author's contribution to this study was to assist in the prototyping, design, and fabrication of the instruments, perform laboratory and field calibrations, assist in the deployment, program the data acquisition hardware, analyze the data, and prepare the manuscript.

REFERENCES

[1] Duncan Carr Agnew. Strainmeters and tiltmeters. *Reviews of Geophysics*, 24(3):579–624, 1986.

[2] John A. Blum. *Development of sensors and techniques to assess earthquake hazards and submarine slope stability.* Ph.D. thesis, University of California San Diego, 2010.

[3] Ben E. Lofgren. *Field Measurement of Aquifer-system Compaction, San Joaquin Valley, California, USA.* United States Geological Survey, 1969. 13 pages.

[4] John D. Milliman and James P. M. Syvitski. Geomorphic/tectonic control of sediment discharge to the ocean: The importance of small mountainous rivers. *The Journal of Geology*, 100(5):525–544, 1987.

[5] Michael S. Steckler, Scott L. Nooner, Syed Humayun Akhter, Sazedul K. Chowdhury, Srinivas Bettadpur, Leonardo Seeber, and Mikhail G. Kogan. Modeling Earth deformation from monsoonal flooding in Bangladesh using hydrographic, GPS, and Gravity Recovery and Climate Experiment (GRACE) data. *Journal of Geophysical Research*, 115:B08407, 2010.

[6] Stefen Taeschler, CEO Dimetix AG. Personal communication, 15 May, 2013.

[7] James P. M. Syvitski, Charles J. Vörösmarty, Albert J. Kettner, and Pamela Green. Impact of Humans on the Flux of Terrestrial Sediment to the Global Coastal Ocean. *Science*, 308(5720):376–380, 2005.

[8] Mark A. Zumberge, Frank K. Wyatt, Dong X. Yu, and Hideo Hanada. Optical fibers for measurement of earth strain. *Applied Optics*, 27(19):4131–4138, October 1988.

Chapter 4

Development of the Borehole Optical Fiber Strainmeter

This chapter describes the development of the Borehole Optical Fiber Strainmeter (BOFS) and a fiber areal strainmeter that were deployed at the Piñon Flat Observatory (PFO) in December of 2011, consisting of parallel, redundant full-borehole length fibers for the BOFS, and a fiber-wrapped cylinder in the case of the areal strainmeter. Included are the results of initial prototyping work, as well as a series of lab and field tests to establish some of the key parameters that govern the performance of the instrument.

4.1 Introduction

4.1.1 Strain Sensing

Strainmeters occupy a unique place with respect to other geophysical measurements, which also implies the potential for quantifying novel behaviors related to the deformation of the Earth's surface. The goal of these instruments is to measure events that take place over time periods too long for seismometers, and too small to be captured by GPS (Figure 4.1). This includes episodic tremor and slip events [11] and other so-called "slow earthquakes" [9, 7] characterized by aseismic slip events that take place over days and months, as well as deformations from

volcanic activity [10].

While the history of strain sensing and strainmeter design is extensive (see Agnew, 1986 [2] for a review), there are two technologies of particular relevance to the current development. The first is the laser strainmeter (LSM) that consists of two surface end monuments separated by some distance (typically several hundred meters) whose relative horizontal displacements are tracked using a Michelson interferometer. The interrogating laser beam propagates through a 0.15 m diameter evacuated pipe to eliminate temperature and humidity induced changes in the index of refraction along the interferometer path.

The other instrument is a down-hole, 4-component system known as the Gladwin Tensor Strainmeter (GTSM) [6]. This device consists of 4 stacked horizontal extensometers that span the inner diameter of its cylindrical downhole package. Three of these are separated in azimuth by 120°, where the fourth is orthogonal to the first for redundancy. Combination of these four gauges provides for an overdetermined system of equations for the complete strain tensor (assum-

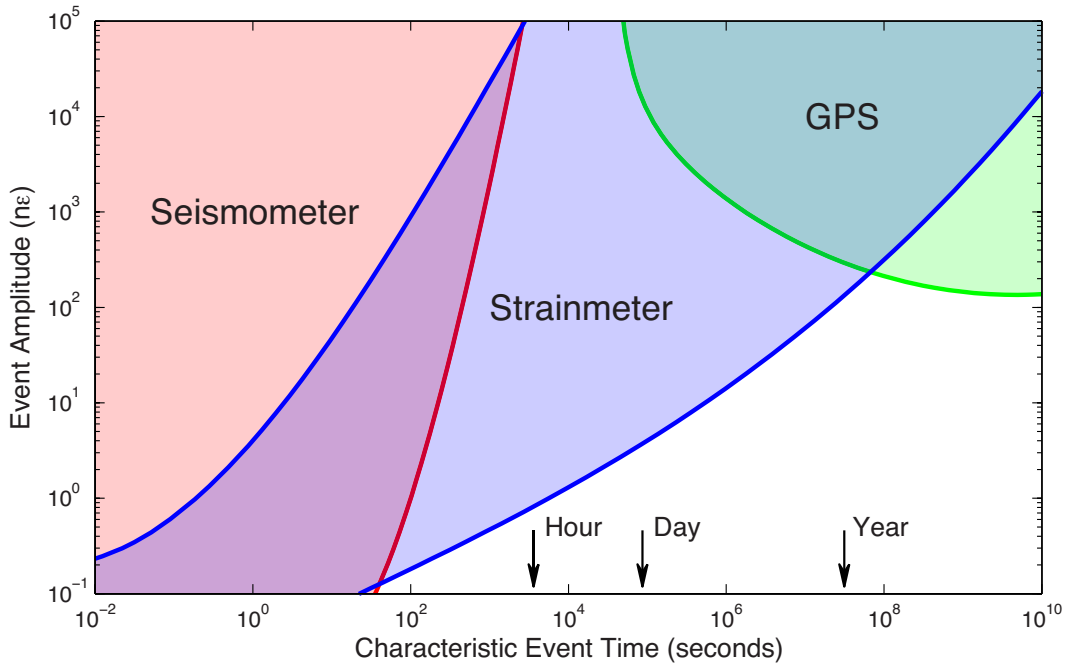


Figure 4.1: Signal amplitude as a function of characteristic event time showing where seismic, strain, and GPS technologies overlap (adapted from [1]).

ing a traction-free halfspace, i.e., no vertical stresses).

A few optical fibers have also been used recently for long base length geophysical strain measurements. The most comparable instrument to the borehole strainmeter discussed in this development is the SAFOD borehole strainmeter developed and installed by Zumberge in 2004, which consists of a loop of optical fiber that extends 782 m below the surface, and whose length changes are measured using interferometry [5]. The SAFOD strainmeter has been used to measure coseismic offsets as well as local Rayleigh wave phase velocities [4], but unfortunately, longer period strains have been contaminated by temperature changes as a result of having the up-hole terminus of the interferometer exposed at the surface. Optical issues such as polarization fading (Chapter 1) have been problematic for this installation and need to be carefully accounted for when analyzing the data.

4.1.2 Rationale for this Development

The primary motivation for this project is to investigate and improve the performance of optical fiber interferometers for measuring long baseline strain in a borehole. A new optical interferometer system is employed that both eliminates polarization fading and provides the signals needed to estimate the optical phase without the use of specialized electronics. The improved thermal environment of BOFS compared to previous deployments allows this system to examine longer period strains such as solid earth tides, as well as better constrain the magnitude of the long term drift in the index of refraction in the optical fibers that competes with and typically obscures the longest period secular strain signals.

BOFS is located at the Piñon Flat Observatory (PFO), which has been a test bed for many geophysical instruments over the last four decades (Figure 4.2). Included among these are the three long baseline laser strainmeters (LSMs) that are considered to be one of the highest quality strain measurement systems currently operating, and thus serves as the primary reference system. In addition to several seismic stations, PFO is also the location of the Plate Boundary Observatory borehole tensor strainmeter B084 that is one of nearly 80 such GTSMs deployed as a part of this program.

This chapter is intended to provide a detailed description of the design, fabrication, and deployment of BOFS and the accompanying areal strainmeter, along with some laboratory and field tests performed during these processes. The actual analysis of the data and the performance of BOFS compared to the LSMs and GTSM for measuring real strain signals in the Earth is covered in the next chapter.

4.2 Mechanical Design

BOFS is similar to previous optical fiber borehole strainmeters in that it consists of an optical fiber stretched vertically between two points in a borehole (Figure 4.3). This new strainmeter has three major mechanical components: the upper sonde, lower sonde, and the optical fibers stretched between them. The borehole and wellhead are also integral parts of the strainmeter since their design also affects the stability and performance of the entire system. Each of these is discussed in detail in the following sections.

4.2.1 Optical Fiber Cables

The principle component and primary vertical strain sensing elements of BOFS are the two fiber cables containing, between them, six optical fibers that extend between the up-hole and down-hole terminations of the strainmeter. These form three redundant vertical strainmeters as well as send and receive light from the areal strainmeter contained in the lower sonde. The first fiber cable (colored red in Figure 4.3) contains four fibers within a gel-filled 1.3 mm diameter, 0.13 mm wall stainless steel tubing coated with polyurethane to a diameter of 3.8 mm for additional ruggedness for deployment. The second cable (colored green in Figure 4.3) is similar but contains only two fibers inside a narrower 1.2 mm stainless steel tube of the same 0.13 mm wall thickness. This fiber cable does not contain water inhibiting gel and has also been coated to a diameter 3.8 mm with polyethylene. Each fiber cable is approximately 250 m (820 feet) long.

The motivation for using two separate fiber cables is that it provides a way

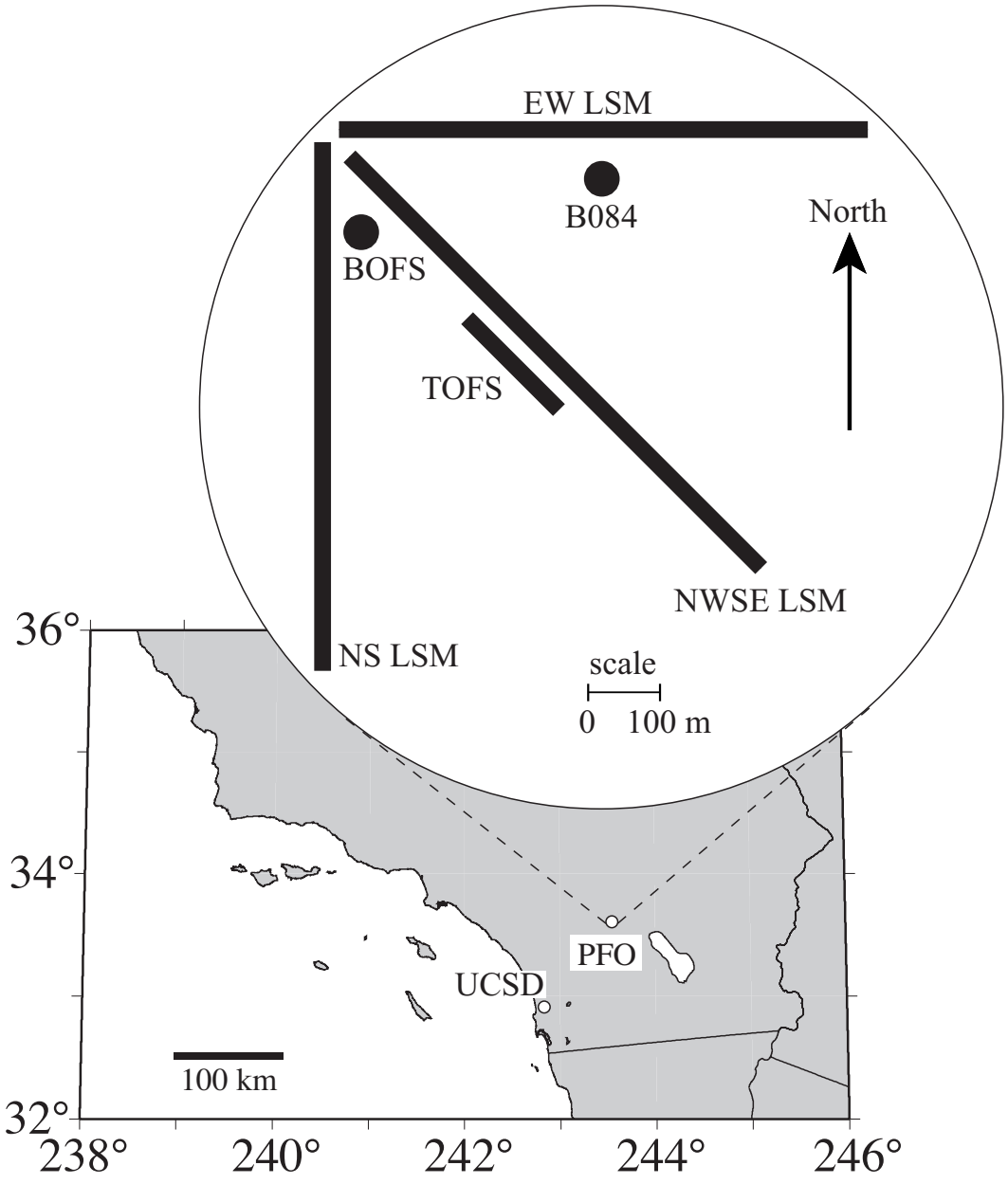


Figure 4.2: PFO layout showing the location of BOFS as well as the three LSMs and GTSM (PBO element B084) just west-northwest from the Salton Sea in Southern California. The horizontal Trench Optical Fiber Strainmeter (TOFS) shown parallel to the NWSE LSM is the subject of Chapter 6.

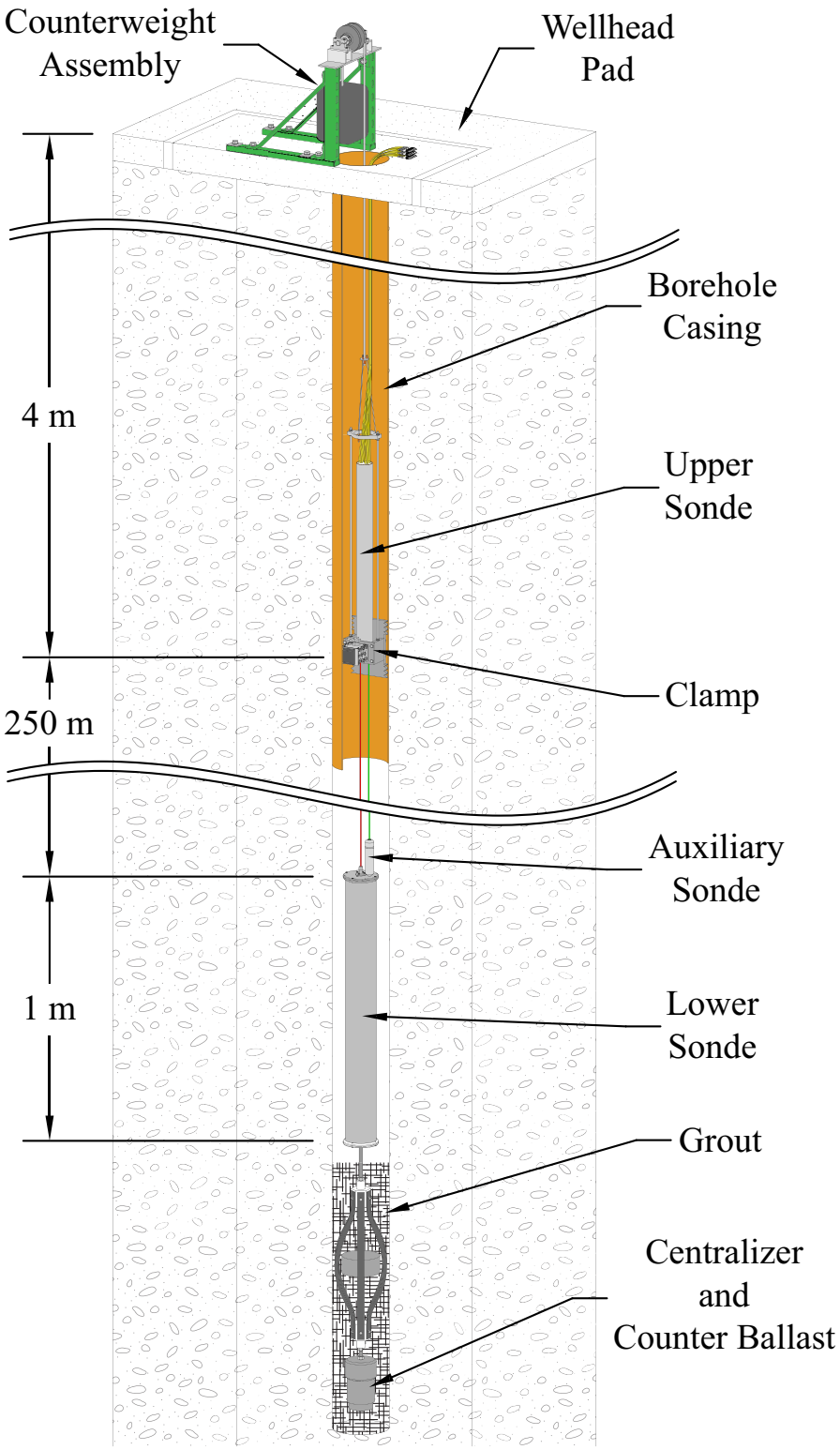


Figure 4.3: Cutaway schematic of BOFS showing each of its major components as well as the counterweight and concrete pads that make up the wellhead.

to divide the tasks of each individual fiber and to guard against different types of potential failure. In the red fiber cable, containing four fibers, two are dedicated to independently measuring vertical strain (herein labeled as "primary" and "secondary"), and the other two fibers interrogate the down-hole areal strainmeter. Having two vertical strainmeters in one cable is beneficial if one is found to be problematic, moreover, the green fiber cable, containing only two fibers, also measures vertical strain (labeled as "auxiliary") in a different (non-gel filled) environment. While the primary and secondary vertical strainmeter fibers terminate inside the lower sonde, the auxiliary vertical strainmeter fibers form a loop contained in a separate down-hole container (similar to the Bangladesh strainmeters) at the top of the lower sonde, returning to the upper sonde to form a strainmeter of nominally twice the sensitivity and serves as a self-consistency check. Furthermore, since the auxiliary fiber cable does not include the water-inhibiting gel commonly used in this type of fiber cabling, any conspicuous difference serves to identify the preferred system in future deployments, in terms of their responses to strain events and longevity.

4.2.2 Upper Sonde

The upper sonde forms the up-hole termination point for all three vertical strainmeters as well as the input and output for all of the optical components. It is clamped to the inside of the borehole about 4 m below the surface to limit the exposure of the up-hole portion of the interferometers to diurnal temperature fluctuations. The main body is a 6 cm diameter, 70 cm long stainless steel cylinder whose base accepts two fiber cable termination fixtures. This base also connects to the wall plate and expandable scissor-jack borehole clamp that secures the upper sonde within the borehole casing.

Figure 4.4 shows one side of the upper sonde with the outer protective stainless steel cylinder removed, revealing some of the components used to interrogate BOFS. Entering the top are twelve, 3 mm diameter, Kevlar reinforced optical fiber communication cables for sending and receiving light from the four interferometers. The 900 μm jacketed fibers within the communication cables pass through a

disc of slightly smaller diameter than the inner diameter of the outer cylinder, and are separated between the front and back sides of the (vertical) inner tray. This inner tray holds the up-hole optical components for the primary and secondary vertical strainmeters on one side, and the auxiliary and areal strainmeters on the other (Figure 4.4). The optical components are secured to the inner tray using component mounts, and the tray itself is connected to the baseplate with another disc.

The upper termination point of the long sensing fibers for the vertical strainmeters takes place inside of the two fiber feedthroughs where the fiber cables and individual fibers are immobilized in epoxy. Both feedthroughs are sealed to the bottom of the baseplate with o-rings, and are each held in place with four small bolts. Fibers within the upper sonde are not held under tension, but also not allowed to be slack, in an attempt to minimize their sensitivity to strains and vibrations of the sonde itself. After assembling the component tray, the outer cylinder is epoxied into the baseplate and the top filled with a layer of epoxy and then polyurethane rubber to form a completely sealed unit.

4.2.3 Lower Sonde and Areal Strainmeter

The lower sonde forms the down-hole terminal point for the primary and secondary vertical strainmeters, and houses the areal strainmeter (Figure 4.5). The lower sonde is a 114 mm diameter, 3 mm wall, 1 m long stainless steel pressure case sealed at both ends by double o-ring bore seal caps. Water-tight fiber feedthroughs similar to that on the upper sonde acts as the lower termination fixture for the fiber cables. Aluminum trays are mounted to the inside of each end cap to hold optical components such as the Faraday mirrors for the primary and secondary vertical strainmeters and all the components for the areal strainmeter (Figure 4.5b,c).

As mentioned above, the BOFS lower sonde pressure case is also intended to serve as an areal strainmeter. Epoxied to the inside of the outer stainless steel pressure case is an 85 cm long, thin-walled aluminum sleeve. This aluminum sleeve has a helical groove on its outer surface that holds approximately 80 m of single mode optical fiber that penetrates into the interior of the sleeve through two slots

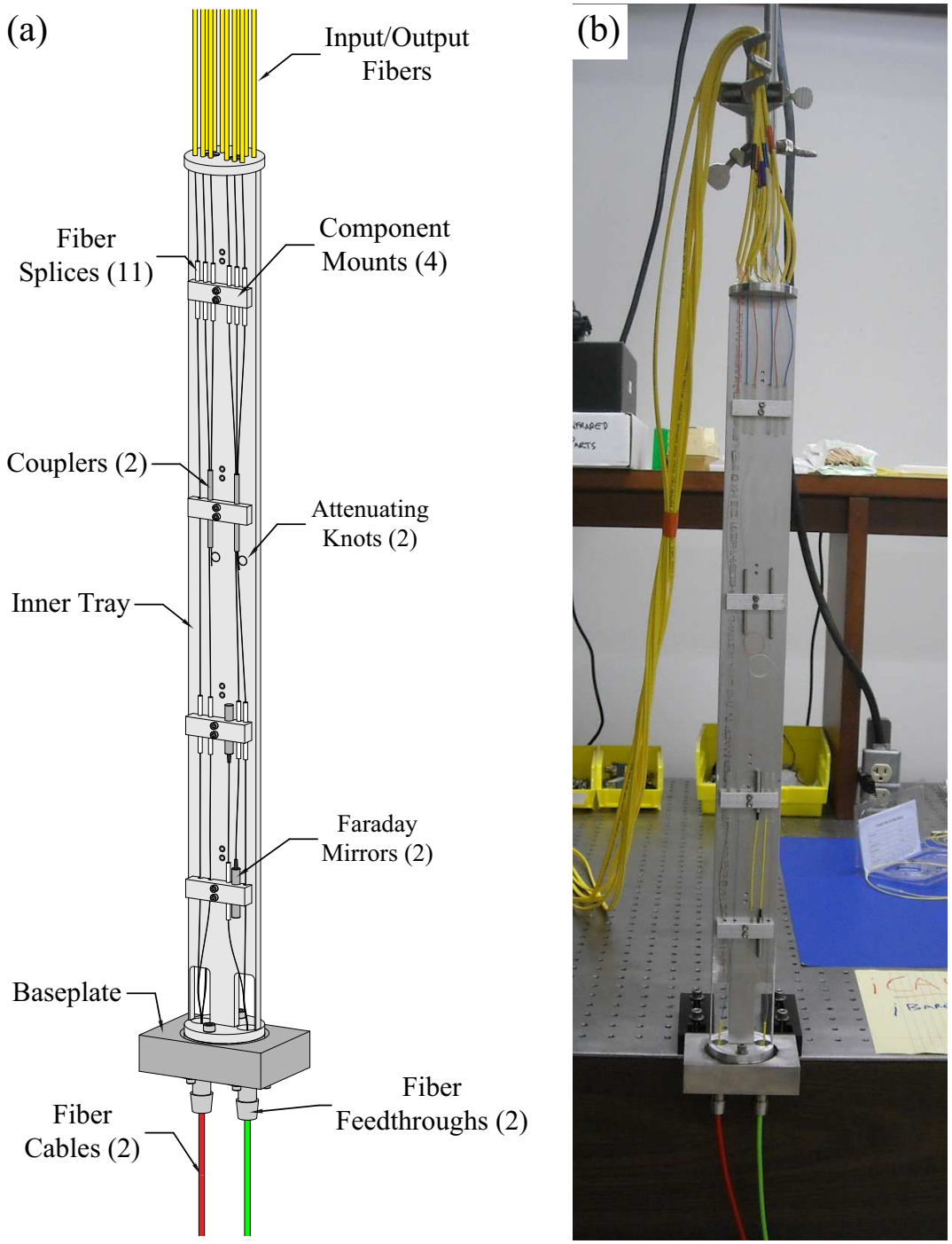


Figure 4.4: Upper sonde, showing the internal view in its planned design (a) and during the actual build (b). This particular view shows the 2×2 coupler and fibers used to interrogate the areal strainmeter on the left of each subfigure, and the 3×3 coupler and Faraday mirrors for the auxiliary vertical strainmeter on the right. The back side (not shown) holds the components for the primary and secondary vertical strainmeters. The optical schematic is shown in Figure 4.8.

that connect to an output of a 3×3 coupler on one end and a Faraday mirror on the other. This fiber-wrapped sleeve is epoxied into the lower sonde and forms the sensing arm of the areal strainmeter interferometer, which is intended to measure the average circumferential strain over 60 cm near the bottom of the borehole.

A separate, smaller auxiliary sonde attached to the top cap of the lower sonde houses the turn-around for the auxiliary vertical strainmeter. This is a 3 cm diameter, 11 cm long stainless steel bottle that is sealed at the top with another fiber feedthrough. The cutaway in Figure 4.5a shows that it only holds a loop of fiber and a protective splice sleeve. While the auxiliary sonde feedthrough serves as the lower termination fixture for the auxiliary vertical strainmeter, the full optical path for this interferometer extends back to the upper sonde.

The final component of the down-hole package is the centralizer assembly that ensures that the areal strainmeter is concentric within the borehole when under suspension (see the bottom of Figure 4.3). This consists of four 2.5 cm wide, 32 mm thick PVC plastic bands that are partially bent between two fixtures separated by $\sim$0.5 m. These flexible bands are designed to deform evenly to match the diameter of the borehole and keep the centerline of the lower sonde in line with the borehole. Several cylindrical steel weights accompany the centralizer to make sure the lower sonde is negatively buoyant in the grout and serve as anchoring points for the entire system once the grout sets.

4.2.4 Wellhead

The wellhead is a major component of BOFS since it is where the upper end of the strainmeter couples to the ground surface. The original aim was to clamp the upper sonde below the near-surface well casing ($\sim$7 m below the surface) to secure the instrument directly to the unfractured rock and also to limit the influence of surface temperature changes as much as possible. However, difficulties during deployment (described in Section 4.4.2) resulted in the upper sonde ending up higher in the borehole than anticipated, thereby requiring the assembly to be clamped to the casing. This was additionally undesirable given that the existing concrete pad was partially coupled to the borehole casing and that it also covered

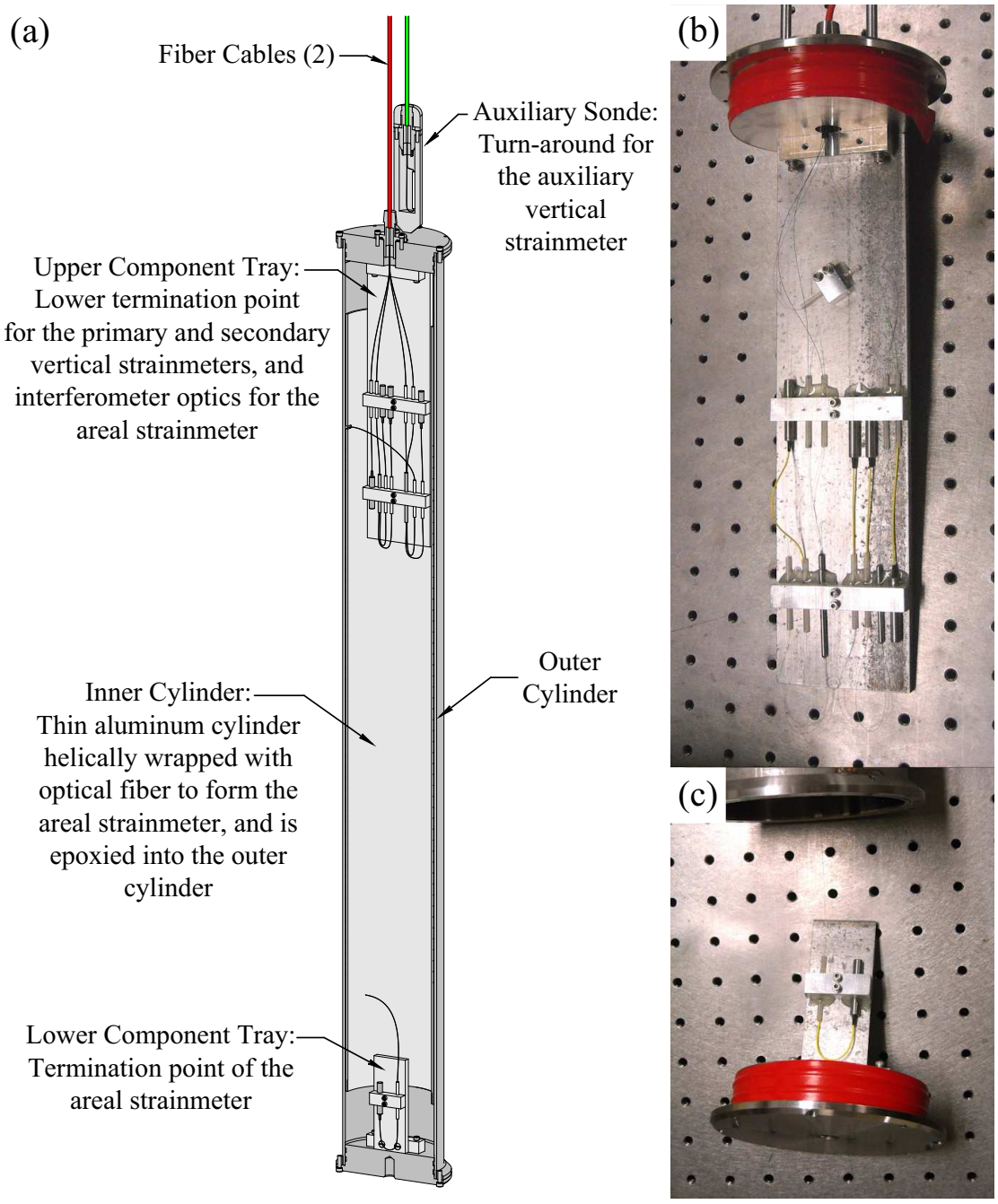


Figure 4.5: Lower sonde, showing the internal view this assembly in its planned design (a) and immediately before final assembly (b,c). The upper component tray holds a 3×3 coupler whose output is connected to one end of the areal strainmeter seen penetrating from the inner cylinder. The lower component tray simply holds the Faraday mirror connected to the other end of the areal strainmeter fiber (this penetration is obscured by the cutaway since it is not on the same plane as the upper penetration).

a fairly large area at the surface. The concrete pad has since been split and the casing decoupled from the ground to several meters depth to limit the influence of the shallow ground on the borehole casing and therefore the upper terminus of the strainmeter. This led to the final configuration of the wellhead shown in Figure 4.6.

A closeup schematic of the counterweight assembly and wellhead pad from Figure 4.3 is shown in Figure 4.6a. The natural boundary for the inner pad was the fiberglass enclosure previously embedded in the concrete (Figure 4.6b), while the outer pad simply supports an insulated "doghouse" surrounding the entire wellhead (Figure 4.6c). These two pads are separated by compliant foam to isolate each from the other.

Upper and lower sonde support cables are routed over two pulleys supported by a steel frame anchored to the inner concrete pad. The upper sonde support cable is under tension to take up the slack and pretension the two fiber cables that make up the vertical strainmeters. It is attached to a counterweight equal to the mass of the upper sonde and the combined tension of the two fiber cables, to limit vertical force, and hence suppress creep of the upper sonde clamp within the wellbore as well as provide additional protection in the case of clamp failure. The lower sonde support cable, used only during deployment, is sufficiently slackened such that it should not exert any tension on the lower sonde. The excess cabling is stored on two spools attached to the backside of the counterweight frame (Figure 4.6b). Not shown are the 1 m long fiberglass insulation plug inserted into the top of the borehole to inhibit air exchange, and an aluminum cap that covers the borehole opening.

4.3 Optical Design

Perhaps the most important new feature of BOFS compared to previous optical fiber strainmeters is that each sensing fiber forms one arm of a polarization-insensitive, passive quadrature Michelson interferometer. This is accomplished using Faraday mirrors and 3×3 couplers as described in Chapter 1, and results in

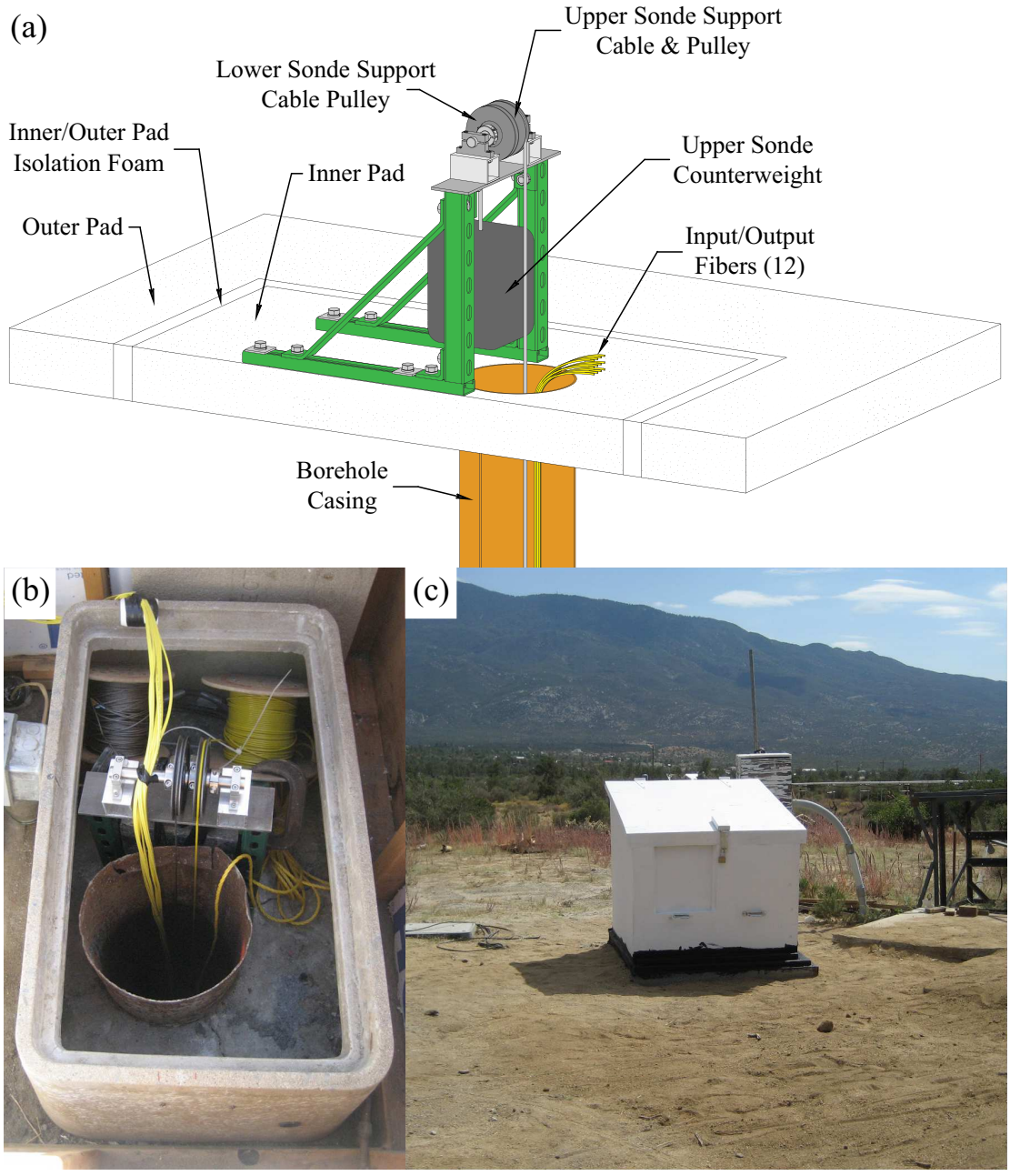


Figure 4.6: BOFS wellhead with counterweight assembly. (a) Counterweight assembly, also showing that the concrete pad attached to the well casing is separate from the outer pad and "doghouse." (b) Top-down view of the wellhead showing the counterweight assembly within the fiberglass enclosure, as well as the excess cabling spools and twelve 3 mm communications fibers. (c) Picture of the insulated "doghouse" surrounding the wellhead.

a completely passive sensor that requires no down-hole electronics.

The four interferometric strainmeters (i.e., the primary, secondary, and auxiliary verticals, as well as the areal) are functionally identical to the diagram shown in Figure 1.4. The optical schematic in Figure 4.7 shows that a total of twelve optical fibers are needed to interrogate the entire system. Input fibers I1, I2, and I4 each go to one input port of the 3×3 couplers C1, C2, and C4 that form the beamsplitters for each of the three vertical strainmeters. Six of the eight output fibers (X1, Y1, X2, Y2, X4, and Y4) are taken from their respective two remaining 3×3 coupler input ports as the two interference fringe signals that are phase shifted by 120° from one-another.

While one port of couplers C1 and C4 immediately terminate in Faraday mirrors (FM1 and FM4), the same output of the secondary vertical strainmeter coupler (C2) is further split into two paths by a wavelength division multiplexer (WDM1; passing into each of its output arms only light of a specified frequency) before terminating in Faraday mirrors FM2 and FM3. This is intended to allow the secondary vertical strainmeter to be operated at both 1310 and 1550 nm wavelengths, with the wavelength selection being necessary because the subsequent Faraday mirrors only provide compensation for birefringence changes within a ± 20 nm wavelength range. This option for dual-wavelength interrogation was added to take advantage of the very small (1 part in 10^4) differential wavelength dependence of the strain and thermo-optic effects of the optical fiber, thereby providing a potential way to discriminate between strain and temperature [8]. However, to date no commercial 1310 nm lasers have yet been identified that have a sufficient coherence length to illuminate this interferometer using a separate laser.

Returning to the other outputs of couplers C1, C2, and C4, the next output to the right of each short reference arm in Figure 4.7 is attached to the sensing arm fiber that exits the upper sonde into its respective fiber cable. The primary vertical strainmeter terminates in the lower sonde in Faraday mirror FM6, whereas the secondary again splits through WDM2 and ends in FM7 and FM8. In the case of the auxiliary vertical strainmeter, the fiber forms a loop in the auxiliary sonde and re-enters the upper sonde to terminate in Faraday mirror FM5. All unused

coupler ports are tied in 8 mm diameter knots that attenuate almost 100% of the input light (at 1550 nm), thereby eliminating parasitic reflections from the ends of the unused fibers.

Interrogation of the areal strainmeter is slightly more complicated. Because the main cable only had four fibers, with only two available for the areal strainmeter, one of these had to double as an input and output pathway. Input fiber I3 enters the upper sonde and is connected to the 2×2 coupler C3 that sends light to the 3×3 coupler C5 in the lower sonde and illuminates the areal strainmeter, as well as receives back one of the two output fringe signals that is generated by coupler C5. This returned light is then passed through C3 with half of it appearing at the upper sonde output fiber labeled Y3. The final output fiber X3 of the upper sonde simply comes from another port of the 3×3 coupler C5 in the lower sonde, delivered by the remaining fiber in that cable. Note that only two of the 3×3 coupler input ports of C5 are used since one fringe signal is extracted from that port via the 2×2 coupler tap C3 in the upper sonde.

The output communications fibers connect to their respective photodetectors (labeled as "XN" and "YN" for N = $1, 2, 3, 4$) and the inputs to the laser inside of the nearby equipment vault. Given the larger attenuation in the areal strainmeter, the 1×4 splitter is specified to provide approximately one-half of the total laser light to this sensor. It is also worth noting that the input light to each interferometer is divided up multiple times with 6 of these paths ending in attenuating knots. This means that the returning fringe signal is generally a very small fraction of the input intensity. However, even the 8 mW laser used in this installation is more than adequate since the amplified photodetectors only require about 40 μW of intensity to obtain an adequately-sized ellipse for analysis by the fringe counting system.

4.4 Fabrication and Deployment

The fabrication and deployment of BOFS took place during the latter half of 2011, with other modifications and reconfigurations continuing for nearly a year

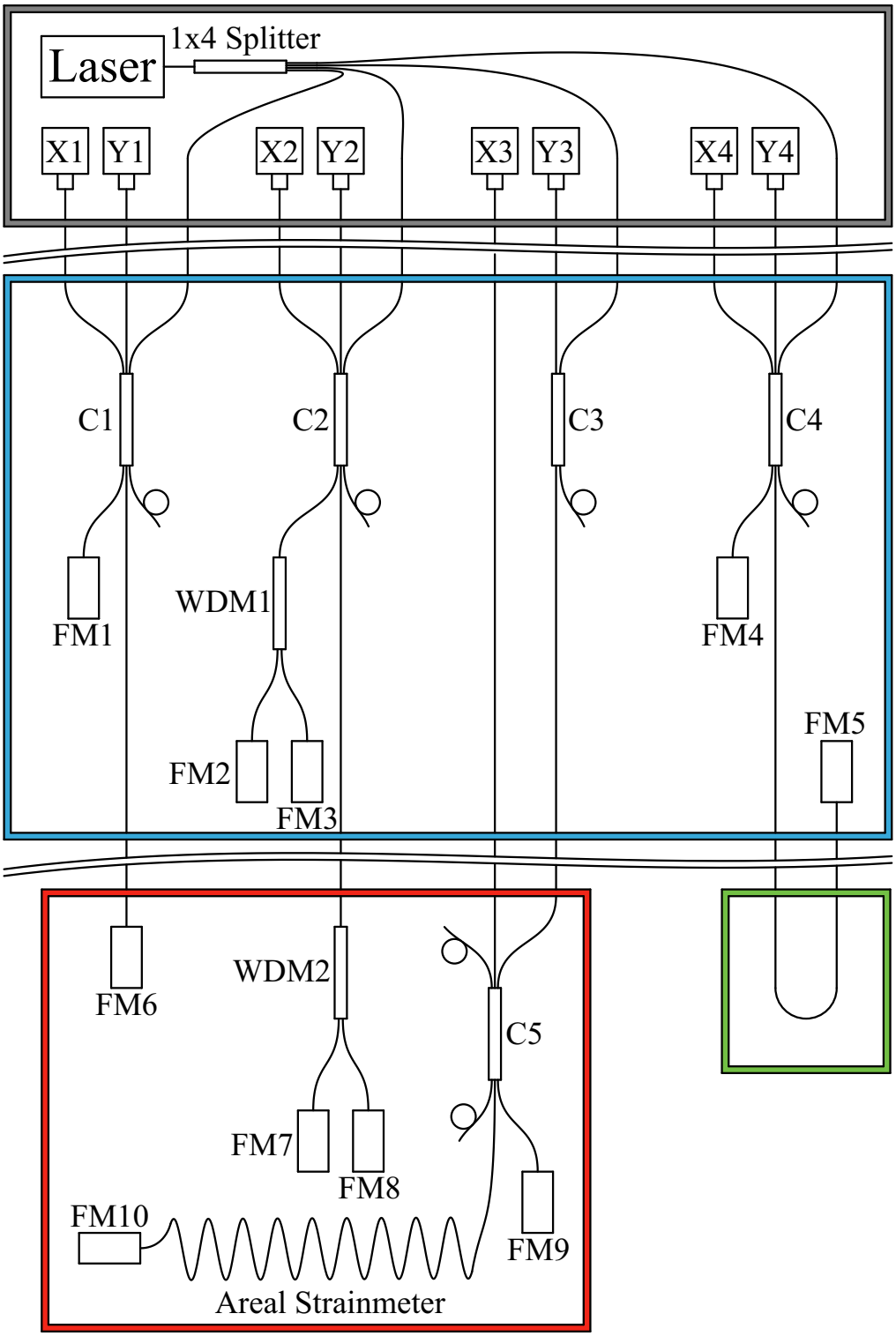


Figure 4.7: Optical schematic for the BOFS upper sonde (boxed in blue), lower sonde (boxed in red), and auxiliary sonde (boxed in green). Connections to the laser and photodetectors contained in the equipment vault are boxed in gray.

after installation in the borehole. The first subsection describes the preparations of the fiber cables and the assembly of the upper and lower sondes, which concludes with a detailed discussion of the two attempts at the creation of an areal strainmeter. This is followed by an account of the actual deployment and some post-deployment observations. Also included are additional details about modifications to the borehole casing and the installation of an up-hole laser frequency reference interferometer.

4.4.1 Fabrication

One of the goals of BOFS is to assess the performance of two different optical fiber cables for use as the primary sensing element. Recall that the red, four-fiber cable consists of a slightly larger diameter gel filled stainless steel tube than the green, non-gel, two fiber cable, as well as having different plastic coatings (polyurethane and polyethylene, respectively). Measurements of the strain (ϵ) versus applied tension (τ_a) of a 30 m length of each fiber cable yielded:

$$\left(\frac{\epsilon}{\tau_a}\right)_{red} = 12.74 \pm 0.13\ \mu\epsilon/\mathrm{N}\ (1.0\%)$$
$$\left(\frac{\epsilon}{\tau_a}\right)_{green} = 14.66 \pm 0.49\ \mu\epsilon/\mathrm{N}\ (3.4\%),$$

implying that, in pre-deployment fabrication, different fiber lengths were needed to achieve the same ultimate tension in each fiber cable. Therefore, both cables were laid out (on the Scripps pier), tensioned to approximately 90 N, and marked at various lengths such that their final cut lengths would match when tensioned in the borehole.

Another design consideration for the upper sonde was to see that the amount of fiber in it was minimized since this is the part closest to the surface and most susceptible to temperature variations. However, the device used to splice two fibers together requires about 10 cm of exposed fiber, and therefore it is impossible with this method to, for example, splice a Faraday mirror 5 mm away from the end of a 3×3 coupler. The other issue is that the fiber must be stripped to the bare glass to be spliced, and subsequently needs be hermetically sealed by a 4 cm long

"splice protector" (see Figure 4.4) to prevent hygroscopic changes in the fiber's optical characteristics.

There are two equivalent approaches for making and assembling a series of optical fiber splices like the ones contained in the upper sonde. The first is to coil up the excess fiber after splicing. Drawbacks to this approach are that such coils need to be secured to prevent creep and limit their sensitivity to vibration. This also implies that this excess fiber (that is a part of the interferometer but not the strainmeter) is concentrated in one location, leading to a larger temperature coefficient per meter of instrument package. The second approach, that was used in BOFS, was that of a long, slender package, such that the excess fiber between splices would be taken up by moving the various components farther apart from each other. In the end, the 70 cm package length was determined by the number of serial components and the footprint of the fiber splicer.

The upper sonde package was permanently sealed after splicing and mounting all the components in the upper sonde. The inner tray and its mounting discs were designed such that the outer cylinder of the upper sonde could be slid over the assembly and epoxied into the baseplate. Sealing the top end also required securing the twelve reinforced, 3mm input/output fiber pigtails (light in, and light out). These 12 m long pigtails consist of a 900 μm, tight-buffered single-mode optical fiber contained in a 3 mm diameter vinyl tube whose excess volume is taken up by many parallel strands of Kevlar fiber. Since the outer cylinder of the lower sonde is longer than the inner tray, a small space approximately 5 cm deep was available between the upper disc and the top of the cylinder. Half of this volume was first filled with epoxy to capture the Kevlar fibers as well as seal the entire package, and a further layer of polyurethane rubber was added to provide strain relief for the long pigtails exiting the upper sonde.

Final assembly of the lower sonde package was fairly straightforward, however, creation of the areal strainmeter required careful preparation and execution. Ideally, to measure the areal strain one would like to passively track the circumferential strain of the cylindrical borehole. However, in practice it is a difficult design challenge to embed a coil of bare optical fiber in the earth at the bottom of a deep

borehole. The design arrived at was that of a layered pressure case, with an outer corrosion resistant stainless steel cylinder and a thin aluminum mandrel wrapped with optical fiber epoxied to its interior.

Specifically, the outer layer of the lower sonde pressure case is a 1 m long, 11.4 cm OD, 10.8 cm ID stainless steel cylinder. The inner layer is an 85 cm long, 10.6 cm OD, 10.2 cm ID aluminum alloy cylinder. This provides an annular gap of approximately 1 mm to accommodate the high strength epoxy used to bond the two cylinders together. A length of single mode, 150 μm diameter, polyimide coated optical fiber (Corning SM-HT) is wrapped within a 125 μm deep helical groove cut along the central 60 cm of the outer surface of the inner cylinder. The choice of the very tough polyimide-coated fiber (requiring specialized splicing equipment) was made to achieve a far better coupling of the fiber to the metal substrate than is possible with acrylate-coated fiber. Both ends of this fiber penetrate from the exterior of the inner cylinder to the interior through a pair of slots (Figure 4.8b).

Several temporary components were used to push epoxy into the annulus between the two cylinders and leave the interior of the lower sonde open after curing. Figure 4.8a shows that the lower end of the inner cylinder is threaded to accept a temporary cap, effectively turning it into a piston. Another temporary, o-ring sealed cap was installed into the base of the outer cylinder whose length was such that the inner cylinder was centered vertically in the longer outer cylinder when the two epoxy caps come into contact. With the both caps in place and the two cylinders separated, a low-viscosity ($\sim$0.6 Pa·s) epoxy was poured into the bottom of the still open outer cylinder. Then the (capped) inner cylinder containing the helically wrapped optical fiber was lowered into the outer cylinder. A weight applied to the inside of the inner cylinder epoxy cap pressed the two epoxy caps together, forcing epoxy into the annulus.

After curing, the two temporary epoxy caps were removed and the two ends of the areal strainmeter fibers were spliced to their optical components. It is worth noting that the two contact faces of the epoxy caps, as well as the threads between the inner cylinder and its epoxy cap were coated with a thin layer of a heavy silicone grease to prevent them from adhering to one another, thereby allowing them

to be more easily removed.

The first attempt at an areal strainmeter was found to be problematic, requiring further tests and development of a second, deployable instrument. This original design had approximately 250 m of optical fiber wrapped around the inner cylinder (a pitch of 32 wraps per 2.5 cm), making the optical path as long as the vertical strainmeters. Optical time domain reflectometry (OTDR) measurements of light passing through this assembly after curing of the epoxy revealed very large attenuation of about -60 dB/km, making it difficult to get sufficient light out of the sensing arm of the interferometer. While not fully understood, subsequent tests (Section 4.5.1) suggested that this was almost certainly due to microbending losses from an insufficiently smooth helical groove coupled with thermal stresses imparted to the mismatched material layers, stemming from the quite noticeable exothermic curing reaction of the epoxy.

The final areal strainmeter was assembled by clearing out the original fiber-wrapped inner cylinder, and epoxying in a second inner cylinder with only ∼80 m of fiber (10 wraps per 2.5 cm). To limit the microbending loss, the helical groove was burnished with stainless steel wire and a similar, but low exothermic epoxy was used to glue it into the outer cylinder. The combination of using a shorter fiber and realization of lower attenuation (-20 dB/km), meant that the new assembly passed an adequate amount of light. The completed package was then subjected to a number of tests described in Section 4.5.

4.4.2 Deployment

Preparations of the existing 260 m deep, 22 cm diameter borehole for the deployment of BOFS started before its construction. Early borehole depth soundings suggested that the bottom of the hole was not solid, making it difficult to get an accurate measurement of its depth. An initial batch of a low-viscosity grout was added to the bottom of the hole through a 3.8 cm diameter tube inserted into the well, which after curing provided a firmer bottom. Subsequent depth soundings provided the information necessary to determine the final length of the fiber cables.

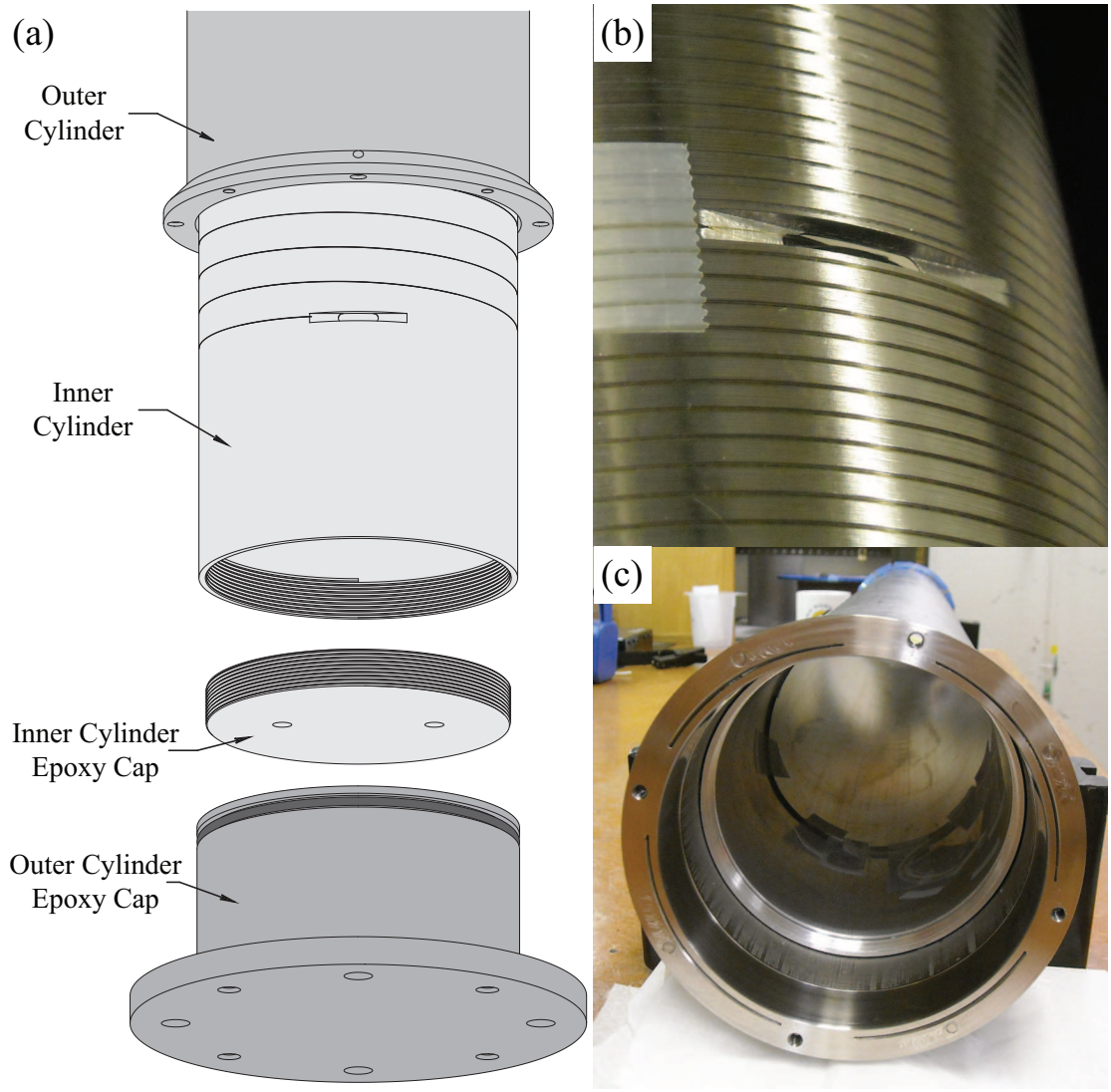


Figure 4.8: Several views of showing the assembly of the lower sonde. (a) An exploded view of the inner and outer cylinder as well as the temporary epoxy caps used to turn the inner and outer cylinders into an epoxy piston. (b) Closeup of one fiber penetration slot showing the fiber entering from the left. This slot was subsequently filled with quick setting epoxy to safely secure the wrapped fiber and provide an epoxy-tight seal. (c) Endfire picture of the bottom of the areal strainmeter in the lower sonde after epoxying with the inner and outer epoxy caps removed.

BOFS was installed into its borehole during the first week of December, 2011. The procedure was similar to that of the Bangladesh strainmeters in that a low-viscosity grout mixture (developed in-house) containing a chemical to extend its curing time (Euclid Chemical admixture Eucon DS) was delivered to the bottom of the hole through a PVC pipe, and the instrument lowered into place as soon as the grout pipe was removed. A volume of grout creating a $\sim$7 m column was delivered to the bottom of the borehole using a procedure to ensure a contiguous emplacement, with the aim that both the centralizer (with counter ballast) and lower sonde would become fully submerged. The pair of fiber cables was payed out using a motorized supply spool accompanied by a separate wire rope attached to the lower sonde to support the weight of the down-hole package as it was lowered into the borehole. This lower sonde support cable ran over a sheave connected to a hanging scale so that the weight of the down-hole package could be monitored as it entered the grout.

The situation became much more complicated at the point where the upper sonde was added into the mix of components being lowered into the borehole, with the need to keep track of tensions in four sets of cables. In addition to the lower sonde support cable were the two fiber cables themselves, the combination of which were only marginally capable of bearing the weight of the lower sonde and counter ballast by themselves. The upper sonde had its own support cable in addition to the 12, non-load bearing communications fibers exiting from the top.

Final tension measurements were conflicting, but in retrospect indicated that the lower sonde was not fully entered into the grout. The force on one of the hanging scales did not show the expected transition indicating that the down-hole package was entering the grout. A decision was made to secure the (many) support cables. It subsequently appears that the lower sonde was incorrectly stopped when the bottom of the centralizer was approximately 5 m from the bottom. (This would have been sufficient if all 7 m of grout were competent, i.e., there was no mixing of grout and borehole water when the grout pipe was removed.) While it is difficult to know exactly why the down-hole package did not fully submerge, we believe that it may be that the grout became quite viscous prematurely, perhaps

on its own (insufficient retardant), or because of the increased hydrostatic load imposed by the ∼230 m of water in the 260 m deep well. Either or both of these may have been overcome with more counter ballast.

Aside from the areal strainmeter not yet being coupled to the borehole wall, other difficulties resulted from the the lower sonde not reaching its planned final depth. The length of the vertical strainmeters was determined such that when tensioned, the upper sonde would remain approximately 7 to 8 meters below the surface. This would have provided greater thermal isolation than its final 4 m depth (determined subsequently when the fibers were tensioned). The most significant concern was that since the borehole is cased with a steel pipe to a depth of about 5.5 m, this higher position in the borehole forced us to clamp the upper sonde to the casing rather than the bedrock. This raised concern that the vertical strain record could be contaminated by surface processes like thermal heaving, ground saturation from rainfall, wind stresses, and erosion. This matter was investigated and mitigated several months after deployment and has proven not to be a significant problem (see below).

Fiber tensioning tests were conducted roughly two weeks following the initial deployment to ensure that the down-hole package was secured to the bottom of the borehole. However, final tensioning, installation of the counterweight assembly, and setting of the upper sonde clamp to the borehole casing did not take place for another nine weeks. The final tension was approximately 130 N per fiber cable, or an initial strain of about 0.17 to 0.18%. A piezoelectric water level transducer (Greenspan PS7000) was installed in mid-August of 2012 to record the response of the water height in the borehole due to tidal forcing.

The most involved work to BOFS since its initial deployment has been to assure better isolation of the borehole casing from the ground surface, and therefore the upper terminus of the vertical strainmeters. Nine months after the initial deployment (roughly six months following the final tensioning and clamping), the original large concrete pad was broken up and the majority of the ground around the well casing was excavated with the intent of parting the casing above the clamp if the casing was found to be only weakly coupled at depth. In fact the casing was

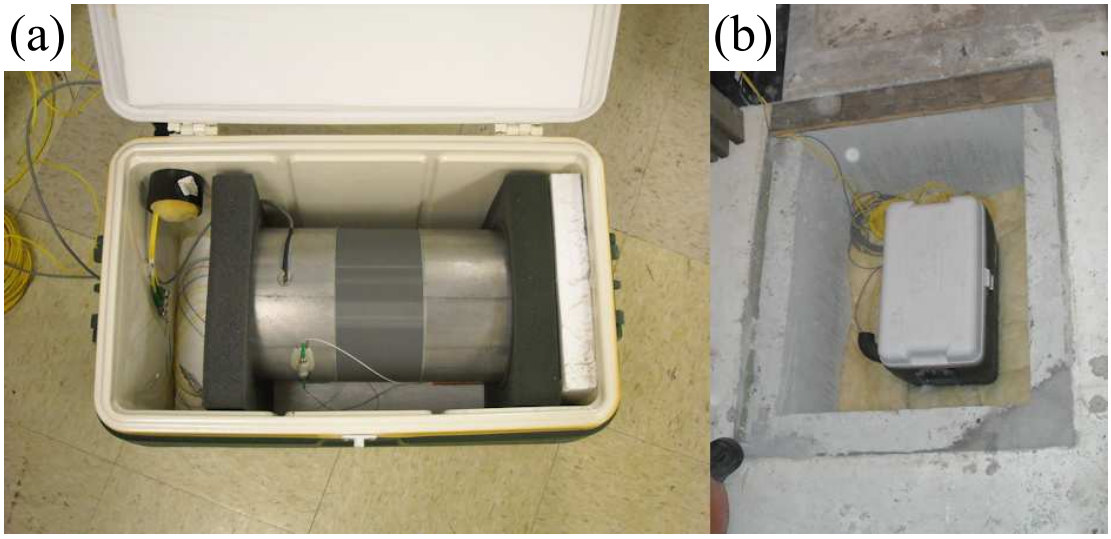


Figure 4.9: Interior and deployed views of the BOFS reference interferometer. (a) The reference interferometer mandrel inside its 60 liter cooler, additionally insulated for thermal stability. Note the thermistor glued to the top of the aluminum cylinder just to the right of the left edge. (b) Reference interferometer cooler in the pit before covering with fiberglass insulation.

found to be very well coupled, and the exposed upper portion of the casing extending 2.5 m from the surface was mechanically isolated from the backfilled surface material by a cylindrical annulus containing perlite to assure long-term uncoupling. The concrete pad attached to the casing at the surface was reduced in surface area, and a separate concrete pad was added to support the insulated "doghouse" covering the entire wellhead (Figure 4.6). In this way, the motion of the casing (to which the upper sonde is clamped) is governed by competent rock several meters below the ground surface rather than by shallow soil subject to spurious displacements caused by weathering. In fact every indication is that the casing is (and was) quite stable.

Since all four BOFS interferometers are unequal arm interferometers, variations in the laser frequency are indistinguishable from optical path length changes (see Equation 1.27). In the absence of a suitably stabilized laser, it was necessary to install a fifth interferometer as a wavelength reference to remove the unwanted optical phase difference changes caused by laser frequency drift. This reference interferometer is maintained in a 75 cm deep concrete pit conveniently located

inside of the underground vault used to house the laser, photodetectors, and fringe counting system approximately 35 m from the wellhead. The interferometer itself is a 20 cm diameter aluminum cylinder wrapped with approximately 265 m of 250 μm diameter, acrylate jacketed optical fiber (Figure 4.9). This wrapped mandrel is mounted inside of a 60 liter cooler using two blocks of soft foam for improved temperature stability and vibration isolation. A thermistor (YSI 44008) is glued to the mandrel given its expected (strong) response to temperature, despite the insulation and its location $\sim$3 m below the ground surface.

Two different lasers have been used to illuminate BOFS. The first laser was an erbium-doped fiber laser (NP Photonics ROCK) operating at 1534 nm with a spectral linewidth of 4.2 kHz, which was used for the first six months after deployment. Currently BOFS is illuminated with an external cavity diode laser (RIO ORION) operating at 1554 nm that has a narrower linewidth of 2.5 kHz. While the wavelength instability, partially determined by the linewidth, is not limiting to the performance of the instrument since it is corrected for in post-processing by the reference mandrel interferometer, the difference between the raw phase records of the vertical strainmeters from two lasers is very striking. Figure 4.10 shows three time series examples of the uncorrected optical phase time series for the primary vertical strainmeter. The upper trace shows that the record is completely dominated by the wavelength noise of the NP Photonics laser. The next two traces show results from the RIO laser operating in two different locations. One month after switching to the RIO laser, it was moved from the equipment rack down to its final location in the pit adjacent to the reference interferometer. The improvement is quite significant and suggests that future developments will greatly benefit by locating the laser system in a stabilized thermal environment.

4.5 Laboratory and Field Tests

While most of the development work using fiber cables for long base borehole strain sensing has been done in the past (for example, references [13, 3]), a fair amount of testing both in the lab and in the field was done. Much of this effort was

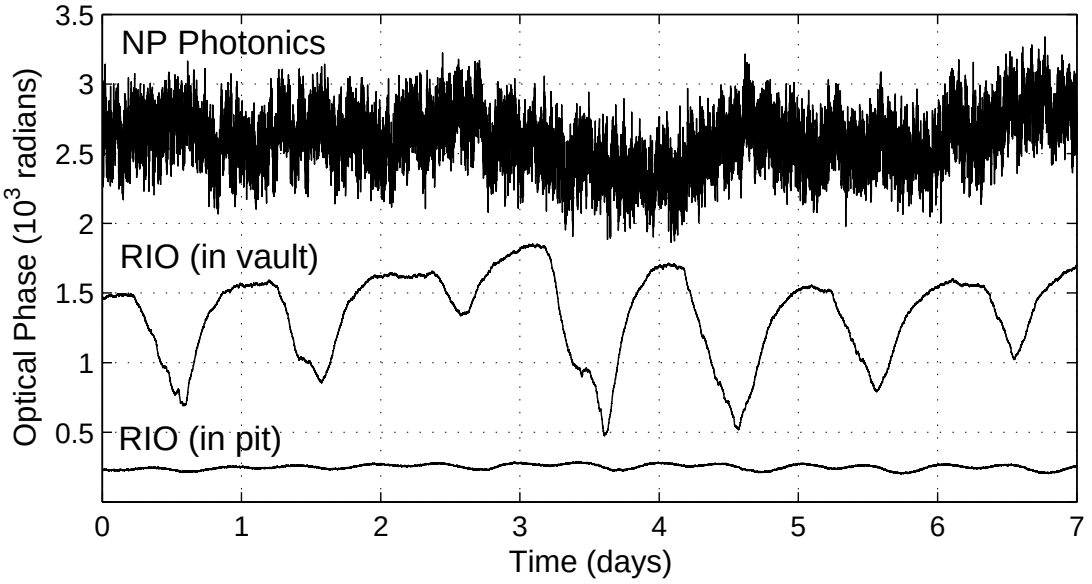


Figure 4.10: Uncorrected time series examples of the two lasers illuminating the BOFS primary vertical strainmeter. The upper trace shows the NP Photonics fiber laser running in the vault, with a peak-to-peak phase noise of over 1,000 radians. The middle trace shows the RIO laser running in the vault whose wavelength drift is clearly dominated by the vault temperature. The lower most trace shows the behavior of the RIO laser after being moved into the pit next to the reference interferometer.

focused on understanding the behavior of the layered, wrapped cylinder for future use as an areal strainmeter. This section describes the subset of these experiments that will be useful for further development of this technology, as well as those that directly impact the performance of BOFS as a tool for scientific research.

4.5.1 Areal Strainmeter Epoxy Tests

A 28 cm long, all-aluminum prototype areal strainmeter was constructed to evaluate the response of a layered, fiber-wrapped cylinder. The inner and outer diameters and wall thicknesses are nearly identical to the final instrument described above. Both the inner and outer cylinders had bottom caps to push up the low-viscosity epoxy pooled in the bottom of the outer cylinder into the annulus. Unlike the final design, however, this prototype used ∼225 m of 250 μm diameter, tight-buffered acrylate fiber rather than the 150 μm diameter, polyimide coated

fiber. Furthermore, the prototype used a closed-coil winding that did not require a helical groove since each wrap was adjacent to the previous. No appreciable heat was generated by the volume of epoxy needed to fill the annulus (about 70 mL), and an acceptable amount of attenuation was measured after the epoxy had cured (∼-0.7 dB/km, or only about 2 to 3 times the nominal reduction expected from bending loss associated with the radius of the cylinder).

Following the unacceptably large attenuation of the first attempt at constructing the actual areal strainmeter (Section 4.4.1), two additional test strainmeters were made. These used a 19 cm long remnant of the stainless steel outer cylinder of the actual lower sonde. Two matching aluminum inner cylinders (also remnants of the final inner cylinder) were fabricated with a 125 μm deep helical groove with a pitch of 32 wraps per 2.5 cm to match the failed areal strainmeter. Approximately 55 m of fiber was wrapped between the pair of fiber-penetration slots identical to the final inner cylinder (Figure 4.8b).

The first test was conducted by wrapping the inner aluminum cylinder with the same 250 μm diameter, tight-buffered acrylate fiber used in the areal strainmeter prototype. After the fiber penetrations were potted with quick-setting epoxy, the attenuation was measured at -2.36 ± 0.04 dB/km. The attenuation was also monitored during the 24 hour curing time of the same epoxy used for both the prototype and the first areal strainmeter (Emerson & Cuming Sycast 1266). No exothermic reaction was expected given the small volume of epoxy used (∼60 mL). The final attenuation after 28 hours had slightly improved to -2.10 ± 0.05 dB/km, consistent with the lack of additional attenuation in the prototype.

The second test was more like the failed attempt at the full areal strainmeter in that the inner cylinder was wrapped with the 150 μm diameter, polyimide coated fiber. The attenuation was measured prior to epoxying at a high level of -9.83 ± 0.06 dB/km. Next, a very low-exotherm epoxy was used with a cure time of 48 hours (Emerson & Cuming Stycast 1264) that had very similar mechanical properties to the previous epoxy. After 5 days, the attenuation more than doubled to -22.83 ± 0.09 dB/km.

While these tests only covered a couple of the possible variables related to

constructing a layered cylinder areal strainmeter, they did confirm that there was something fundamentally different about the use of the smaller diameter, polyimide coated fiber. The greater attenuation of the 250 μm diameter acrylate coated fiber when wrapped into a helical groove compared to wrapped around the outside of a smooth cylinder (i.e., the first epoxy test versus the prototype) further suggests that the roughness of the groove itself may be a factor. This roughness is more of a concern in the case of the polyimide coated fiber since the jacketing is far less compliant than the acrylate, and the amplitude of the roughness is larger compared to the diameter of the fiber. Therefore, we believe that the excessive attenuation in the first version of the full areal strainmeter was caused by microbending losses, exacerbated by the length of the fiber.

There are several outstanding possibilities that will need to be explored in order to better understand the behavior of the layered cylinder optical fiber strainmeter concept. Aside from the surface roughness, there was no control over the tension under which the fiber was wrapped about the inner cylinder, other than it was sufficient to ensure that the fiber would not unravel during epoxying. Greater tension may increase attenuation by forcing the fiber to more closely follow the surface. The epoxies used were observed to shrink during curing, which may be prestressing the cylinders since a continuous increase in attenuation with time was observed in the second epoxy test and in the final areal strainmeter assembly. The relationship between annular stress and attenuation was further investigated by heating and cooling the second test fixture and both the failed and final areal strainmeters. These tests showed a decrease in attenuation (i.e., an improvement) of approximately 2.4 dB/km/°C as the temperature increased.

4.5.2 Areal Strainmeter Pressure Tests

It was essential to test the final areal strainmeter as much as possible in the lab before deployment, since this was the first time an instrument of this type was attempted. One such test was to measure its sensitivity to hydrostatic pressure. This turned out to be rather fortuitous since the areal strainmeter ended up above the grout and subjected to pressure changes induced by tidal water height changes

in the borehole. The test itself was conducted with a PVC pressure chamber designed to fit the lower sonde package and provide a feedthrough for the fiber cable. After being filled with water, the chamber was pressurized several times with compressed air from between 0 and 275 kPa (about 40 PSI). A linear least-squares fit to the optical phase change induced by a given gauge pressure from all four of the measurements was:

$$\frac{\Delta\phi}{\Delta P} = -\left(46.19 \pm 0.11\right) \times 10^{-3} \text{ radians/Pa } (0.24\%).$$

The positioning of the areal strainmeter above the borehole grout also allowed the pressure sensitivity to be tested in-situ. The first test was done following the tensioning tests two weeks after deployment. Two slugs of approximately 60 liters of water were added to the borehole about two hours apart. Each was predicted to raise the water level by about 1 m, and the result was an optical phase change of about 440 radians. This corresponds to an increase in pressure of about 9.5 kPa, or just under the 9.8 kPa expected for 1 m of water.

This pressure test was affirmed with the addition of the piezoelectric water level transducer, providing a way to accurately measure the change in water height. A similar test to the previous was performed shortly following the installation of the water level transducer. Three slugs of 20 liters were poured into the well about 45 minutes apart. A fit to the optical phase versus the pressure change from the measured water height yielded:

$$\frac{\Delta\phi}{\Delta P} = -\left(46.427 \pm 0.012\right) \times 10^{-3} \text{ radians/Pa } (0.03\%),$$

which is just over $+2\sigma$ from the lab result, but overall a well-established value.

4.5.3 Areal Strainmeter Load Tests

The response of the areal strainmeter package to axial loading was another simple test performed in the lab. As previously pointed out, the areal strainmeter is subjected to hydrostatic pressure changes from tidal water level changes. These pressure changes also induce very small changes in the size of the lower sonde, e.g., an increase in pressure causes the lower sonde package to shrink. Since the

fiber cables and therefore the vertical strainmeters are attached to the lower sonde, this implies that pressure changes may also couple into the vertical strain record. The opposite of this effect may also be present in that tensional changes in the fiber cables may couple into the areal strainmeter record by pulling on the lower sonde package. While these two effects are expected to be very small, it is essential to estimate their magnitudes to determine whether they are a potential source of contamination.

The axial load test was performed by placing and removing an increasing amount of weight on the upper cap of the lower sonde. The optical phase change induced by the mass combined with the acceleration of local gravity yields an axial load sensitivity in radians per Newton. A total of six masses were used and the axial load sensitivity was determined by a linear least-squares fit to the optical phase change versus axial load.

While the very large optical attenuation in the first areal strainmeter assembly made it unsuitable for deployment, it was possible to form a very faint interferometer in the lab. The axial load sensitivity for the failed areal strainmeter was found to be:

$$\frac{\Delta\phi}{\Delta F} = +\,(2.748 \pm 0.038)\ \text{radians/N}\ (1.4\%),$$

and for the final areal strainmeter:

$$\frac{\Delta\phi}{\Delta F} = +\,(1.075 \pm 0.009)\ \text{radians/N}\ (0.8\%).$$

Note that if the axial load sensitivity were proportional to the amount of fiber wrapped on the inner cylinder (i.e., if the Butter and Hocker relationship in Equation 1.19 were valid for this case), the final areal strainmeter would be $2.748 \times 10/32 \approx 0.859$ radians/N.

Tension was applied to the lower sonde support cable two weeks after installation to establish that the lower sonde package (mostly the centralizer) was fixed in the grout. This cable is attached to an eye bolt threaded into the top cap of the lower sonde. If pulling on this cable has the opposite effect of applying an axial load, it should provide a way to verify the lab measurements. A total of four

tensions were applied to the lower sonde support cable resulting in an axial tension sensitivity of:

$$\frac{\Delta\phi}{\Delta F} = -\left(0.57 \pm 0.14\right) \text{ radians/N (24\%)},$$

which despite the rather large uncertainty as a result of the crudeness of the test, is a factor of two smaller than the lab measured value.

Regardless of the outcome of the field test, it is interesting to use the lab measured axial load sensitivity to calculate the extent to which the vertical strain signal can couple into the areal strain record. The daily vertical Earth strain tide amplitude is about 30 nϵ, which by inverting the percentage strain per unit tension presented in Section 4.4.1 yields a tension of approximately 2×10^{-3} N. This corresponds to a phase change of only about 2 milliradians, or an equivalent pressure of 50 mPa (5 μm of water), which is small enough to disregard.

4.5.4 Other Post-Installation Tests

The two field tests discussed in this section are perhaps the most significant since they relate to how the instrument responds to stimulus at the wellhead. Recall that one consequence of clamping the upper sonde to the borehole casing was that it could be coupled to the ground through its surrounding concrete pad. Therefore, it was important to measure the extent of this coupling. A second test deals with the counterweight assembly for limiting creep in the upper sonde clamp. Despite the efforts to make the clamp as rigid as possible, it is important to establish whether changes in the counterweight can impact the vertical strain records.

Prior to the work separating the casing from the surface material, an experiment was conducted to gain some insight into how well coupled the casing was to the surface around the pad. This experiment consisted of four people approaching the wellhead and sitting on the aforementioned "doghouse" to see if there was an appreciable vertical strain signal. Given that the result was expected to be small, this was repeated 10 times so that all the approaches could be stacked to provide a more robust average and reduce its variance. The result of this pad loading test is shown in Figure 4.11. To put this into context, consider the vertical strain ϵ_z of

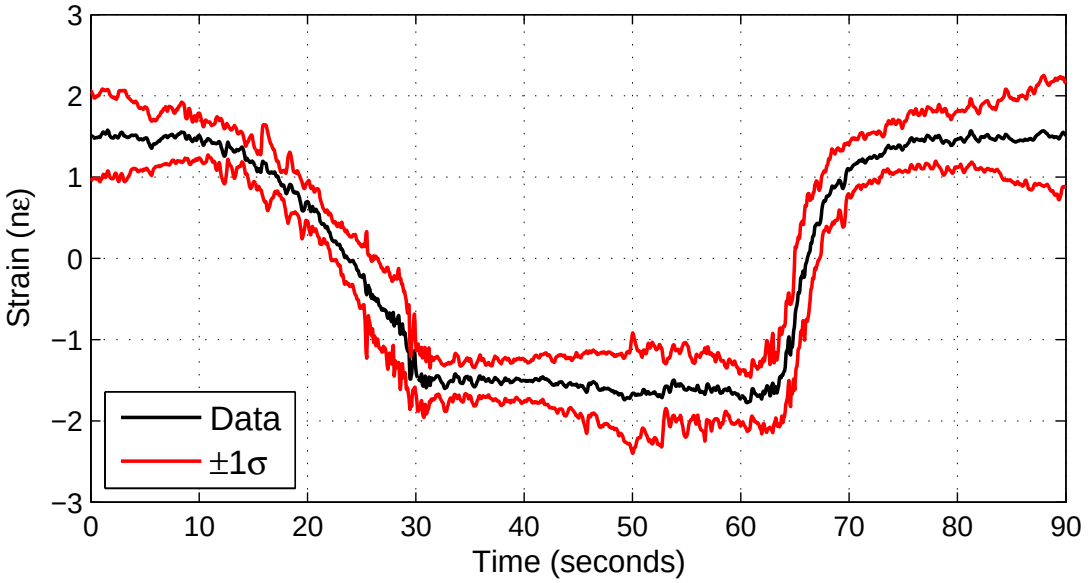


Figure 4.11: Average results from the wellhead concrete pad loading experiment with uncertainties. The first and last 30 seconds represents the approach and retreat of the four people from the wellhead, while the middle 30 seconds corresponds to the four people sitting on the doghouse. While there does appear to be somewhat of a downward ramp during the approach (0 to 30 seconds), there is similar trend for the retreat (60 to 90 seconds).

a pressure P acting on a homogeneous elastic half-space:

$$\epsilon_z = \frac{P}{E}(1+\nu)(1-2\nu),$$

where E is the Young's modulus and ν is the Poisson's ratio. Assuming a load of about 3200 N ($\sim 86 \pm 5$ kg per person) over the original pad area of approximately 6.8 ± 0.4 m^2, a Poisson's ratio of 0.27 (see section 5.4.1), and the given observed vertical strain of 3.0 ± 0.5 nϵ, this yields a Young's modulus of $E = 96 \pm 33$ GPa. While this is much larger than previously observed values around 50 GPa between 15 and 35 m depth [12], it is consistent with the ∼70 GPa for granite when accounting for the large uncertainty. This result indicates that surface coupling through the wellhead pad is not significant.

The counterweight assembly (Figure 4.6a) is loaded with a mass of approximately 38 kg to counteract the tension in the fiber cables (∼130 N each), the weight of the cables, and the weight of the upper sonde (∼12 kg), in order to reduce stress

on the upper sonde clamp. An experiment was conducted one month after final tensioning to test the sensitivity of the vertical strainmeters to the stability of the counterweight. This was accomplished by adding and removing an additional mass of 7 kg to the counterweight a total of four times. The resulting amount of strain induced on the vertical strainmeters per unit of additional back-tension on the upper sonde support cable was found to be $+94.4 \pm 1.4$ pϵ/N. This implies that an acceleration of as much as 1.5 m$\cdot$s^{-2} ($\sim$0.16 g) is needed to produce a strain of 1 nϵ.

4.5.5 Relative Path Lengths and Calibration

Relative length scale factors must be determined to relate the length of the reference interferometer to each sensing interferometer in order to remove unwanted laser wavelength fluctuations. This is required since it is impractical to build a reference mandrel that is precisely the same length as each component, especially considering that even the primary and secondary vertical strainmeters contained in the same fiber cable have slightly different path lengths due to the WDMs used in the latter.

This was accomplished by varying the laser wavelength and comparing the resulting optical phase outputs between the various interferometers. To understand why this works, consider solving the optical path imbalance relationship in Equation 1.37 for $\Delta\lambda$:

$$\Delta\lambda = \frac{\lambda_0}{L_0}\Delta L,$$

as well as rewriting the phase-displacement relationship shown in Equation 1.27 for ΔL:

$$\Delta L = \frac{\lambda}{4\pi\mu}\Delta p.$$

Combining these two equations results in the following expression relating the wavelength change as a function of the optical phase change:

$$\Delta\lambda = \frac{\lambda_0^2}{4\pi n L_0}\Delta p.$$

Now consider changing the wavelength of a laser that illuminates two interferometers of different base lengths L_S and L_R ("Strainmeter" and "Reference," respectively). Assuming the same wavelength shift is imparted to both interferometers (i.e., they are both using the same laser) one can divide the previous equation by itself for these two base lengths. Therefore, the relative phase shift (Δp_S and Δp_R) of one interferometer relative to the other can be expressed as:

$$\frac{\Delta p_S}{\Delta p_R} = \frac{L_S}{L_R}. \tag{4.1}$$

Three minutes of phase data were acquired while inducing a wavelength shift of approximately 114 pm on the 1534 nm laser illuminating all five interferometers. This was accomplished by simply changing the wavelength setting on the laser front panel, which induces a temperature change of the laser cavity and therefore its output wavelength. Linear least-squares fits were performed between the phase outputs of the strainmeters and the reference interferometer to arrive at the scale factor needed to match the wavelength fluctuation amplitudes seen by each interferometer. Figure 4.12 shows an example of one such fit, and the results are summarized in Table 4.1.

Table 4.1: Scale factors relating the length of the reference interferometer to each BOFS strainmeter.

Strainmeter	Ratio (radian/radian)
PV	$0.94264762 \pm 0.00000054$
SV	$0.94307772 \pm 0.00000053$
AV	1.8839629 ± 0.0000010
AR	$0.300409654 \pm 0.000000079$

These scale factors can also be used to determine the base length of the instrument. The length of the reference interferometer was measured at $L_R = 266.41 \pm 0.03$ m using an EDM, implying that the length of the tensioned primary vertical is close to 251 m. Topside length measurements along with the final tension indicate that only the centralizer is secured in the grout, thereby increasing the

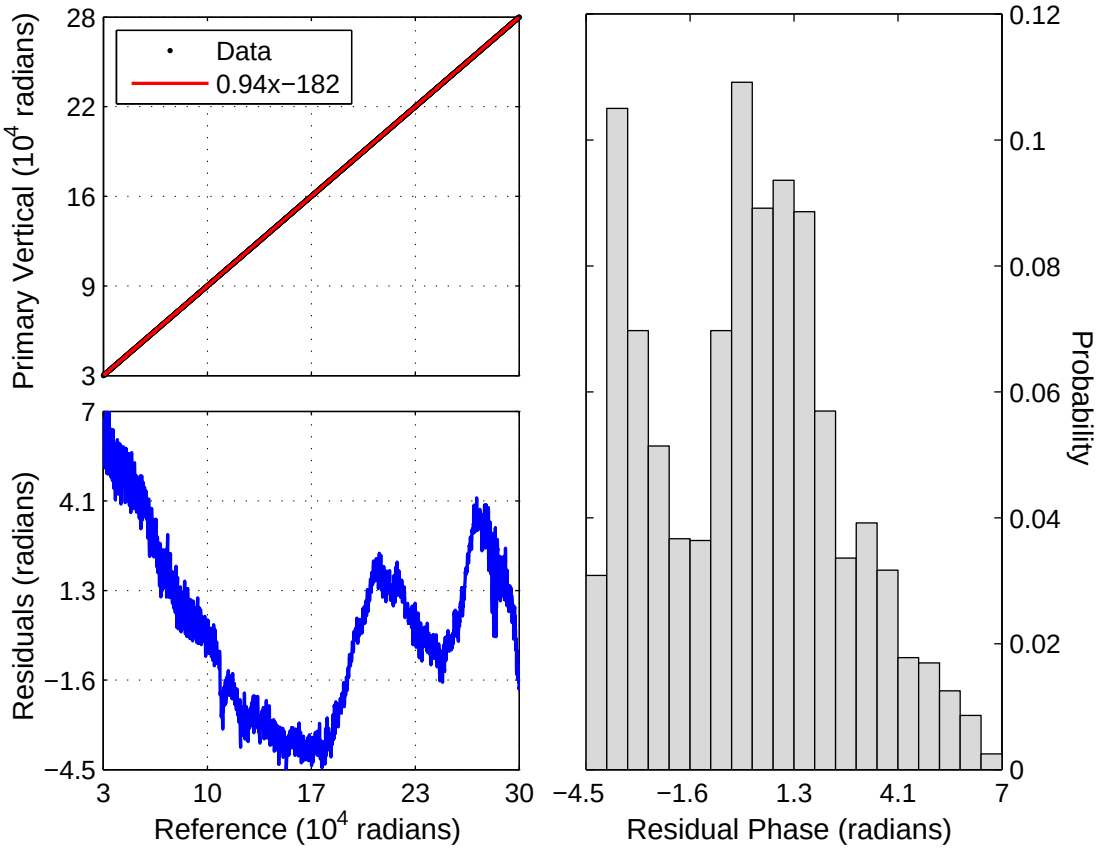


Figure 4.12: Example fit between the phase output of the primary vertical strainmeter and the reference interferometer. While the statistical uncertainties are less than 1 parts-per-million, the peak-to-peak residuals are ∼12 radians, or several parts-per-thousand.

base length of the verticals by the 1 m lower sonde package length.

Assuming a base length of 252 ± 1 m, a wavelength of $\lambda = 1553.4 \pm 1.0$ nm, and a strain-optic constant of $\mu = 1.158 \pm 0.012$, the calibration factor for the three vertical strainmeters (primary, secondary, and auxiliary, or PV, SV, and AV, respectively) can be calculated with Equation 1.32:

$$C = \frac{4\pi\mu}{\lambda} L_0.$$

which yields:

$$C_{PV/SV} = 0.4255 \pm 0.0046 \text{ n}\epsilon\text{/radian } (1.1\%)$$

$$C_{AV} = 0.5932 \pm 0.0064 \text{ n}\epsilon\text{/radian } (1.1\%).$$

The relative gains are, of course, known much better. Note that the same strain-phase relationship is not valid for the areal strainmeter, as was shown in Section 4.5.3. This implies that the calibration of the areal strainmeter will have to be determined empirically.

4.6 Conclusions and Future Work

An interferometric borehole optical fiber strainmeter was installed at the Piñon Flat Observatory that has been successfully recording signals of geophysical interest since late February of 2012. This completely passive instrument includes three redundant vertical strainmeters and is prepared for a novel, down-hole areal strainmeter with no electronics. The up-hole package is located 4 m below the ground surface to isolate it from short period (less than 1 cycle per day) temperature changes. For redundancy, two cables under tension with multiple fibers track the vertical deformation over a baseline of 250 m between the up-hole and down-hole packages. While the vertical strainmeters appear to operate flawlessly, the failure to properly grout in the areal strainmeter has (so far) limited its use to serving as a system null-test, though it has found utility as an alternate laser wavelength reference (Section 5.2.2).

While no major changes have been made since the borehole casing was decoupled from the main wellhead pad, the plans have been readied for re-grouting the areal strainmeter. This would require installing another grout tube, flushing out the well to remove any material that has settled into the bottom of the borehole, and delivering competent grout around the lower sonde. There are some concerns with this procedure, one of which is the possibility of damaging the fiber cables.

There are several lessons in optical fiber strainmeter design that can be learned from the development of BOFS. The first concerns the use of an unequal arm interferometer along with the concomitant need for a separate or independent reference interferometer to compensate for apparent length changes due to laser wavelength fluctuations. Obviously this approach is a less than ideal since

it introduces another source of possible noise (mandrel instability). However, the performance of such a reference could be significantly improved by exploiting the very stable thermal environment at the bottom of the borehole. Specifically, a mechanically uncoupled, fiber-wrapped mandrel could have been included in the lower sonde or in separate down-hole pressure case. For this installation it would have required either sacrificing the areal strainmeter (i.e., not epoxying it to the interior of the lower sonde pressure case), replacing one of the fiber cables with a more expensive cable containing additional optical fibers, or adding a third fiber cable.

Another design approach is that of an "inverted BOFS," where the light for each interferometer arm is split down-hole. In other words, all the 3×3 couplers would be contained in the lower sonde and the upper sonde would only contain the Faraday mirrors (and WDMs) from the vertical strainmeters. The principle advantage of this approach would be to maximize the temperature stability of the optical fiber that is a part of the optical path of the interferometer, but is not in the sensing arm of the strainmeter. While this is only 0.1% of the total optical path, it would also drastically simplify the optical design and potentially the ruggedness of the upper sonde. The disadvantage to this approach is that it would require a fiber cable with roughly twice the number of optical fibers to interrogate each interferometer.

A final lesson deals with the intricacies of deploying multiple, relatively fragile fibers of differing elastic constants along with a heavy, independent down-hole component. It is the complexity of this operation that lead to the failure to recognize that the instrument was not installed to its full depth thereby not permitting the proper grouting of the areal strainmeter. The motivation for this approach was the concern of being able to reuse the (very expensive) borehole in the future or in the event that the instrument failed during or shortly after deployment. Eliminating this would have opened up the possibility of first deploying the instrument and then grouting the entire borehole, and therefore ensuring the proper emplacement of the areal strainmeter. Moreover, filling the entire borehole with grout would certainly improve on the background noise levels, as presented in Chapter 5.

4.7 Acknowledgments

Don Elliott and Billy Hatfield provided very valuable assistance with the site preparation and installation, as well as many subsequent modifications. We would also like to acknowledge Ross Bell, John Dai, and Michael Fanton for their many hours of labor during the well pad reconstruction, as well as the additional assistance of Joel White and Heinz Wuhrmann during deployment. David Horwitt, David Chavez, and Jui-Yuan Chang for provided the hardware and software engineering and support for acquiring the BOFS data, and Hans-Werner Braun managed the data network infrastructure.

Portions of this chapter are being prepared for publication in the following manuscript: **Scott DeWolf, Frank K. Wyatt, and Mark A. Zumberge. "Improved Vertical Optical Fiber Borehole Strainmeter Design for Measuring Earth Strain."** The author's contribution to this study was to carry out the prototyping, assist in the design, fabricate the components of the instrument, perform laboratory and field calibrations, assist in the deployment, analyze the data, and prepare the manuscript.

REFERENCES

[1] GTSM Technologies Advanced Frequently Asked Questions (FAQs). http://www.gtsmtechnologies.com/pdf/GTSM_FAQ_2.pdf. Accessed: 2013-11-04.

[2] Duncan Carr Agnew. Strainmeters and tiltmeters. *Reviews of Geophysics*, 24(3):579–624, 1986.

[3] John A. Blum. *Development of sensors and techniques to assess earthquake hazards and submarine slope stability*. Ph.D. thesis, University of California San Diego, 2010.

[4] John A. Blum, Heiner Igel, and Mark A. Zumberge. Observations of Rayleigh-Wave Phase Velocity and Coseismic Deformation Using an Optical Fiber, Interferometric Vertical Strainmeter at the SAFOD Borehole, California. *Bulletin of the Seismological Society of America*, 100(5A):1879–1891, 2010.

[5] John A. Blum, Scott L. Nooner, and Mark A. Zumberge. Recording Earth Strain With Optical Fibers. *IEEE Sensors Journal*, 8(7):1152–1160, July 2008.

[6] Michael T. Gladwin. High-precision multicomponent borehole deformation monitoring. *Review of Scientific Instruments*, 55(12):2011–2016, 1984.

[7] Malcolm J. S. Johnston and Alan T. Linde. Implications of crustal strain during conventional, slow, and silent earthquakes. In *International Handbook of Earthquake and Engineering Seismology*, volume 81A, chapter 36, pages 589–605. Academic Press, San Diego, California, 2002.

[8] J. D. C. Jones and R. McBride. Multiplexing optical fiber sensors. In *Optical Fiber Sensor Technology*, volume 2, chapter 4, pages 158–159. Springer, Boston, Massachusetts, 1998.

[9] Alan T. Linde, Michael T. Gladwin, Malcolm J. S. Johnston, Ross L. Gwyther, and Roger G. Bilham. A slow earthquake sequence on the San Andreas fault. *Nature*, 383:65–68, 1996.

[10] Alan T. Linde and I. Selwyn Sacks. Continuous monitoring of volcanoes with borehole strainmeters. In *Mauna Loa Revealed: Structure, Composition, History, and Hazards*, pages 171–185. American Geophysical Union, Washington, D. C., 1995.

[11] Garry Rogers and Herb Dragert. Episodic tremor and slip on the cascadia subduction zone: The chatter of silent slip. *Science*, 300(5627):1942–1943, 2003.

[12] Frank K. Wyatt. Displacement of Surface Monuments: Vertical Motion. *Journal of Geophysical Research*, 94(B2):1655–1664, 1989.

[13] Mark A. Zumberge, Frank K. Wyatt, Dong X. Yu, and Hideo Hanada. Optical fibers for measurement of earth strain. *Applied Optics*, 27(19):4131–4138, October 1988.

Chapter 5

Observations from the Borehole Optical Fiber Strainmeter

5.1 Introduction

Building on the development work of the previous chapter, we now explore the data collected since the deployment of the Borehole Optical Fiber Strainmeter (BOFS). The first major topic relates how the data raw interferometer data are processed to estimate the vertical strain record. This is followed by several assessments of the instrument's performance by examining potential environmental influences and comparisons with other collocated strainmeters using several geophysical phenomena.

There are a number of key ideas that are worth noting before presenting the details. The first relates to the failure to properly couple the areal strainmeter to the borehole, which makes it useful as a laser frequency reference after adjusting for changes in the borehole water level. Moreover, with another independent measurement of the laser frequency, the existing installation could serve to put bounds on the inherent stability of the areal strainmeter design.

We report here on BOFS as a triply-redundant vertical strainmeter in the absence of the down-hole areal strainmeter component. As pointed out in the previous chapter, two of the three vertical strainmeters are contained in one fiber

cable and are labeled as the primary and secondary, or PV and SV, respectively. The third, auxiliary vertical strainmeter (AV) is contained in a separate fiber cable parallel to the first that is nominally twice as sensitive as the other two.

The final point concerns the fact that unlike in Chapter 6, there are no other measurements of vertical strain at PFO that can be used to directly compare to BOFS. However, the vertical strain ϵ_z can be inferred from the areal strain ϵ_A at the surface assuming a traction-free half-space using the relationship:

$$\epsilon_z = \frac{-\nu}{1-\nu}\,\epsilon_A, \tag{5.1}$$

where $\epsilon_A = \epsilon_1 + \epsilon_2$ are two orthogonal horizontal strains, and ϵ_z is the vertical strain. (Note that for a Poisson solid ($\nu = 0.25$), the vertical strain is -1/3 of the areal strain.) This relationship is used throughout this chapter to compare the sum of the north-south and east-west laser strainmeters (LSM areal) to the vertical strain recorded by BOFS.

5.2 Data Analyses

The raw optical phase output of each interferometer consists of a variety of unwanted signals in addition to the desired vertical strain signal. The most obvious (from Figure 4.10) are the apparent length changes caused by laser wavelength fluctuations. Temperature is also present in the optical phase record of the laser wavelength reference, which is the result of both mechanical and optical changes in the reference mandrel and laser. Changes in the well temperature, monitored at only one point of the open borehole is also thought to contribute to the variance of the records. Vertical deformation in the strain record due to changes in atmospheric pressure may also be removed to further reduce the variance of the record.

Two methods have been developed for correcting the observed, raw optical phase data output by the fringe counting system, removing the known effects, and converting it into the desired vertical strain time series. While the goal of each method is the same, they differ in complexity and in the number of assumptions made to arrive at the final estimates, as well as in their noise characteristics.

The purpose of this section is to describe these two "correction" procedures

and provide estimates of the coefficients used to remove each of the unwanted signals from the raw time series. The first is the most direct method. It uses the fiber-wrapped, aluminum cylinder reference interferometer located up-hole in the adjacent equipment vault (Figure 4.9). Since the (intended) down-hole areal strainmeter is uncoupled to the borehole, it too can be used as a laser wavelength reference. These will be referred to as the "up-hole" and "down-hole" correction methods, respectively. The differences between each method and its effect on the final observations are presented in this chapter, and the complete cross spectra and time series results for each correction step are provided in Appendix A.

5.2.1 Up-Hole Laser Wavelength Correction

Correcting the vertical strain records for unwanted laser wavelength fluctuations using the up-hole reference mandrel first requires removing the influence of ambient temperature changes on the up-hole reference mandrel itself. The temperature is recorded using a thermistor glued directly to the mandrel whose resistance is converted to a voltage using a Wheatstone bridge. Given that these are very small temperature changes ($\sim 10^{-3}$ °C per day), the recorded voltage needs to be filtered to remove uncorrelated noise caused by electronic amplification. A 1,000-second lowpass filter is used and the result is scaled by $(154 \pm 2) \times 10^3$ rad/°C, or approximately 61 $\mu\epsilon$/°C (assuming Equation 1.32 is valid for a 266 m, helically-wrapped mandrel).

Next, this residual time series must be scaled to match the raw strainmeter records. This is necessary since the length of each interferometer is different, and the amount of apparent length changes caused by wavelength changes are proportional to the path-length imbalance of the interferometer (see Section 1.5.4). These dimensionless scale factors have already been determined in the post-installation experiment described in Section 4.5.5, and are summarized in Table 4.1.

The final correction — actually a signal of geophysical interest — is to remove the apparent vertical displacement due to barometric pressure changes, and also to convert the result to strain using the calibration factors computed in Section 4.5.5. This correction is perhaps the most confusing since the cross spectral results

(Figure A.3) show that there is only coherent energy between the two signals in a fairly narrow frequency band (roughly 5×10^{-5} to 1×10^{-4} Hz). A least-squares fit between the two time series yields a coefficient of -0.1103 ± 0.0007 rad/Pa (approximately -47 pϵ/Pa for the primary vertical strainmeter) that is roughly consistent with the cross spectral magnitude results in that same frequency band. Since the coherence is very weak at higher frequencies – very little high frequency signal energy is correlated with this pressure – the barometric pressure record is low-pass filtered with a corner frequency of 10^{-3} Hz before applying the correction.

The up-hole wavelength reference correction to the vertical strain records can be summarized as:

- Suppress the amplifier noise from the reference mandrel thermistor record using a 1,000-second lowpass filter.
- Remove temperature signal from reference mandrel interferometer record using a factor of $(154 \pm 2) \times 10^3$ rad/°C.
- Remove the residual reference mandrel interferometer signal from the vertical strainmeter records using the scale factors presented in Section 4.5.5.
- Remove the (low pass filtered) barometric pressure scaled by the empirically determined -0.1103 ± 0.0007 rad/Pa from remaining vertical strainmeter interferometer records.
- Convert the result to nϵ using the calibration factors computed in Section 4.5.5.

5.2.2 Down-Hole Laser Wavelength Correction

The principle advantage of the down-hole reference mandrel (i.e., the uncoupled areal strainmeter) is that it is located in an extremely stable temperature environment. It also does not suffer from the large and unexplained long-period drift observed in the up-hole reference that will be discussed in an upcoming section. However, the down-hole reference is sensitive to pressure changes from atmospheric variations as well those from tidal water level changes.

Therefore, the first step is to remove the water level and barometric pressure signals from the down-hole reference interferometer record. This is relatively straight-forward in the case of the barometric pressure acting on the (uncemented) areal strainmeter since it is simply requires scaling the record by the $(-46.2 \pm 0.1) \times 10^{-3}$ rad/Pa calibration factor obtained from the laboratory and field experiments described in the previous chapter. The piezoelectric water level transducer signal has a calibration factor of 9.042 ± 0.009 Volts/m, which can be converted to a pressure using the well-known hydrostatic relationship:

$$p = \rho\, g\, h.$$

Assuming a water density of $\rho = 1,000$ kg/m^3, an acceleration due to local gravity of $g = 9.8$ m/s^2, and the previous phase-pressure calibration results in a conversion factor of -453 ± 10 radians per meter of water level change, or about 50 rad/Volt. Since there is very low coherence above about 10^{-3} Hz, both the water level and barometer data are first low-pass filtered (Figures A.4 and A.5, respectively).

As with the up-hole reference, the resulting up-hole wavelength correction signal must also be scaled to match the path imbalances of the vertical strainmeters. While these are not the same as with the up-hole reference scale factors, they can be derived from the results in Table 4.1 since each ratio is relative to the same 266 m long reference mandrel. For example, the primary vertical strainmeter scale factor (PV) relative to the down-hole reference mandrel (AR) is simply:

$$\frac{PV}{AR} = \frac{0.9426}{0.3004} \approx 3.138.$$

The effect of atmospheric pressure on the earth can again be removed from the down-hole reference corrected vertical strainmeter record. This is done using the same -0.1103 ± 0.0007 rad/Pa coefficient as in the up-hole corrected data. The final time series is then converted to nϵ. In summary, the correction procedure using the down-hole reference interferometer is as follows:

- Remove the 10^{-3} Hz low-pass filtered water level signal from the down-hole reference mandrel record using the -453 ± 10 rad/m calibration factor derived above.

- Also remove 10^{-3} Hz low-pass filtered barometric pressure signal from the down-hole reference interferometer record using the $(-46.2 \pm 0.1) \times 10^{-3}$ rad/Pa lab/field phase-pressure coefficient from Chapter 4.

- Remove the residual down-hole interferometer signal from the raw vertical records using their respective scale factors.

- Remove the (low-passed) barometric pressure scaled by -0.1103 ± 0.0007 rad/Pa from remaining vertical strainmeter interferometer records.

- Convert the result to nϵ using the calibration factors computed in Section 4.5.5.

Since these are all linear corrections, there is nothing that prohibits the removal of the barometric pressure in one step using a combined scale factor. However, this is not done in practice given that there are indeed two different effects here, one on the downhole areal strainmeter and the other in the earth .

5.2.3 Time and Frequency Domain Comparisons Between the Up-Hole and Down-Hole Correction Methods

The two correction methods presented above result in final strain records that differ in several ways. Figure 5.1a shows a 1-day time-domain example of the two correction procedures, where each record has been scaled into nϵ using the 0.4255 nϵ/rad calibration factors calculated in Section 4.5.5. This shows that there is some difference between the two correction time series (red and magenta) at both long and short periods.

One key difference between the two methods is the noise level for frequencies above about 0.1 Hz. This is perhaps best illustrated in Figure 5.1b, which shows a 2-hour closeup of the region highlighted in gray in the previous subfigure. While both corrected records seem to share most of the longer period characteristics, the down-hole corrected vertical strain record clearly contains energy at a period of approximately 7 seconds. This is further evidenced by the inset plot of the difference between the two corrected time series.

Figures 5.2 shows the cross spectra results using 592 days of 5-minute sampled (detided) data and a 12 day window of 1 Hz sampled data. Each estimate is the result of an adaptive sine multitaper cross spectrum estimation method [6, 7]. The unity line in Figure 5.2c,d (in red) draws attention to the expected result (if both techniques removed all the instrumental noise) and makes it clear where the two corrected signals differ from one another. While the coherence generally drops off below about 10^{-5} Hz, there appears to be about a scale factor of 1 to 1.3 in the up-hole corrected series relative to the down-hole in the 10^{-4} to 10^{-3} Hz frequency band.

The strongest motivation for using the down-hole correction comes from the very high drift in the up-hole corrected data. Figure 5.3 shows that the up-hole corrected primary vertical strainmeter record needs to be scaled down by almost an order of magnitude to even approximately match the two-year behavior of the same instrument using the down-hole correction. This is most likely due to the increased temperature sensitivity of the up-hole reference mandrel and/or some aging effect of the mandrel itself.

5.3 General Observations

This section examines some of the broadest features seen in the BOFS strain records, which includes some inter-comparisons between the BOFS verticals as well as the inferred vertical strain (by way of Equation 5.1) from the combined north-south and east-west LSMs, as well as the areal signal derived from the GTSM. Quantitative analyses of known geophysical signals like solid earth tides and earthquake surface waves are considered in Section 5.4.

5.3.1 Time Series

Figure 5.3 shows an 18 month strain record for the BOFS primary vertical strainmeter as well the inferred vertical stain from the LSM and GTSM areal strainmeters at PFO. This plot starts about 3 months after deployment to coincide with the installation of the borehole temperature logger, which was installed

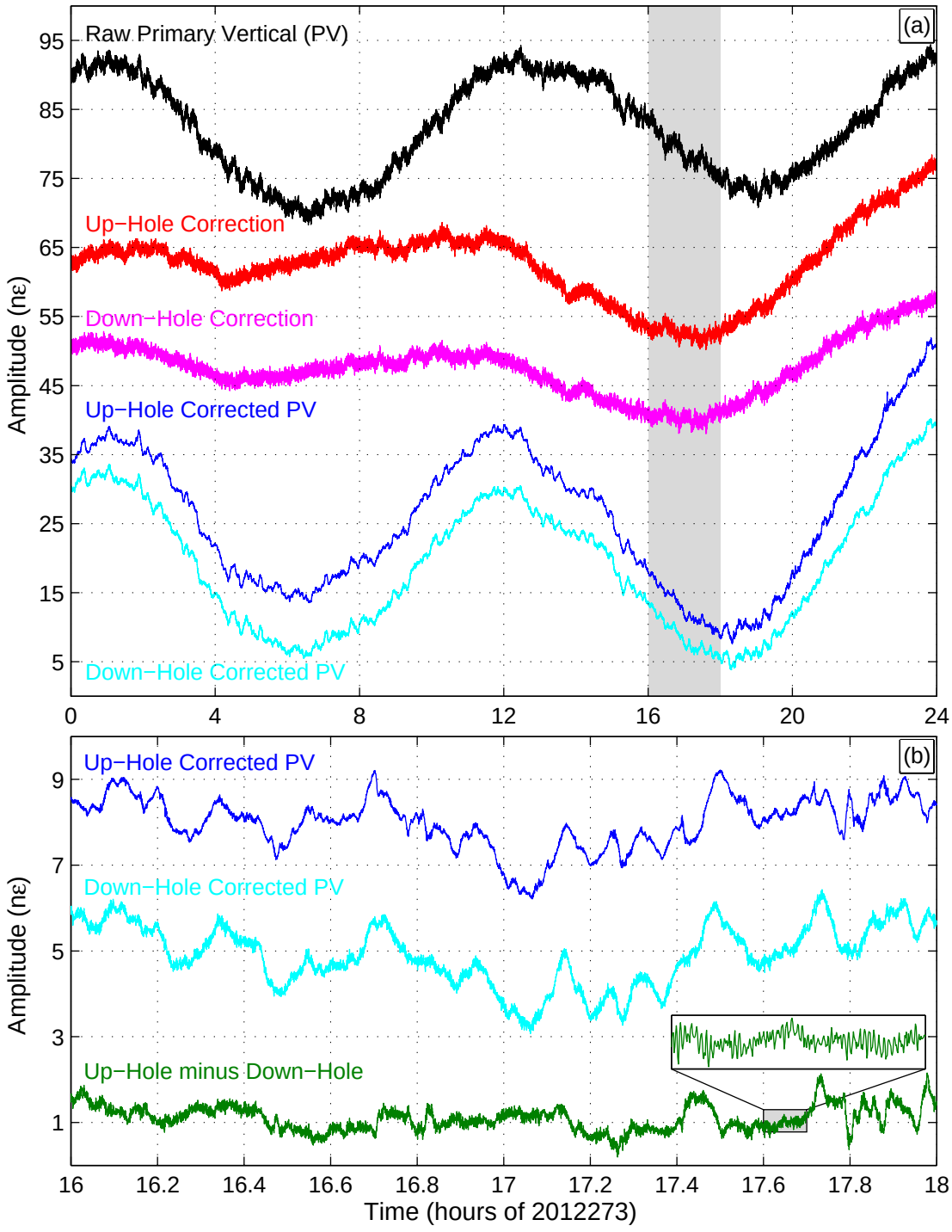


Figure 5.1: Raw primary vertical strainmeter record along with both the up-hole and down-hole correction series. (a) 1-day time series showing the raw, correction, and corrected series. (b) 2-hour closeup of the two corrected time series and their difference, with an additional 6-minute closeup (inset) to show the ∼7-second period residual unique to the down-hole correction.

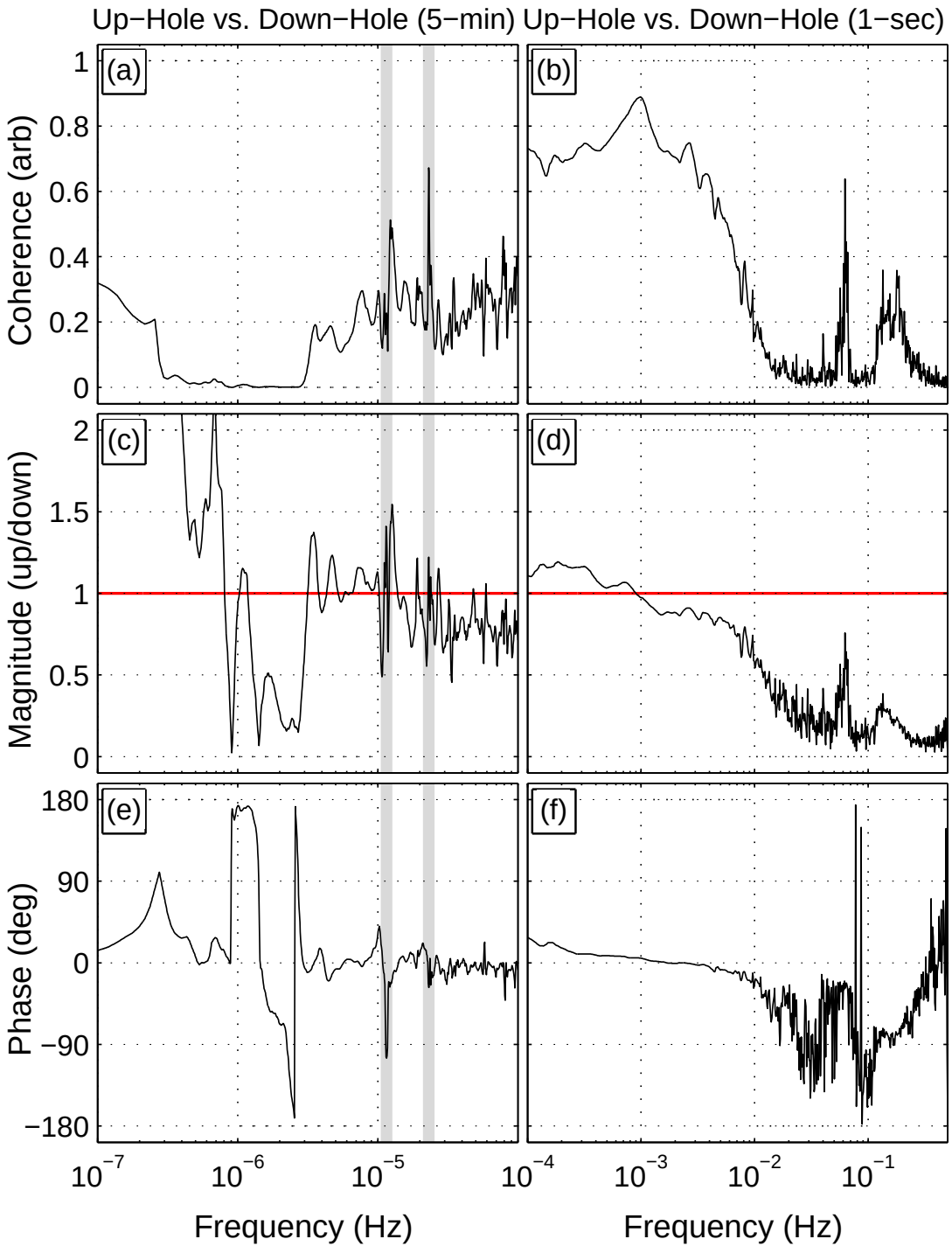


Figure 5.2: Cross spectrum between the up-hole and down-hole corrected series for a 5-minute sampled, 590-day (left) and 1-second sampled, 12-day (right) time windows. (a,b) Cross spectrum magnitude-squared coherence, (c,d) magnitude, and (e,f) phase. Unity magnitude is represented by the red line in (c,d).

about 30 days after clamping the upper sonde. The artifacts in the BOFS vertical strain records are the result of large temperature transients from repacking the up-hole reference mandrel at about 2012153, and the aforementioned in-situ areal strainmeter pressure calibration tests on 2012241.

It is obvious that the long period behavior of BOFS is governed by the seasonal temperature signal. This is present in the corrected record, subjected to the influence of a well temperature change — in the space above the water table and below the upper sonde — of $\sim 5°C$ over the nearly two-year deployment period (Figure 5.3). There is also a clear phase lag of the vertical strain with respect to this well temperature record. A more detailed investigation of this relationship is provided in Section 5.3.3.

The higher frequency behavior of the up-hole and down-hole corrected BOFS and the other strainmeters is presented in Figure 5.4. Each has been detrended but left unfiltered, and both the tided and detided signals are presented. This presents yet another example of the difference between the two correction methods, since the drift is much more pronounced in the up-hole corrected vertical strain record and there is a much larger residual at 1 CPD. Also obvious is the additional and persistent higher frequency noise common to both verticals not found in either of the other two strainmeters (LSM and GTSM). This noise is present in the Figure 5.1a, the character of which is more evident in the Figure 5.1b closeup. While the exact source is unknown, and very likely due (in part) to temperature variations in the open well-bore water column, it is quite significant with an approximate amplitude of 2 to 3 nϵ peak-to-peak, or about 10% of the tidal amplitude.

5.3.2 Spectra

Spectra from the BOFS primary vertical using both correction methods, as well as the areal strain from the combined LSMs and the areal component of the GTSM using the calibration matrix of Hodgkinson [4] are shown in Figure 5.5. These spectra are Guassian kernel smoothed, Hann-weighted periodograms. A closeup of the one and two cycle per day tidal bands and accompanied by

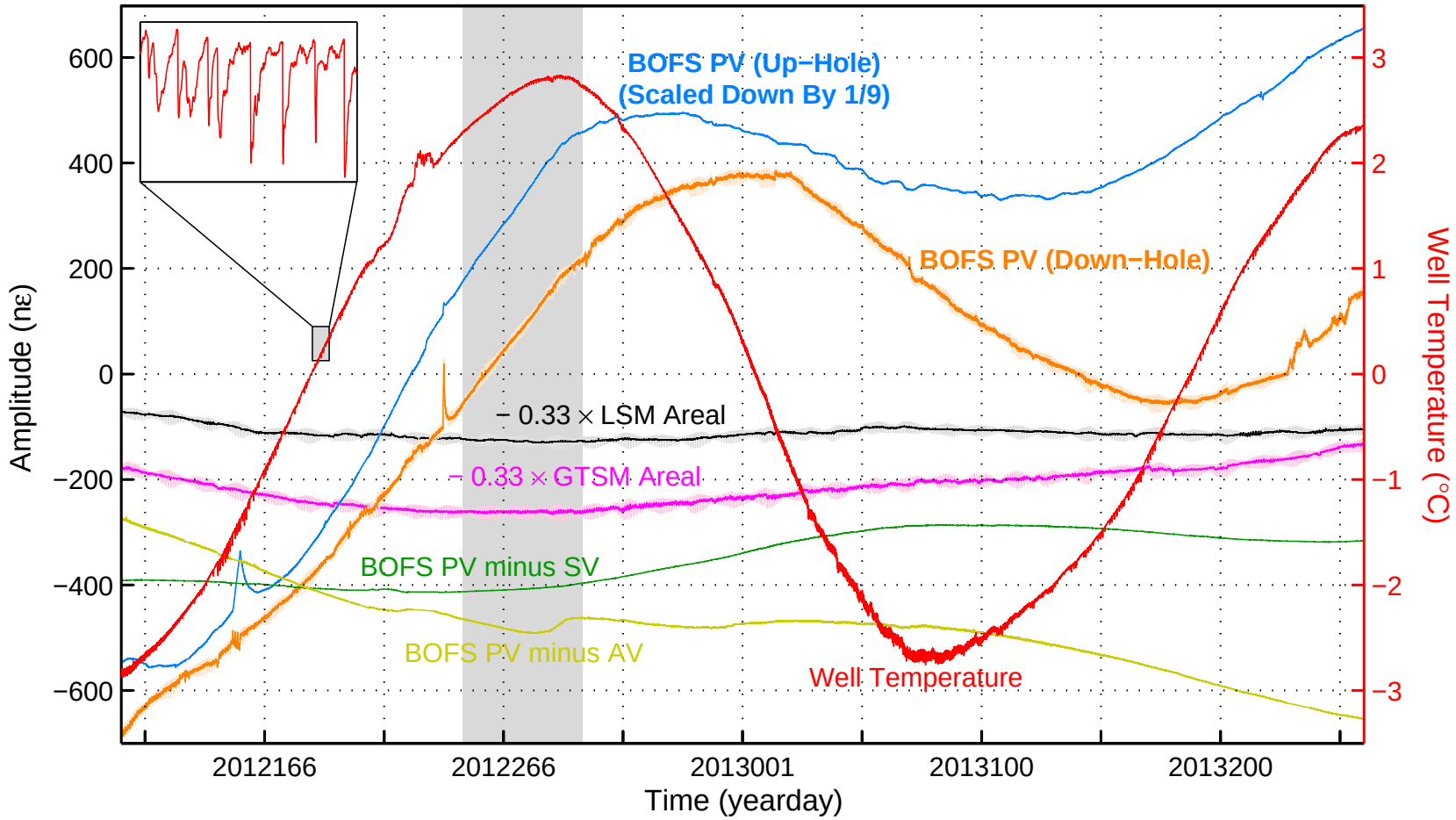


Figure 5.3: 18-month time series plots of the up-hole and down-hole corrected BOFS vertical strain along with the equivalent vertical strain derived from the LSM and GTSM areal strain. Differences between two of the three redundant verticals (PV-SV and PV-AV) are shown near the bottom of the plot. The BOFS well temperature record is also included in red, with a (detrended) 7-day closeup shown as an insert (0.06 °C full-scale).

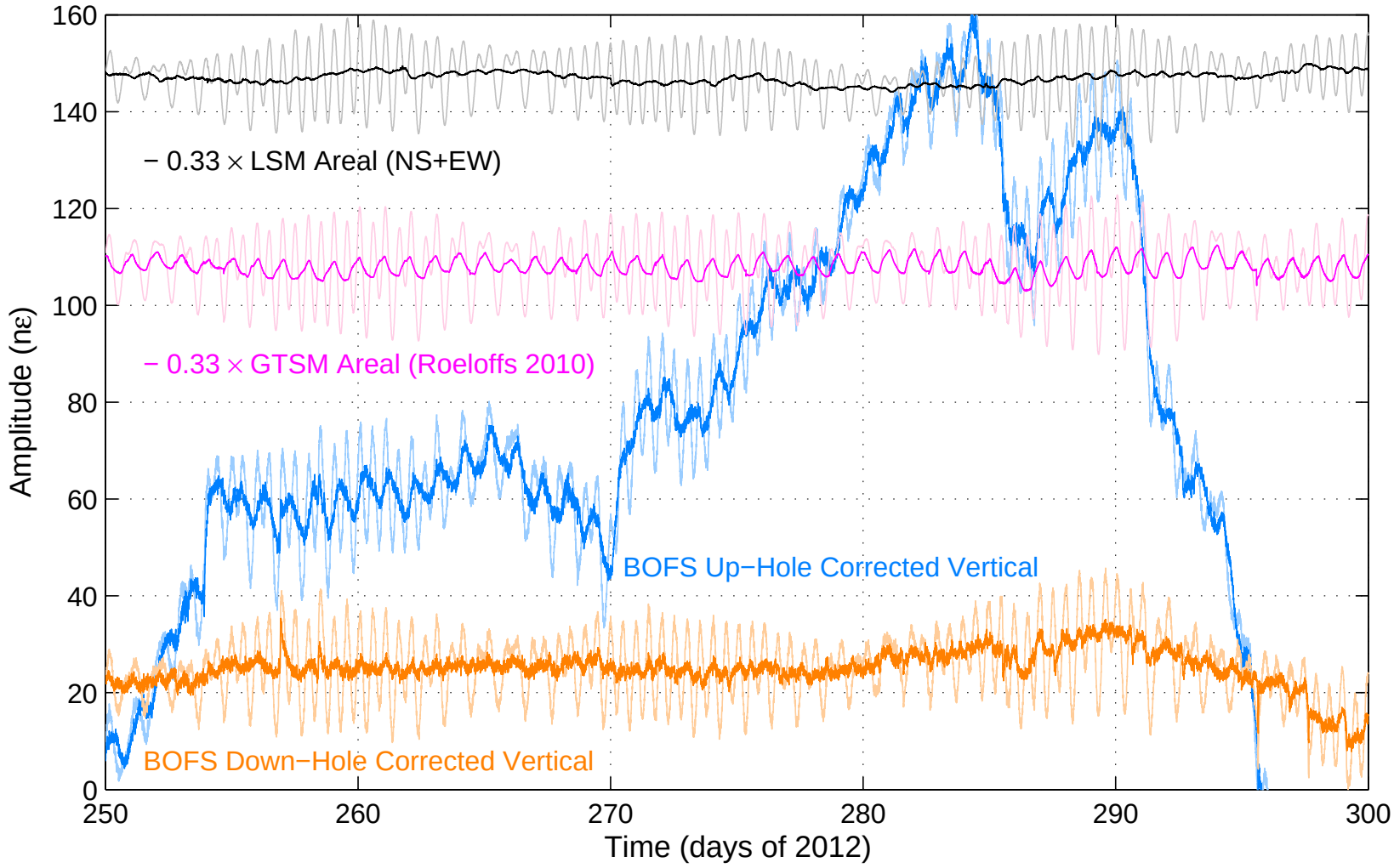


Figure 5.4: Tided and detided time series excerpt (labeled in gray) from the previous plot spanning a 50-day interval. Note that the data have been detrended and offset, but otherwise left unaltered.

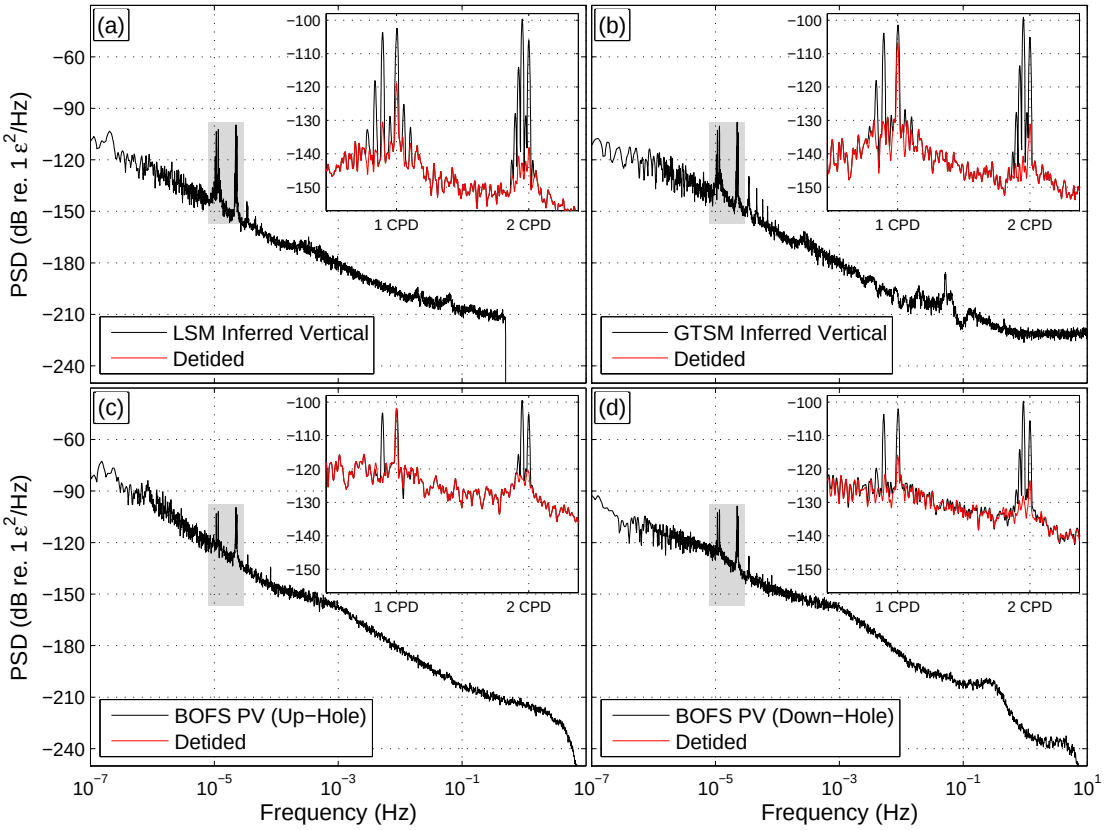


Figure 5.5: Spectra from the BOFS primary vertical strainmeter and the inferred vertical strain from the LSM and GTSM areal strain records. (a) Inferred vertical strain from LSM areal. (b) Inferred vertical strain from the GTSM areal using the calibration matrix of Roeloffs 2010 [8]. (c) Up-hole corrected BOFS primary vertical (PV). (d) Down-hole corrected BOFS primary vertical. A closeup of the tidal band is shown in each inset to illustrate the tided and detided spectral levels.

a spectrum estimate of the same time series with the best-fit tidal components removed (see Section 5.4.1) are shown in the inset plot. Note that the two areal strains have been rescaled to represent the inferred vertical strain (i.e., multiplying the time series by -1/3), and only data from the native 1 Hz sampled LSM data were used.

Some of the most distinct differences among the instruments are at the lowest frequencies. At the very longest periods ($\sim 1 \times 10^{-7}$ Hz) the spectral level of the up-hole corrected BOFS is about 16 dB higher than for the down-hole corrected, which is still another ∼14 dB above the inferred vertical strain from either

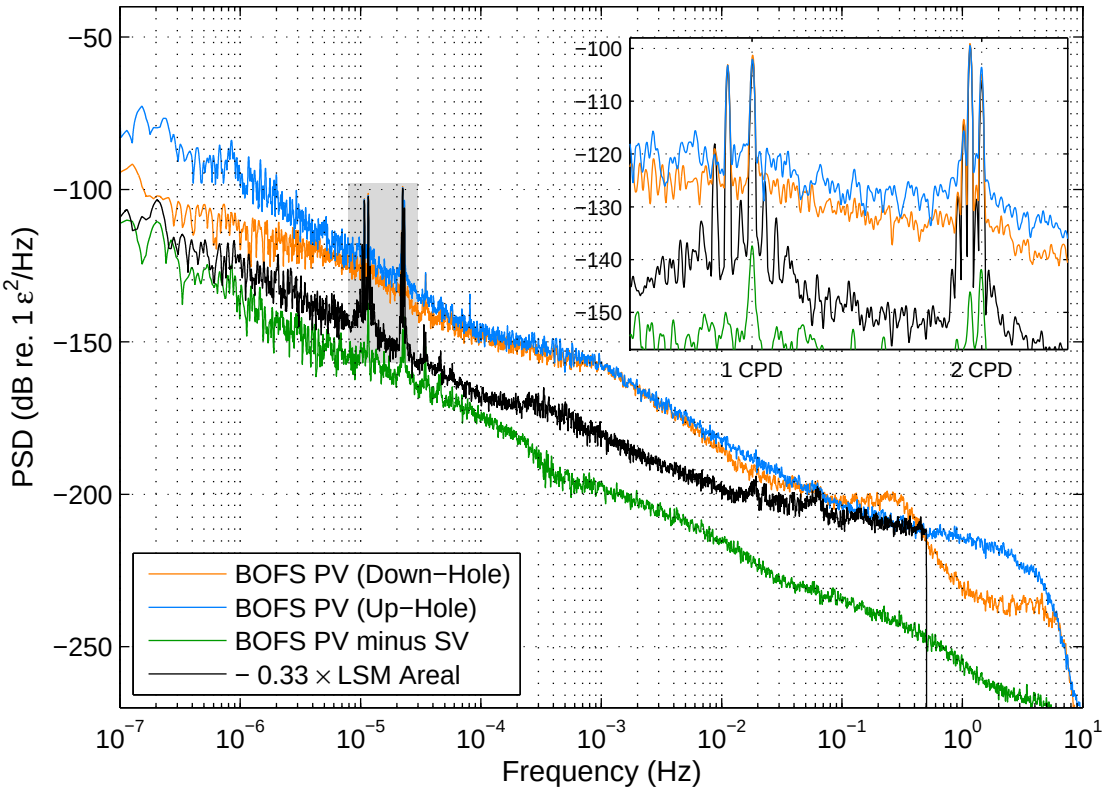


Figure 5.6: Combined spectra from the LSM, both up-hole and down-hole corrected BOFS, and the difference between two redundant BOFS verticals (PV-SV).

the LSM or GTSM. The power between 1 and 2 CPD (the intertidal band) is generally 20 dB higher on BOFS than the LSM, though, for the two correction methods, it is about 5 to 6 dB lower for the down-hole corrected data than for the up-hole corrected data.

A more direct comparison between the LSM and BOFS is shown in Figure 5.6, where the inset plot again highlights the intertidal region. The power spectrum of the difference between two of the three redundant vertical strainmeter fibers (PV minus SV, i.e., the two optical fibers contained in the same cable) is also shown. While there is excellent agreement for the largest amplitude tides (further explored in Section 5.4.1), the signal-to-noise levels are clearly lower for BOFS. In general, the spectral levels on BOFS are about 20 dB higher than that of the LSM until approximately 0.1 Hz, where the 0.5 Hz Nyquist frequency of the LSM obscures further comparison.

Figure 5.6 provides another example of the differences between the two correction methods. The down-hole corrected data systematically outperforms the up-hole corrected data except in the band 0.1 to 0.5 Hz. This is the band previously identified in the inset plot to Figure 5.1b. While the cause of this is unknown, the down-hole corrected spectral levels are as much as 20 dB lower than the up-hole for frequencies above 0.5 Hz.

The spectrum of the difference series (BOFS PV minus SV in Figure 5.6) is one measure of the intrinsic capabilities of this optical fiber strainmeter development. While the lack of data makes comparisons below about 10^{-6} Hz difficult, this measurement of the instrument "self-noise" is as much as 40 dB below the up-hole corrected vertical strain record and more than 25 dB lower than the LSM above 10^{-4} Hz. The inset plot also shows a 10 to 12 dB peak in the difference spectral level at 1 CPD that is due to some unknown effect, such as thermally-induced tractions between the two fibers.

5.3.3 Temperature

The influence of temperature is always a major concern, and is clearly the most significant component of the long period signal for the data collected so far (Figure 5.3). This was a concern at the outset, which is what motivated placing the upper termination point of the vertical strainmeters 4 m below the surface. To test the efficacy of this approach, an autonomous temperature logger (RBR Ltd. model TR-1060) was placed along side the upper sonde as near as possible to the upper termination point of the three vertical strainmeters. While this logger is quite good, with a 0.002 degree accuracy and annual drift rate as well as a 50 micro degree resolution, it was only intended to provide an upper-bound on the temperature variation in the well in the space above the water surface (at 32 m depth).

Several rough estimates of the temperature coefficient of the vertical strainmeters can be made from the time series. Looking at the first year of data, the up-hole corrected results give a value of about 1.6 $\mu\epsilon/^{\circ}$C, but this is complicated by the exceptional high rate of drift likely governed by aging of the mandrel. The

temperature coefficient of the down-hole corrected data is about 0.2 $\mu\epsilon/^{\circ}$C for the time period from 2012090 to 2013001, and drops by about a factor of two during the second year. This is an order of magnitude lower than the standard thermo-optic results computed back in Chapter 1, which is roughly 15 radians per degree per meter, or about 1.6 $\mu\epsilon/^{\circ}$C. However, it is more consistent with the roughly 25 m of un-submerged fiber, since it is quite unlikely that the recorded temperature acts over the entire length of the instrument.

Cross spectrum analysis between the BOFS primary vertical strainmeter and the borehole temperature are presented in Figure 5.7. The adaptive sine multitaper method was used on the complete 536-day record at 5-minute sampling (note that the temperature logger uses a sample period of 1-minute). Unlike the time series estimates, the 1 and 2 CPD magnitude estimates are only about 2 times larger for up-hole corrected data. While there is decent coherence at 1 and 2 CPD, the lack of phase stability across this band makes it difficult to arrive at a suitable transfer function. This is most likely due to the artifacts (noise) in the recorded temperature data (see inset on Figure 5.3) as a result of operating the signal being at the limits of the resolution of the logger (the average diurnal temperature change is only $\sim$10 μ°C).

5.3.4 Other Environmental Noise

The motivation for this section is to investigate potential causes of the jagged, 300 to 1,000-second variations seen in the final vertical strainmeter time series (e.g., Figure 5.1b) by comparing it to environmental observables other than the well temperature.

The up-hole corrected primary vertical strain record has been chosen, along with the up-hole reference mandrel, the mandrel temperature signal, barometer, borehole water level, as well as the wind speed measured by a nearby anemometer. Each of these are presented in Figure 5.8, where they have been scaled to loosely match the strain record. None of the five signals appear to be a one-for-one match to the fluctuations in the strain record.

Cross spectrum analysis further shows that there is no phase stability be-

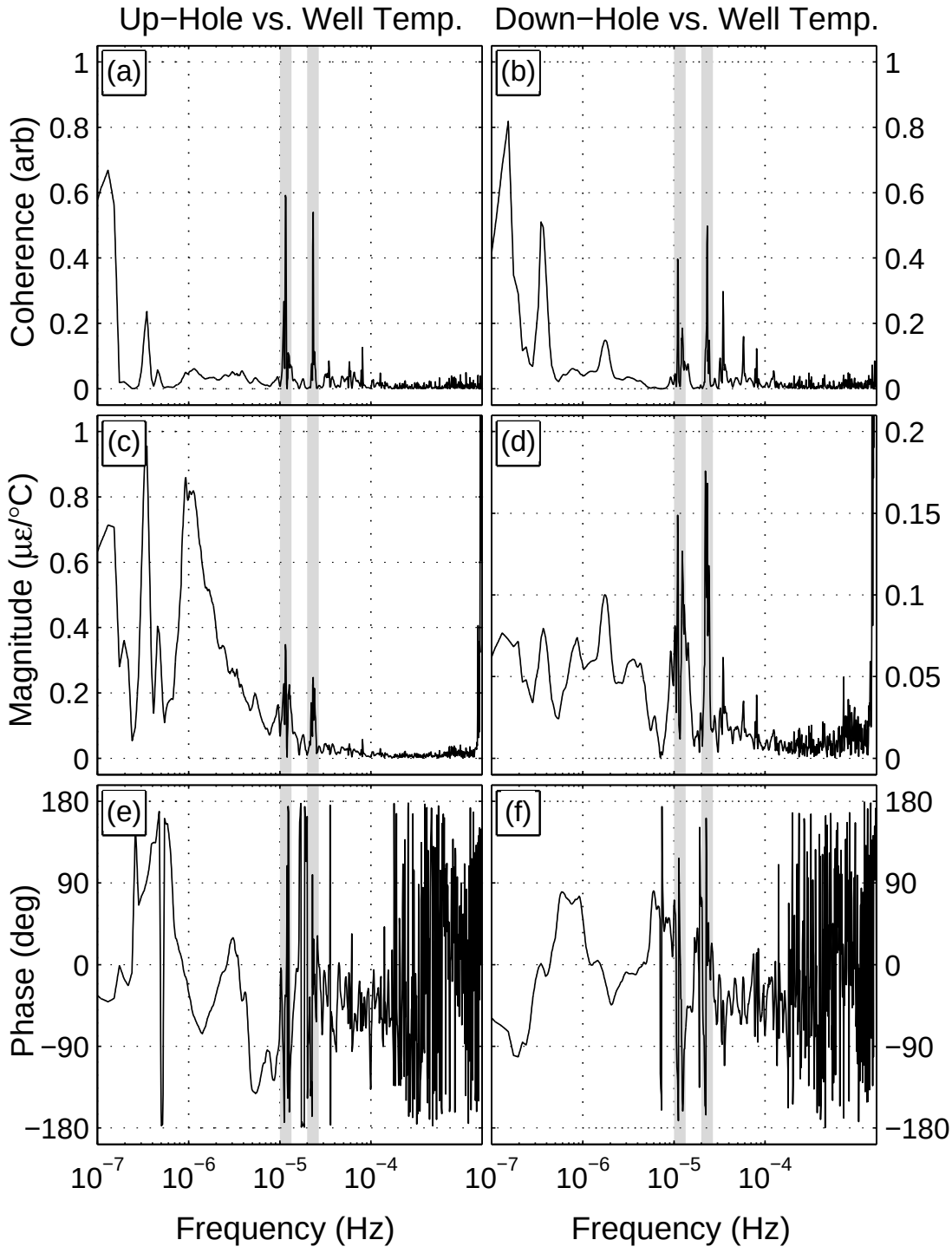


Figure 5.7: Cross spectrum between the up-hole (left) and down-hole (right) corrected vertical strain and borehole temperature for a 536-day time window. (a,b) Cross spectrum magnitude-squared coherence, (c,d) magnitude, and (e,f) phase.

tween these signals nor substantial coherence. This is reassuring in the case of the reference, its temperature, and the barometer since their known effects have already been removed. The lack of correlation between the water level and the vertical strain record is also encouraging since it was anticipated that axial strains due to pressure loading of the areal strainmeter (over its length) were predicted to be very small (∼20 pϵ/Pa). These results indicate that the source of this noise in the vertical strain record cannot be determined with the measurements currently available.

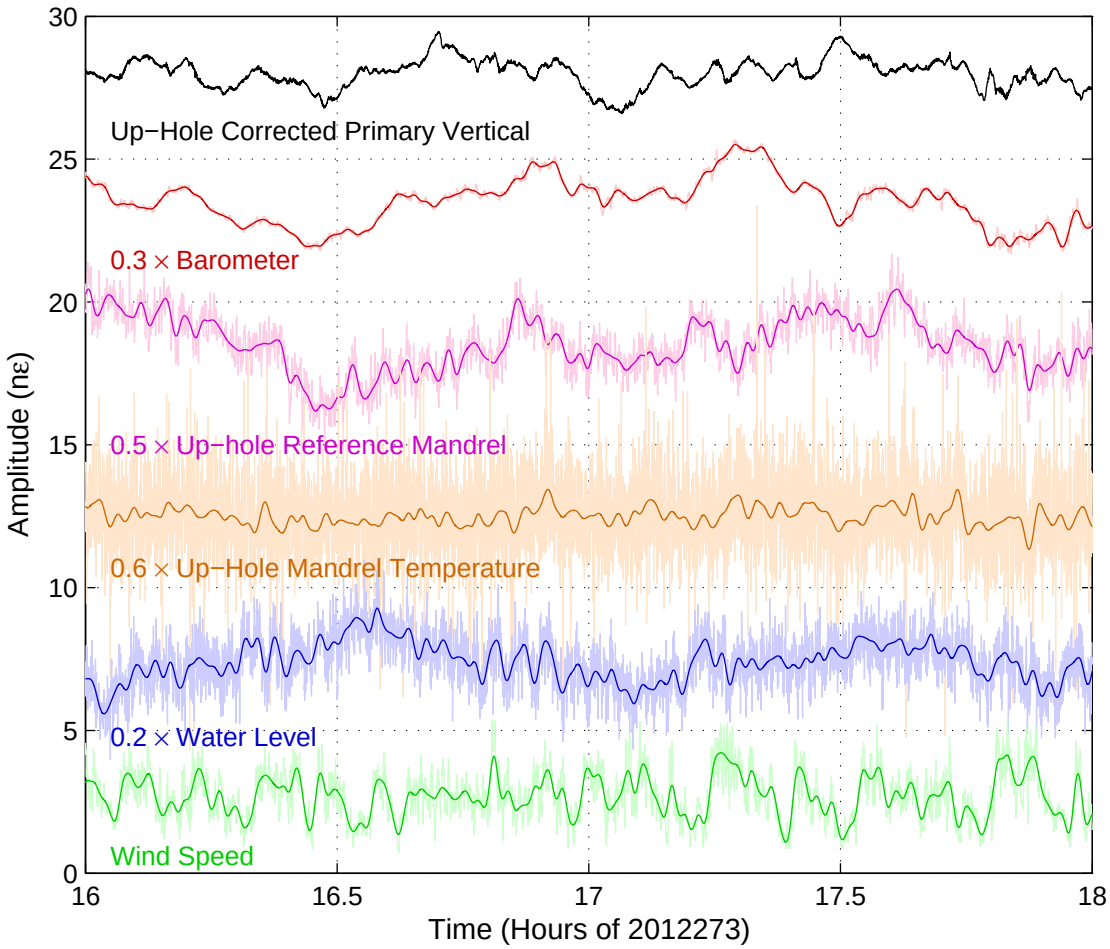


Figure 5.8: Time series of the up-hole corrected vertical strain and several environmental observables including the up-hole reference mandrel phase and mandrel temperature. Each signal has been arbitrarily offset and represented twice: the 10^{-4} Hz high pass filtered record shown in the faint curves and the 10^{-4} to 10^{-2} Hz bandpass filtered record shown as the solid curves.

5.4 Geophysical Signals

The most readily observable vertical strain signals are the solid earth tides and earthquakes. While there are no other long-base vertical strainmeters at the Piñon Flat Observatory to compare to BOFS, the vertical strain is inferred from horizontal strains using Poisson's ratio. This approach has been used before at PFO. For example, Wyatt et al. [9] found a Poisson's ratio of roughly 0.25 (that varied about 15%) at PFO by comparing the tides on the sum of the north-south and east-west LSMs to the Sacks-Everston dilatometer (volumetric strainmeter).

This section compares the solid earth tide and surface wave amplitudes observed by BOFS vertical strainmeters and the areal strain computed from the NS and EW LSMs to arrive at several estimates for Poisson's ratio. The areal component of the GTSMs are also included using the previously published calibration matrices by Roeloffs [8] and Hodgkinson [4]. This section concludes with a time series example to demonstrate the capabilities of BOFS for recording coseismic offsets.

5.4.1 Earth Tides

One way to assess the performance of BOFS relative to the other strainmeters at PFO is by comparing the vertical and areal strain amplitudes of the solid Earth tides at several well-known periods. The two constituents considered here are the principle lunar semidiurnal "M2" and the lunar diurnal "O1" with periods of 12.42 and 25.82 hours, respectively. These are chosen because they are sufficiently far away in frequency from potentially disturbing effects of the diurnal and semidiurnal signals whose periods average to 12 and 24 hours (e.g., temperature and atmospheric tides).

Since the period of each tidal constituent is known, a linear least-squares can be used to extract the amplitude and phase for each frequency. A common approach is to model the tidal time series $x(t)$ as [5]:

$$x(t) = b_0 + b_1 t + \sum_{k=1}^{N} A_k \cos(2\pi f_k t) + B_k \sin(2\pi f_k t),$$

where b_0 and b_1 represent the offset and drift components, respectively, and A_k and B_k are the "in-phase" and "quadrature" terms for the k^{th} tidal constituent at a frequency of f_k. The amplitudes and phases for each frequency are calculated using the well-known relationships:

$$M_k = \sqrt{A_k^2 + B_k^2}$$
$$P_k = \arctan\left(\frac{B_k}{A_k}\right).$$

24-component tidal fits were performed on all BOFS vertical strain records as well as the areal strains from the NS + EW LSM and GTSM using the manufacturer's (denoted by an "M" for brevity) calibration and two others from the literature (likewise shortened to "R" when employing the results of Roeloffs, 2010 [8], and "H" for Hodgkinson, 2013 [4]). The time series spanned 590 days between 2012060 and 2013287. The results for the M2 tidal constituent are shown in Table 5.1, and Table 5.2 for O1, where all phases are relative to the predicted tide-generating potential. Examples of the best-fit tides and their residuals have been previously presented in Figure 5.4.

Table 5.1: Best-fit amplitude and phases from the vertical and areal strain records M2 tidal constituent.

Instrument	M2 Amplitude (nϵ)	Phase (°)
LSM Areal	17.636 ± 0.005	35.38 ± 0.02
GTSM Areal (M)	10.235 ± 0.008	30.37 ± 0.04
GTSM Areal (R)	21.164 ± 0.014	32.77 ± 0.04
GTSM Areal (H)	19.895 ± 0.014	31.12 ± 0.04
BOFS PV (Up-Hole)	6.406 ± 0.019	212.62 ± 0.17
BOFS PV (Down-Hole)	6.469 ± 0.008	213.25 ± 0.07

The overall fits to the data appear to be satisfactory with statistical uncertainties well below 1%. Recall that the negative sign in Equation 5.1 indicates that the phases should be 180° out of phase with each other. Comparing the BOFS

Table 5.2: Best-fit amplitude and phases from the vertical and areal strain records O1 tidal constituent.

Instrument	O1 Amplitude (nϵ)	Phase (°)
LSM Areal	7.688 ± 0.005	-50.12 ± 0.04
GTSM Areal (M)	4.780 ± 0.008	-54.51 ± 0.09
GTSM Areal (R)	8.692 ± 0.014	-54.59 ± 0.09
GTSM Areal (H)	9.067 ± 0.014	-52.36 ± 0.09
BOFS PV (Up-Hole)	2.836 ± 0.019	121.10 ± 0.38
BOFS PV (Down-Hole)	3.068 ± 0.008	125.67 ± 0.14

primary vertical with respect to the LSM areal (BOFS-LSM) shows this to be approximately the case:

$$\begin{aligned} \text{M2:}\ & 177.24 \pm 0.17^\circ \text{ Up-Hole} \\ & 177.87 \pm 0.07^\circ \text{ Down-Hole} \\ \text{O1:}\ & 171.22 \pm 0.38^\circ \text{ Up-Hole} \\ & 175.79 \pm 0.14^\circ \text{ Down-Hole} \end{aligned}$$

While these technically do not agree with the predicted phase shift of 180° (with Z-scores ranging from 15 to 30σ), the statistical uncertainties are most likely optimistic.

To compare the amplitudes of the vertical and areal strains, the Poisson's ratio results are shown in Tables 5.3 and 5.4 for the O1 and M2 constituents, respectively. The estimates derived from the LSM / BOFS amplitude ratios appear to match fairy well with the exception of the 5% larger O1 estimate from the down-hole corrected data. While the three GTSM amplitudes differ from one-another, the Roeloffs and Hodgkinson calibrated data are more consistent with a Poisson's ratio of 0.25 than the default calibration.

A table of the BOFS/BOFS amplitude ratios for each pair of redundant sensing fibers are also included in Table 5.5 as a self-consistency check. While 8

Table 5.3: Inferred Poisson's ratio results using the vertical and areal strain amplitudes of the best-fit M2 tidal constituent.

Areal	Vertical	Poisson's Ratio
LSM Areal	BOFS PV (Up-Hole)	0.2663 ± 0.0006
LSM Areal	BOFS PV (Down-Hole)	0.2682 ± 0.0002
GTSM Areal (M)	BOFS PV (Down-Hole)	0.3873 ± 0.0003
GTSM Areal (R)	BOFS PV (Down-Hole)	0.2341 ± 0.0002
GTSM Areal (H)	BOFS PV (Down-Hole)	0.2454 ± 0.0003

Table 5.4: Inferred Poisson's ratio results using the vertical and areal strain amplitudes of the best-fit O1 tidal constituent.

Areal	Vertical	Poisson's Ratio
LSM Areal	BOFS PV (Up-Hole)	0.2696 ± 0.0013
LSM Areal	BOFS PV (Down-Hole)	0.2853 ± 0.0005
GTSM Areal (M)	BOFS PV (Down-Hole)	0.3909 ± 0.0007
GTSM Areal (R)	BOFS PV (Down-Hole)	0.2608 ± 0.0006
GTSM Areal (H)	BOFS PV (Down-Hole)	0.2528 ± 0.0005

of the 12 results are inconsistent with the expected amplitude ratio of 1 at the 1σ level, all but one agree at 3σ. The consistency among the errors for each trio of ratios is also striking since one would expect that the variance between the two fibers in the same cable (PV/SV) would be less than those between the two fibers in separate cables (PV/AV and SV/AV).

5.4.2 Surface Waves

Surface waves from teleseismic earthquakes are another way to estimate Poisson's ratio and to compare the signal-to-noise levels of the vertical and areal

Table 5.5: Intercomparison of the BOFS vertical strainmeter amplitude rations for the M2 and O1 tidal lines.

Instruments	M2 Amp. Ratio (nϵ/nϵ)	O1 Amp. Ratio (nϵ/nϵ)
PV/SV (Up-Hole)	0.992 ± 0.004	1.012 ± 0.009
PV/AV (Up-Hole)	1.004 ± 0.004	1.016 ± 0.009
SV/AV (Up-Hole)	1.012 ± 0.004	1.004 ± 0.009
PV/SV (Down-Hole)	0.995 ± 0.002	1.005 ± 0.004
PV/AV (Down-Hole)	1.006 ± 0.002	1.004 ± 0.004
SV/AV (Down-Hole)	1.011 ± 0.002	1.000 ± 0.004

strainmeters. This section presents the results comparing all three BOFS vertical strainmeters to the areal strain observed by both the LSM and GTSM for 36 surface wave producing earthquakes. Since the vertical strains are roughly one-third of the amplitude of the horizontal strains, and BOFS generally has higher noise levels, a hand-selected subset of the events used for evaluating the performance of the horizontal strainmeters in Chapter 6 was considered here (and listed in Appendix B). The analysis time window was also determined individually for each earthquake.

The record segment encompassing each earthquake was subjected to some manipulation before analysis. Given the possibility of some (coupled) seismic signal from the down-hole reference interferometer, and the relatively short duration of each event, the raw BOFS vertical strainmeter records were corrected using the up-hole reference interferometer. All strain records were then detrended and bandpassed between 0.01 and 0.10 Hz using a 3^{rd}-order Butterworth filter before analysis. This was necessary given the different roll-offs of the anti-aliasing filters used by each instrument, and justified since surface wave periods are usually in the 15 to 20 second range. The 20 Hz BOFS and GTSM data were decimated to 1 Hz sampling and delayed by 2 seconds to match the output of the LSM to compensate for the phase delay imposed by its anti-aliasing filter.

The relative amplitude of each pair of sensors was estimated by least-squares fitting one time series to the other. However, not all of the instruments being compared share the same data acquisition hardware and suffer from some differential timing errors. This was compensated for by offsetting one series in time relative to the other and finding both the time delay and amplitude ratio for which the squared residual was a minimum. A series of 500 time delays over a ± 3 second time range was considered by applying phase shifts in the frequency domain. Note that conventional cross spectrum analysis was found to be inadequate since the duration of each event was too short to appreciably reduce the variance by segmented averaging (i.e., Welch's method).

Figure 5.9 shows an example of four surface wave fits from a magnitude 7.3 earthquake located off the east coast of Honshu, Japan on December 7th, 2012. The first shows the fit between the BOFS primary vertical (PV) strainmeter and the areal strain measured by the sum of the NS and EW LSMs (Figure 5.9a). The LSM areal is also compared to the BOFS auxiliary vertical strainmeter (AV) (Figure 5.9b), and the BOFS PV and AV compared to each other (Figure 5.9c). These two results provide a self-consistency check since the AV/PV amplitude ratio is 1.0037 ± 0.0005, which agrees with the 1.003 ± 0.001 scale factor ratios relative to the LSM areal. The final plot (Figure 5.9d) compares the BOFS PV to areal strain output by the GTSM using the calibration matrix of Roeloffs 2010 [8]. These results are quite good with an RMS residual of $\sim$0.1 nϵ for an SNR of about 26 ($\sim$28 dB).

Ensemble results for the vertical strain to areal strain amplitude ratio converted to Poisson's ratio (Equation 5.1) are shown in Table 5.6. The LSM/BOFS results are in very good agreement with a Poisson solid ($\nu = 0.25$) with an ensemble standard deviation of just under 5%, and is perfectly consistent with previous results [9]. It is also reassuring that all three vertical strainmeters yield the same result, indicating that they are adequately calibrated with respect to one another at the 5% level. While the disagreement between the GTSM and LSM results is not surprising by itself, it is worth noting that the ensemble uncertainty in the GTSM using the Hodgkinson 2013 calibration matrix is half of the LSM/BOFS

and nearly one-fifth that of the other two GTSM results.

Table 5.6: Ensemble averages for the Poisson's ratio using 36 earthquakes.

Areal	Vertical	Poisson's Ratio
LSM Areal	BOFS PV	0.254 ± 0.012
LSM Areal	BOFS SV	0.253 ± 0.012
LSM Areal	BOFS AV	0.254 ± 0.012
GTSM Areal (M)	BOFS PV	0.349 ± 0.024
GTSM Areal (R)	BOFS PV	0.212 ± 0.023
GTSM Areal (H)	BOFS PV	0.215 ± 0.005

Table 5.7 presents the ensemble averages from comparing each pair of the redundant BOFS vertical strainmeter amplitudes for the same 36 earthquakes. These results are consistent with no significant difference between the three fibers. This also shows that the two strainmeter fibers in the same cable (PV and SV) are more closely matched than the results where the two fibers are contained in separate cables (PV and AV, as well as SV and AV).

Table 5.7: Intercomparison of the BOFS vertical strainmeter amplitude ratios using 36 earthquakes.

Instruments	Amplitude Ratio ($n\epsilon/n\epsilon$)
PV/SV	0.9994 ± 0.0006
PV/AV	1.0016 ± 0.0094
SV/AV	1.0021 ± 0.0091

5.4.3 Coseismic Offsets

Figure 5.10 shows an example of a coseismic offset captured by the BOFS primary vertical at the onset of the March 11th, 2013 Anza, CA earthquake. This

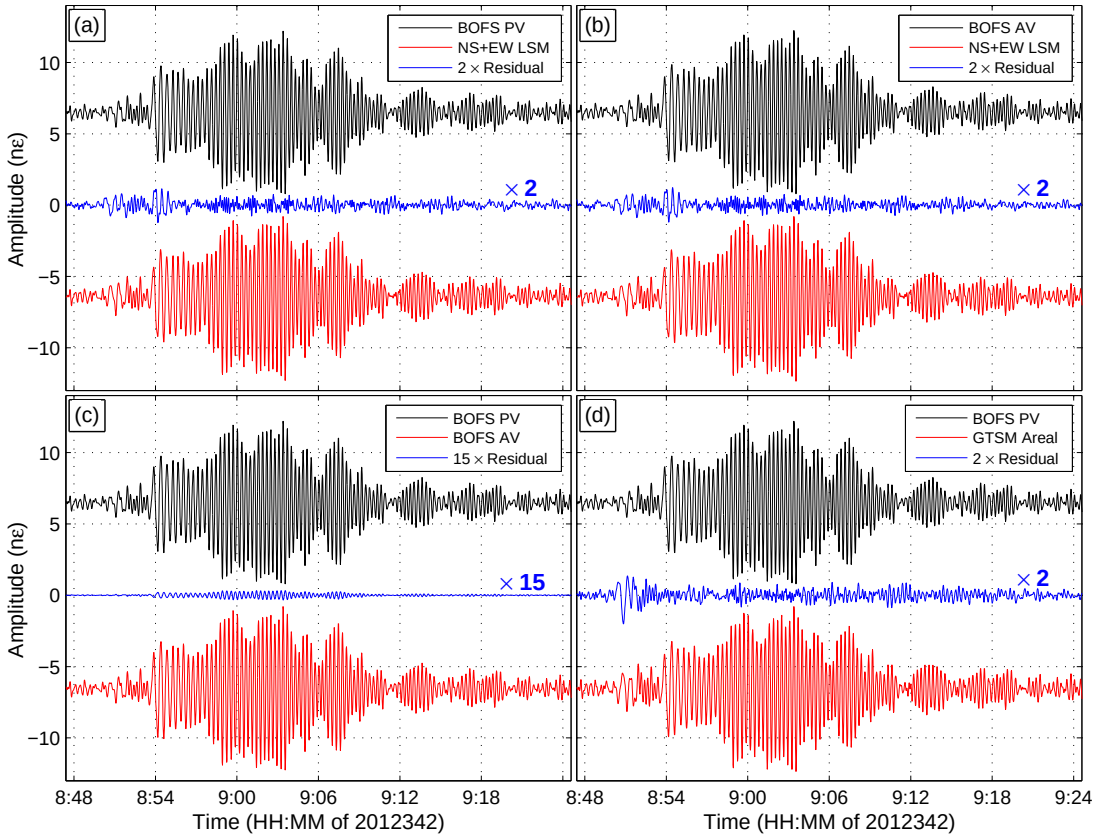


Figure 5.9: Surface wave fit results from 1 of the 36 teleseismic earthquakes used to compare BOFS to the LSM and GTSM. (a) Fit of the LSM areal to the BOFS primary vertical (PV). (b) Fit of the LSM areal to the BOFS auxiliary vertical (AV). (c) Comparison between the BOFS PV and AV. (d) Fit between the BOFS PV and the GTSM using the calibration matrix of Roeloffs 2010 [8]. Note that the residual time series have been scaled up by a factor of 2 except for the PV/AV, which has been scaled by 15.

magnitude 4.7 event occurred only 12 km from PFO, and did not exceed the maximum strain rate of 20 $\mu\epsilon$/s (1 $\mu\epsilon$ per sample). The inferred vertical strain from the areal strain recorded by the GTSM is also presented (this same event is also considered in Reference [1]); the ground motions did exceed the allowed strain for the LSMs. A 0.1 Hz, 4^{th}-order Chebyshev type 1 low pass filtered version of the original time series is used to smooth the results and feature the offsets.

There are several notable features of this event as it relates to the performance of the instrument. The first is that the RMS noise level is about 6 times larger (0.2 vs. 1.2 nϵ) for the BOFS vertical strain compared to the GTSM (Figure

5.10a). The other is that while the ∼5 nϵ offsets appear to agree very well, the event appears to be about the same amplitude as the background noise on BOFS. This significantly limits the number of potential events that can be examined since this is an almost ideal seismic event.

5.5 Discussion

5.5.1 Data Analyses

The two data correction methods illustrate the complexity in attempting to remove unwanted signals from the raw interferometer record. In most cases the correction signals have a very high SNR and the magnitude of the effect is well known from lab and/or field experiments (e.g., laser frequency correction). Certain frequency bands can be safely disregarded where the coherence between the signals is low, as it is in the case of the water level correction to the down-hole reference.

However, complications arise when the use of correction signals actually introduces unwanted noise. For example, the 7-second noise found in the down-hole corrected data may be due water level changes in response to microseisms (see the inset in Figure 5.1b). This may simply be a consequence of the choice of low-pass filtering the water level data before removing it from the down-hole reference signal. This leads to an interesting dilemma since leaving-in the high frequency content of the water level signal will also mean including other noise.

The other risk is over or under correcting the data due to insufficient knowledge of the scale factor used to remove the unwanted signal. This is probably not the case for the scale factor used to relate the various interferometer lengths since their relationship is determined by simple physics. However, this is not as obvious in other cases. Once again consider the water level correction to the down-hole reference. The magnitude spectrum (Figure A.4b) shows that the nominal value of 453 radians per meter may be ∼8% too high. This may be partially responsible for the 5% overestimate in the O1 tidal line compared to the up-hole corrected data.

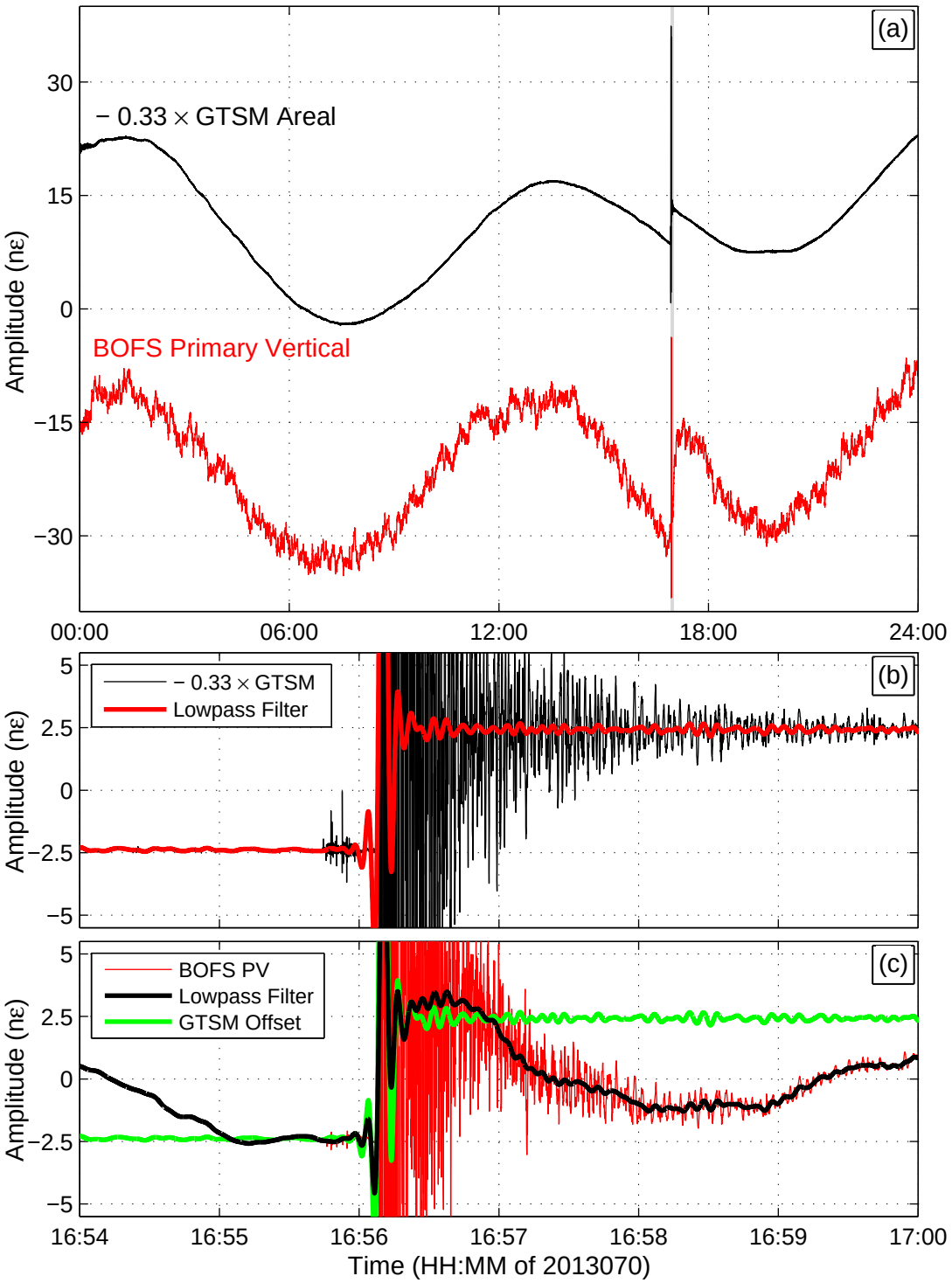


Figure 5.10: Example of a coseismic offset from the M4.7 Anza earthquake. (a) The earthquake in the context of the daily record. (b) Coseismic offset on the inferred vertical from the GTSM areal using the calibration matrix of Hodgkinson 2013 [4], and (c) BOFS primary vertical (PV).

5.5.2 General Observations

There is a clear seasonal temperature signal in the vertical strain record. While this is not unexpected, the phase discrepancy between the vertical strain and the well temperature indicates that the thermal environment between the surface and the water level (∼30 m down) cannot be adequately compensated for by this single measurement. The relatively short length of the records-to-date, coupled with the inability to correct for the well temperature makes it very difficult to estimate a meaningful drift rate in the vertical strainmeters.

The cause of the 300 to 1,000-second noise in the corrected vertical strain record remains unexplained. Unfortunately, the well temperature log is not of sufficient quality and resolution to resolve temperature changes of this amplitude over these periods. Cross spectrum analysis between the vertical strain record and a variety of environmental observables lack the coherence and phase stability to explain this noise.

Temperature profiles taken before deployment suggest that there are potential locations of fluid exchange from fractures in the rock. Therefore, without knowledge of the time history of the integrated temperature profile in this "open" borehole it is not possible to meaningfully correct for well temperature changes. This is also the most likely cause for the unexplained noise in the vertical strain record.

Spectrum analyses also show clear differences between the two correction methods, as well as the overall noise levels compared to the LSM and GTSM. The power levels of the down-hole corrected data are lower at the longest and shortest periods compared to the up-hole corrected data, with the exception of a 9 to 10 dB increase in the 0.1 to 0.5 Hz band in the down-hole data. Noise levels in the intertidal band are approximately 15 to 20 dB higher on BOFS than the LSM and GTSM.

5.5.3 Geophysical Signals

Comparisons of the tidal and surface wave amplitudes between BOFS vertical strainmeters and the areal strain measured by the LSM are consistent with a

Poisson's ratio slightly larger than 0.25. These results are partially summarized in Table 5.8. While the O1 component for the down-hole corrected primary vertical is an outlier compared to the other tidal results, it is only $+2.6\sigma$ from the value determined from the surface wave analysis.

Excellent agreement was found between each of the redundant vertical strainmeters for both tidal and surface wave analyses. While there was increased variance of the amplitude ratios between the two strainmeters in separate fiber cables (PV/AV and SV/AV) compared to the two in the same fiber cable (PV/SV) for the surface wave analysis, this was not found in the tidal results. This is most likely due to the statistical differences between estimating the variance from an ensemble of measurements (i.e., the variance in 36 least-squares fits) and the variance in a single least-squares fit parameter.

Table 5.8: Summary of the Poisson's ratio results from tidal lines M2, O1, and the surface wave fits.

Instruments	M2	O1	Surface Waves
LSM / BOFS PV (Up)	0.2663 ± 0.0006	0.2696 ± 0.0013	0.254 ± 0.012
LSM / BOFS PV (Down)	0.2682 ± 0.0002	0.2853 ± 0.0005	n/a

5.6 Conclusions and Future Work

For this BOFS installation, 18 months of data have been investigated to assess the performance of three redundant vertical borehole strainmeters deployed at PFO. The longevity of this system speaks to the benefits of this all-fiber system and, in particular, to the techniques used to seal the compliant cables to their down-hole sondes. Two different methods are presented to correct for apparent strains caused by laser wavelength fluctuations, each with their own benefits and limitations. The down-hole reference was found to perform better overall with the exception of an unidentified noise source in the 0.1 to 0.5 Hz band. Regardless of the method used, there is a persistent and unexplained 300 to 10,000 second, 2 to

3 nϵ peak-to-peak noise source clearly evident in the corrected time series.

Comparisons between the redundant vertical strain sensing components of BOFS and the LSM were found to be consistent with a Poisson's ratio near 0.25. The M2 and O1 tidal constituents were found to be in very good agreement with each other and also consistent with the surface wave analysis. Intercomparisons of the three BOFS vertical strainmeters were found to be in excellent accord. There does not appear to be any discernible difference between the gel-filled fiber cable used for the primary and secondary vertical strainmeters, and the non-gel-filled fiber cable used in the separate auxiliary vertical strainmeter, despite the particularly uneven stress inherent in the suspended fibers in the non-gel-filled cable, operating without the benefit of buoyancy effects.

Estimation of an overall drift rate similar to the $\sim$1 $\mu\epsilon$/yr seen in other optical fiber strainmeters [3, 2] was complicated by the clear seasonal temperature signal. The phase lag indicates (unsurprisingly) that the simple point measurement taken at the upper termination fixture is not representative of the thermal environment of the vertical strainmeters and is therefore insufficient for removing this effect.

An understanding of the aforementioned 300 to 10,000 second noise as well as the seasonal temperature signal would be greatly enhanced with the development of a high-precision, length-integrated temperature measurement system. This is not an easy obstacle to overcome since electronic methods typically lack the sensitivity needed to correct for very small (sub-$\mu\,^{\circ}$C) temperature fluctuations, and optical methods (e.g., an un-tensioned optical fiber) are very sensitive to strains such as those caused by thermal-induced tractions.

Another significant limitation of this development is the need to correct the data for unwanted strains due to laser wavelength changes. Clearly the very large ($\sim$10 $\mu\epsilon$ per year) drift in the up-hole reference interferometer, most likely due to the oxidation of the aluminum mandrel the fiber is wrapped upon, severely limits its usefulness. Given that this particular mandrel was not intended for long-term use, it could be improved by using a more stable quartz mandrel wrapped with a more rigidly-clad polyimide fiber.

The down-hole mandrel has proven to be more effective, but it will be need to be replaced with a longer term solution once plans proceed to properly grout it into the borehole. While future deployments may include an uncoupled, down-hole reference mandrel, the most obvious solution for wide application is to arrive at a solution for a frequency-stabilized, narrow-linewidth (long coherence length), infrared laser. Commercial systems do exist, but they lack the coherence length to illuminate a 250 m imbalanced interferometer. Very likely a combination of a stabilized source (for correction at low frequencies) and an improved down-hole mandrel would provide the best means for suppressing laser noise due to laser frequency instability.

Development of this new borehole vertical strainmeter system represents a significant improvement from previous systems both in terms of its response to tidal and longer period signals. The still-to-be-done proper coupling of the novel down-hole areal strainmeter should also be very significant in driving the future development of new composite optical fiber assemblies for measuring the full earth-strain tensor.

5.7 Acknowledgments

We are especially indebted to Duncan Agnew and Billy Hatfield for their insights into processing the data as well as providing consistency checks during various stages of these analyses, and to Robert Parker for providing the multitaper cross spectrum analysis code. David Horwitt, David Chavez, and Jui-Yuan Chang for provided the hardware and software engineering and support for acquiring the BOFS data, and Hans-Werner Braun managed the data network infrastructure.

Portions of this chapter are being prepared for publication in the following manuscript: **Scott DeWolf, Frank K. Wyatt, and Mark A. Zumberge. "Improved Vertical Optical Fiber Borehole Strainmeter Design for Measuring Earth Strain."** The author's contribution to this study was to carry out the prototyping, assist in the design, fabricate the components of the instrument, perform laboratory and field calibrations, assist in the deployment, analyze the data, and prepare the manuscript.

REFERENCES

[1] Andrew J. Barbour. *Investigations of fluid-strain interaction using Plate Boundary Observatory borehole data*. Ph.D. thesis, University of California San Diego, 2014.

[2] John A. Blum, Heiner Igel, and Mark A. Zumberge. Observations of Rayleigh-Wave Phase Velocity and Coseismic Deformation Using an Optical Fiber, Interferometric Vertical Strainmeter at the SAFOD Borehole, California. *Bulletin of the Seismological Society of America*, 100(5A):1879–1891, 2010.

[3] John A. Blum, Scott L. Nooner, and Mark A. Zumberge. Recording Earth Strain With Optical Fibers. *IEEE Sensors Journal*, 8(7):1152–1160, July 2008.

[4] Kathleen Hodgkinson, John Langbein, Brent Henderson, Dave Mencin, and Adrian Borsa. Tidal calibration of plate boundary observatory borehole strainmeters. *Journal of Geophysical Research: Solid Earth*, 118(1):447–458, January 2013.

[5] Rich Pawlowicz, Bob Beardsley, and Steve Lentz. Classical tidal harmonic analysis including error estimates in MATLAB using T_TIDE. *Computers & Geosciences*, 28(8):929–937, 2002.

[6] Kurt S. Riedel and Alexander Sidorenko. Minimum bias multiple taper spectral estimation. *IEEE Transactions on Signal Processing*, 43(1):188–195, 1995.

[7] Kurt S. Riedel and Alexander Sidorenko. Adaptive smoothing of the log-spectrum with multiple tapering. *IEEE Transactions on Signal Processing*, 44(7):1794–1800, 1996.

[8] Evelyn Roeloffs. Tidal calibration of Plate Boundary Observatory borehole strainmeters: Roles of vertical and shear coupling. *Journal of Geophysical Research*, 115:B06405, June 2010.

[9] Frank K. Wyatt, Duncan Carr Agnew, Alan T. Linde, and I. Selwyn Sacks. Borehole strainmeter studies at Piñon Flat Observatory. *Year Book Carnegie Institute of Washington*, 82:533–538, 1983.

Chapter 6

The Trench Optical Fiber Strainmeter

6.1 Introduction

An all-fiber horizontal strainmeter is a natural extension of the development work done with the borehole systems to this point. While seemingly obvious, this has never been attempted since it comes with its own set of obstacles. This is in part due to the difficulty of deploying trustworthy end monuments that would make such an attempt yield meaningful results (recall that one of the first uses of optical fiber strainmeters was to correct for unwanted monument motions in the laser strainmeter systems). The other has to do with the large temperature coefficient of the optical fiber itself that can partially, at best, be dealt with through an expensive and labor intensive burial process.

However, it is very useful to measure strain at higher frequencies where the effects of monument heaving and temperature are not as significant. For example, combined seismometer and strainmeter measurements can be used to estimate local material properties such as the Rayleigh wave velocity [5], and to better understand the propagation of seismic energy.

Another potentially useful application would be to use several horizontal optical fiber strainmeters to calibrate some of the nearly 80 Gladwin Tensor Strain-

meters (GTSMs) deployed as a part of the Plate Boundary Observatory program. The calibration of these instruments has been the subject of a number of studies comparing the response of its 4 constitutive extensometers to the predicted (theoretical) solid Earth tides [10, 19, 13] and to the seismic strain field inferred from wavefield gradiometry [9]. Each method suffers from imperfect knowledge of the true strain field that could be directly measured using optical fiber strainmeters.

The aim for this study was to develop and evaluate an inexpensive long base horizontal optical fiber strainmeter that is easy to assemble and deploy. Given the large temperature coefficient of the fiber, this instrument is intended for deployment in a trench and has come to be known as the Trench Optical Fiber Strainmeter, or TOFS. Since this was the first deployment of this kind, this report covers findings from our prototype installation.

6.2 Design, Fabrication, and Deployment

This section describes some of the many design choices made during the development of TOFS, the implications of which will drive future development.

6.2.1 Mechanical and Optical Design

The basic concept for TOFS is simply that of an extended borehole strainmeter (extensometer) turned on a side. Rather than a vertical fiber cable anchored at the bottom and secured under tension at the top of a borehole, the TOFS fiber cable is deployed horizontally in a trench and stretched between two end monuments (Figure 6.1). The most significant design difference is that TOFS is an equal-arm interferometer whose reference arm is a spool of fiber contained in a "mandrel box" immediately adjacent to one end monument to take advantage of the matching thermal environment and to permit operation of the strainmeter with an unstabilized light source. The sensing arm contained in the fiber cable exits this box and is secured to one monument by the front termination fixture. At the opposite end, the fiber cable is secured to the other end monument by the rear termination fixture. Each of these elements are discussed in more detail below.

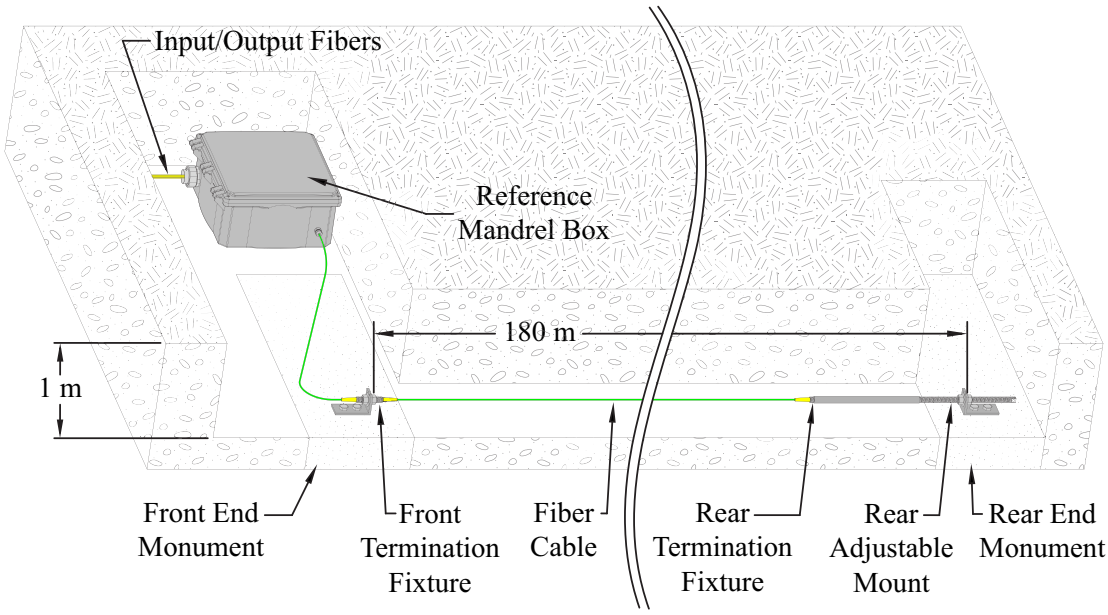


Figure 6.1: Cutaway schematic of a single TOFS showing each of its major components as deployed.

The horizontal strain sensing arm of TOFS is an optical fiber cable containing two redundant optical fibers. This is the same cable used for the auxiliary vertical strainmeter in BOFS consisting of a 1.2 mm diameter, 0.13 mm wall thickness stainless steel tube coated to a diameter 3.8 mm with polyethylene. Recall that this particular cable does not contain water inhibiting gel. In the installation at PFO there are actually two TOFS deployed in the same trench with 90 and 180 m cable lengths, the details of which are discussed in Section 6.2.3.

As their names imply, the front and rear termination fixtures are the end points of the strain sensing portion of the fiber cable. These serve the dual purpose of securing the fiber cable to the end monuments and immobilizing the stainless steel tube and the fibers within. The front termination fixture (Figure 6.2) is a $\sim$8 cm long piece of ANSI 5/8"-11 threaded rod counterbored to hold a strain relief boot at each end, and with a 5 mm diameter through-hole. The fiber cable is separated to expose a short length of optical fiber within the fixture, and the whole interior is filled with a very strong, low-viscosity epoxy.

Figure 6.3a shows the rear termination fixture assembly, which includes the termination fixture itself where the stainless tube and fibers are immobilized with

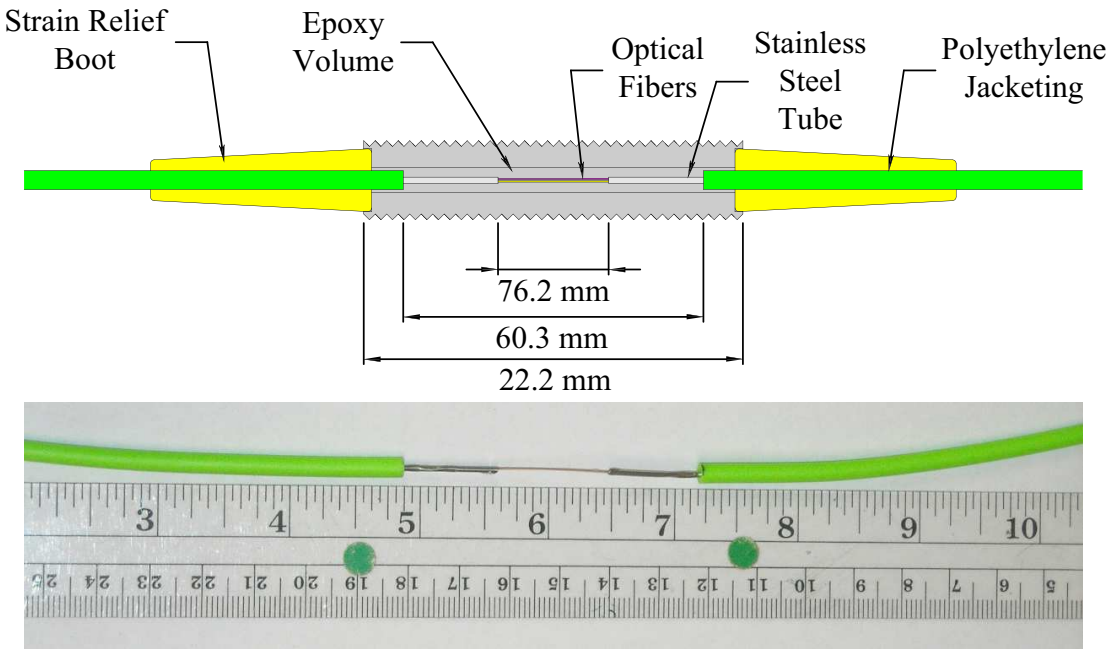


Figure 6.2: Cutaway view of the front termination fixture. The top schematic shows the threaded rod whose center hole forms the epoxy volume used to hold the polyethylene jacket, stainless steel tube, and optical fibers that make up the fiber cable. The bottom photograph shows an actual "window-stripped" fiber cable before being epoxied inside of the threaded rod.

epoxy. This also serves as one cap of a "splice bottle," which is a 19 mm diameter, 3 mm wall stainless steel tube housing. A Faraday mirror is spliced to the end of each optical fiber, and a plastic protection sleeve used to hermetically seal the exposed glass needed to make the splice. Both the Faraday mirrors and splice protectors are epoxied to a 1.6 mm diameter, 20 cm long stainless steel rod that is also epoxied into the rear termination fixture volume (Figure 6.3b). This was done to prevent the fibers from twisting when screwing the splice bottle to the front termination fixture as well as to limit their motion once enclosed. The other end of the splice bottle is capped with a 30 cm length of ANSI 5/8"-11 stainless steel threaded rod, which serves as a length-adjustable mount to the end monument (the reason for this is described later in this section). As with the front fixture, the threads are sealed with epoxy to prevent water from entering the splice bottle.

The aforementioned "mandrel box" is a 37 cm high, 34 cm wide, 18 cm deep polycarbonate box that houses the reference arm of the interferometer and

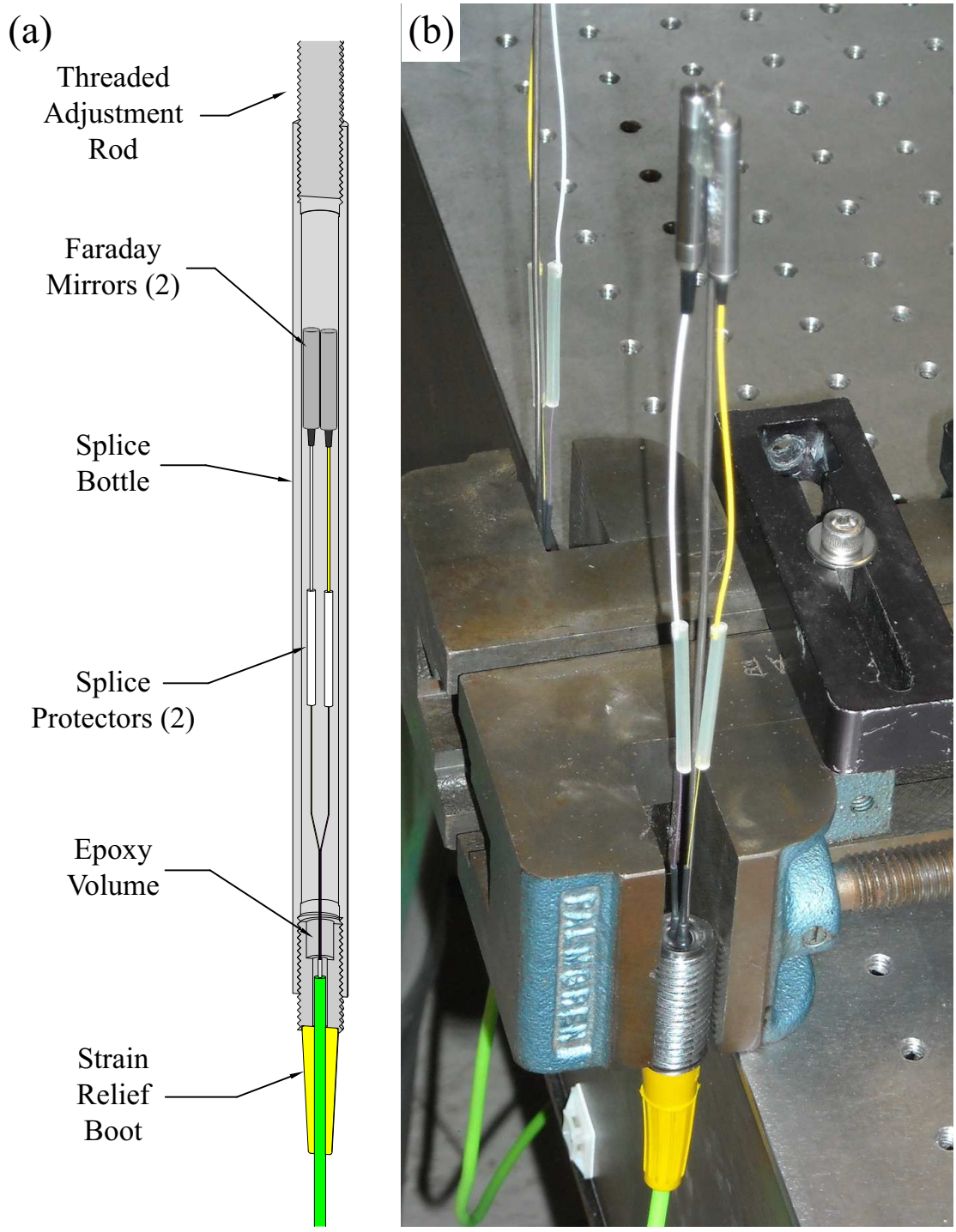


Figure 6.3: Cutaway schematic of the rear termination fixture assembly. (a) Interior of the splice bottle showing the epoxy volume used to secure the incrementally stripped fiber cable, splice protectors, and Faraday mirrors. (b) Picture of the interior of a splice bottle showing the Faraday mirrors attached to the stainless steel rod embedded into the epoxy volume.

also serves as the main connection hub for the strainmeter (Figure 6.4). The majority of the box is taken up by a 206 mm OD, 200 mm ID quartz cylinder that is either 60 or 90 mm high for the 90 or 180 m TOFS, respectively. This is held in place by a mount made of top and bottom trays of VHMW plastic (chosen for its low coefficient of friction), each with an oversized groove ∼0.8 mm deep to prevent lateral escape of the cylinder. The lower mandrel mount stands off from the bottom of the box by about 5 mm. Both the separation of the mandrel mount from the box and the oversized groove are attempts to limit the influence of any differential thermal expansions of the box, mandrel mounts, and ultimately the mandrel itself, since stresses on the mandrel will show up as a strain signal.

While the interferometer itself requires no electronics, a fiber-wrapped piezoelectric cylinder, mandrel thermistor, and heater were added to the mandrel box for this test system. The piezo allows for modulation of the interferometer path length for ellipse filling, if desired, which is useful for setting photodetector gains as well as preventing ellipse-parameter estimation errors during extended quiet periods (see Section 1.3.1). A thermistor (YSI 44008) is epoxied to an unwrapped portion of each mandrel to examine the potential usefulness of a mandrel-temperature correction. Each mandrel box also includes a 2 kOhm power resistor (not shown in Figure 6.4), generating about 0.45 W of heat in an attempt to stratify the air and limit thermal convection.

One concern with this prototype installation is the fiber cable between the mandrel box and the front termination fixture that is required to interrogate the sensing arm of the interferometer. This short-lengthed (∼1 m) "leader" cable is a part of the interferometer but not a part of strain measurement. The purpose for separating the mandrel box from the front termination fixture was to better match the thermal environment of the reference mandrel to that of the fiber cable. The mandrel box is buried so that the fiber spool is at the same depth as the fiber cable, and is positioned sufficiently far from the concrete end monument to limit the influence of its thermal mass (given its different properties from the surrounding material).

The optical design for TOFS is that of the basic polarization insensitive,

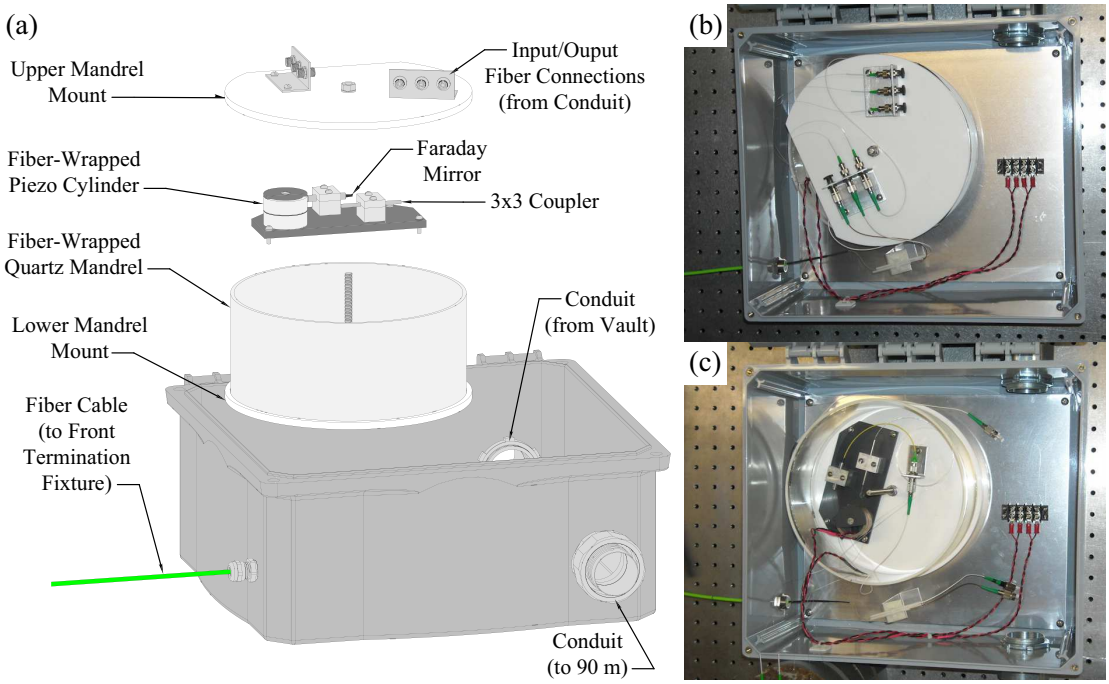


Figure 6.4: Partially exploded view of the 180 m TOFS mandrel box. (a) Diagram showing the major subcomponents of a mandrel box. (b) Top view of the 180 m mandrel box with the upper mandrel mount in place and all the internal optical connections made. (c) Same view as (b) but with the upper mandrel mount off to reveal the fiber-wrapped piezo and interferometer optical components.

equal-arm Michelson interferometer described in Chapter 1. Figure 6.5 shows the optical layout used for both TOFSs. The basic system is an equal arm interferometer illuminated by an inexpensive diode laser. For this to function well it was essential to get the optical path lengths as closely matched as possible. This is not only to assure that the path-length difference was within the coherence length of the laser, but also to limit any apparent strain signal caused by laser wavelength drift. For this, the rear termination fixture is equipped with a length of threaded rod so that the physical length of the fiber cable can be adjusted by about ± 15 cm. The last notable optical design feature is that the one of the two redundant fibers within the fiber cable terminates in a 1310 nm Faraday mirror, while the other fiber ends in a 1550 nm Faraday mirror. Therefore, the overall strainmeter can be operated at either wavelength by switching fibers and swapping in the matching Faraday mirror inside of the mandrel box (Figure 6.4a).

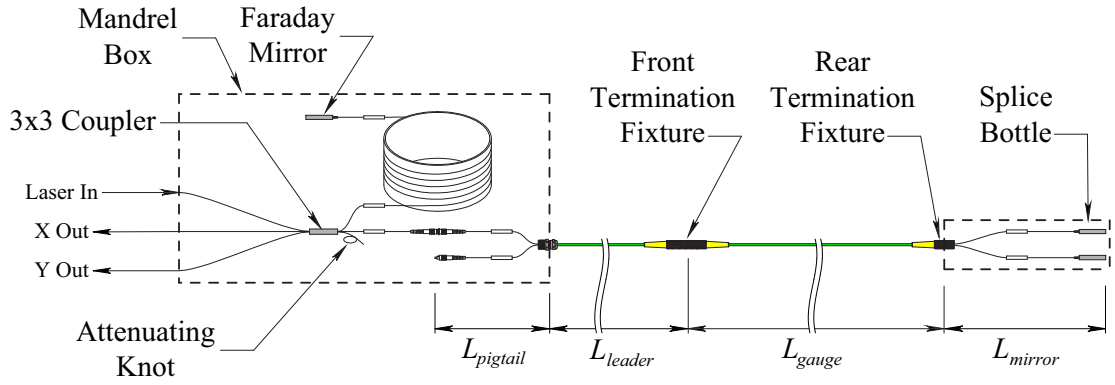


Figure 6.5: Mechano-optical design for TOFS showing the tensioned fiber cable length L_{gauge} along with the various untensioned lengths that make up the strain sensing arm of the interferometer.

6.2.2 Fabrication

The design of TOFS was intended to be simple as possible to make it easy to assemble and deploy, however, there are several aspects of its fabrication that are worth noting. Recall that the optical path length difference between the reference and sensing arms of the interferometer must be as close to zero as possible to minimize any apparent strain signals from wavelength variations in the laser. To this end, consider that the optical path length of the untensioned fiber cable is:

$$L_{opt} = nL_{gauge} + nL_0,$$

where n is the index of refraction, L_{gauge} is the length of fiber cable to be stretched (i.e., between the front and rear termination fixtures), and L_0 is the sum of the non-tensioned fiber lengths (see Figure 6.5):

$$L_0 = L_{pigtail} + L_{leader} + L_{mirror}.$$

The optical path length of the tensioned fiber cable is:

$$\begin{aligned}\Delta L_{opt} &= L'_{opt} - L_{opt} \\ &= n\Delta L_{gauge} + \Delta n L_{gauge} \\ &= \mu \Delta L_{gauge},\end{aligned}$$

where $\mu \approx 1.16$ is the linear strain-optic coefficient previously derived in Chapter 1. To match the optical length of the tensioned fiber cable, the mandrel must be wrapped with a physical length of fiber corresponding to:

$$\begin{aligned} L_{mandrel} &= \frac{L'_{opt}}{n} \\ &= \frac{\mu}{n}\Delta L_{gauge} + L_{gauge} + L_0 \\ &= \left(1 + \frac{\mu}{n}\epsilon\right) L_{gauge} + L_0, \end{aligned}$$

where $\epsilon = 0.002$ is the initial strain desired for the sensing arm. Therefore, the length of fiber on the mandrel can be computed with knowledge of the monument spacing (given that $L_{monument} = (1 + \epsilon)\, L_{gauge}$), the various lengths of fiber cable assembly (e.g., L_0), and the intended initial strain.

In practice it can be difficult to measure many tens of meters of optical fiber with reasonable accuracy, therefore an electronic distance measurement (EDM) unit was used to arrive at the final length of fiber on the mandrel. The conversion from physical length to EDM length (and its uncertainty) is well known from previous experiments. Combining this with the various lengths described above and their uncertainties led to an estimated EDM length for the reference fiber that was good to several cm. Since it is easier in the field to additionally stretch the sensing cable than to shorten the reference mandrel fiber, the long fiber cable was terminated several cm shorter (and the reference mandrel fiber several cm longer) than the nominal.

Another concern was the interaction between the plastic mandrel mounts and the fiber wrapped quartz cylinder mandrel itself. When assembled, the mandrel is designed to sit under its own weight within the shallow, oversized groove in the lower mandrel mount. The upper mandrel disk is double-nutted so that it can be secured without squeezing the mandrel, and its final position is intended to be just in contact with the top of the quartz cylinder. These features allow for the mandrel to slip against both mandrel mounts with minimal resistance. In fact in some temperature change tests, it was possible to introduce episodes of 3 to 5 minute period "chatter" in the recordings, presumably due to slippage of the mandrel.

Assembly of the termination fixtures required some additional care to make sure that all the components were adequately bonded. After stripping the fiber cables and properly positioning them within the termination fixtures, a high strength, low viscosity epoxy was injected into the fixture volume. This was done with the fixtures in a vertical position so that any bubbles air would escape from the top. In the case of the front termination fixtures, the second strain relief boot was epoxied into place after the main fixture had cured. It is essential to note that each exposed end of the stainless fiber cable tubing was sealed with a fast-curing, high-viscosity epoxy to prevent the intrusion of the low-viscosity epoxy into the interior of the tubing.

6.2.3 Deployment

Both TOFSs were deployed in a 1 m deep, 0.5 m wide trench parallel to the NWSE LSM (Figure 4.3) during July of 2012. The choice of the trench depth was governed in part by the knowledge that deeper burial implied greater insulation from surface temperature fluctuations. For example, a 1 cycle per day temperature change at the surface is attenuated by a factor of 25 at 1 m depth for the native material at PFO (this is a result of the so-called "wine cellar problem" [21]). In reality, the final depth was largely determined by the earth and the limitations of the heavy equipment used to excavate the trench.

The trench is located approximately 20 m west of the NWSE LSM and spans about the second quarter of its length. This is roughly 185 m southwest of the GTSM deployed in borehole B084. Four 1.5 m long, 0.3 m wide, 0.5 m deep concrete end monuments were poured at distances of 0, 10, 100, and 180 m from the northwest end of the trench. Figure 6.6a shows the plan view of the two strainmeters attached to their end monuments, with the 180 m TOFS spanning from the first to farthest (0 and 180 m) end monuments and the 90 m the 10 and 100 m monuments.

The design of the trench was intended to maximize the common mode rejection of thermal variations between the mandrels and fiber cables. Many days of effort went into ensuring that the bottom of the trench was leveled to follow the

surface such that the fiber cables would be at a constant depth and better match the thermal environment of the fiber-wrapped mandrels. In practice this turned out to be problematic since the fiber cables are under tension and would not follow any shorter wavelength topographic variations. Therefore, sifted material had to be added underneath the fiber cables in several places to support the subsequent overburden and suppress any residual movement of the fiber cables through the infilled material.

Figures 6.6b and c show several photographs taken during the strainmeter installation after completion of the trenching and end monuments. The initial installation of the 180 m TOFS failed when the fiber cable came unbonded from the front termination fixture after tensioning. This was due to the epoxy softening as a result of excessive heating of the fixture after being left in the desert sun for several hours (truly an uncomfortable place to work). This fixture was remade along with some additional fiber cable clamps to take some tension off of the fixtures during installation. Ice packs and shades were used the following week to prevent a repeat of this failure.

After anchoring and tensioning both fiber cables, final length adjustments were made using the threaded rod that is a part of each rear termination fixture assembly. Recall that the primary advantage of using an equal-arm interferometer was to minimize apparent strains caused by changes in the laser wavelength. The path imbalance of the interferometer can be estimated by imposing a known wavelength or frequency variation and measuring the resulting optical phase change. In this case, an NP Photonics ROCK fiber laser thermally tuned to 1534.062 nm was modulated with a ± 10 V sinusoidal signal at 1 Hz, which induces a frequency change of roughly ± 150 MHz. Lab tests using progressively imbalanced interferometers whose differential path lengths (ΔL) were determined using an EDM showed that this modulation produces:

$$\frac{\Delta\phi}{\Delta L} = 0.552 \pm 0.002 \text{ radians/m } (0.4\%)$$

where the sign of the optical phase change is negative relative to the input modulation if the length of the fiber on the mandrel is longer than that of the fiber cable, and positive if reversed. Each interferometer was interrogated using this

modulated laser and length adjusted such that the 1 Hz signal was minimized by visually inspecting the bandpass filtered phase record. Note that this is highly unlikely to produce a perfectly balanced interferometer for any time other than that when the adjustment was made given the unusual temperature conditions during the adjustments and inevitable induced strain from reburial. However, this was the best that could be done and it did show that the paths could in fact be balanced (i.e., there were no gross path length errors).

Additional items were added to the trench for improved robustness, temperature measurement, and connectivity. Wire mesh was used to cover portions of the instruments after some partial backfilling to limit damage from the final backfilling and provide rodent protection. A set of four thermistors were added 2, 4, 6, and 8 m from the first end monument and can be seen in Figure 6.6b as a bundle of black cables on the left side of the trench. These can be run individually or in series to provide a means to determine the temperature of a portion of the fiber cable. Figure 6.6a shows that the conduit used to operate the two strainmeters passes through the 180 m mandrel box to the 90 m, the other end of which runs to a junction box (labeled as "CB1" in Figure 2.4) and eventually to the same vault that houses the lasers, detectors, and fringe counting system as BOFS (Chapter 4) and the OFIS (Chapter 2).

After anchoring and tensioning both the 90 and 180 m strainmeters, the trench was backfilled by hand with approximately 0.3 m of sifted material, and a week later fully filled with native material using a backhoe. While both instruments were installed, initially there was only enough equipment to run the 180 m strainmeter. However, the 90 m was able to be brought online in mid-December of 2012.

6.2.4 Calibration

The nominal calibration factor for each TOFS can be readily calculated from the strain-phase relationship in Equation 1.32 derived in Chapter 1:

$$C = \frac{4\pi\mu}{\lambda} L_0.$$

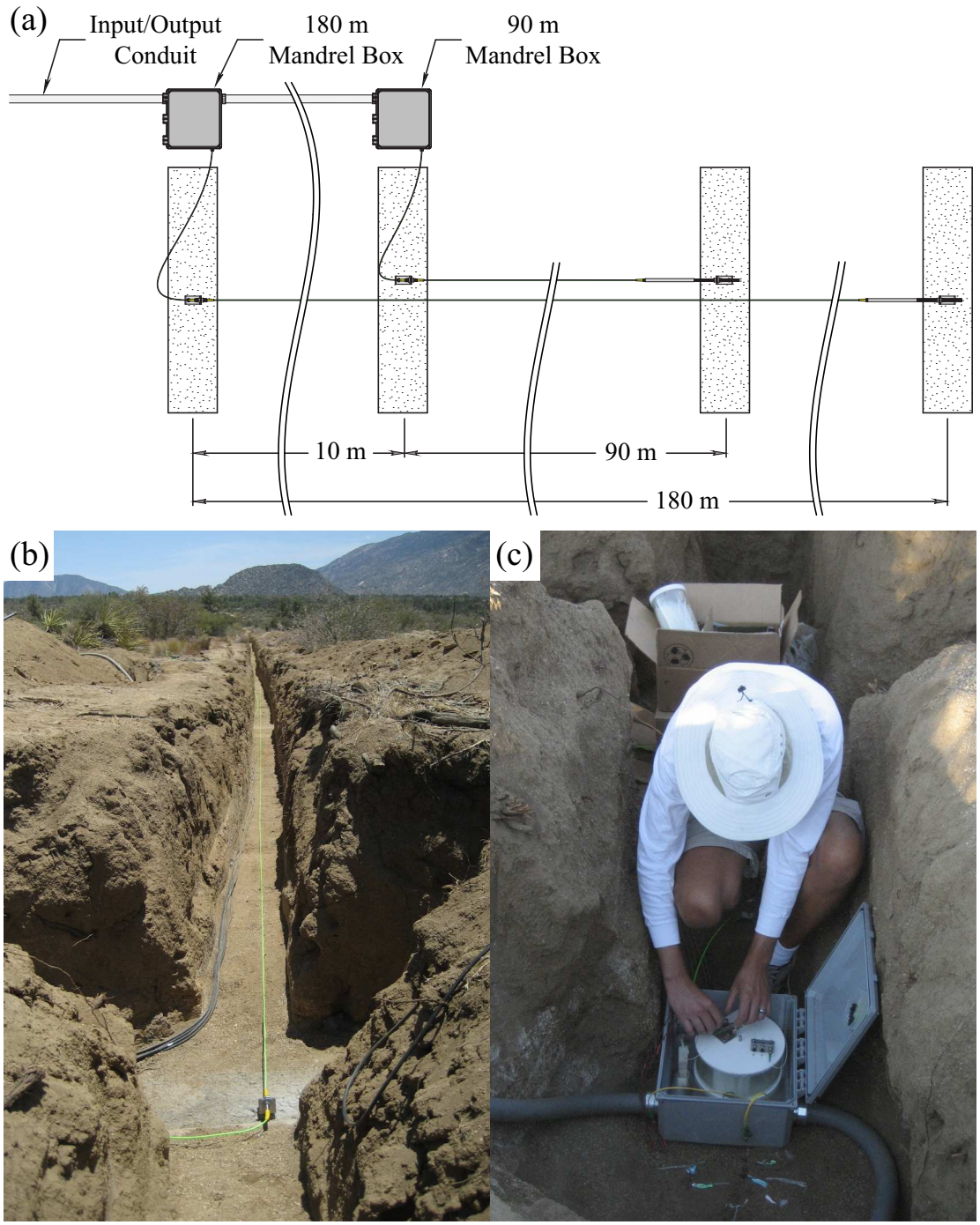


Figure 6.6: Plan view and several pictures of the TOFS deployment. (a) Plan view of both 90 and 180 m TOFS as deployed, showing the four concrete monuments at 0, 10, 100, and 180 m and their connections to the two strainmeters. (b) Along trench photograph during the deployment showing the front termination fixture of the 180 m TOFS. (c) The 180 m reference mandrel box in the trench along side the concrete monument as it is being connected.

Using the previously estimated value of $\mu = 1.158 \pm 0.012$, the nominal calibration factors for the two instruments are:

$$\text{90 m:} \quad L_0 = 89.53 \pm 0.10 \text{ m}$$
$$\lambda = 1307.6 \pm 1.0 \text{ nm}$$
$$C_{90} = 1.004 \pm 0.011 \text{ n}\epsilon\text{/radian (1.1\%)}$$

$$\text{180 m:} \quad L_0 = 179.9 \pm 0.1 \text{ m}$$
$$\lambda = 1553.4 \pm 1.0 \text{ nm}$$
$$C_{180} = 0.5932 \pm 0.0064 \text{ n}\epsilon\text{/radian (1.1\%)}$$

The design of TOFS allows for an in-situ calibration by changing the length of the fiber cable a known amount with the threaded rod while recording the optical phase signal output by the fringe counting system. However, no such measurements were made due to time constraints during deployment.

6.3 Data Analyses

One of the advantages of using equal-arm interferometric strainmeters is that the recorded optical phase signal is simply a scaled version of the ground strain, and does not require removal of a separate laser frequency signal (as done for BOFS in Chapter 5). However, there are data gaps from power outages (that also cause the optical phase to reset to zero) and time intervals when the optical phase determination is incorrect owing to improper ellipse fitting. These artifacts are removed by appropriately offsetting the data and interpolating over the gaps in order to provide a contiguous data record that can be transformed into the frequency domain for filtering and spectrum estimation.

The data from the NWSE LSM comes in several forms. A fully-corrected 5-minute sampled time series has been maintained for decades for the PFO LSMs, which is used for tide-fitting in Section 6.5.1. Raw, 1 Hz quarter-fringe data is available for the surface wave results (Section 6.5.3), and several weeks of high-resolution, 20 Hz sampled data have been acquired on the NWSE LSM using the

"femtometer" fringe counting system (Section 1.3.1) that is used for both TOFS. This 20 Hz data provided the records for computing the high-frequency spectra (Section 6.4.2), wind noise results (Section 6.4.4), and microseismic analysis (Section 6.5.2).

All GTSM data was acquired through the Incorporated Research Institutions for Seismology (IRIS) Data Management Center, which provides automated data requests using the `MATLAB` programming language. Since the GTSM consists of four extensometers, there are a total of four time series that need to be converted into the desired (NWSE) strain component. The first step is to apply a 3×4 "calibration matrix" to compute the ground strains from the extensometer time series. While this matrix is provided by the manufacturer, several others exist in the literature to better account for local anisotropies. The two used in this work are from Roeloffs [19] and Hodgkinson [13]. The final step is to compute the strain along the NWSE ($-45°$) azimuth using a strain rotation equation [1].

6.4 General Observations

The purpose of this section is to present the results of some exploratory data analysis. This includes some qualitative analysis of the general features seen in the time series and power spectra as well as some inter-comparisons between the 90 and 180 m TOFS as well as the nearby NWSE LSM and NWSE component of the GTSM. A more rigorous approach is taken to determine the impact of barometric pressure and temperature on the performance of the instrument for measuring seismic and tidal signals. Quantitative analyses of these geophysical signals are considered in Section 6.5.

6.4.1 Time Series

The 10 month time series plot in Figure 6.7 shows some of the most conspicuous features of the TOFS data compared to the other two NWSE strainmeters at PFO. This plot starts about 5 months after deployment, and several days after the 90 m instrument was brought online in late 2012. While this excludes the initial

settling period, it does encompass nearly one seasonal temperature cycle shown by the trench temperature on the right y-axis.

The most notable feature of the two TOFS records is the magnitude of the drift relative to each other and to the LSM and GTSM. This is not surprising given that TOFS was designed for faithfully recording short-period signals of one-half day and shorter. Despite this, both fiber strainmeters share a similar downward trend as well as some of the longer period excursions. For example, there are 4 or 5 correlated excursions, with periods of roughly two weeks, evident in the first 90 days. While there appears to be a seasonal signal in the temperature record, it is less obvious in the strain record. A more rigorous examination of the temperature response can be found in Section 6.4.3.

Figure 6.8 shows an example of the higher frequency character of the 180 m TOFS compared to the NWSE LSM. This record, high pass filtered with a corner frequency of approximately 5.8 μHz to suppress signals having periods longer than 2 days, is a particularly well-behaved example where the difference between the two instruments is only $\sim$20 nϵ peak-to-peak, or less than half of the tidal amplitude. The 1 CPD contamination shown in the residual time series is often two or three times larger than in this example. However, deeper burial and better end monuments would improve the performance of TOFS for measuring diurnal tides.

6.4.2 Power Spectra

Figure 6.9 shows the power spectra from both the 90 and 180 m TOFS, as well as the NWSE LSM and the NWSE component of the GTSM using the calibration matrix of Hodgkinson [13]. These spectra are Guassian kernel smoothed, Hann-weighted periodograms. Each plot is inset with a closeup of the one and two cycle per day tidal bands and accompanied by a spectrum estimate of the same time series with the best-fit tidal components removed (see Section 6.5.1).

There are several clear differences among the signal levels of the four instruments being compared in Figure 6.9. The signal level near 1 cycle per year ($\sim 1 \times 10^{-7}$ Hz) is approximately 50 dB higher on the TOFS compared to the other two instruments. This along with the 20 dB higher intertidal power levels

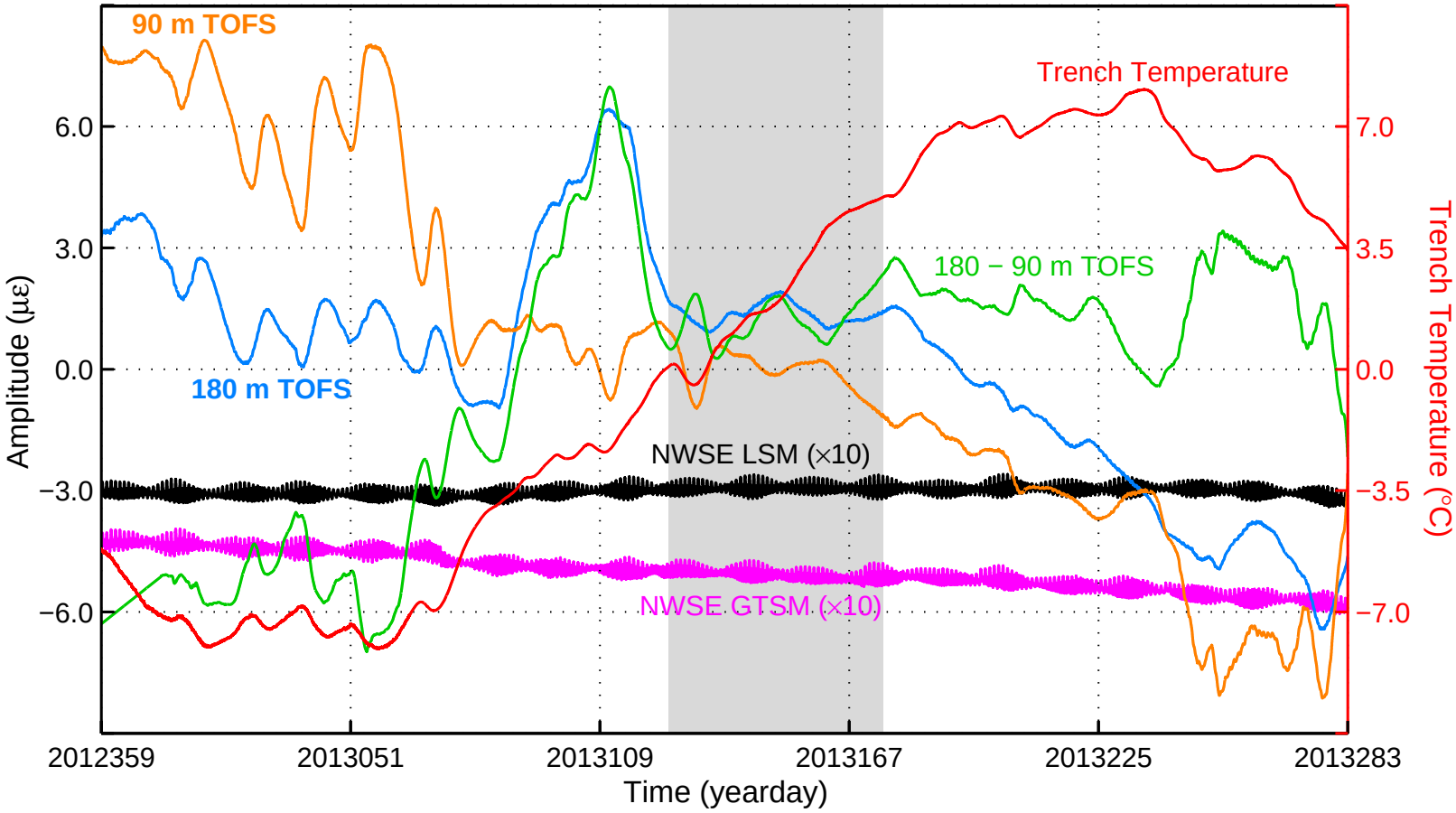


Figure 6.7: 10-month time series plots of some of the signals under consideration in this chapter. Both the 180 m (cyan) and 90 m (brown) TOFS signals are shown along with their difference (green). The NWSE LSM (black) and NWSE GTSM (magenta) have been scaled by a factor of 10. The integrated trench temperature (i.e., the thermistors in series) are also presented for comparison, with scale on the right y-axis. Note that none of the time series has been detrended, but they have been artificially offset for easier viewing.

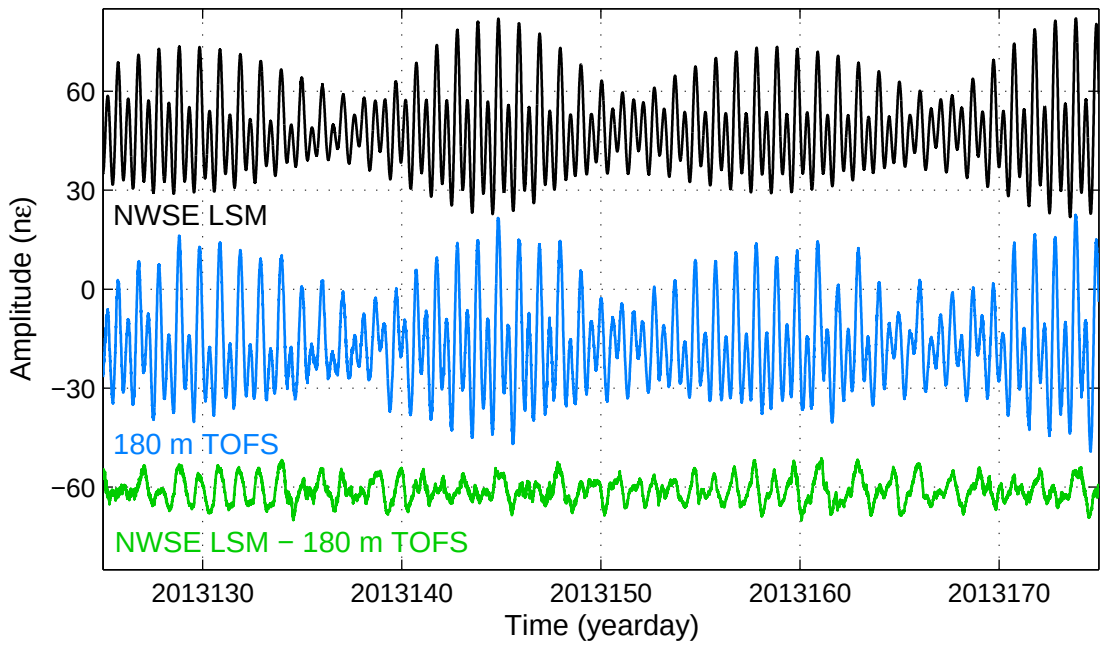


Figure 6.8: A select 50-day time series (from the region highlighted in gray in Figure 6.7) of the 180 m TOFS, after 2-day high pass filtering, along with the NWSE LSM and their difference.

(i.e., the spectra between 1 and 2 CPD) are not surprising given the much larger 1 CPD temperature contamination. However, the M2 tidal line just below 2 CPD ($\sim 2.2 \times 10^{-5}$ Hz) has a signal-to-noise of over 30 dB relative to the detided signal for the length of the data segment used here (290 days).

At higher frequencies, the TOFS and LSM spectra appear to be in agreement. For the GTSM the amplitudes of the microseisms around 0.15 Hz appear to match the TOFS, but flatten with increasing frequency while the others (TOFS and LSM) continue downward in power until the signals roll off due to the anti-aliasing filter applied by the fringe counting system. The GTSM also has some noise at frequencies lower than the microseism peak not found in the other instruments. This noise and spectral flattening in the GTSM spectra have been previously documented and are related to the instrument's power supply and least-count noises, respectively [2].

Figure 6.10 shows a more direct comparison between the NWSE LSM and TOFS, as well as between the two TOFS. There is very good agreement for the

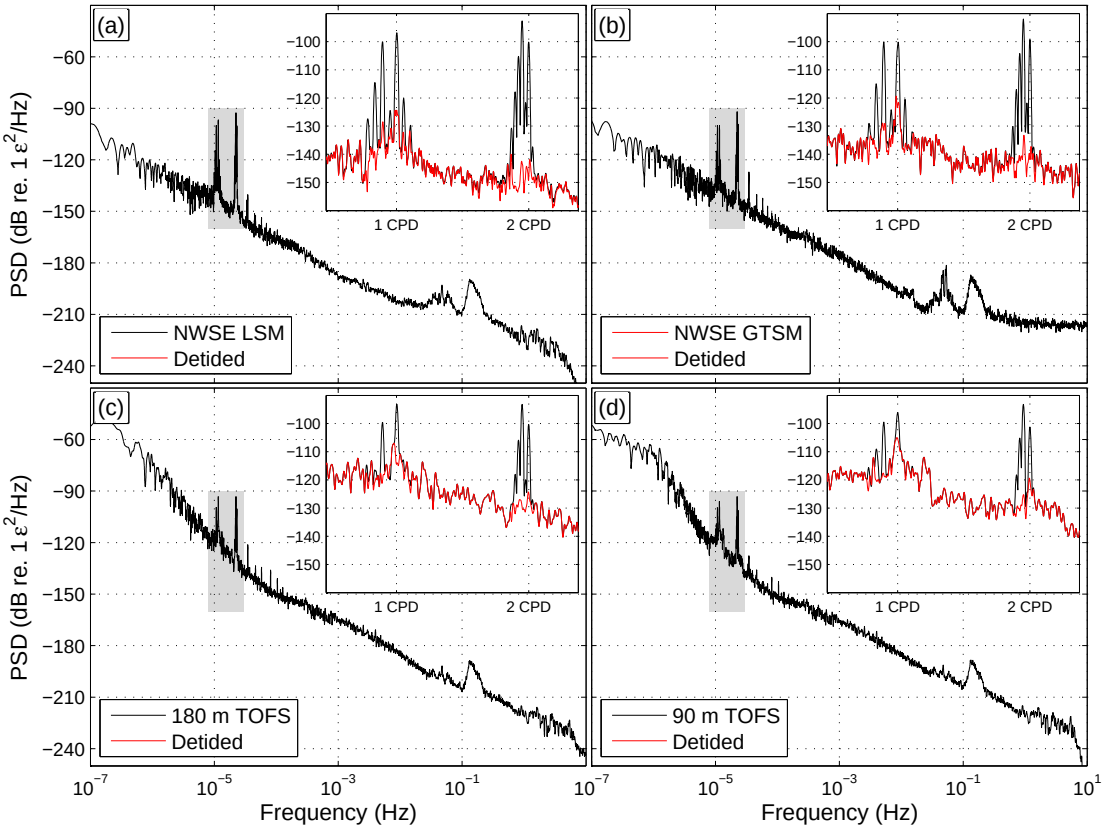


Figure 6.9: Individual spectra from each of the four collocated strainmeters at PFO. (a) NWSE LSM. (b) NWSE GTSM using the calibration matrix from Hodgkinson [13]. (c) 180 m TOFS. (d) 90 m TOFS. The inset plots show the one and two cycle per day tidal regions (highlighted in gray in the main plots) with and without the tides.

microseism band (0.1 to 0.2 Hz) and for several tidal lines at periods just below 2 CPD. The 180 and 90 m spectra almost perfectly overlap, despite their very different long-period behavior in the time domain. The power spectrum from the difference of the 180 and 90 m TOFS time series is one measure of the potential capabilities of these two systems. While the spectral level of the difference is indistinguishable from the instruments themselves below $\sim 10^{-4}$ Hz, it is as much as 15 dB lower until the microseism band. This difference is only about 6 to 10 dB above the NWSE LSM for periods between 25 and 10,000 seconds, implying that the ultimate performance of TOFS nearly matches that of the LSM at seismic frequencies. It is worth pointing out here that these power levels are significantly

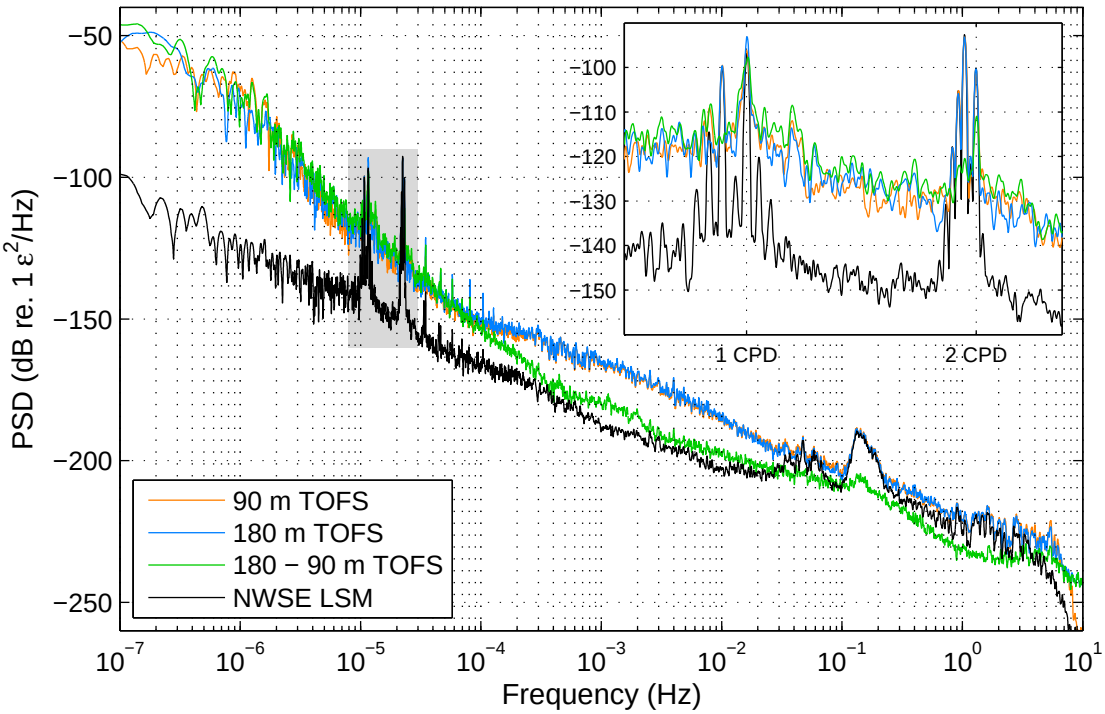


Figure 6.10: Combined spectra from the LSM, both TOFS, and the difference between the two TOFS.

lower than that for BOFS (cast into equivalent units) indicating either that horizontal earth measurements are less noisy or that (for example) open-hole vertical strain measurements, with fibers, are unduly noisy.

6.4.3 Temperature

The trench and mandrel thermistors buried along with the TOFS provide a way to examine some of the tradeoffs of an equal-arm interferometric strainmeter that, despite its 1 m burial depth, is still subjected to surface temperature variations. Key among these is the potential to directly compensate for the relatively large, approximately 12 $\mu\epsilon/°$C temperature coefficient of the optical fiber associated with both the reference mandrel and fiber cable sensing elements. The other is to evaluate the efficacy of burying a reference mandrel at the same depth as the fiber cable, a primary aim in the design. For example, a smaller than expected temperature coefficient would be indicative of common-mode rejection of

temperature between the two interferometer arms. Furthermore, since an optical path length increase in the reference arm of the interferometer yields a negative optical phase change, an anti-correlated temperature signal would suggest that the magnitude of the effect is larger on the reference mandrel.

We first consider the mandrel thermistor record. Its sensor is glued directly to the cylinder which supports the fiber for the reference arm. Unfortunately, there is only one data window of sufficient quality due to problems with the electronics used to measure the thermistor resistance. These data are only for the 180 m TOFS and span approximately 110 days starting on 2012210 and running to 2012320. It is essential to note that the best-fit Earth tides have been removed from the strain record (see Section 6.5.1) in these analyses.

Preliminary estimation of a strain-mandrel temperature scale factor was performed using a linear least-squares technique, consisting of time shifting a given temperature time series segment and fitting it to an equal length interval of detided strain data. Since 1 and 2 CPD are the dominant periods in each record, this method is heavily biased towards minimizing the energy between the two records at these frequencies. This technique was found to be problematic since the best-fit scaling computed over one time period appeared to either over or under correct the data when applied to a different time period. An examination of the time dependence is shown in Figure 6.11, where the strain-mandrel temperature coefficient for the 180 m TOFS is estimated using a 7-day sliding window over the 110 day period. Restricting the analysis to only the fits exceeding an r^2 of 0.8, the mean value is 1.9 ± 1.2 $\mu\epsilon/^{\circ}$C. This large uncertainty is reasonable based on the temporal variation seen in Figure 6.11 since the estimate varies considerably.

A more sophisticated frequency domain approach is presented in Figure 6.12. This technique uses the adaptive sine multitaper approach of Riedel and Sidorenko [17, 18], which averages the spectra using a series of variable bandwidth tapers to reduce variance and maintain frequency resolution. The entire mandrel thermistor and detided 180 m TOFS strain records were used (at 5-minute sampling) to obtain maximal frequency resolution, and the sign of the temperature data was again flipped to yield phase estimates close to 0°. The resultant empiri-

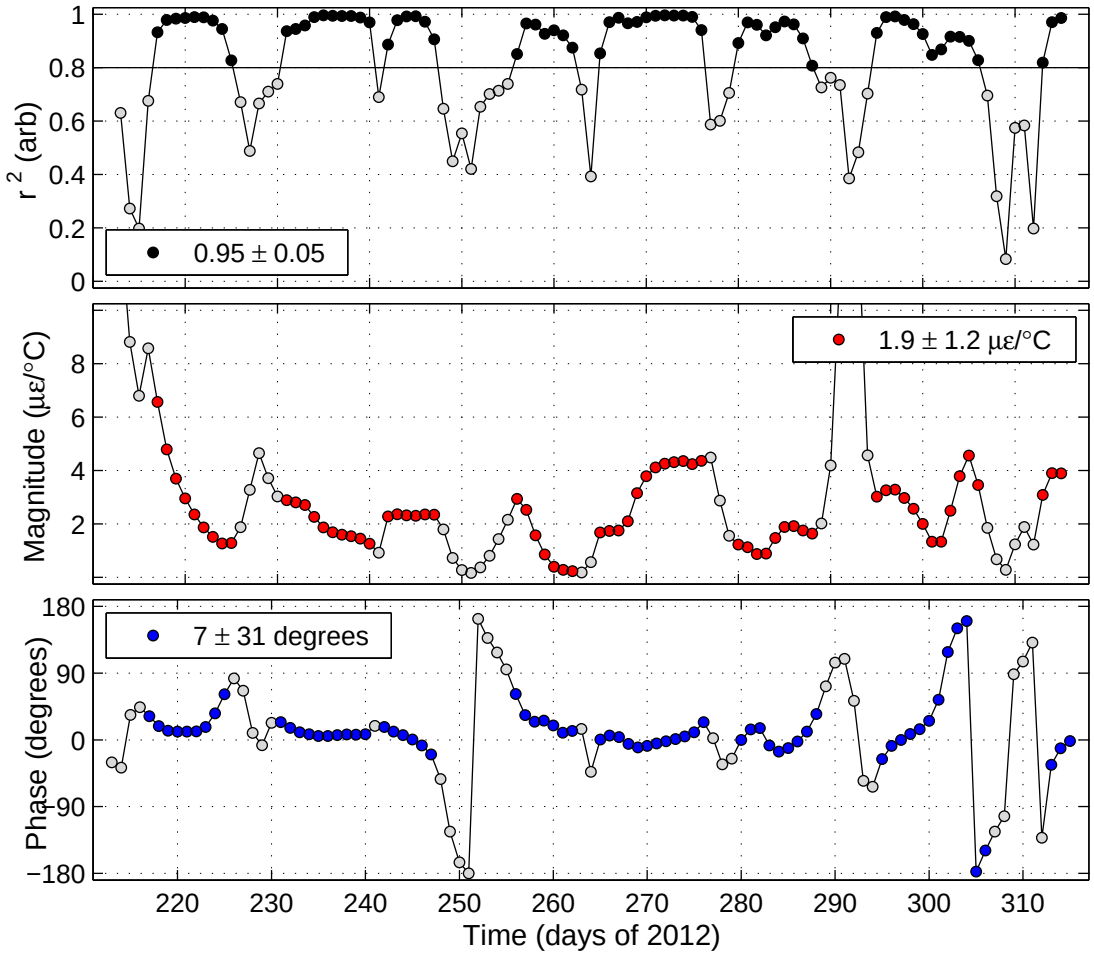


Figure 6.11: Strain-mandrel temperature calibration factor as a function of time for the 180 m TOFS estimated by least-squares using a 7-day sliding window. The middle plot shows the value of the coefficient in $\mu\epsilon/°\text{C}$, and the top and bottom plots show the coefficient of determination (r^2) and phase between the two signals, respectively. Note that the colored plot markers are data where $r^2 \geq 0.8$.

cal transfer function estimates (ETFEs) show that the coherence values are above 0.9 at 1 and 2 CPD, however, the magnitudes are quite different from each other at roughly 15 and 40 $\mu\epsilon/°\text{C}$, respectively, and this yields an inconclusive result.

This same time and frequency domain analysis was applied to the trench temperature data. This record spans nearly 300 days of data and coincides with the operation of both the 90 and 180 m TOFS. Unfortunately, the resulting strain-trench ETFEs are even more perplexing than for the mandrel. The sliding time

window analyses reveal month long periods of correlation and anti-correlation and as much as a factor of 4 variability even using 60-day windows. The right trio of plots in Figure 6.12 show the multitaper cross spectra for the 90 m instrument, where low coherence and poor phase stability make the magnitude estimates untrustworthy. Detailed inspection of the data shows that this analysis is complicated by temporal evolution of the scaling factors, even to the extent that the sign changes over different segments of the data.

6.4.4 Wind Noise and Barometric Pressure

Comparisons between the TOFS time series and environmental observables suggested that there is a relationship between the signal power and the wind velocity. While wind has been identified as a source of strain noise as early as Benioff, 1959 [3], the effect is usually assumed to be negligible compared to other noise sources. However, it is expected for these prototype instruments since both mandrel boxes contain a large concentration of pressure-sensitive optical fibers (approximately -4.2 pϵ/Pa at infrared wavelengths [12]) that are coupled to the atmosphere, a concession made in the development of the prototype system. The conduit pathway to the surface not only admits barometric pressure changes from atmospheric tides, but also stagnation pressure fluctuations from wind blowing against the above ground conduit junction box.

While the understanding of these effects for these early TOFS installations may not be applicable in later implemenations, establishing the background wind noise levels based on the LSM is useful. Both TOFS and NWSE LSM records were examined for the influence of wind velocity with the aid of an ultrasonic anemometer that is a part of a Vaisala WXT-510 meteorological station located approximately 200 m west of the fiber strainmeters. The RMS signal-power levels were computed for a very large number of 60-second, non-overlapping windows for each strain record and sorted into 1 m/s mean wind speed bins. This data spanned the 444 day period from 2012210 to 2013287 for the 180 m TOFS and NWSE LSM, and the 297 day period starting on 2012356.

Figure 6.13 shows the median and 5/95 percent confidence intervals of the

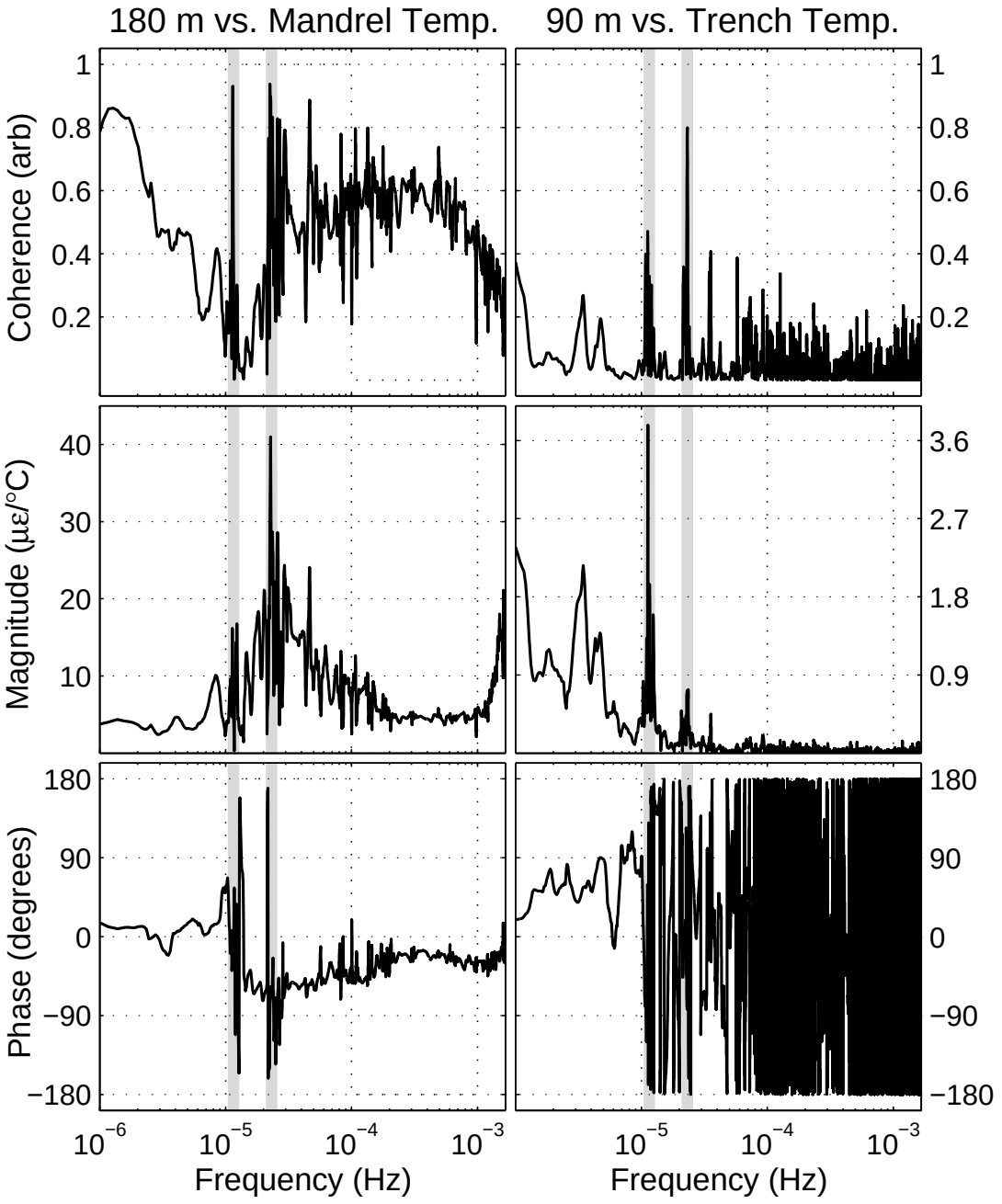


Figure 6.12: Two adaptive sine multitaper empirical strain-temperature transfer function estimates (ETFE) used to investigate the potential use of the two thermistor records for removing temperature noise from the strain signals. The two examples plotted are for the 180 m TOFS strain-mandrel (left) and 90 m TOFS strain-trench (right) ETFEs. The three plots for each instrument are the magnitude-squared coherence (top), magnitude in units of $\mu\epsilon/^{\circ}$C (center), and phase (bottom). The vertical gray bars in each plot indicate 1 (left) and 2 (right) CPD periods.

RMS power for each 1 m/s wind speed bin, along with the best-fit trend. This fit was performed in dB and each mean-squared power was weighted inversely by the variance the RMS values within a given wind speed bin. The results show that wind noise is approximately 3 times more significant in TOFS than the LSM, despite the former being buried 1 m below the surface. There is also a slight directional dependence of this effect not present in the NWSE LSM that does not coincide with the azimuth of the strainmeter nor the prevailing wind direction (roughly northeast to southwest).

The pressure sensitivity of the TOFS reference mandrels and their coupling to the atmosphere can also be observed in the barometric pressure record. To this end, adaptive multitaper ETFEs were computed between each TOFS and corresponding barometric pressure record for the 269-day period spanning 2012360 to 2013263. While the $\pm$10 Pa resolution of the barometric pressure sensor on the Vaisala WXT-510 was found to be insufficient at higher frequencies (<2 CPD), a high resolution record ($\pm$0.1 Pa) was obtained from a nearby Paroscientific 6000-16B microbarograph from the Global Seismographic Network station located at PFO. The strain records were detided and decimated to match the 1 Hz sampling of the barometer.

The ETFEs for both the 90 and 180 m TOFS are shown in Figure 6.14, which are the result of averaging 22 adaptive multitaper estimates taken from 12-day non-overlapping windows. As with the temperature analysis, the sign of the barometer time series was reversed to obtain a phase near zero. The resulting coherence only approaches, at best, $\sim$0.8 over the 10^{-4} to 10^{-3} frequency band with an amplitude ranging from 60 to 65 pϵ per Pascal. Low coherence ($\sim$0.2) at 1 and 2 CPD indicates that the response to atmospheric tides is less significant than what is most likely correlated wind noise between the strain and barometer records in the aforementioned high-coherence frequency band.

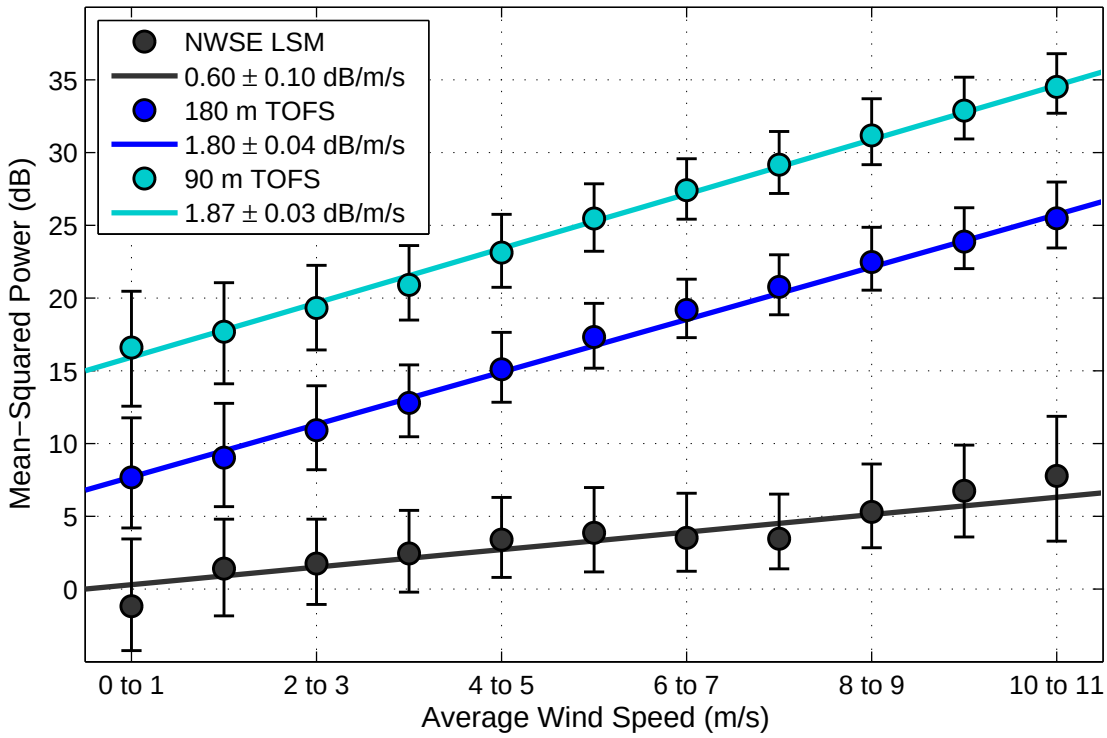


Figure 6.13: Mean strain power versus wind speed for both fiber strainmeters and the NWSE LSM. The data points and error bars correspond to the median and 5th and 95th percentiles of the collection of RMS values found in each wind speed bin.

6.5 Geophysical Signals

There are a number of naturally occurring phenomena that can be used to compare the performance of the horizontal fiber strainmeters to the other strainmeters at PFO. The signals considered in this section are the solid Earth tides, microseisms generated by ocean waves, and surface waves from teleseismic earthquakes. This section concludes with an example of the ability of TOFS to record coseismic offsets from a nearby earthquake.

6.5.1 Earth Tides

Solid Earth tides are an excellent calibration signal for comparing TOFS to the laser strainmeter because its constituent periods are very well known. While

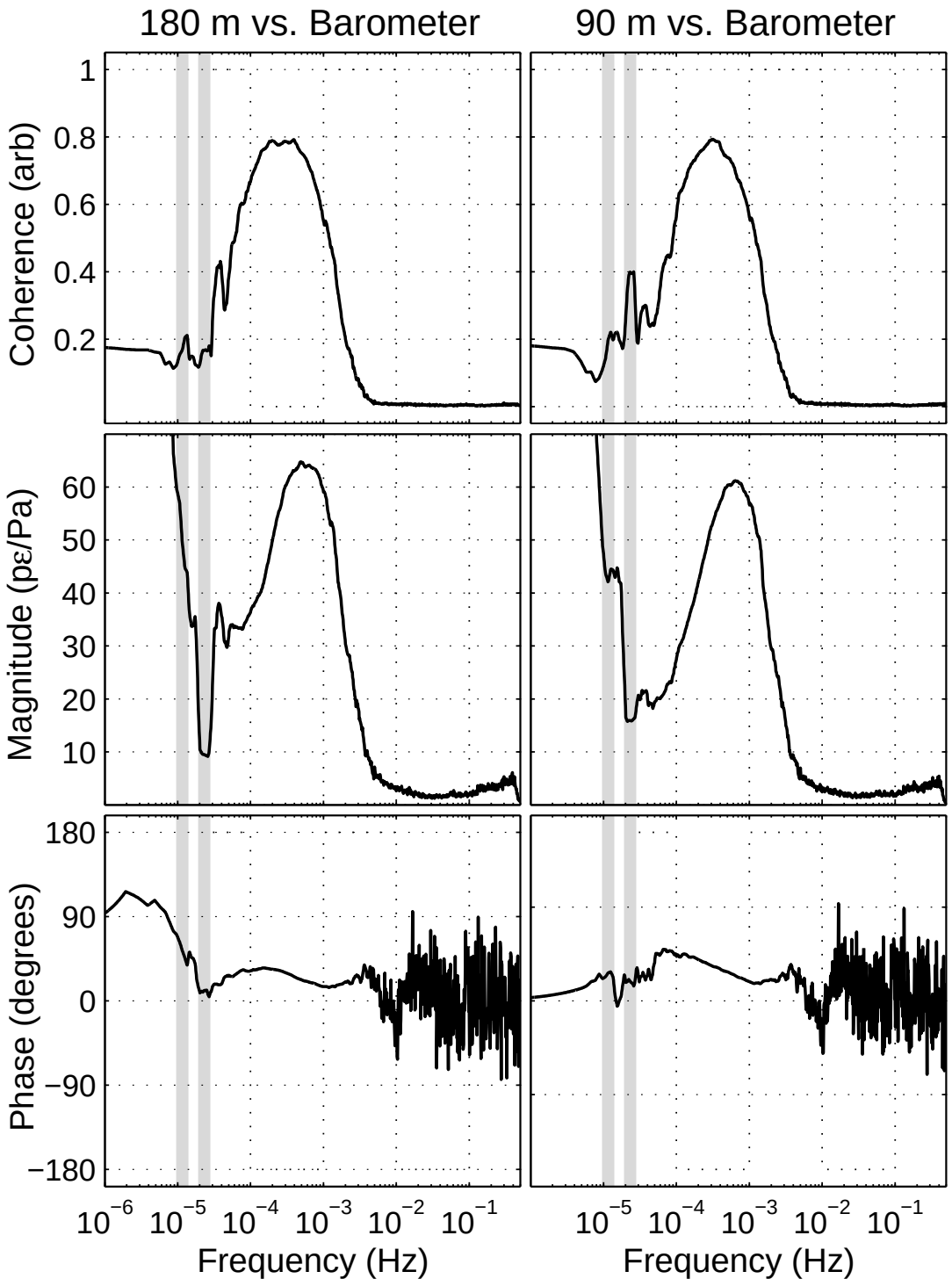


Figure 6.14: Strain-pressure empirical transfer function estimates using an adaptive sine multitaper method used for investigating the influence of barometric pressure changes on the strain record. These two examples follow the same format as Figure 6.12.

TOFS was not designed for long periods, it was intended to be able to resolve the principle lunar semidiurnal tide, denoted symbolically as "M2." Since it has a period of 12.42 hours, it is sufficiently far enough away in frequency from other semidiurnal signals with an average period of 12 hours (e.g., temperature).

Since the period of each tidal component is known, a linear least-squares can be used to extract the amplitude and phase for each frequency. A common approach is to model the tidal time series $x(t)$ as [15]:

$$x(t) = b_0 + b_1 t + \sum_{k=1}^{N} A_k \cos(2\pi f_k t) + B_k \sin(2\pi f_k t),$$

where b_0 and b_1 represent the offset and drift, respectively, and A_k and B_k are the "in-phase" and "quadrature" terms for the k^{th} tidal constituent at a frequency of f_k. The amplitudes and phases for each frequency are calculated using the well-known relationships:

$$M_k = \sqrt{A_k^2 + B_k^2}$$
$$P_k = \arctan\left(\frac{B_k}{A_k}\right).$$

Simply fitting tidal sinusoids to the raw time series data proved to be ineffective for estimating M2 given the large 1 CPD temperature contamination and the other large excursions prevalent in Figure 6.7. An example of the residual when fitting to the unfiltered TOFS data is shown in Figure 6.15. The top plot shows that the best-fit tidal record to the unfiltered data is very different in both amplitude and frequency content compared to the fit to a highpass filtered version of the data. This has a clear effect on detided time series shown in Figure 6.15b.

Fitting the highpass filtered data required some additional care to ensure the best possible results. A fit can be performed on data with gaps of various lengths at any time by simply excluding the times at which they occur. However, such data gaps must then be filled with interpolated data to easily filter the time series. Large offsets must also be avoided to limit data loss from filter "ring." The filter used in this analysis is a 3^{rd}-order Butterworth with a low cutoff frequency of 5.8×10^{-6} Hz, or 0.5 cycles per day. (This filter attenuates the amplitude of M2 by only about 2 parts-per-thousand and introduces a phase shift of about $-0.05°$.)

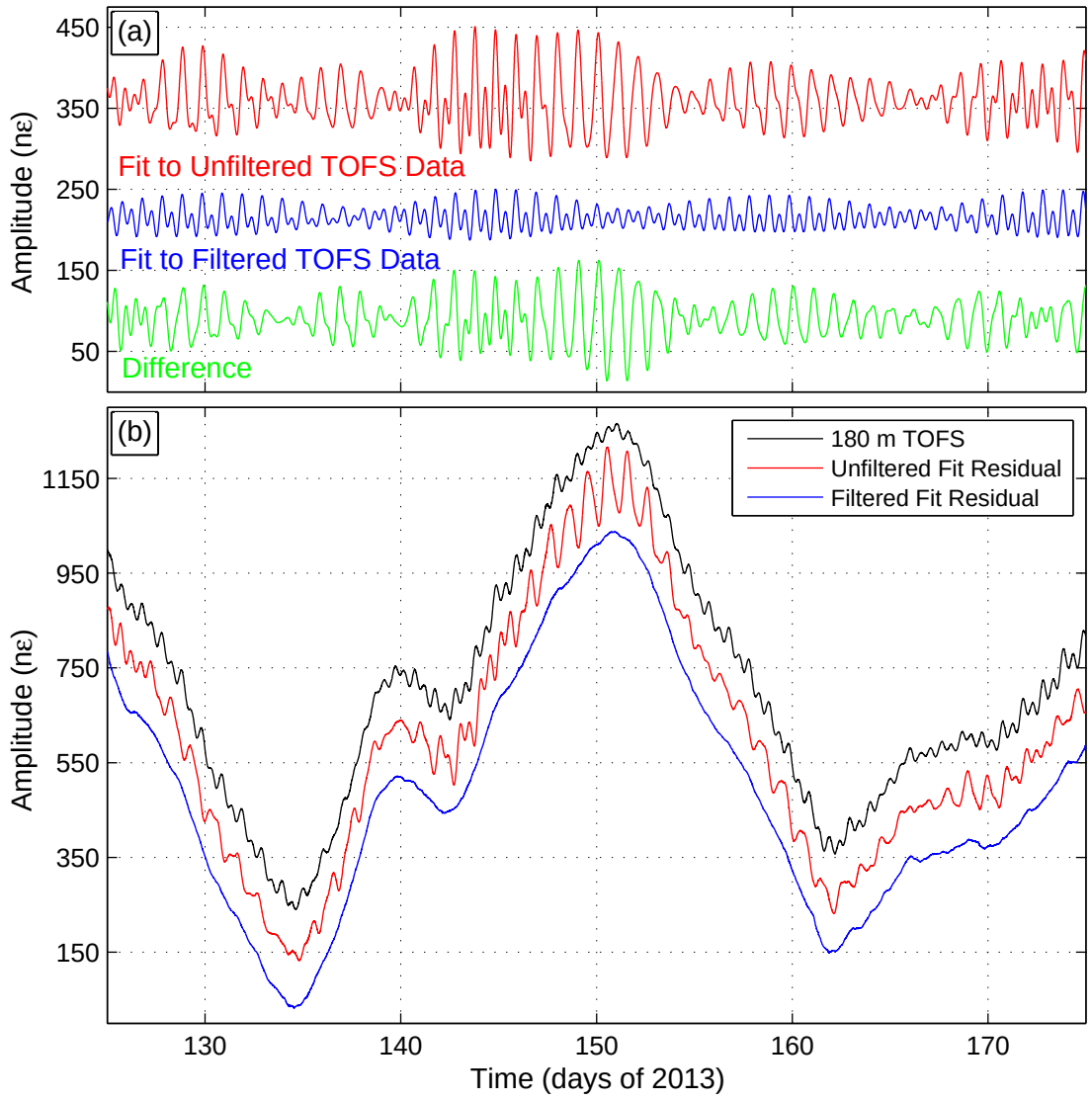


Figure 6.15: Tidal fits to filtered and unfiltered TOFS data. (a) Best-fit results using the unfiltered data (red) and 2-day highpass filtered data (blue), and their residual (green). (b) Original and detided time series using the fit results from (a).

Tidal fits were performed on both TOFS and NWSE LSM signals. Each gap-corrected, 5-minute sampled, 2-day highpass filtered time series spanned the 297-day interval from 2012356 to 2013287. The results for the M2 tidal constituent are shown in Table 6.1, where the phases are relative to the predicted tide-generating potential. Comparing the M2 phase response of the fiber strain-

meters to the LSM shows differences of:

$$180 \text{ m:} \quad +0.70^\circ \pm 0.17^\circ$$

$$90 \text{ m:} \quad -0.28^\circ \pm 0.27^\circ,$$

which are in accord (within 1%). However, there is a statistically significant and unexpected difference in the amplitudes. This is best illustrated in the lower part of Table 6.1 that shows the amplitude ratios and propagated uncertainties.

Table 6.1: Least-squares fit results for the M2 tidal constituent (top), and amplitude ratios (bottom).

Instrument	M2 Amplitude (nϵ)	Phase (°)
NWSE LSM	13.0254 ± 0.0044	41.345 ± 0.019
180 m TOFS	13.256 ± 0.040	42.04 ± 0.17
90 m TOFS	13.609 ± 0.065	41.06 ± 0.27

Ratio	Amplitude Ratio (nϵ/nϵ)
180 m / LSM	1.0177 ± 0.0031
90 m / LSM	1.0448 ± 0.0050
90 m / 180	1.0266 ± 0.0058

6.5.2 Microseisms

Microseisms caused by distant ocean waves are another persistent signal that can be used to compare the two fiber strainmeters to each other and to the LSM. The energy propagates as Rayleigh waves, traveling at speeds around 3 km/s, which for periods of roughly 6 seconds yields wavelengths of 20 km, much longer than the scale of the strainmeters. Their amplitudes are typically several orders of magnitude smaller than the tides ($\sim$0.1 nϵ peak-to-peak). Microseismic signals are usually too small to be resolved by the native fringe counting system employed

by the LSM (0.1803 nϵ per least-count). However, several weeks of NWSE LSM data were collected with the much higher resolution, 20 Hz system used by the fiber strainmeters.

Since the frequency of interest lies roughly between 0.1 and 0.2 Hz, even a short record can provide sufficient data for analysis. In this case, the record spans roughly 26 days from 2013261 through 2013287. The data were split into 409.6 second (8192 samples), non-overlapping windows that were detrended and processed using the same adaptive sine multitaper cross-spectrum estimator used in Sections 6.4.3 and 6.4.4. This resulted in over 5,500 cross spectra, which is sufficient to compute the cumulative distribution functions (CDFs) of each stack of coherence, magnitude, and phase estimates as a function of frequency, and is shown in Figure 6.16.

As expected, the coherence is a maximum in the frequency range of the microseisms and drops off to either side, and the median phase estimates hover near 0°. The cause for the set of frequency spikes in the LSM data at integer multiples of approximately 1 Hz is unknown (perhaps the recording system), but fortunately is outside of the band of interest.

The medians of each magnitude estimate in the microseism band shows a systematic amplitude difference between TOFS and the LSM similar to that found in the tidal analysis. However, the 5/95th percent confidence intervals encompass an amplitude ratio range from 0.8 to 1.2, suggesting that this difference is not significant given the variability in the data. Therefore, the bootstrap resampling method [8] is employed to estimate the variability in the median in an attempt to better constrain the differences in the amplitude ratios.

Figure 6.17 focuses on the cross spectra results from 0.1 to 0.23 Hz, highlighting the data where the coherence exceeds 0.9. The median coherence, magnitude, and phase where the coherence is a maximum is highlighted in green at a frequency of $\sim$0.15 Hz. The median is also shown by the solid blue horizontal line along with its 5/95th percent bootstrapped confidence intervals shown by the blue dashed lines. These quantities are represented numerically in the legend for each figure, as well as in Table 6.2. Despite the very small amplitudes of these

signals and the very high demands on the (linearity of) the ellipse fitting and fringe counting system, these results are in very good accord with the tidal findings.

Table 6.2: Medians and confidence intervals for the amplitude ratios of the strainmeters, where the coherence is a maximum in the microseismic band.

Ratio	Amplitude Ratio (nϵ/nϵ)
180 m / LSM	1.023 (1.021 1.026)
90 m / LSM	1.051 (1.048 1.055)
90 m / 180	1.015 (1.014 1.017)

6.5.3 Surface Waves

Teleseismic earthquakes can produce surface waves of varying amplitudes depending upon their magnitude and distance to the receiver, thereby providing a very useful signal for comparing instruments over a wide dynamic range. This section presents the results of the intercomparison between the 90 m TOFS, 180 m TOFS, and NWSE LSM for a collection of nearly 70 surface wave producing earthquakes. These events are also used to investigate the potential for using horizontal fiber strainmeters as a way to calibrate the GTSMs.

69 earthquakes were chosen by visually inspecting the time series filtered between 10 and 100 seconds and selecting events that produced surface wave amplitudes greater than 2 nϵ peak-to-peak (this turns out to be approximately 18 to 20 LSM least-counts for its native logger). The duration of each earthquake was also determined manually based on when the signal amplitude appeared to be indistinguishable from the background noise. Each selected event was matched to its earthquake source by comparing the travel times from a catalog of all events greater than a magnitude 5 to their arrivals at PFO. While this matching was automated, it was easy to verify each event by hand. (A complete table of events is provided in Appendix B.)

Each record segment was detrended and bandpassed between 0.01 and 0.10

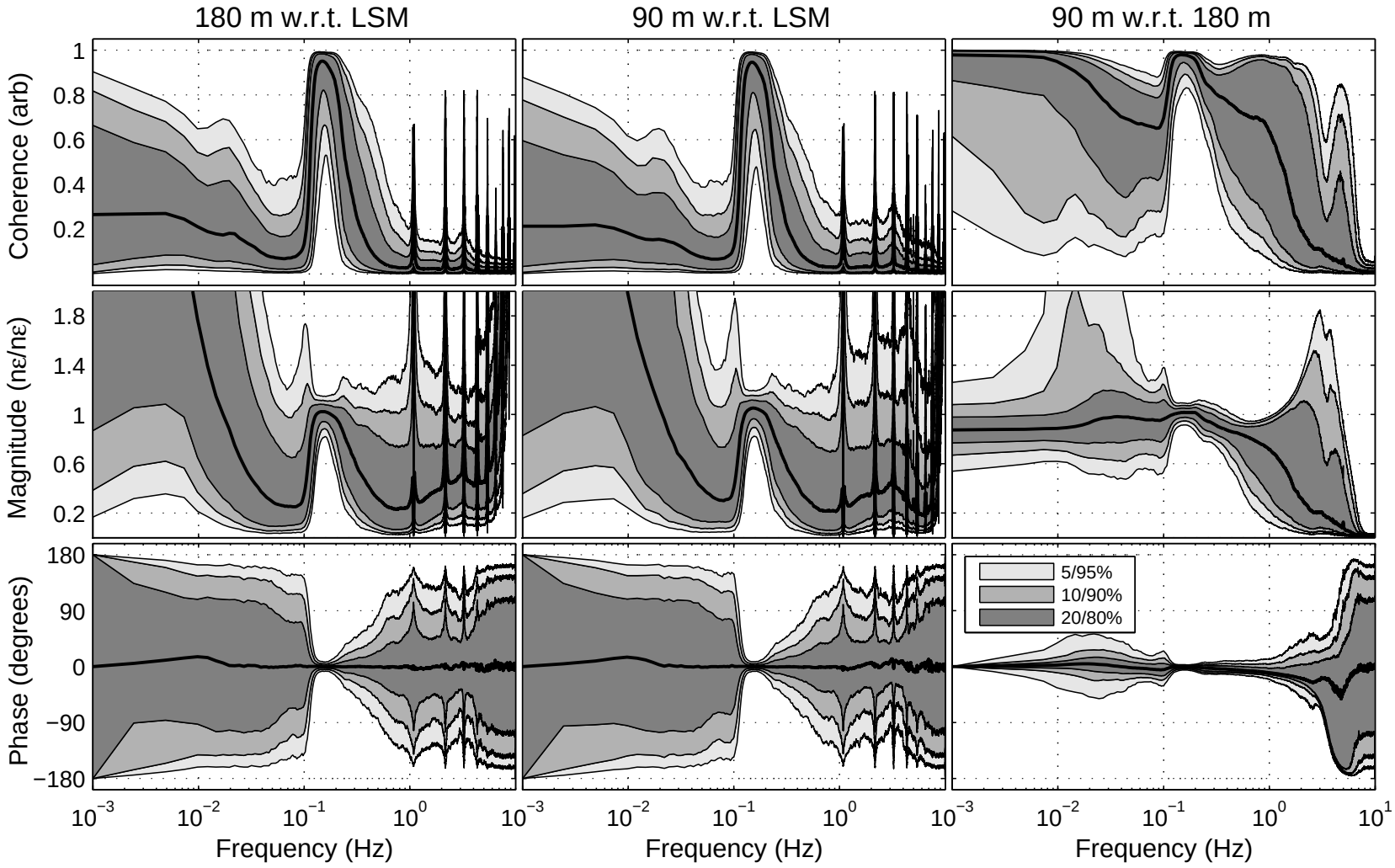


Figure 6.16: Strain-strain empirical transfer function estimates using the adaptive sine multitaper method used to investigate the behavior of TOFS with respect to the NWSE LSM.

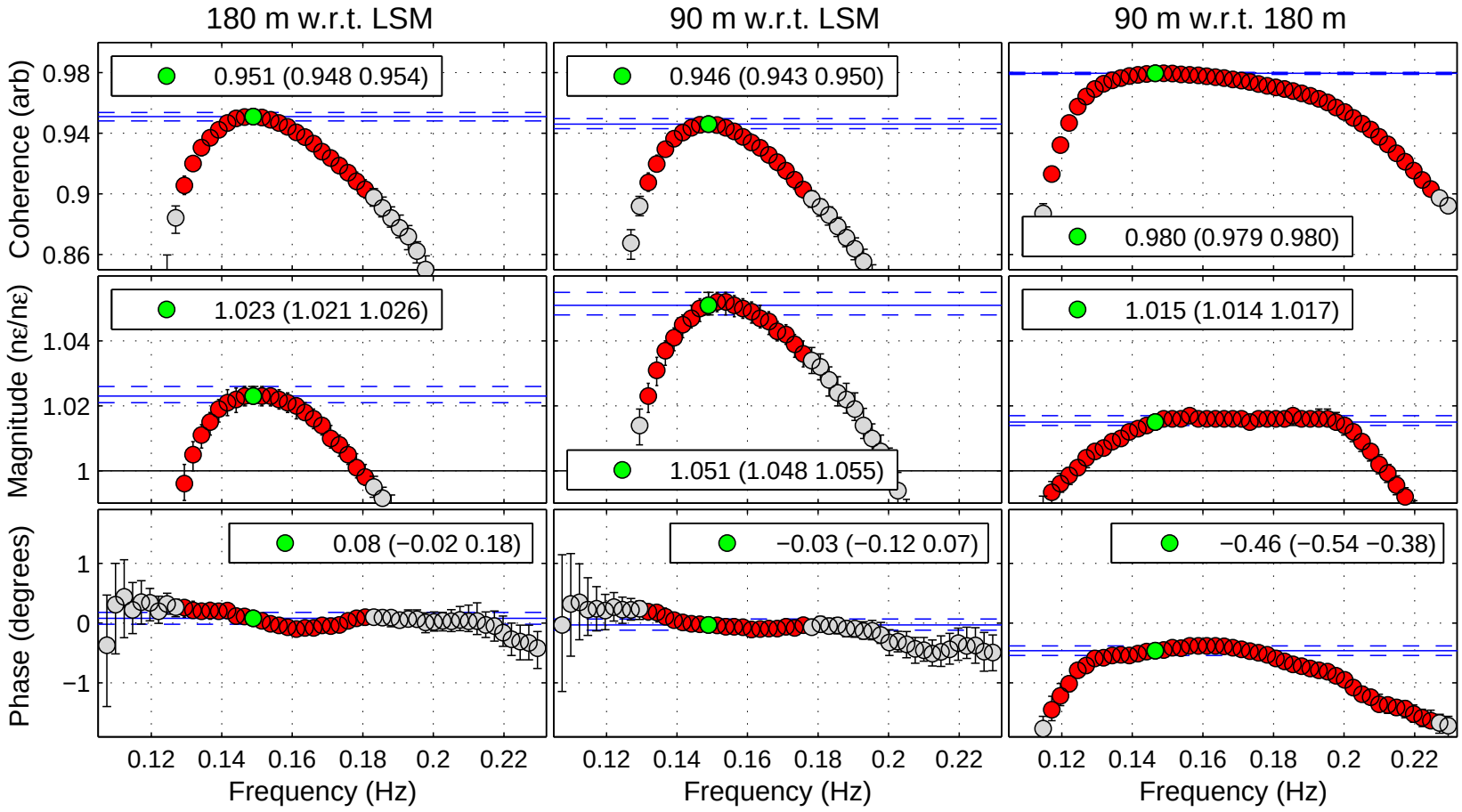


Figure 6.17: Closeup of the median strain-strain ETFEs in the microseism band with confidence intervals estimated by bootstrap resampling. The top, middle, and bottom plots show the coherence, magnitude, and phase estimates from the cross spectral analysis comparing the 180 m (left) and 90 m (middle) TOFS to the NWSE LSM, and the 90 m to the 180 m TOFS (right). The data points in red correspond to coherences exceeding 0.9, and the 50th and 5/95th percent confidence intervals of the point where the coherence is a maximum.

Hz (100 to 10 seconds) using a 3rd-order Butterworth filter before analysis. This was necessary given the different roll-offs of the anti-aliasing filters used by each instrument, and justified since the surface waves of interest (with very long wavelengths) are in the period range of 15 to 20 seconds. The 20 Hz TOFS and GTSM data were decimated to 1 Hz sampling and the LSM data suitably advanced by 2 seconds to account for filtering delays.

Comparisons between each pair of sensors were carried out by time shifting and least-squares fitting one signal relative to the other. A line search over fractional time delays from -3 to +3 seconds was carried out to find the delay (due to logger timing differences) and scale factor with the minimum squared residual. Frequency domain analysis was also performed, but found to be problematic given the relatively short duration of each event and the need for many averaging segments needed to reduce the variance in the cross spectra.

Figure 6.18 shows an example of four surface wave fits from a magnitude 6.9 earthquake located 84 km southeast of Ozernovskiy, Russia on February 28th, 2013. These fits between the 180 and 90 m TOFS are each with respect to the NWSE LSM, each other, and the best two-channel fit of the GTSM to the 180 m TOFS record. The fit between the 180 and 90 m TOFS is excellent ($\sim$11 pϵ RMS residual) perhaps as expected, while the RMS residual between the fiber strainmeters and the LSM and GTSM are also very good (34 and 65 pϵ, respectively).

Despite the high quality of fits between the various strainmeters, once again there is a systematic difference between their amplitudes, i.e., the time series have to be scaled to achieve the best possible fit. The 180 and 90 m TOFS are 1.0758 ± 0.0008 and 1.0810 ± 0.0008 times more sensitive than their nominal calibration factors presented in Section 6.2.4. While these statistical uncertainties are quite small for this particular event, the discrepancy holds up after computing the ensemble average over all 69 earthquakes (see Table 6.3).

Recall that one of the motivations for developing the TOFS was to determine its potential use as a way to calibrate the GTSMs [14]. The decimated and bandpass filtered records from the 4 GTSM extensometer gauges were fit to the 180 m TOFS record for each earthquake using a simple linear regression of the

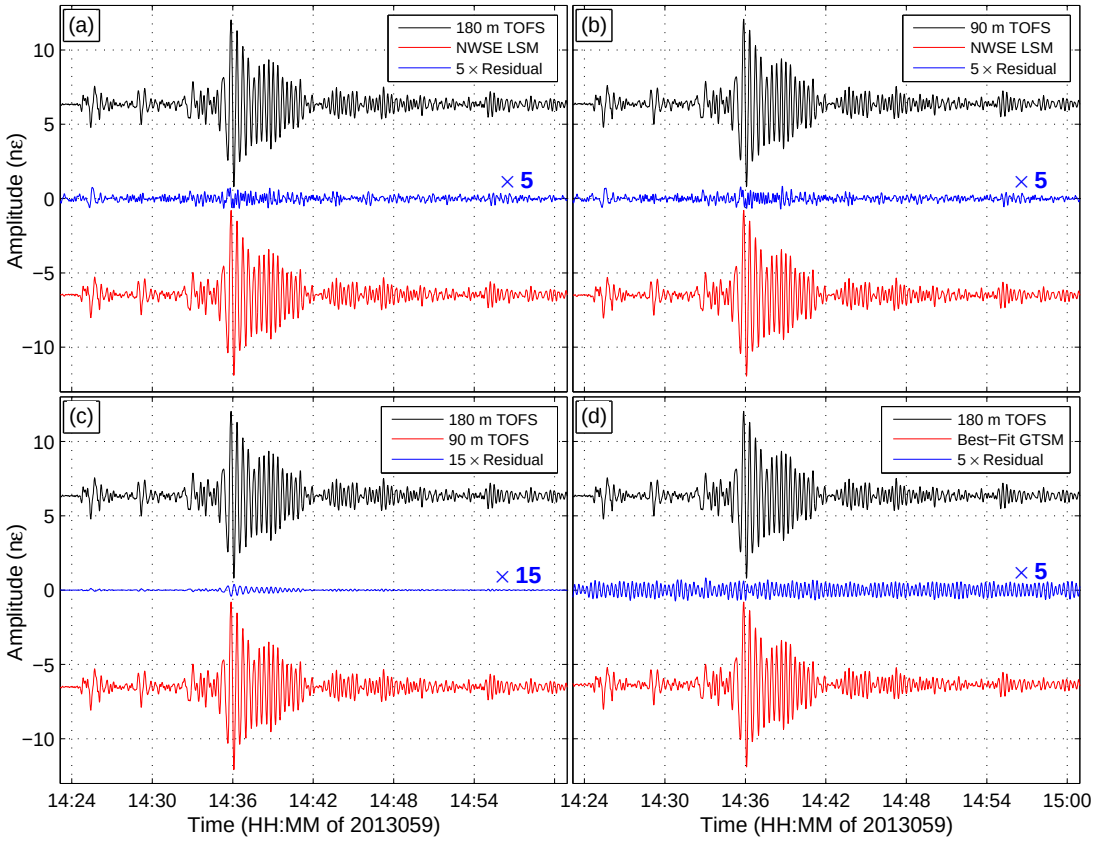


Figure 6.18: Surface wave fits for the M6.9 Russian earthquake. Note that in each case the time series in red has been scaled to fit the time series in black, and the residual in blue has been amplified by a factor of 5.

Table 6.3: Ensemble statistics for the amplitude ratios for the strainmeters from 69 surface wave fits.

Ratio	Amplitude Ratio (nϵ/nϵ)
180 m / LSM	1.067 ± 0.022
90 m / LSM	1.079 ± 0.019
90 m / 180	1.011 ± 0.013

form:

$$\epsilon_{TOFS} = c_0\epsilon_{CH0} + c_1\epsilon_{CH1} + c_2\epsilon_{CH2} + c_3\epsilon_{CH3},$$

where c_n and ϵ_{CHn} are the four gauge coefficients and strain signals from the

Table 6.4: Ensemble statistics for best-fit GTSM gauge coefficients to the 180 m TOFS strainmeter. The left table is for the 4-channel fits, and the right for only channels 1 and 2.

Gauge	Coefficient (nϵ/nϵ)
CH0	0.085 ± 0.070
CH1	0.596 ± 0.072
CH2	0.510 ± 0.082
CH3	0.102 ± 0.098

Gauge	Coefficient (nϵ/nϵ)
CH0	not fit
CH1	0.593 ± 0.024
CH2	0.565 ± 0.016
CH3	not fit

$n = 0, 1, 2, 3$ extensometer channels, respectively. A similar line search over the same ± 3 second advances/delays was performed on all gauges simultaneously (i.e., gauge-dependent time shifts were not allowed), and the best-fit gauge coefficients are summarized in Table 6.4. The large ensemble uncertainties in the CH0 and CH3 gauge fits suggest that they do not contribute to the fit. Therefore, a similar fit was performed just using CH1 and CH2, the results of which are presented on the right side of Table 6.4. Note that since one of the extensometer of the GTSM is nominally in-line with the TOFS axis (CH1) we would expect only the coefficient for this to be significantly different from zero, were it not from the complicating coupling factors associated with borehole strainmeters.

Both the overall agreement of the time-series fits of the TOFS to the GTSM, and the small uncertainties of the gauge coefficients are supportive of the idea of using (a set of) near-surface TOFS for the in-situ calibration of the PBO borehole strainmeters.

6.5.4 Coseismic Offsets

TOFS is also capable of measuring coseismic offsets from nearby events, as illustrated in Figure 6.19. The highlighted event is the largest M5.5 event from a series of approximately 200 events known as the 2012 "Brawley Swarm." A 4^{th}-order Chebyshev type 1 filter with a 100-second corner frequency is used to feature the offsets. While the 0.8 to 1 nϵ offsets on the two instruments appear similar, it is

difficult to quantitatively assess whether there is a systematic amplitude difference as in the tidal, microseismic, and surface wave analyses.

6.6 Discussion

6.6.1 Design, Fabrication, and Deployment

The relative simplicity of this prototype TOFS makes it an attractive design for inexpensive fabrication and easy deployment of a long base strainmeter, where long-period stability is not an objective. The equal-arm form of the interferometer permits high performance with inexpensive diode lasers and a system capable of operating on solar power.

In terms of fabrication, assembling the fiber cable and termination fixtures to the mandrel box in the field proved to be problematic given the small 9 μm diameter, single-more optical fiber cores and the dusty environment within the trench. This required multiple attempts at mating the fiber connectors that attach the sensing fiber to the rest of the interferometer to achieve acceptable insertion losses and strongly suggest a new procedure where all the critical fiber splices are completed in the lab, resulting in a fully ready-to-deploy system.

Clearly the most challenging aspect of this TOFS deployment was the excavation and preparation of the trench, both of which required time and effort. Despite the desire to have the bottom of the trench follow the surface and so be in the same thermal environment, the fiber cable was not able to follow the smaller undulations of the topography. The use of more substantial heavy equipment and a crew dedicated to surveying and leveling/backfilling would greatly accelerate this aspect of the work.

The end-monuments for this installation consisted of simple concrete emplacements, their (only) shallow depth likely contribute substantially to the pronounced CPD signal (owing to surface thermal stresses) and overall lack of long-term stability. New installations are planned where the end-monuments are better isolated from environmental influences through the use of driven-rods, to serve as deeper anchoring.

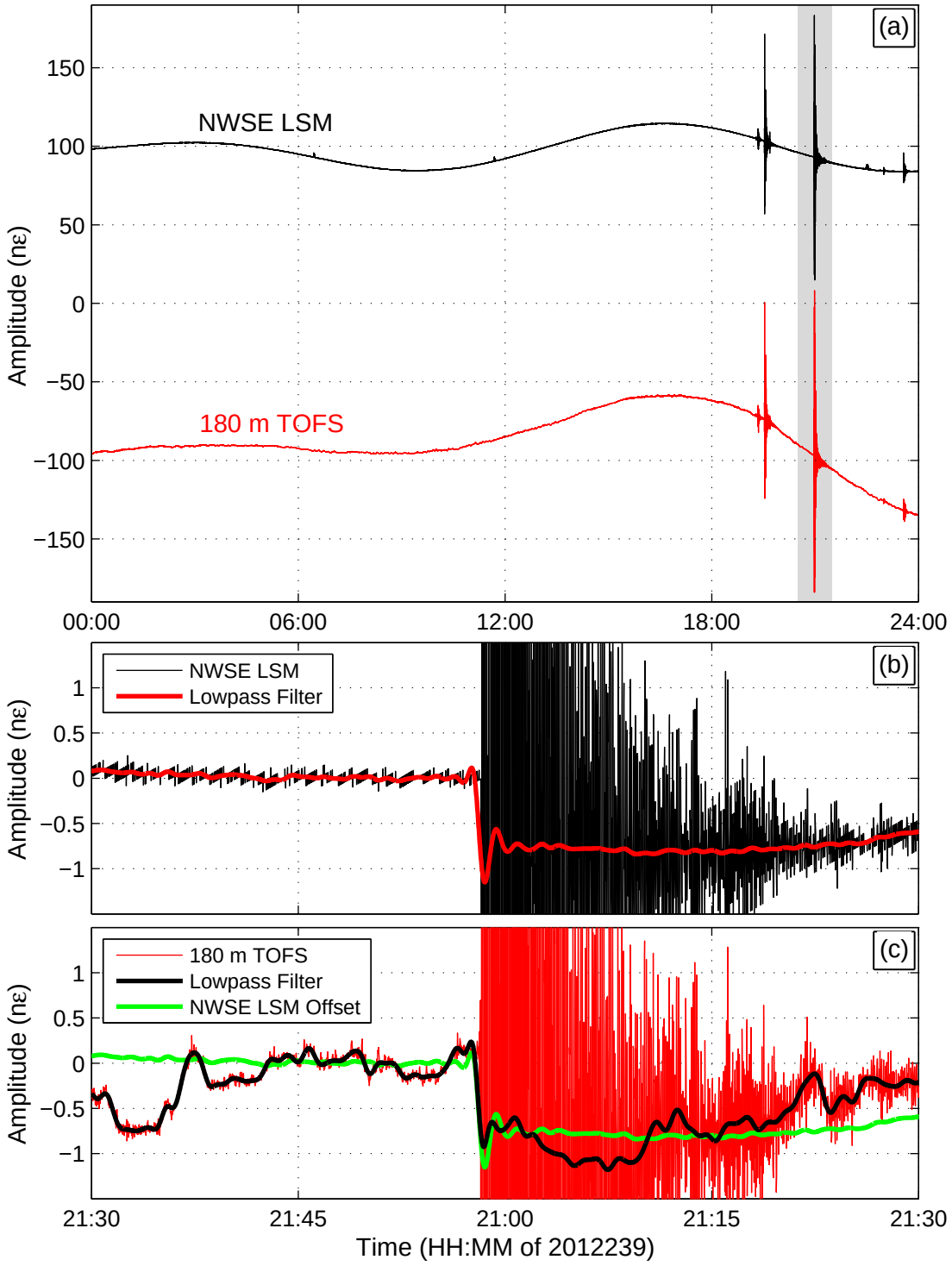


Figure 6.19: Example of a coseismic offset from the largest Brawley swarm earthquake. (a) The M5.5 earthquake in the context of the daily record. (b) Coseismic offset on the NWSE LSM, and (c) 180 m TOFS.

6.6.2 General Observations

Results from the cross spectrum analyses of the thermistor data illustrates some of the difficulties in estimating suitable calibration coefficients for correcting the strain record for unwanted temperature changes. This analysis was fraught from the outset since the observed strain record (i.e., the output of the fringe counting system) is some unknown combination of the changes in the mandrel temperature, the distributed fiber cable temperature, and the strain in the fiber cable. The observation of different strain-mandrel temperature calibration factors in the cross spectra at 1 and 2 CPD is likely due to this ambiguity. The low coherence and poor phase stability in the strain-trench temperature cross spectra are most likely a result of the fact that the combined measurements of the four discrete thermistor records, only spanning a small fraction (3%) of the trench, are not representative of the entire fiber cable temperature. Unfortunately, this makes the scaling estimates unreliable despite the several hundred averages that went into them.

Non-stationarity also plays a role in the temperature analysis, which also impacts the efficacy of attempts to compensate for temperature changes to the buried reference mandrel. The time dependence of the strain-mandrel coefficient is indicative of changes in the physical characteristics of the material surrounding the mandrel and/or fiber cable (i.e., settling). For example, there have been no significant rainfall events since the initial TOFS deployment, to re-cement the ground, which is expected to have an effect on the material porosity and thermal conductivity. More recent moderate rainfall events have pooled water over the 90 m reference mandrel and this increased the recorded diurnal strain signal, out of phase with the thermistor records, and so indicating less thermal resistance. This effect was subsequently reduced by adding more native material over the mandrel box to increase its effective depth of burial.

The wind noise results are surprising given that the wind-strain coupling is several times smaller on the LSM. The directional dependence of the wind noise levels loosely corresponds to the rectangular cross section of the junction box at the surface. This suggests that the reference mandrel may be acting as a mi-

crophone that is recording the stagnation pressure fluctuations caused by wind blowing against the junction box [16]. However, this is difficult to assess since the uncertainties in each wind direction bin are of similar size to this directional effect.

It is particularly worth noting that there is no clear barometric response at and near 1 and 2 CPD despite each mandrel being exposed to an atmospheric pressure signal that is very energetic at these periods. In this prototype installation (with an unsealed reference mandrel) a large signal is expected. Recall that the tides were removed from the data prior to analysis. If there were a significant barometric pressure response, it may be biasing the tidal fits. Therefore, it is possible that some function of the atmospheric tides were also removed along with the strain tides. A more disturbing possibility is that the fiber cable itself may have a small leak, thereby allowing barometric pressure to affect both arms of the interferometer — mandrel and sensing — equally at long periods.

Perhaps the most perplexing issue regarding the wind noise and barometric pressure results is that of the sign of the effect. Recall that the nominal pressure sensitivity of an unclad optical fiber is approximately -4.2 pϵ/Pa. This implies that a positive pressure (compressional stress) results in a negative optical path length change. Holding the length of the sensing arm constant, a negative optical path length change in the reference arm of the interferometer results in a positive optical phase change. Therefore, if the observed pressure effect were strictly due to the mandrel, it would imply that a positive pressure would result in a positive phase shift. This contradicts observation, since the sign of the barometric pressure record is in fact negative (recall that it was flipped in Figure 6.14 to yield cross spectrum phase estimates near 0°).

One possible explanation can be found by accounting for the acrylate coating on the reference mandrel fiber. Hocker showed that with the proper choice of coating one can not only amplify the strain-pressure effect 10-100 times, but can also reverse its sign [11]. Using this result for infrared wavelengths and for the up-jacketing of the 125 μm diameter fiber to 250 μm with UV-curable acrylate, the nominal strain-pressure calibration factor would be $+37 \pm 5$ pϵ/Pa, where the uncertainty is largely due to the varying properties of acrylate found in the liter-

ature [7]. While this only gets us half way to the ∼60 pϵ shown in Figure 6.14, it is supportive of this model.

6.6.3 Geophysical Signals

The tidal, microseismic, and surface wave results all indicate that TOFS is more sensitive than its nominal calibration factor. The summary results from these three analyses are presented in Table 6.5. Each amplitude ratio estimate is the result of a different type of analysis: a least-squares fit between a model and data for the tides, cross spectrum analysis for the microseisms, and a least-squares fit between two time series for the surface waves. Each have their own assumptions about stationarity, correlated residuals, etc., and each are violated to some degree.

Table 6.5: Summary of amplitude ratios from the tidal, microseismic, and surface wave analyses.

Ratio	Tidal	Microseismic	Surface Wave
180 m / LSM	1.0177 ± 0.0031	1.023 (1.021 1.026)	1.067 ± 0.022
90 m / LSM	1.0448 ± 0.0050	1.051 (1.048 1.055)	1.079 ± 0.019
90 m / 180	1.0266 ± 0.0058	1.015 (1.014 1.017)	1.011 ± 0.013

From these disparate methods of analysis, three findings stand out: (1) the fiber strainmeters are recording greater strains, (2) the 90 m / 180 m ratio is different from unity (∼1.02), and approximately remains the same, and (3) the surface wave amplitude ratios appear to be much higher than the other results. While the earthquakes are more energetic, there is no clear relationship between the signal amplitude and the resulting amplitude ratios. Furthermore, the average earthquake amplitude is only about 1/3 of the tidal signal.

There are three possibilities why the TOFS-to-LSM amplitude ratios appear to be greater than unity. First, the LSM could be underestimating the strain. This is unlikely since the wavelength is very well known (using a polarization-stabilized helium-neon laser), and the evacuated-path distance between the two

monuments has been measured to fractions of a percent of its base length. While the instruments are close to one another and along the same azimuth, it is possible that the strain field is not uniform over the two very different base lengths. Previous work by Berger and Beaumont suggests that there may be lateral inhomogeneities due to geology and topography along the same azimuth at PFO on the order of 1-2% [4] at tidal periods. The final possibility is that this discrepancy is due to the behavior of TOFS. While there was no in-situ calibration done on these instruments, the strain-optic coefficient is well established.

However, there are some plausible physical mechanisms that may explain why TOFS is more sensitive than the LSM. The most unlikely among these is the nonlinearity of the strain-optic effect, which has been previously measured at [22]:

$$\mu = 1.158\,(1 + 1.35\epsilon)\,,$$

implying an increase of only 1.35×10^{-6} for a strain of 1 $\mu\epsilon$, which is an order of magnitude larger than the largest strain event analyzed in this chapter. Another very unlikely explanation is related to the fact that the fiber cable does not follow a straight line. This would result in a discrepancy between the instrument base length (the distance between the monuments) and fiber gauge length (the length of fiber being strained). However, a 5% discrepancy would require a mismatch of 9 m in the 180 m instrument, which is implausible.

More likely is the violation of the assumption that the optical fiber is subjected purely to axial strain, which is required by the Butter and Hocker relationship shown in Equation 1.19 [6]. Consider the two fibers contained in the stainless tube that comprises the fiber cable. There are several interactions that a given fiber can have within this configuration: each fiber can come in contact with the side of the stainless tubing as well as the other fiber. In fact, one fiber can be twisted around the other. This can result in an increase in radial stress coincident with an increase in axial stress, thereby amplifying the total change in the index of refraction of the optical fiber.

To very briefly flesh this out, consider the more generalized strain-optic

effect derived by Sirkis [20]:

$$\phi\left(\epsilon_1,\epsilon_2,\epsilon_3\right)=\frac{\pi n_0}{2\lambda}\int_\Gamma\left\{4\left(1+\epsilon_3\right)-n_0^2\left[\left(\epsilon_1+\epsilon_2\right)p_{11}+\left(\epsilon_1+\epsilon_2+2\epsilon_3\right)p_{12}\right]\right\}ds,$$

where ϵ_i are the normal strains (ϵ_3 being the axial strain) and the other parameters have been previously defined in Chapter 1. Assuming that the integrand is constant (i.e., no path-dependent strains) and the path is a straight line:

$$\int_\Gamma ds=\int dz=L_0,$$

the optical phase difference, $\Delta\phi=\phi-\phi\left(0\right)$, can be simplified to:

$$\Delta\phi\left(\epsilon_1,\epsilon_2,\epsilon_3\right)=\frac{\pi n_0 L_0}{2\lambda}\left\{4\epsilon_3-n_0^2\left[\left(\epsilon_1+\epsilon_2\right)p_{11}+\left(\epsilon_1+\epsilon_2+2\epsilon_3\right)p_{12}\right]\right\}.$$

Therefore, using the previous values from Chapter 1 the relative contribution of each normal strain can be expressed as:

$$\frac{2\lambda\Delta\phi}{\pi n_0 L_0\left(4-2n_0^2p_{12}\right)}=\epsilon_3-0.27\left(\epsilon_1+\epsilon_2\right),$$

which suggests that a positive contribution to the observed phase difference could be made in the presence of negative off-axis strains.

The substantial discrepancy between the combined tidal and microseismic results and those from the seismic surface waves remains unreconciled and an area of active research into both the strainmeters and the earth.

6.7 Conclusions and Future Work

A pair of horizontal, interferometric optical fiber strainmeters have been installed at the Piñon Flat Observatory. These prototype instruments are the first of their kind, and have been successfully recording signals of geophysical interest since late July of 2012. Both interferometers are deployed in a 1-m deep trench parallel to an existing northwest-to-southeast laser strainmeter that serves as a reference.

As evident in Figure 6.10 these new long base instruments have demonstrated noise levels that approach those of much more substantial systems, for

the frequencies from the tides through the seismic band, and offer the prospect of broad use for a number of geophysical studies. In particular they could be employed, even as temporary installations, to establish the average strain field at locating of existent PBO borehole strainmeters, and with this a better understanding of the response of these systems [14].

For these sensors, exposure to environmental variables is problematic, but expected in the case of temperature. The use of collocated thermistors were found to be ineffective at consistently correcting the strain record for surface temperature changes. This is most likely due to the changing thermal characteristics of the native material still undergoing re-cementation. Exposure of the highly sensitive reference mandrel to atmospheric pressure as well as wind noise, while not readily explained, are not a cause of significant noise.

A variety of comparisons were made between both the 90 and 180 m long TOFS and the collocated NWSE LSM using three different geophysical signals. While the overall agreement was quite good, a statistically significant, systematic amplitude discrepancy was found between TOFS and the LSM. Disturbingly, this disagreement was found to differ depending upon the signal under consideration. Specifically, a 2% and 5% discrepancy was found for the 180 and 90 m TOFS, respectively, compared to the NWSE LSM for both the large amplitude, long period M2 tidal constituent and very small and high frequency microseisms. This is to be compared to a 7% and 8% difference for the earthquake surface wave analysis.

While there are many potential explanations for this amplitude ratio discrepancy, a consensus is building around the idea of signal-induced-noise. Whether this is a result of nonlinearity introduced by imperfect ellipse fitting by the fringe counting system, monument motions, or off-axis strain-induced index-of-refraction changes is difficult to ascertain with the current setup. However, future deployments using improved end monuments and pressure sealed mandrel vessels will help eliminate some of these possibilities.

There are several clear areas for improvement in the design of future TOFSs. The most obvious is increased thermal insulation that can only be achieved through deeper burial. Based on decades of experience with LSMs, more deeply anchored

end monuments will greatly improve the long period behavior by suppressing thermal stress effects. Most importantly, it is absolutely essential to develop a reliable, high-precision method for measuring the integrated trench and mandrel temperatures.

The development of this prototype TOFS has significantly clarified the challenges involved in using optical fibers for horizontal strain measurement. These lessons will not only be applied to future land-based strainmeters, but also for the seafloor optical fiber strainmeter project currently underway.

6.8 Acknowledgments

We graciously acknowledge Don Elliott, Billy Hatfield, Ross Bell, John Dai, Michael Fanton, and Jerry Ross for their many hours of effort during the excavation, trench preparation, installation, and many other efforts large and small. Heinz Wuhrmann and John Bjork provided assistance machining various components. Duncan Agnew and Billy Hatfield provided many insights and much assistance into processing the data. We are especially indebted to Robert Parker for his invaluable assistance performing consistency checks on the amplitude ratio analyses as well as for providing the multitaper cross spectrum code. David Horwitt, David Chavez, and Jui-Yuan Chang for provided the hardware and software engineering and support for acquiring the TOFS data, and Hans-Werner Braun managed the data network infrastructure.

REFERENCES

[1] GTSM Technologies Advanced Frequently Asked Questions (FAQs). http://www.gtsmtechnologies.com/pdf/GTSM_FAQ_2.pdf. Accessed: 2013-11-04.

[2] Andrew J. Barbour and Duncan Carr Agnew. Noise Levels on Plate Boundary Observatory Borehole Strainmeters in Southern California. *Bulletin of the Seismological Society of America*, 101(5):2453–2466, 2011.

[3] Hugo Benioff. Fused-Quartz Extensometer for Secular, Tidal, and Seismic Strains. *Geological Society of America Bulletin*, 70(8):1019–1032, 1959.

[4] Jonathan Berger and Christopher Beaumont. An Analysis of Tidal Strain Observations from the United States of America. *Bulletin of the Seismological Society of America*, 66(6):1821–1846, 1976.

[5] John A. Blum, Heiner Igel, and Mark A. Zumberge. Observations of Rayleigh-Wave Phase Velocity and Coseismic Deformation Using an Optical Fiber, Interferometric Vertical Strainmeter at the SAFOD Borehole, California. *Bulletin of the Seismological Society of America*, 100(5A):1879–1891, 2010.

[6] C. D. Butter and G. B. Hocker. Fiber optics strain gauge. *Applied Optics*, 17(18):2867–2869, 1978.

[7] Scott DeWolf. *Optical and Mechanical Behavior of the Optical Fiber Infrasound Sensor*. M.S. thesis, University of California San Diego, 2009.

[8] B. Efron and R. J. Tibshirani. *An Introduction to the Bootstrap*. Monographs on Statistics and Applied Probability 57. Chapman and Hall, New York, 1993. 456 pages.

[9] Elige Buckhanan Grant. *Gladwin Tensor Strainmeter Calibration using Seismic Data: Instrument Calibration Methods and Wave Gradiometry Applications*. Ph.D. Thesis, University of Memphis, 2010.

[10] R. H. G. Hart, Michael T. Gladwin, R. L. Gwyther, Duncan Carr Agnew, and Frank K. Wyatt. Tidal calibration of borehole strain meters: Removing the effects of smallscale inhomogeneity. *Journal of Geophysical Research*, 101(B11):25553–25571, 1996.

[11] G. B. Hocker. Fiber optic acoustic sensors with composite structure: an analysis. *Applied Optics*, 18(21):3679–3683, 1979.

[12] G. B. Hocker. Fiber-optic sensing of pressure and temperature. *Applied Optics*, 18(9):1445–1448, 1979.

[13] Kathleen Hodgkinson, John Langbein, Brent Henderson, Dave Mencin, and Adrian Borsa. Tidal calibration of plate boundary observatory borehole strainmeters. *Journal of Geophysical Research: Solid Earth*, 118(1):447–458, January 2013.

[14] John Langbein. Effect of error in theoretical Earth tide on calibration of borehole strainmeters. *Geophysical Research Letters*, 37(L21303), 2010.

[15] Rich Pawlowicz, Bob Beardsley, and Steve Lentz. Classical tidal harmonic analysis including error estimates in MATLAB using T_TIDE. *Computers & Geosciences*, 28(8):929–937, 2002.

[16] Richard Raspet, Jeremy Webster, and Kevin Dillion. Framework for wind noise studies. *Journal of the Acoustical Society of America*, 119(2):834–843, 2006.

[17] Kurt S. Riedel and Alexander Sidorenko. Minimum bias multiple taper spectral estimation. *IEEE Transactions on Signal Processing*, 43(1):188–195, 1995.

[18] Kurt S. Riedel and Alexander Sidorenko. Adaptive smoothing of the log-spectrum with multiple tapering. *IEEE Transactions on Signal Processing*, 44(7):1794–1800, 1996.

[19] Evelyn Roeloffs. Tidal calibration of Plate Boundary Observatory borehole strainmeters: Roles of vertical and shear coupling. *Journal of Geophysical Research*, 115:B06405, June 2010.

[20] James S. Sirkis. Unified approach to phase-strain-temperature models for smart structure interferometric optical fiber sensors: part 1, development. *Optical Engineering*, 32(4):752–761, 1993.

[21] Donald L. Turcotte and Gerald Schubert. *Geodynamics*. Cambridge University Press, Reading, Massachusetts, second edition, 2002.

[22] Mark A. Zumberge, Frank K. Wyatt, Dong X. Yu, and Hideo Hanada. Optical fibers for measurement of earth strain. *Applied Optics*, 27(19):4131–4138, October 1988.

Appendix A

Borehole Optical Fiber Strainmeter Corrections

The purpose of this appendix is to provide a graphical supplement to the corrections applied to the raw BOFS interferometer time series described in Sections 5.2.1 and 5.2.2. Each plot follows the same format, with the cross spectra broken into their three components: (a) magnitude-squared coherence, (b) magnitude, and (c) phase. The final plot, (d), shows the original (or residual from the previous plot where applicable) in black, the correction signal scaled into the units of the preceding record in red, and the residual between the two in blue.

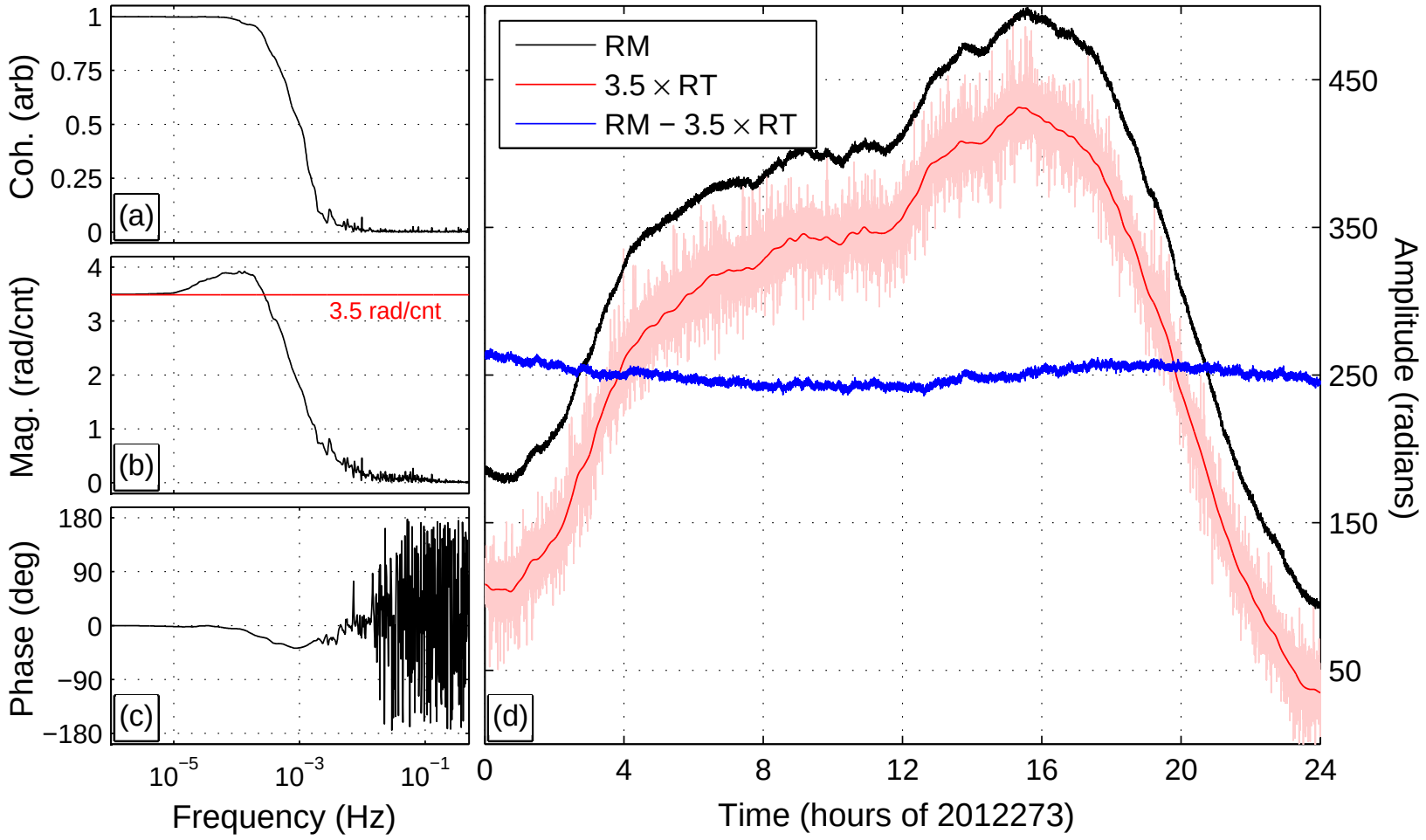


Figure A.1: Cross spectra and time series for the up-hole temperature correction to the reference mandrel record. The raw reference mandrel signal, RM, is shown in black, along with the raw and 1,000-second low pass filtered reference mandrel thermistor record, RT (red), and their residual (blue).

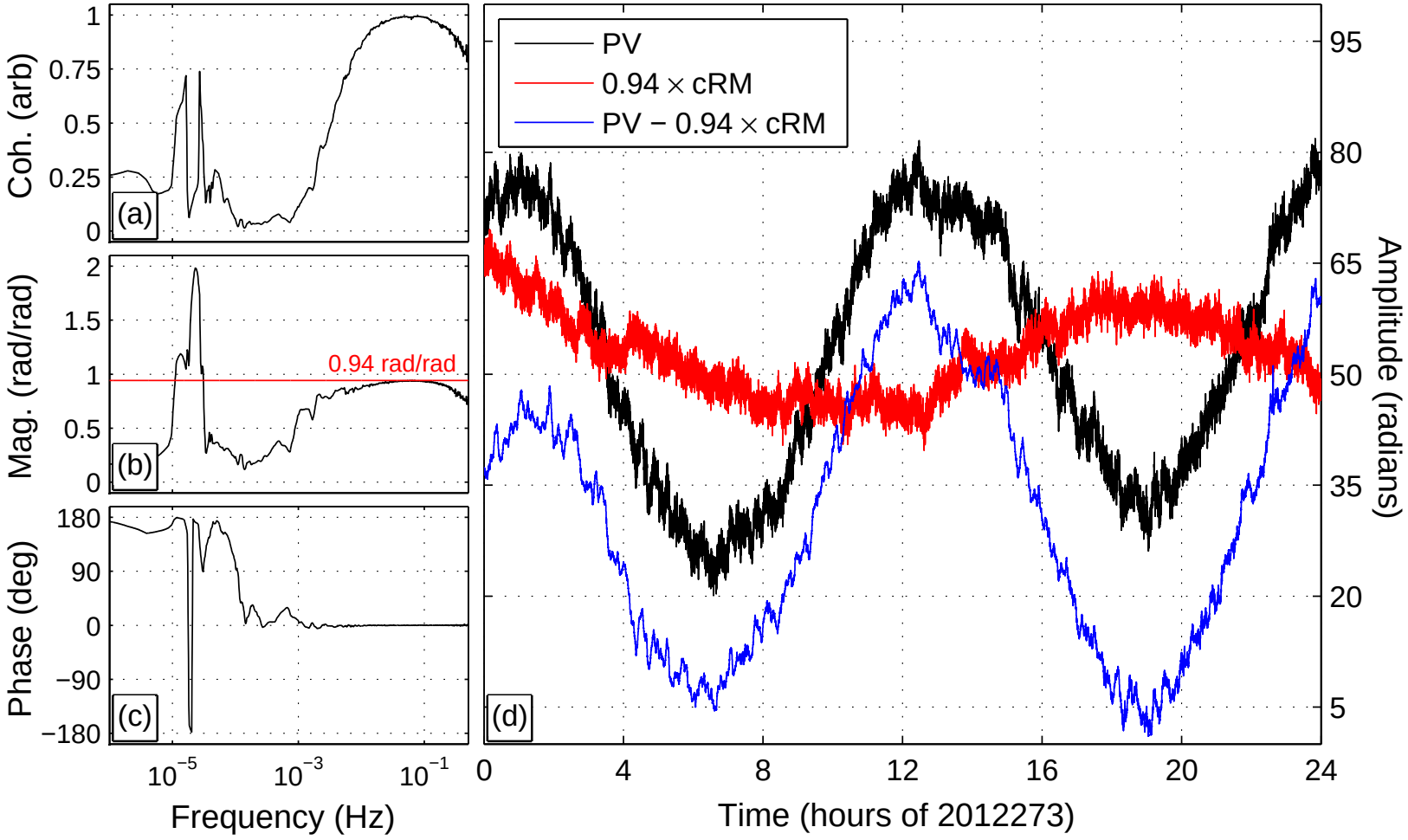


Figure A.2: Cross spectra and time series for the up-hole laser wavelength correction to the raw primary vertical strainmeter record. The raw primary vertical strain signal, PV, is shown in black, along with the temperature-corrected reference mandrel record, cRM (red), and their residual (blue).

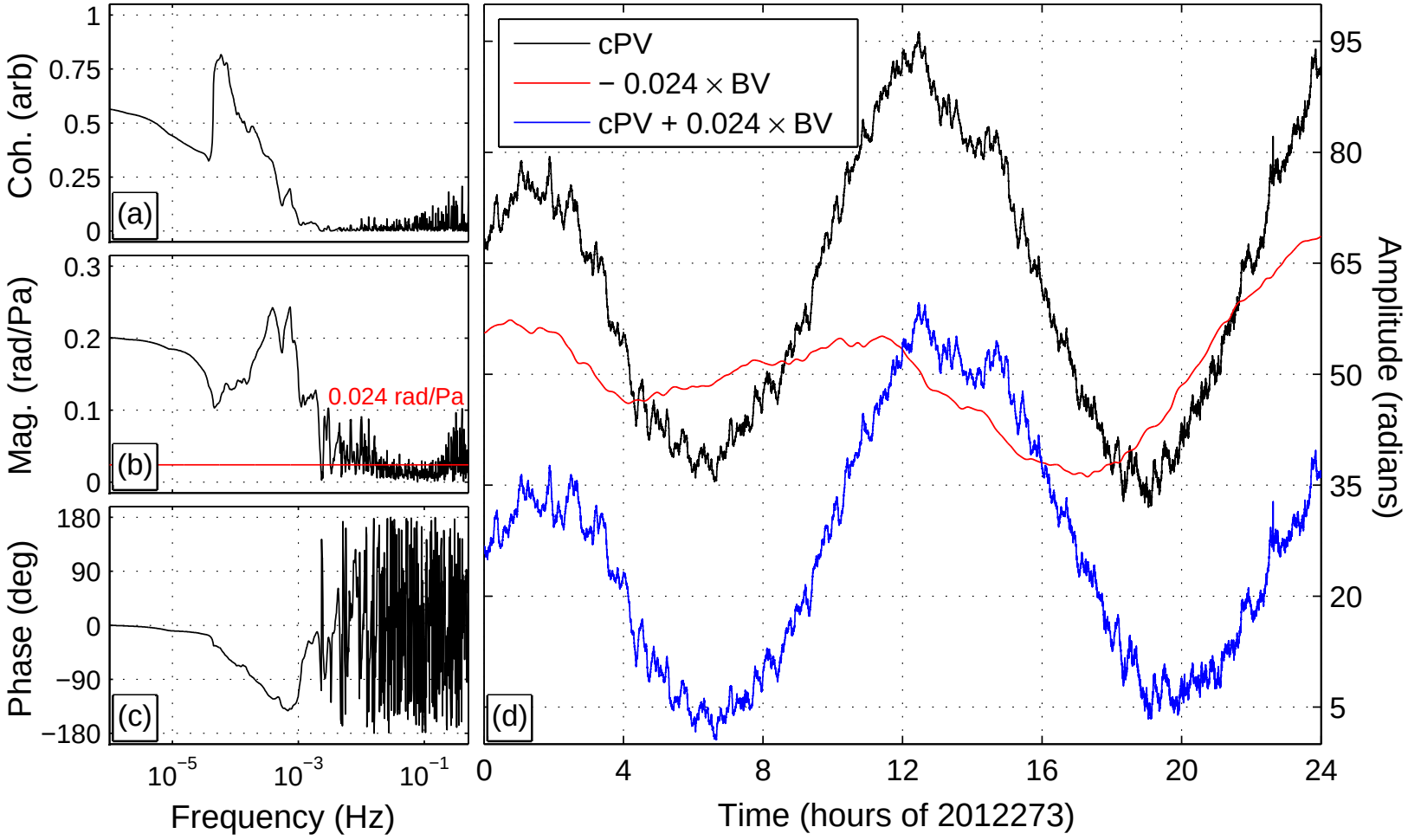


Figure A.3: Cross spectra and time series for the barometric pressure correction to the up-hole-corrected primary vertical strainmeter record. The up-hole-corrected primary vertical strain signal, cPV, is shown in black, along with the 1,000-second low pass filtered barometric pressure record, BV (red), and their residual (blue).

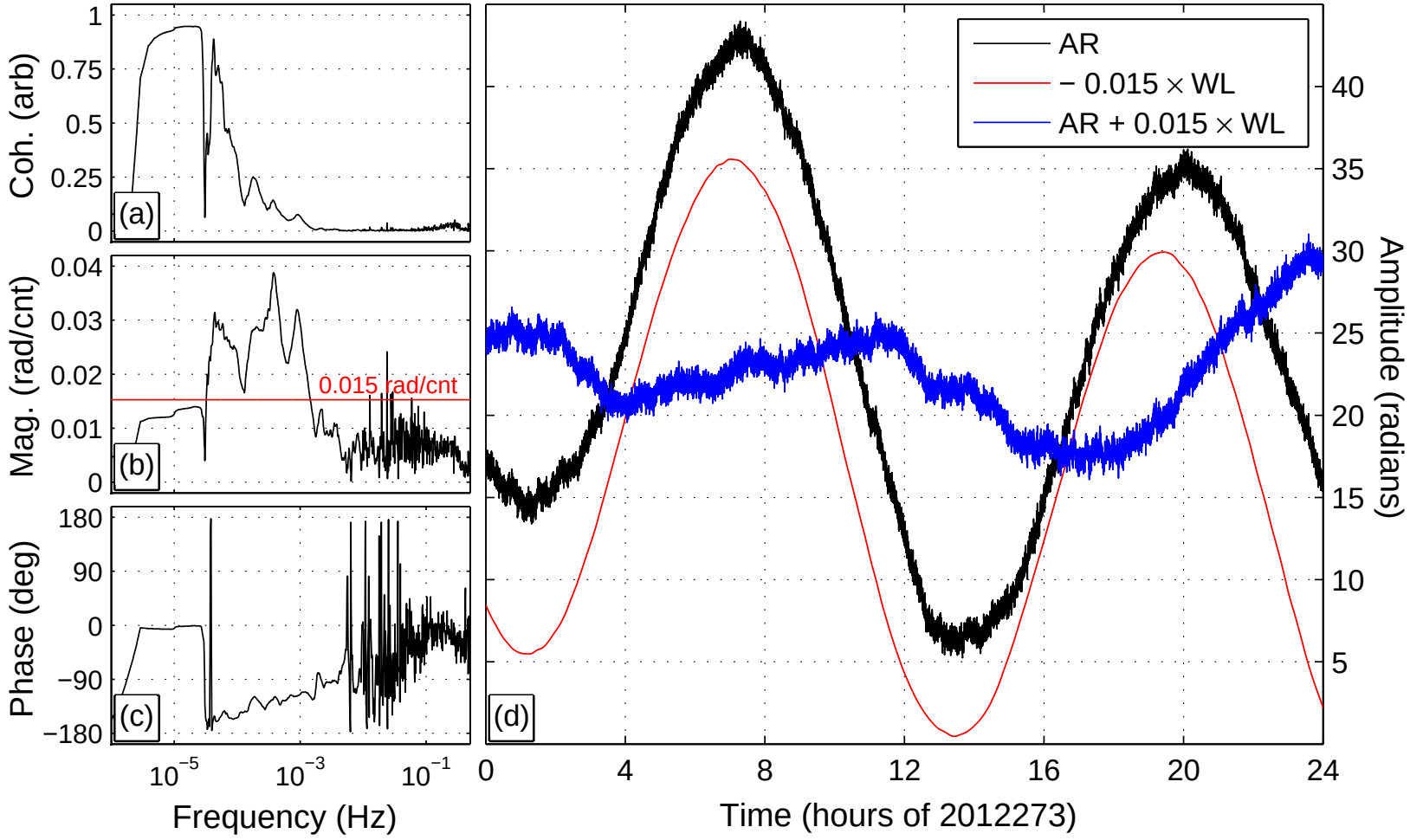


Figure A.4: Cross spectra and time series for the down-hole water level correction to the raw areal strainmeter record. The raw areal strainmeter signal, AR, is shown in black, along with the 1,000-second low pass filtered water level record, WL (red), and their residual (blue).

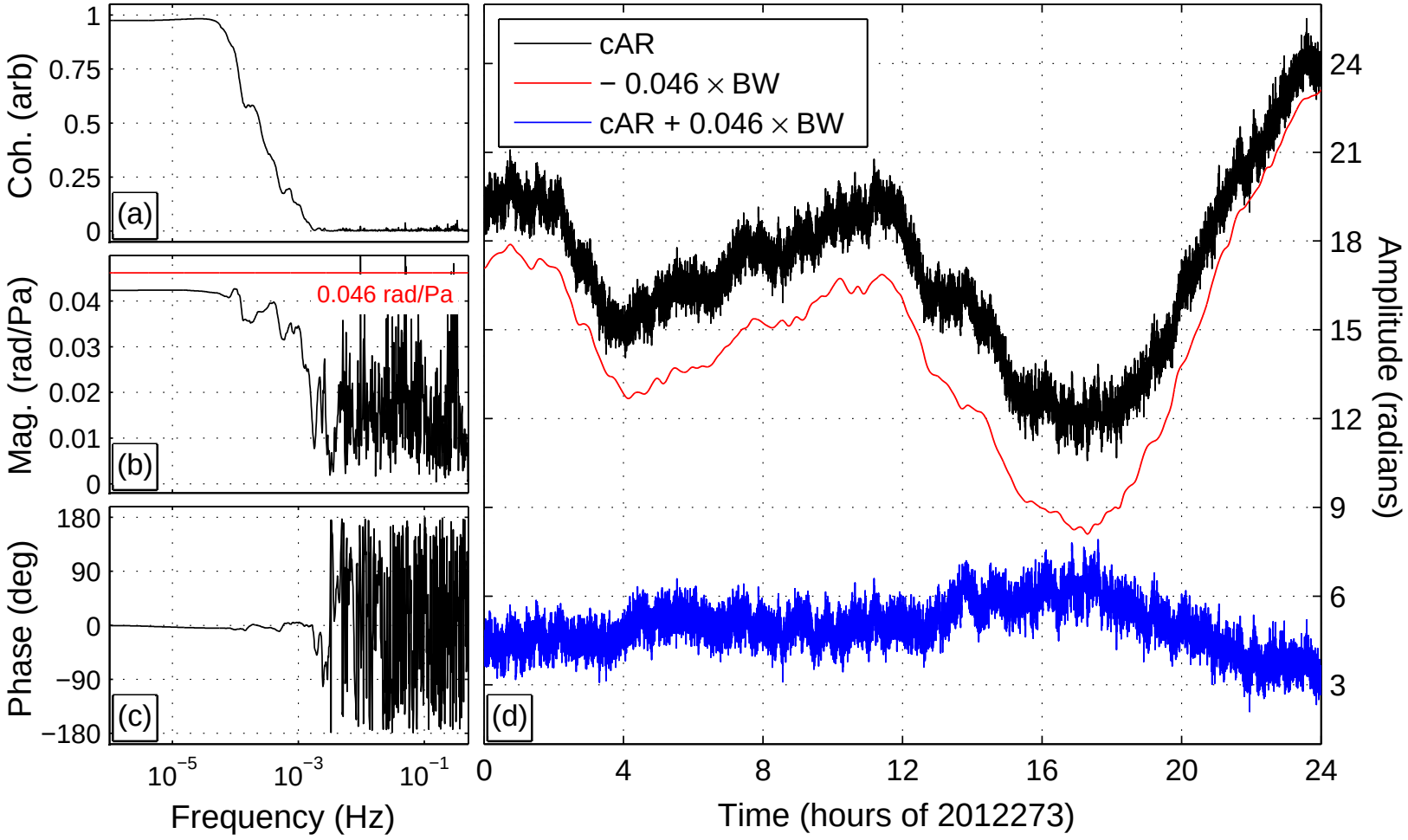


Figure A.5: Cross spectra and time series for the down-hole barometric pressure correction to the water level corrected areal strainmeter record. The water level corrected areal strain signal, cAR, is shown in black, along with the 1,000-second low pass filtered barometric pressure record, BW (red), and their residual (blue).

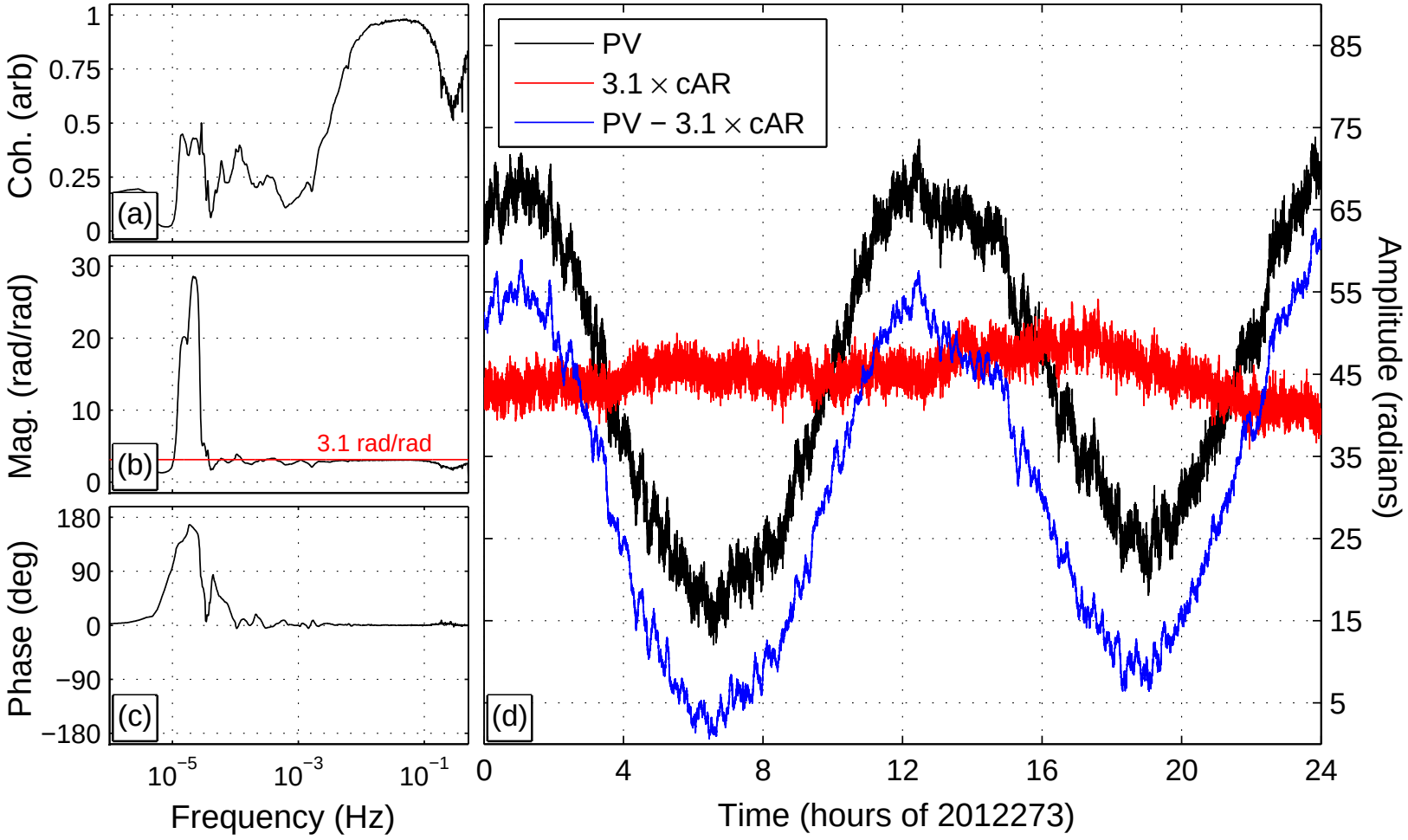


Figure A.6: Cross spectra and time series for the down-hole laser wavelength correction to the raw primary vertical strainmeter record. The raw primary vertical strain signal, PV, is shown in black, along with the water level and barometric pressure corrected areal strain signal, cAR (red), and their residual (blue).

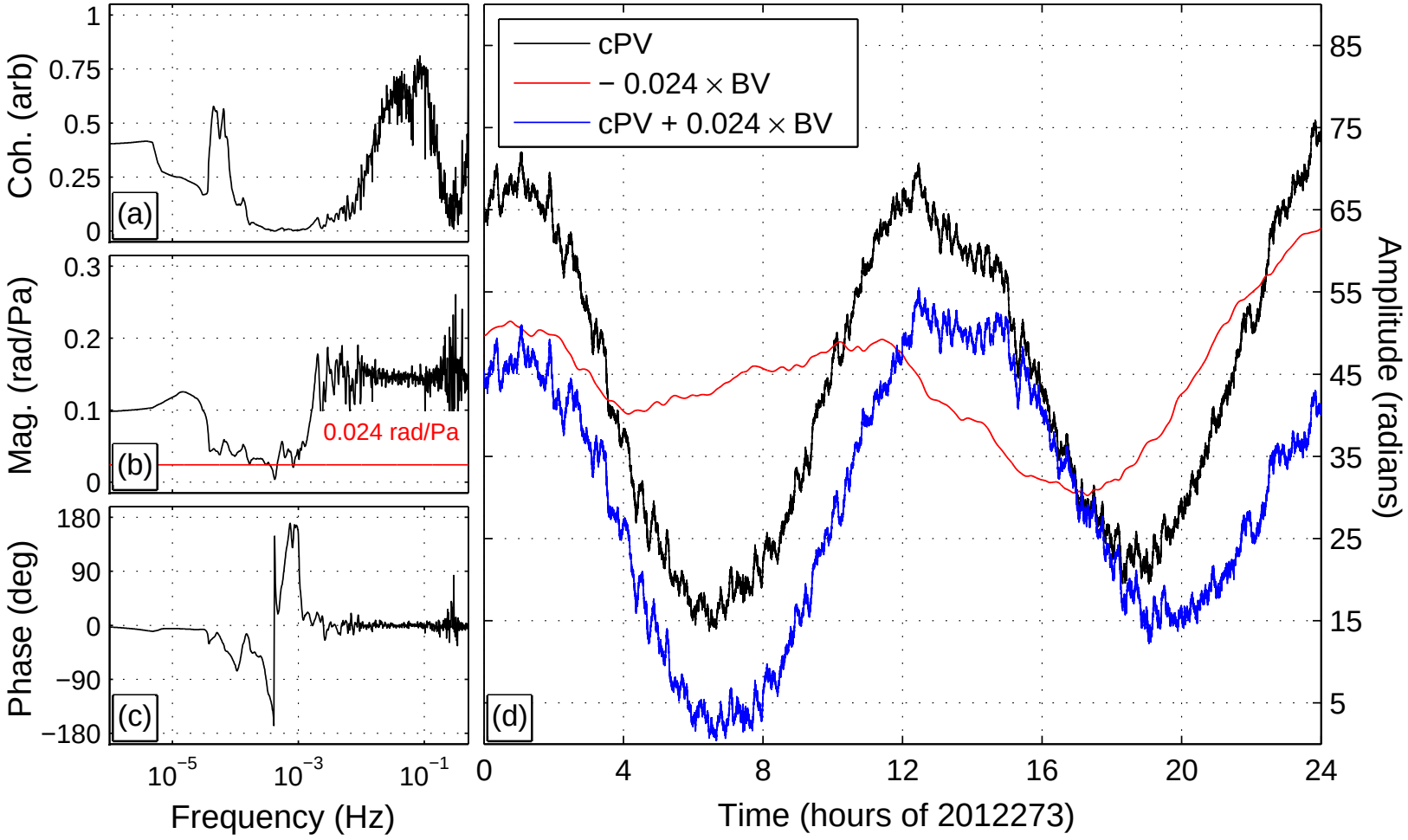


Figure A.7: Cross spectra and time series for the final barometric pressure correction to the down-hole-corrected primary vertical strainmeter record. The down-hole-corrected primary vertical strain signal, cPV, is shown in black, along with the 1,000-second low pass filtered barometric pressure record, BV (red), and their residual (blue).

Appendix B

Earthquakes Used In Surface Wave Analyses

This appendix presents the 69 earthquakes used in the surface wave analyses for TOFS (Section 6.5.3), and the subset of 36 events for BOFS (Section 5.4.2) highlighted in gray. Note that the start time for each event is the approximate arrival time at the Piñon Flat Observatory, and is given in epoch time (or "Unix time," seconds from January 1, 1970).

Table B.1: Earthquakes used in the surface wave analyses in Section 5.4.2 (in gray) and 6.5.3 (all events).

#	Year	Day	Start (ep)	Dur (s)	Mag	Dep (km)	Lat (°)	Lon (°)	Dist (km)	Az (°)	Name
1	2013	144	1369374800	7200	8.3	609	54.9	153.3	7030	-40	Sea of Okhotsk
2	2013	037	1360113800	9000	8.0	29	-10.7	165.1	9616	-105	76 km W of Lata, Solomon Islands
3	2012	302	1351393700	9000	7.8	14	52.8	-132.1	2469	-26	Haida Gwaii, Canada
4	2012	227	1344913700	3600	7.7	583	49.8	145.1	7773	-43	158 km ENE of Poronaysk, Russia
5	2013	106	1366110200	7200	7.7	82	28.1	62.0	13151	1	83 km E of Khash, Iran
6	2013	267	1380023400	9900	7.7	15	27.0	65.5	13280	-2	61 km NNE of Awaran, Pakistan
7	2012	244	1346418100	9000	7.6	28	10.8	126.6	11725	-65	Philippine Islands region
8	2012	249	1346856500	7200	7.6	35	10.1	-85.3	4114	122	Costa Rica
9	2013	005	1357376600	3600	7.5	10	55.4	-134.6	2800	-25	Southeastern Alaska
10	2012	312	1352306400	3600	7.4	24	14.0	-91.8	3306	125	Offshore Guatemala
11	2013	143	1369330100	7200	7.4	171	-23.0	-177.1	8989	-126	282 km SW of Vaini, Tonga
12	2012	240	1346042400	5400	7.3	28	12.1	-88.6	3699	124	Off the coast of El Salvador
13	2012	274	1349023100	3600	7.3	170	1.9	-76.4	5455	122	San Agustin, Colombia
14	2012	342	1354869000	7200	7.3	31	37.9	143.9	8526	-53	Off the east coast of Honshu, Japan
15	2013	188	1373222800	7200	7.3	386	-3.9	153.9	10214	-93	Taron, Papua New Guinea
16	2013	196	1373898200	9000	7.3	31	-60.9	-25.1	13291	146	218 km SSE of Bristol Island, South Sandwich Islands
17	2013	109	1366341300	5400	7.2	112	46.2	150.8	7579	-48	251 km ENE of Kuril'sk, Russia
18	2012	345	1355159500	7200	7.1	155	-6.5	129.8	12600	-82	229 km NW of Saumlaki, Indonesia
19	2013	039	1360337900	7200	7.1	21	-10.9	166.0	9550	-106	31 km SE of Lata, Solomon Islands
20	2013	268	1380127980	3600	7.1	40	15.8	-74.5	4634	105	46 km SSE of Acari, Peru
21	2013	096	1365224800	5400	7.0	66	-3.5	138.5	11617	-85	240 km E of Enarotali, Indonesia
22	2013	242	1377880400	5400	7.0	34	51.6	-175.4	5059	-48	94 km ESE of Adak, Alaska
23	2013	033	1359815300	5400	6.9	107	42.8	143.1	8298	-48	19 km SSW of Obihiro, Japan
24	2013	040	1360419800	5400	6.9	145	1.1	-77.4	5436	123	2 km N of Yacuanquer, Colombia
25	2013	059	1362061100	3600	6.9	41	50.9	157.3	6929	-45	84 km SE of Ozernovskiy, Russia

Table B.1: Earthquakes used in the surface wave analyses in Section 5.4.2 (in gray) and 6.5.3 (all events).

#	Year	Day	Start (ep)	Dur (s)	Mag	Dep (km)	Lat (°)	Lon (°)	Dist (km)	Az (°)	Name
26	2012	243	1346334500	5400	6.8	14	71.4	-10.6	7017	20	93 km NW of Olonkinbyen, Svalbard and Jan Mayen
27	2012	316	1352598400	5400	6.8	14	23.0	95.9	12849	-33	56 km NNE of Shwebo, Myanmar
28	2013	030	1359577600	5400	6.8	45	-28.1	-70.6	8389	139	56 km NNE of Vallenar, Chile
29	2013	039	1360323700	7200	6.8	16	-10.9	165.9	9560	-106	21 km SSE of Lata, Solomon Islands
30	2013	134	1368492200	5400	6.8	602	18.7	145.3	9596	-70	40 km W of Agrihan, Northern Mariana Islands
31	2013	271	1380355440	7200	6.8	12	27.2	65.5	13250	-2	85 km NNE of Awaran, Pakistan
32	2013	038	1360264900	7200	6.7	10	-11.0	1 65.6	9587	-106	36 km SSW of Lata, Solomon Islands
33	2013	045	1360848200	5400	6.6	10	67.6	142.6	7025	-25	135 km WSW of Druzhina, Russia
34	2013	110	1366417200	7200	6.6	14	30.3	102.9	11793	-35	56 km WSW of Linqiong, China
35	2013	225	1376409080	3600	6.6	12	5.8	-78.2	5013	119	98 km WSW of Mutis, Colombia
36	2012	298	1351039900	5400	6.5	17	10.1	-85.3	4115	122	Costa Rica
37	2012	316	1352672400	3600	6.5	20	14.1	-92.2	3269	126	Offshore Guatemala
38	2012	321	1353090600	5400	6.5	29	49.3	155.4	7123	-46	Kuril Islands
39	2013	060	1362145100	3600	6.5	29	50.9	157.4	6922	-45	89 km SE of Ozernovskiy, Russia
40	2013	069	1362957300	7200	6.5	29	-6.6	148.2	10914	-93	32 km E of Finschhafen, Papua New Guinea
41	2013	113	1366760300	5400	6.5	23	-3.9	152.1	10380	-92	31 km N of Rabaul, Papua New Guinea
42	2013	166	1371318300	3600	6.5	36	11.7	-87.0	3856	122	46 km W of Masachapa, Nicaragua
43	2013	247	1378262450	5400	6.5	40	51.6	-174.8	5017	-48	77 km SSW of Atka, Alaska
44	2012	224	1344689700	7200	6.4	11	38.3	46.8	11832	14	Northwestern Iran
45	2012	270	1348703200	4200	6.4	16	51.6	-178.3	5261	-48	Andreanof Islands, Aleutian Islands, Alaska
46	2013	032	1359758300	7200	6.4	10	-11.1	165.4	9620	-106	66 km SW of Lata, Solomon Islands
47	2012	269	1348616800	1600	6.3	10	24.7	-110.2	1166	147	Baja California Sur, Mexico
48	2012	302	1351450700	5400	6.3	9	52.7	-132.6	2479	-26	Haida Gwaii, Canada
49	2012	317	1352753200	3600	6.3	9	57.8	-142.8	3336	-28	Gulf of Alaska
50	2012	349	1355481200	3600	6.3	13	31.1	-119.7	411	-132	Off the west coast of Baja California

Table B.1: Earthquakes used in the surface wave analyses in Section 5.4.2 (in gray) and 6.5.3 (all events).

#	Year	Day	Start (ep)	Dur (s)	Mag	Dep (km)	Lat (°)	Lon (°)	Dist (km)	Az (°)	Name
51	2012	223	1344624300	5400	6.2	13	52.6	-167.4	4524	-46	Fox Islands, Aleutian Islands, Alaska
#	Year	Day	Start (ep)	Dur (s)	Mag	Dep (km)	Lat (°)	Lon (°)	Dist (km)	Az (°)	Name
52	2012	304	1351565600	3600	6.2	9	52.4	-131.9	2423	-26	Haida Gwaii, Canada
53	2013	233	1377089010	3600	6.2	20	16.9	-99.4	2521	133	13 km NNW of San Marcos, Mexico
54	2012	313	1352340300	3600	6.1	14	49.2	-128.5	2000	-26	Vancouver Island, Canada region
55	2013	112	1366593600	3600	6.0	30	18.1	-101.9	2249	136	20 km NNW of La Union, Mexico
56	2013	246	1378239800	1800	6.0	6	51.2	-130.4	2262	-26	191 km WSW of Bella Bella, Canada
57	2012	282	1349677600	3600	5.9	14	25.1	-109.6	1155	143	Gulf of California
58	2013	031	1359626500	2400	5.9	10	55.6	-134.7	2821	-24	101 km W of Craig, Alaska
59	2013	247	1378254460	2400	5.9	10	51.2	-129.9	2237	-25	163 km SW of Bella Bella, Canada
60	2013	013	1358094600	2400	5.7	10	25.9	-110.1	1055	143	Gulf of California
61	2013	254	1378904250	2400	5.7	10	-4.6	-104.8	4427	162	Central East Pacific Rise
62	2012	222	1344479800	2400	5.6	10	19.9	-109.3	1675	153	Revilla Gigedo Islands region
63	2012	232	1345363800	2400	5.6	10	47.8	-128.6	1875	-29	Off the coast of Washington
64	2012	239	1346014600	1200	5.5	9	33.0	-115.5	107	127	Southern California
65	2012	279	1349467600	2400	5.5	10	23.6	-108.5	1357	143	Gulf of California
66	2012	239	1346009400	1200	5.4	12	33.0	-115.5	107	128	Southern California
67	2012	295	1350802500	1200	5.4	9	36.3	-120.8	501	-52	Central California
68	2013	264	1379766060	1200	5.4	10	27.8	-105.7	1215	119	20 km WSW of Naica, Mexico
69	2012	240	1346109400	1200	5.2	10	30.5	-113.9	417	144	Gulf of California